UAB
Universitat Autònoma de Barcelona

Probing gravity with weak lensing and clustering from mock galaxy surveys

Cristian Nery Viglione Muñoz

Universitat Autònoma de Barcelona

Doctoral Thesis

Probing gravity with weak lensing and clustering from mock galaxy surveys

Author:
Cristian Nery Viglione Muñoz

Director:
Pablo Fosalba Vela
Tutor:
Rafel Escribano Carrascosa

A thesis submitted in fulfillment of the requirements
for the degree of Doctor of Philosophy

in the

Institute of Space Sciences (ICE-CSIC/IEEC)
Department of Physics

December 10, 2024

UNIVERSITAT AUTÒNOMA DE BARCELONA

Abstract

Department of Physics

Institute of Space Sciences (ICE-CSIC/IEEC)

Doctor of Philosophy

Probing gravity with weak lensing and clustering from mock galaxy surveys

by Cristian Nery Viglione Muñoz

English version

The quest for a theoretical explanation of the Universe's observed accelerated expansion has necessitated the inclusion of the cosmological constant (Λ) as a dark energy component. This constant behaves as a negative pressure, or effectively as "repulsive" gravity, on large cosmological scales. Alternatively, several modified gravity models have been proposed to account for this acceleration without relying on a cosmological constant. The proliferation of these gravity theories has highlighted the need to develop robust methods for testing their validity.

As part of the main project of this thesis, we present the first computation of the gravity model testing parameter E_G using realistic simulated galaxy mocks. The study focuses on measuring the E_G estimator within the framework of General Relativity (GR) and $f(R)$ gravity models, leveraging high-fidelity simulated galaxy catalogs. Our primary aim is to assess the potential of future galaxy surveys to detect deviations from standard gravity using this widely adopted estimator that combines galaxy clustering and weak gravitational lensing. Our findings indicate that, for an all-sky galaxy survey and without accounting for observational systematics, E_G can be estimated accurately and with minimal bias for both gravity models across all redshifts. However, the error bars are too large to definitively distinguish between the theories. Alternatively, we propose a straightforward null test of gravity based on redshift-space distortion (RSD) clustering. This test suggests that, with precise modeling of small-scale behavior in future galaxy surveys, significant departures from standard gravity could potentially be detected.

We developed tools to probe gravity from 2-point correlation functions for galaxy clustering and galaxy weak lensing. For galaxy clustering, we primarily conducted linear galaxy bias calculation using angular power spectra and growth rate estimates derived from multipoles of the correlation function. For gravitational lensing, we computed the magnification bias factor and performed 3×2pt analyses on GR and $f(R)$ galaxy mocks. This expertise enabled us to deliver accurate calculations for various forecasts for the *Euclid* mission and some minor contributions for the DESI mission.

In this thesis, we detail the methodologies and tools developed throughout the PhD research, which facilitated the achievement of these results. These tools include advanced techniques for calculating galaxy clustering and lensing statistics, which also served to validate the simulated

mocks used in the study. During this process, we identified and resolved errors in the generation of the dark matter and galaxy catalogs through persistent testing and troubleshooting. While these setbacks delayed progress and complicated the production of final results, they provided valuable insights into theoretical implementations and cosmological simulations, ultimately enriching our understanding of these topics.

Spanish version

La búsqueda de una explicación teórica para la expansión acelerada observada del Universo ha requerido la inclusión de la constante cosmológica (Λ) como un componente de energía oscura. Esta constante actúa como una presión negativa o, efectivamente, como una "gravedad repulsiva" a escalas cosmológicas grandes. Alternativamente, se han propuesto varios modelos de gravedad modificada para explicar esta aceleración sin depender de la constante cosmológica. La proliferación de estas teorías de gravedad ha resaltado la necesidad de desarrollar métodos sólidos para probar su validez.

Como parte del proyecto principal de esta tesis, presentamos el primer cálculo del parámetro E_G para probar modelos de gravedad utilizando catálogos simulados de galaxias realistas. El estudio se centra en medir el estimador E_G en el marco de la Relatividad General (GR) y los modelos de gravedad $f(R)$, aprovechando catálogos simulados de galaxias de alta fidelidad. Nuestro objetivo principal es evaluar el potencial de futuras sondas de galaxias para detectar desviaciones de la gravedad estándar utilizando este estimador ampliamente adoptado que combina *galaxy clustering* y *galaxy lensing*. Nuestros resultados indican que, para una población de galaxias de todo el cielo y sin considerar sistemáticas observacionales, E_G puede ser estimado con precisión y con sesgo mínimo para ambos modelos de gravedad en todos los *redsfhits*. Sin embargo, las barras de error son demasiado grandes para distinguir de manera concluyente entre las teorías. Como alternativa, proponemos una hipótesis nula sencilla de la gravedad basada en el *clustering* de distorsiones en el espacio de *redshifts* (RSD). Esta prueba sugiere que, con un modelado preciso del comportamiento a pequeña escala en futuras sondas de galaxias, podrían detectarse potencialmente desviaciones significativas de la gravedad estándar.

Hemos desarollado herramientos para calcular las funciones de correlación de dos puntos para *galaxy clustering* y el *galaxy weak lensing*. Para *galaxy clustering*, realizamos principalmente cálculos del *linear galaxy bias* utilizando *angular power spectrums* y del *growth rate* utilizando los multipolos de la función de correlación. Para *galaxy lensing*, calculamos el factor del *magnification bias* y realizamos análisis 3×2pt en simulaciones de galaxias bajo GR y $f(R)$. Esta experiencia nos permitió realizar cálculos precisos para diversas predicciones de la misión *Euclid* y algunas contribuciones menores a la misión DESI.

En esta tesis, detallamos las metodologías y herramientas desarrolladas a lo largo de la investigación doctoral, las cuales facilitaron la obtención de estos resultados. Estas herramientas incluyen técnicas avanzadas para calcular las estadísticas del *clustering* y *lensing* de galaxias, que también sirvieron para validar los catálogos simulados utilizados en el estudio. Durante este proceso, identificamos y resolvimos errores en la generación de los catálogos de materia oscura y galaxias mediante pruebas persistentes y procesos de depuración de código. Aunque estos contratiempos retrasaron el progreso y complicaron la obtención de los resultados finales, proporcionaron valiosas perspectivas sobre las implementaciones teóricas y las simulaciones cosmológicas, enriqueciendo en última instancia nuestra comprensión de estos temas.

Acknowledgements

"I never wanted to save the world or make everyone happy. I never wanted to play God like that. If I could just save my family, and my friends... If I could just be a hero like that, I'd be happy." —Kyoko Sakura

En primer lugar, quiero expresar mi más sincero agradecimiento a mi familia por su constante apoyo a lo largo de estos años. En especial, a mis padres, quienes me han respaldado y acompañado en los momentos buenos y malos de mi investigación. Aunque sé que nunca podré devolverles todo lo que me han dado, espero al menos que puedan mirar esta tesis con orgullo, a pesar de que, seguramente no entiendan su contenido, pese a su apreciado intento. A mis dos hermanos, Matías y Enelí, quienes siempre han sido inseparables de mí. Siempre los he considerado más como mis iguales y grandes amigos que como mis hermanos menores. A mi cuñado Frank, el único nuevo integrante de la familia desde que nos mudamos a este país. Gracias por abrir un nuevo capítulo de felicidad en la vida de mi hermana y por brindarnos, con vuestra boda, un recuerdo hermoso junto a quienes pudieron acompañarnos en ese viaje.

También quiero agradecer a toda mi familia en Argentina, con quienes había perdido contacto después de nuestra mudanza a Cataluña hace 20 años. Sin embargo, este lazo se renovó cuando me surgió la oportunidad de venir a investigar, por pura coincidencia, a Córdoba, Argentina, mi ciudad natal, gracias al programa LACEGAL. Esta experiencia me permitió estar en el Instituto de Astronomía Teórica y Experimental, a menos de un kilómetro de donde vivía mi abuela, mientras esperaba la beca FPI para hacer el doctorado. Así que también agradezco profundamente a mi abuela, quien me recibió con los brazos abiertos y me cuidó con mucho cariño, de la misma manera que lo hizo el resto de la familia de Córdoba, Laborde y Pergamino, con especial mención a mi tía Marlene y a Diego, durante esos tres meses tan significativos para mí. También quiero mencionar a mis primos Mady, Álex, Leo, Ely y Benja, con quienes, tras recuperar el contacto, hemos mantenido una cercanía inquebrantable junto con mis hermanos, a pesar de la distancia. La pandemia nos brindó una oportunidad para organizar actividades en línea que realizamos todas las semanas, lo cual fortaleció aún más nuestra relación. A mi madrina Gaby, que aunque nunca se me ha dado bien seguir sus guías religiosas, valoro profundamente sus palabras y el interés que siempre ha mostrado por mi trabajo.

Quiero expresar mi más profundo agradecimiento a mi director de tesis, Pablo Fosalba, por su invaluable apoyo y guía a lo largo de estos años. Fue él quien me abrió las puertas al fascinante mundo de la investigación en cosmología, despertando en mí un interés que ya había germinado desde pequeño, cuando soñaba con explorar el espacio. Antes de terminar mi carrera en Física, tuve la oportunidad de realizar mis prácticas externas bajo su dirección, experiencia que marcó un antes y un después en mi camino académico. La paciencia, dedicación y amabilidad de Pablo hicieron que mi aprendizaje sobre los conceptos fundamentales de la cosmología y sus aplicaciones a modelos teóricos y observaciones fuera no solo enriquecedor, sino también placentero. Gracias a su guía, fui construyendo paso a paso mi carrera en la investigación, desde el máster y una estancia de tres meses en Argentina hasta el inicio y ahora la culminación de mi doctorado. Ha sido un viaje largo, lleno de retos y experiencias gratificantes, aunque no exento de momentos frustrantes. Sin embargo, el apoyo constante de Pablo hizo que esos obstáculos fueran más llevaderos, y su orientación fue clave para superar cada desafío. No cabe duda de que he llegado hasta aquí gracias a su ayuda.

A mis compañeros de investigación cercanos, la amabilidad y la experiencia de Isaac Tutusaus, así como las interacciones de estudiante de PhD a estudiante de PhD con Marc Alemany, me fueron invaluables para discutir y mejorar mi metodología.

I am also grateful to Francesca Lepori, the project leader of all my collaborations with Euclid, whose composure and determination were crucial in helping me achieve the best possible results, despite my delays due to being constantly occupied with other tasks.

También quiero mencionar a otros compañeros de PhD: Pablo Renard, Benjamin Camacho y mi viejo amigo y compañero de despacho Iván Martín, con quienes estuve muy cerca durante el PhD y pude compartir experiencias y dudas, así como muy buenos recuerdos, dado nuestros gustos tan similares. Nuestro peculiar Music Club virtual durante la pandemia siempre será un gran recuerdo que quedará entre nosotros.

A la gente del IATE, que me dieron un trato excepcional: Diego Lambas, el director, que me dio una gran bienvenida y se aseguró de que siempre estuviese a gusto en el instituto; Elizabeth González y Martín Chalela, quienes me guiaron con gran amabilidad durante mi estancia. Y, por último, a mis compañeros de despacho del IATE, Laura Baravalle y Gabriel Oio, con quienes compartí buenos momentos y muchos mates.

A els meus bons amics fora del món de la investigació: Sergi Sánchez, amb qui sempre puc comptar i passar una bona estona, i Oriol Nadal, que sempre està disposat a escoltar-me i donar-me qualsevol tipus de consell.

I would also like to express my gratitude to those who indirectly contributed to the completion of this thesis by providing efficient public codes (such as pyCCL, MultiNest, FCFC, COMET and Polspice) that enabled complex cosmological calculations. A special thanks goes to David Alonso, whose pyCCL code was not only incredibly helpful for every project in this thesis, but who also offered valuable quick support whenever I encountered issues or doubts regarding the code.

This work has made use of CosmoHub, developed by PIC (maintained by IFAE and CIEMAT) in collaboration with ICE-CSIC. It received funding from the Spanish government (grant EQC2021-007479-P funded by MCIN/AEI/10.13039/501100011033), the EU NextGeneration/PRTR (PRTR-C17.I1), and the Generalitat de Catalunya.

Contents

A mi primo Álex, con quien compartí muchas risas, sueños e intereses, incluyendo un amor por los misterios del Universo. Espero que, desde algún rincón de las estrellas, siga velando por este camino y guiando mi rumbo.

To my cousin Álex, with whom I shared many laughs, dreams, and interests, including a love for the mysteries of the Universe. I hope that, from some corner of the stars, he continues to watch over this journey and guide my path.

"Those who are no longer with us receive more flowers than those still here because regret is stronger than gratitude"
—Violet Evergarden

—My Journey through the Cosmos—

"When you hit the point of no return, that's the moment it truly becomes a journey. If you can still turn back, it's not really a journey."
—Atsuko Ishizuka, A Place Further than the Universe

"Those who seek out the truth must not be arrogant. You must not laugh at miracles just because they cannot be explained scientifically. You must not turn away from the beauty of this world."
—Kotomi Ichinose, Clannad

"Never think the stars you see are all the stars there are."
—Atsuko Ishizuka, A Place Further than the Universe

"Nothing Is True, Everything Is Permitted."
—Ezio Auditore da Firenze

Chapter 1

Cosmological background

Cosmology, as the scientific study of the universe in its entirety, seeks to unravel the mysteries of its origin, evolution, structure, and ultimate fate. It encompasses a wide range of phenomena that can be observed and deduced from the electromagnetic waves (mostly light) that arrives us. Due to the limited speed of the light, our telescopes capture light emitted at different time periods allowing us to obtain information of the formation and evolution of the universe. Cosmologists have formulate many theoretical predictions in order to explain and reproduce the history and the contents of our Universe which are included on the current most accepted standard model of cosmology known as Lambda cold dark matter (or ΛCMD). This model despise having many observational agreements is still under testing since there are many things that cosmologists do not understand. One of this things is the very same substance that gives the Λ name to the model. Describing this model will be the starting point to the theoretical framework since current alternative theories to this paradigm are derived from it due its impressive validity with current observations. In this introductory chapter we provide descriptions and information for key concepts in cosmology that will be crucial to understand the previous chapters of this thesis.

1.1 The Cosmological principle

The cosmological principle is a foundational concept in cosmology which asserts that, when observed on sufficiently large scales, the Universe exhibits two key characteristics: homogeneity and isotropy.

Homogeneity refers to the idea that the Universe, when viewed over large distances, is uniform and appears the same in its structure and composition. This means that, on these vast scales, there is no special or preferred location within the Universe; every region of the Universe has a similar distribution of matter and energy.

Isotropy, on the other hand, implies that the Universe looks the same in all directions when observed from any given point. This means that, regardless of the direction in which we look, the overall appearance of the Universe remains the same, with no particular direction being unique or different from any other.

The cosmological principle suggests that when the Universe is viewed on a sufficiently large scale, the properties of the universe are the same for all observers. This amounts to the strongly philosophical statement that the part of the universe which we can see is a fair sample, and that the same physical laws apply throughout. In essence, this in a sense says that the universe is knowable and is playing fair with scientists [96].

The principle breaks down at sufficient small scales due to formation of matter structures. It is apparent that when we see at the sky we can see different structures in different directions:

like planets, stars, galaxies, clusters, etc... which breaks isotropic. The same can be said about homogeneity since there are regions of the universe with less matter, like voids, and some with more, like galaxy clusters. But this idea of the cosmological principle at sufficient large scales, which implies that we are not in any special part of the universe, was vital to formulate the idea of the Big Bang theory as we will see in the following chapters.

1.2 The expanding universe and Hubble's Law

In 1929, the astronomer Edwin Hubble observed and determined the distances and radial velocities of numerous galaxies, discovering that the majority were receding from us, with their speed increasing the farther they were from Earth.

Hubble's Law describes the relationship between the radial velocity v_z of a galaxy and its distance from an observer on Earth [99]:

$$v_z = zc = H_0 d \tag{1.1}$$

In this equation, z represents the redshift of the galaxy's observed spectrum. This redshift occurs because the wavelength of light stretches as it travels through the expanding universe, causing the galaxy's spectrum to shift toward the red end. By measuring this redshift, we can determine the velocity at which the galaxy is receding from us. The Hubble constant, H_0, quantifies the rate of this expansion and is defined as the inverse of a time period. The existence of this constant H_0 indicates that the universe is expanding, with more distant galaxies receding faster due to the greater amount of space between them and us.

The Hubble constant also serves as a biased estimator of the universe's age. Specifically, $\frac{1}{H_0}$ represents the time when the universe was compressed into a single point. Since H_0 is time-dependent, its current value is approximately $100\,h\,\mathrm{km/s/Mpc}$, where h denotes the measurement uncertainty. Recent observations suggest h is between 0.68 and 0.74 [7], which corresponds to an estimated age of 14.4 billion years. However, this estimate assumes non-accelerated expansion, which is not the case for our Universe.

Since the Hubble parameter depends on time, for galaxies at different distances from us the observed light comes from different times due to the finite speed of the light. Then the Hubble's law expressed in Eq. (1.1) is only valid for small distances and therefore is called the local Hubble's law. To account for this, we introduce the scale factor of the universe, a, which ranges from 0 at the Big Bang to 1 at the present time. This scale factor represents the relative size of the universe compared to its current size. For example, $a = 0.2$ indicates the time when the Universe was five times smaller.

The scale factor a relates proper coordinates to comoving coordinates, which do not change with the Universe expansion, as described in:

$$dr = a(t)\, d\chi \tag{1.2}$$

This equation shows that, by convention, the comoving coordinates match the proper coordinates at the present time. It also implies that:

$$dv = \frac{dr}{dt} = \frac{da(t)}{dt}\, d\chi = \frac{\dot{a}}{a}\, dr = H\, dr \tag{1.3}$$

Here, $H \equiv \frac{\dot{a}(t)}{a(t)}$ indicates that H is a function of time. Combining Equations (1.1) and (1.3), we get:

$$zc = c\frac{d\lambda}{\lambda} = \frac{\dot{a}}{a}\,dr = c\frac{da}{a} \rightarrow \frac{da}{a} = \frac{d\lambda}{\lambda} \tag{1.4}$$

This result implies that, during a short time interval dt, the fractional change in a photon's wavelength is equal to the fractional increase in the universe's size. This phenomenon is known as cosmological redshift. From this, we derive:

$$z = \frac{\lambda_{observed} - \lambda_{emitted}}{\lambda_{emitted}} = \frac{a(t_{reception}) - a(t_{emission})}{a(t_{emission})} \tag{1.5}$$

Taking the reception time as the present time ($a = 1$), we get:

$$a(t) = \frac{1}{1+z} \tag{1.6}$$

This equation directly relates the observed redshift to a specific time in the universe's history, reflecting its relative size. Since redshift is easier to measure, this method effectively estimates cosmic time.

Using Eq. 1.4, we can derive the exact form of Hubble's Law for an arbitrary $H(t)$ over a time interval (t_1, t_2):

$$z = \frac{da}{a} = \frac{1}{a}\int_{t_1}^{t_2} \frac{da}{dt}\,dt = \frac{1}{a}\int_{t_1}^{t_2} a(t)\,H(t)\,dt \tag{1.7}$$

The adimensional reduced Hubble constant is normally used, which is defined as:

$$h \equiv \frac{H_0}{100\ \text{km/s/Mpc}} \tag{1.8}$$

1.3 The Metric of the Universe

As presented in Eq. 1.2, the scale factor is the key to describe an expanding universe transforming from comoving distance to the proper distances at any given time. Typically, a metric is used to carry out this transformation, providing an essential framework for making quantitative predictions within a universe in constant expansion. The metric that accurately describes an expanding, homogeneous, and isotropic universe is the FLRW[1] metric [58]. Using General Relativity this metric can be derived as an exact solution to Einstein field equations, but its general form can be derived from the fundamental principles of homogeneity and isotropy without directly invoking Einstein's equations. In this context, the spacetime interval ds in spherical coordinates is represented as:

$$ds^2 = -c^2dt^2 + a^2(t)\left(d\chi^2 + f_k^2(\chi)d\Omega^2\right), \tag{1.9}$$

[1] Which is an abbreviation of the names of the scientists that developed this metric: Friedmann, Lemaître, Robertson and Walker

where χ is the radial comoving distance, Ω represents the solid angle, and f_k is a function that accounts for the radius of curvature k of the space, expressed as:

$$f_k(\chi) = \begin{cases} \sqrt{k}^{-1} \sin(\chi\sqrt{k}) & \text{if } k = +1 \text{ (closed space)}, \\ \chi & \text{if } k = 0 \text{ (flat space)}, \\ \sqrt{|k|}^{-1} \sinh(\chi\sqrt{|k|}) & \text{if } k = -1 \text{ (open space)}. \end{cases} \tag{1.10}$$

The curvature parameter k has units of length^{-2}. A positive curvature indicates a spherical or closed Universe, whereas a negative curvature corresponds to a hyperbolic or open Universe. However, since observational data suggests that the universe is flat or nearly flat, this thesis will proceed under the assumption that the Universe is completely flat.

One of the key advantages of this metric is its capacity to incorporate gravity directly. Rather than treating gravity like an external force influencing objects with mass within a gravitational field, this metric integrates gravity into the structure of space-time itself, allowing particles to move freely within this curved framework. This approach is especially important for understanding phenomena such as gravitational lensing, which will be examined later in this thesis, as it requires analyzing light propagation through a not completely homogeneous universe.

1.4 The Cosmic Microwave Background

The Cosmic Microwave Background (CMB) is the radiation emitted from the last scattering surface during the epoch of recombination at redshift $z \approx 1100$. As the Universe expands, the temperature of this radiation decreases due to the stretching of wavelengths, as described in the previous section. In the Big Bang model, the Universe began in a hot, dense state where electrons could not bind to nucleons. Consequently, photons were unable to escape the plasma because free electrons caused Thompson scattering over short distances. Once the Universe cooled to a temperature of approximately 3300 K, the first atoms began to form, allowing electrons to decouple from matter and travel freely through space. The CMB is composed of these photons, which have now reached us. These photons have also been redshifted by the cosmological expansion, resulting in a measured temperature of approximately 2.73 K [99]. This corresponds well with the results predicted by Eq. 1.4 for black-body radiation which became a good indicator of the validity of the Hubble parameter and the Big Bang Theory as a whole.

The CMB radiation is nearly isotropic in all directions; however, precise instruments have detected small variations of around 10^{-4} K. These anisotropies arise from inhomogeneities in the atom distribution at the time of recombination, caused by initial quantum fluctuations. These fluctuations created density variations in the primordial Universe, as described by Eq. (1.11), causing photons escaping these regions to expend more energy to overcome higher gravitational potentials, resulting in slightly higher cooling. This phenomenon is known as gravitational redshift.

$$\delta = \frac{\rho - \bar{\rho}}{\rho} \tag{1.11}$$

where $\bar{\rho}$ is the mean density of the Universe. These density fluctuations grew linearly over time by accreting more matter due to their increased gravitational influence. Eventually, these fluctuations became large enough to form the large-scale structures observed today, resulting in an inhomogeneous Universe on small scales. On these scales, fluctuations grow non-linearly,

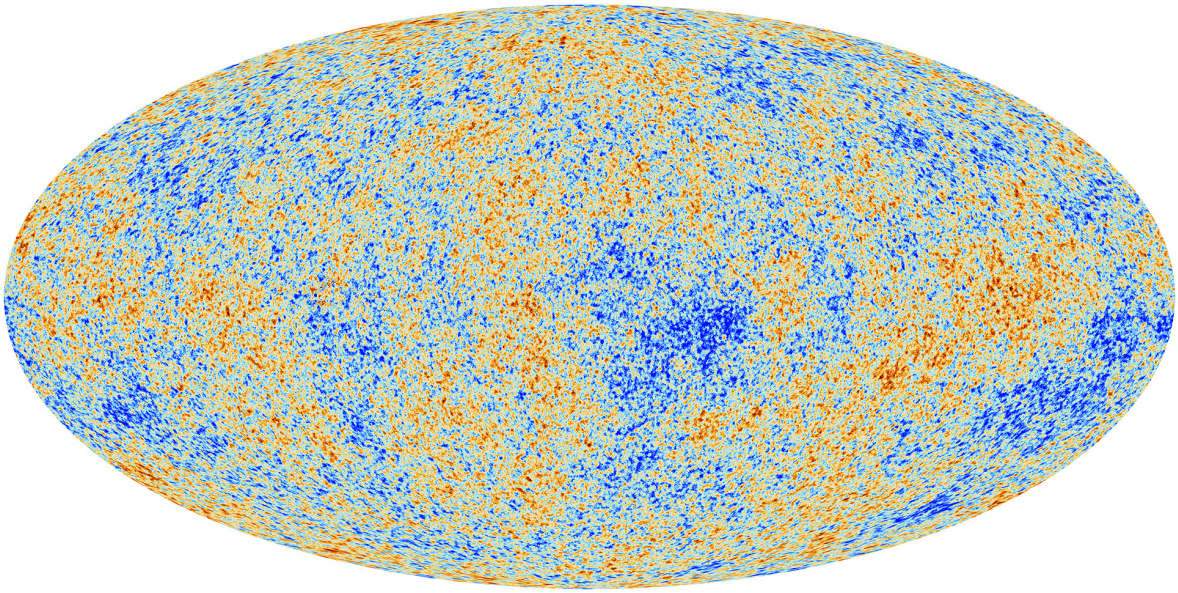

FIGURE 1.1: Full sky map of the CMB with observable anisotropies as color variations: warmer regions are redder and cooler are bluer. Image obtained with Planck

necessitating approaches such as higher-order perturbation theory or non-analytic models like N-body simulations (see Chapter 3).

The CMB anisotropies provide valuable information. They not only reveal the initial mechanisms that seeded large cosmological structures but also offer insights into the composition and geometry of the Universe. By measuring the angular spectrum of the CMB small temperature anisotropies (see Section 2.6.4) and comparing them to theoretical predictions, we infer that the Universe is flat, with $\Omega_{\text{tot}} = 1$. Currently, uncertainties in the value of Ω_{tot} make it challenging to conclusively determine the Universe's flatness. Since as the flatness problem establishes is hard to believe that from all the possible values that Ω_{tot} could take it had to be exactly 1. From the CMB angular spectrum, we also deduce the Universe's composition, obtaining present-day density values: $\Omega_{0,b} \approx 0.05$, $\Omega_{0,\text{DM}} \approx 0.27$, $\Omega_{0,r} \approx 5 \times 10^{-5}$, and $\Omega_{0,\Lambda} \approx 0.68$ [7].

Since the CMB is sensitive to the total matter distribution along its path to the observer, this allows us to infer details regarding structure evolution in the Universe. In this regard, cosmologists have used the gravitational lensing of CMB to study the evolution of density perturbations.

1.5 The ΛCDM model

The ΛCDM model serves as the prevailing framework for describing the Universe. This model establishes an expanding, accelerating Universe driven by a mysterious component known as Dark Energy, characterized by the cosmological constant Λ. The majority of the Universe's mass consists of Cold Dark Matter (CDM), which is non-relativistic and clusters under gravitational influence in matter halos, where galaxies reside. Dark Matter, which does not emit light, is inferred through its gravitational effects, with gravitational lensing providing a crucial method for mapping the Universe's mass distribution by observing the deflection of light caused by Dark Matter's gravitational pull.

The ΛCDM model integrates the theory of the Big Bang as the origin of the Universe, adhering to the cosmological principle that the Universe is homogeneous and isotropic on large scales. It is compatible with the concept of cosmological inflation, which explains the uniformity and fluctuations observed in the Cosmic Microwave Background (CMB). Furthermore, the model assumes that General Relativity governs gravitational interactions on cosmological scales.

In this model, the Universe is described as flat (Euclidean), comprising Dark Energy (Λ), Dark Matter (CDM), baryonic matter, and radiation.To fully specify the ΛCDM model, one must provide the values of Ω_m, Ω_b, the Hubble constant H_0, the optical depth at reionization τ, the spectral index n_s, and the curvature fluctuation amplitude A_s (or σ_8). All other cosmological parameters can be derived from these six fundamental values which will be covered in the following chapters.

1.6 General Theory of Relativity

Einstein's Theory of General Relativity (GR) describes gravity as a geometric property of space and time, providing an extension to Newton's law of universal gravitation and special relativity. According to this theory, the presence of mass and energy distorts the space-time fabric, causing objects to travel along paths called geodesics, which represent the paths of least action in a curved space-time framework, unless influenced by an external force. This curvature results in the bending of light along geodesic lines, directing it towards masses that distort space-time.

1.6.1 Einstein–Hilbert action

The usual starting point to GR is the Einstein–Hilbert action, which is the one that encapsulates the dynamics of the gravitational field in general relativity. This action allows to obtain the Einstein's field equations which are a fundamental part of this theory. It takes the following form[2] [149]:

$$S_{\mathrm{EH}} = \frac{1}{2\kappa} \int R\sqrt{-g}\, d^4x, \tag{1.12}$$

In this equation, $\kappa = 8\pi G$ where G is the gravitational constant, g is the determinant of the metric, R is the Ricci scalar related to the Ricci tensor : $R = g_{\mu\nu}R^{\mu\nu}$. The Ricci tensor depends on the metric and its derivatives:

$$R_{\mu\nu} = \frac{\partial \Gamma^{\lambda}_{\lambda\mu}}{\partial x^{\nu}} - \frac{\partial \Gamma^{\lambda}_{\mu\nu}}{\partial x^{\lambda}} + \Gamma^{\lambda}_{\mu\sigma}\Gamma^{\sigma}_{\nu\lambda} - \Gamma^{\lambda}_{\mu\nu}\Gamma^{\sigma}_{\nu\sigma} \tag{1.13}$$

Here, $\Gamma^{\lambda}_{\mu\nu}$ denotes the Christoffel symbols of the second kind:

$$\Gamma^{\lambda}_{\mu\nu} = \frac{1}{2} g^{\lambda\kappa} \left(\frac{\partial g_{\kappa\mu}}{\partial x^{\nu}} + \frac{\partial g_{\kappa\nu}}{\partial x^{\mu}} - \frac{\partial g_{\mu\nu}}{\partial x^{\kappa}} \right) \tag{1.14}$$

The FLRW metric in this notation can be defined as a 4-dimensional manifold:

[2] For simplicity, natural units where $c = 1$ are assumed.

$$g_{\mu\nu} = \begin{pmatrix} c^2 & 0 & 0 & 0 \\ 0 & -a(t)^2 & 0 & 0 \\ 0 & 0 & -a(t)^2 & 0 \\ 0 & 0 & 0 & -a(t)^2 \end{pmatrix} \tag{1.15}$$

The first element on the diagonal, g_{00}, corresponds specifically to the time coordinate, while the remaining diagonal elements, g_{11}, g_{22}, and g_{33}, represent the spatial components of the metric. The absolute value of g_{00} is equal to c, the speed of light.

Returning to (1.12), we need to incorporate a Lagrangian term, $\mathcal{L}_{\mathrm{M}}$, corresponding to the matter field and the cosmological constant in order to account to the accelerated expansion of the Universe.

$$S = \int \left[\frac{1}{2\kappa}(R - 2\Lambda) + \mathcal{L}_{\mathrm{M}} \right] \sqrt{-g}\ \mathrm{d}^4x \tag{1.16}$$

This Lagrangian is related to the energy-momentum tensor $T_{\mu\nu}$, which assuming a perfect isotropic fluid can be expressed as:

$$T^{\mu\nu} = \begin{pmatrix} \rho & 0 & 0 & 0 \\ 0 & -p & 0 & 0 \\ 0 & 0 & -p & 0 \\ 0 & 0 & 0 & -p \end{pmatrix}, \tag{1.17}$$

where ρ is the density and p is the pressure. The non-diagonal components are zero to preserve isotropy, as required by the cosmological principle. The energy-momentum tensor $T_{\mu\nu}$ is symmetric, with components representing energy density T_{00}, energy flux or momentum density T_{0i}, pressure T_{ii}, and momentum flux or shear stress T_{ij}.

1.6.2 Einstein's field equations

Einstein's field equations encapsulate General Relativity, detailing the core relationship between space-time and mass/energy. Solving these non-linear differential equations for a homogeneous and isotropic universe yields the FLRW metric, as described in section 1.3. However, gravitational lensing requires consideration of the Universe's inhomogeneities on smaller scales. In this section we will perform the derivation of these equations [149].

With the action defined in (1.16) we can apply the stationary-action principle, which tells us that the variation of the action with some fixed constraints is zero.

$$\delta S = 0 \tag{1.18}$$

where the variation of each component is given by:

$$\delta(\sqrt{-g}) = -\frac{1}{2\sqrt{-g}}\delta g = \frac{1}{2}\sqrt{-g}\,(g^{\mu\nu}\delta g_{\mu\nu}) = -\frac{1}{2}\sqrt{-g}\,(g_{\mu\nu}\delta g^{\mu\nu}) \tag{1.19}$$

$$\frac{\delta R}{\delta g^{\mu\nu}} = R_{\mu\nu} \tag{1.20}$$

$$\delta\Lambda = 0 \tag{1.21}$$

$$T_{\mu\nu} = -2\frac{\delta\mathcal{L}_{\mathrm{M}}}{\delta g^{\mu\nu}} + g_{\mu\nu}\mathcal{L}_{\mathrm{M}} \tag{1.22}$$

For the last equation the definition for the energy-momentum tensor has been used and its relation to the matter Lagrangian. The same goes to the Ricci scalar and its relation to the Ricci tensor.

If we apply the variation to the Einstein–Hilbert action:

$$\begin{aligned}\delta S = \int \Bigg[& \frac{\sqrt{-g}}{2\kappa}\frac{\delta R}{\delta g^{\mu\nu}} + \frac{R}{2\kappa}\frac{\delta\sqrt{-g}}{\delta g^{\mu\nu}} \\ & - \frac{\Lambda}{\kappa}\frac{\delta\sqrt{-g}}{\delta g^{\mu\nu}} + \sqrt{-g}\frac{\delta\mathcal{L}_{\mathrm{M}}}{\delta g^{\mu\nu}} + \mathcal{L}_{\mathrm{M}}\frac{\delta\sqrt{-g}}{\delta g^{\mu\nu}}\Bigg]\delta g^{\mu\nu}\,\mathrm{d}^4x\end{aligned} \tag{1.23}$$

So now we can apply the relation of the action principle defined in (1.18) to the expression in brackets in the previous equation:

$$\frac{1}{2\kappa}\frac{\delta R}{\delta g^{\mu\nu}} + \frac{R}{2\kappa}\frac{1}{\sqrt{-g}}\frac{\delta\sqrt{-g}}{\delta g^{\mu\nu}} - \frac{\Lambda}{\kappa}\frac{1}{\sqrt{-g}}\frac{\delta\sqrt{-g}}{\delta g^{\mu\nu}} + \frac{\delta\mathcal{L}_{\mathrm{M}}}{\delta g^{\mu\nu}} + \frac{\mathcal{L}_{\mathrm{M}}}{\sqrt{-g}}\frac{\delta\sqrt{-g}}{\delta g^{\mu\nu}} = 0 \tag{1.24}$$

where we have divided everything by $\sqrt{-g}$. Now we can use the relations defined in (1.19) and (1.20) to obtain:

$$\frac{1}{2\kappa}R_{\mu\nu} - \frac{R}{4\kappa}g_{\mu\nu} + \frac{\Lambda}{2\kappa}g_{\mu\nu} + \left(\frac{\delta\mathcal{L}_M}{\delta g^{\mu\nu}} - \mathcal{L}_M\frac{g_{\mu\nu}}{2}\right) = 0 \tag{1.25}$$

Multiply by 2κ:

$$R_{\mu\nu} - \frac{R}{2}g_{\mu\nu} + \Lambda g_{\mu\nu} + \kappa\left(2\frac{\delta\mathcal{L}_M}{\delta g^{\mu\nu}} - \mathcal{L}_M g_{\mu\nu}\right) = 0 \tag{1.26}$$

Apply relation (1.22):

$$R_{\mu\nu} - \frac{R}{2}g_{\mu\nu} + \Lambda g_{\mu\nu} - \kappa T_{\mu\nu} = 0 \tag{1.27}$$

Finally we express the final relation with the energy term to the right and using $\kappa = 8\pi G$ to obtain the Einstein field equation:

$$R_{\mu\nu} - \frac{1}{2}Rg_{\mu\nu} - \Lambda g_{\mu\nu} = 8\pi G T_{\mu\nu}. \tag{1.28}$$

1.6.3 Friedmann equation

In the FLRW metric, the scale factor $a(t)$ is the only parameter that changes with time in a flat Universe. Understanding and predicting the evolution of $a(t)$ is fundamental to any

cosmological model. By using (Eq. 1.28), the Friedmann equations establish a link between $a(t)$ and the contents of the Universe.

Although the Einstein field equation are complex, the FLRW metric simplifies it into an exact solution. Within this framework, the Christoffel symbols from (Eq. 1.14) vanish when involving two or three temporal indices, leaving two types of non-zero Ricci tensor components: R_{00} and R_{ij}. Using the FLRW metric with zero curvature ($k = 0$) [58]:

$$R_{00} = -3\frac{\ddot{a}}{a}, \quad T_{00} = \rho, \quad g_{00} = 1 \tag{1.29}$$

While the Ricci scalar is given by:

$$R = -\frac{6}{a^2}\left(\ddot{a}a + \dot{a}^2 + k\right) \tag{1.30}$$

Applying these results to Eq. 1.28 with $\mu, \nu = 0$:

$$3\left(\frac{\dot{a}}{a}\right)^2 + 3\frac{k}{a^2} - \Lambda c^2 = 8\pi G\rho, \tag{1.31}$$

which can be rewritten as:

$$\left(\frac{\dot{a}}{a}\right)^2 = \frac{8\pi G}{3}\rho + \frac{\Lambda}{3} - \frac{k}{a^2} = H^2 \tag{1.32}$$

This differential equation, known as the first Friedmann equation, describes how the rate of change of the scale factor is connected to the physical properties of the Universe.

Now, considering the spatial components with $i = j$:

$$R_{ij} = -g_{ij}\left(\frac{2k + 2\dot{a}^2 + a\ddot{a}}{a^2}\right), \quad T_{ij} = -p, \quad g_{ij} = -a^2 \quad (i = j) \tag{1.33}$$

and substituting them into Eq. 1.28:

$$\frac{\ddot{a}}{a} + \frac{1}{2}\left(\frac{\dot{a}}{a}\right)^2 = -4\pi G p + \frac{\Lambda}{2} - \frac{k}{2a^2}$$

Subtracting half of the first Friedmann equation from this yields the second Friedmann equation:

$$\frac{\ddot{a}}{a} = \dot{H} + H^2 = -\frac{4\pi G}{3}(3p + \rho) + \frac{\Lambda}{3} \tag{1.34}$$

This time the equation describes how the scale factor acceleration is connected to the physical properties of the Universe.

1.7 Fundamental Components of the Cosmos

In order to continue the relation between Universe's physical properties and the energy content we need to account for all the different energy components since each one of them has evolved in a different manner due to the expansion [58].

1.7.1 Radiation

Radiation consists of massless photons, with their energy determined by their wavelength:

$$E = \frac{h_P c}{\lambda_\gamma}, \tag{1.35}$$

where h_P represents the Planck's constant (where the index P is used to distinguish it from the reduced Hubble parameter), and λ_γ is the photon's wavelength. This relationship has significant consequences: as the Universe expands, the density of radiation decreases due to the increasing volume, and the energy/frequency of the photon also diminishes, as their wavelength stretches in proportion to the scale factor a. Since the photon density scales inversely with the cube of a and their energy scales inversely with a, the energy density of radiation scales inversely with the fourth power of a. Thus,

$$\rho_r = \rho_{r0} a^{-4}. \tag{1.36}$$

1.7.2 Matter and Dark Matter

Matter can be related to energy using Einstein's mass-energy equivalence principle:

$$E = mc^2, \tag{1.37}$$

indicating that energy and mass are directly proportional. The Universe can be considered a closed system so matter conservation can be assumed, then the energy density of matter depends solely on the volume. The matter energy density decreases because the same amount of energy is spread over a larger volume when the Universe increases in size. Since space has three dimensions, any physical volume scales with the cube of the scale factor $a(t)$, leading to the matter energy density being inversely proportional to the cube of the distance. Setting the current scale factor $a(t_0) = 1$ and denoting the present-day matter density as ρ_{m0}, the matter density at any time t can be related to the current density by:

$$\rho_m = \frac{\rho_{m0}}{a^3}. \tag{1.38}$$

This density encompasses both visible matter (baryonic matter) and dark matter. Dark matter is inferred from multiple observations (e.g., galaxy rotation curves, gravitational lensing) but remains undetected by direct means, with its exact nature still unknown. Also, dark matter is typically considered to interact only through gravity, which means that it does not experience collision due to electromagnetic repulsion nor emits or absorbs electromagnetic radiation. However, on cosmological scales, where gravity dominates, both baryonic and dark matter can be treated similarly in their gravitational effects.

1.7.3 Dark Energy

The cosmological constant, Λ, from Eq. (1.28), can be interpreted as a form of energy density that remains constant over time, independent of the scale factor $a(t)$. To integrate this constant energy density into the total energy density of the universe, it must share the same units as the matter and radiation energy densities, which is expressed as:

$$\rho_\Lambda = \frac{\Lambda}{8\pi G}. \tag{1.39}$$

Since Λ is constant, this implies:

$$\rho_\Lambda = \rho_{\Lambda 0}. \tag{1.40}$$

This equation suggests that Λ is equivalent to a vacuum energy density, intrinsic to space itself, persisting even in the absence of matter. This energy is known as dark energy and it is thought to drive the accelerating expansion of the Universe within the framework of the Friedmann equations. However, the true nature of dark energy remains a mystery.

As of now, the cosmological constant is the most commonly used model for dark energy, leading to the nomenclature of the ΛCDM model. But alternative models are also explored since we still have little information about the meaning of this constant. The behavior of these alternative dark energy forms is often presented as an equation of state, typically written as:

$$p = \omega\rho. \tag{1.41}$$

where:

$$\omega = \begin{cases} -1 & \text{for vacuum energy (or cosmological constant),} \\ \omega(a) & \text{for variable dark energy, often corresponding to a scalar field,} \\ < -1 & \text{for phantom energy (a form of unstable vacuum energy).} \end{cases}$$

The parameter ω and the equation of state are also applicable in modeling the behavior of all the substances of the universe. For example, $\omega = 1/3$ for radiation (accounting for radiation pressure) and $\omega = 0$ for matter (treated as a fluid without pressure).

1.7.4 Evolution of Energy Densities

To analyze the different epochs of the Universe, it's essential to determine the relative contributions of each component. We define dimensionless cosmological parameters as:

$$\Omega_{i,0} \equiv \frac{\rho_{i,0}}{\rho_{cr}}, \tag{1.42}$$

where $\rho_{i,0}$ represents the current density of the i-component and ρ_{cr} is the critical density:

$$\rho_{cr} = \frac{3H_0^2}{8\pi G}. \tag{1.43}$$

The critical density is the density required for a flat universe ($k = 0$) given the Hubble parameter H_0. If the actual density exceeds this density, the space is closed; if it is lower, the space is open. The first Friedmann equation can be expressed as [58]:

$$H^2(z) = H_0^2 \left[\Omega_{m,0}(1+z)^3 + \Omega_{r,0}(1+z)^4 + \Omega_{de,0}(1+z)^{3(1+w)} + \Omega_{k,0}(1+z)^2\right], \tag{1.44}$$

where $\Omega_k = -\frac{k}{H_0^2}$. This leads to the consistency relation:

$$\sum_i \Omega_i + \Omega_k = 1, \tag{1.45}$$

where i includes all components except curvature.

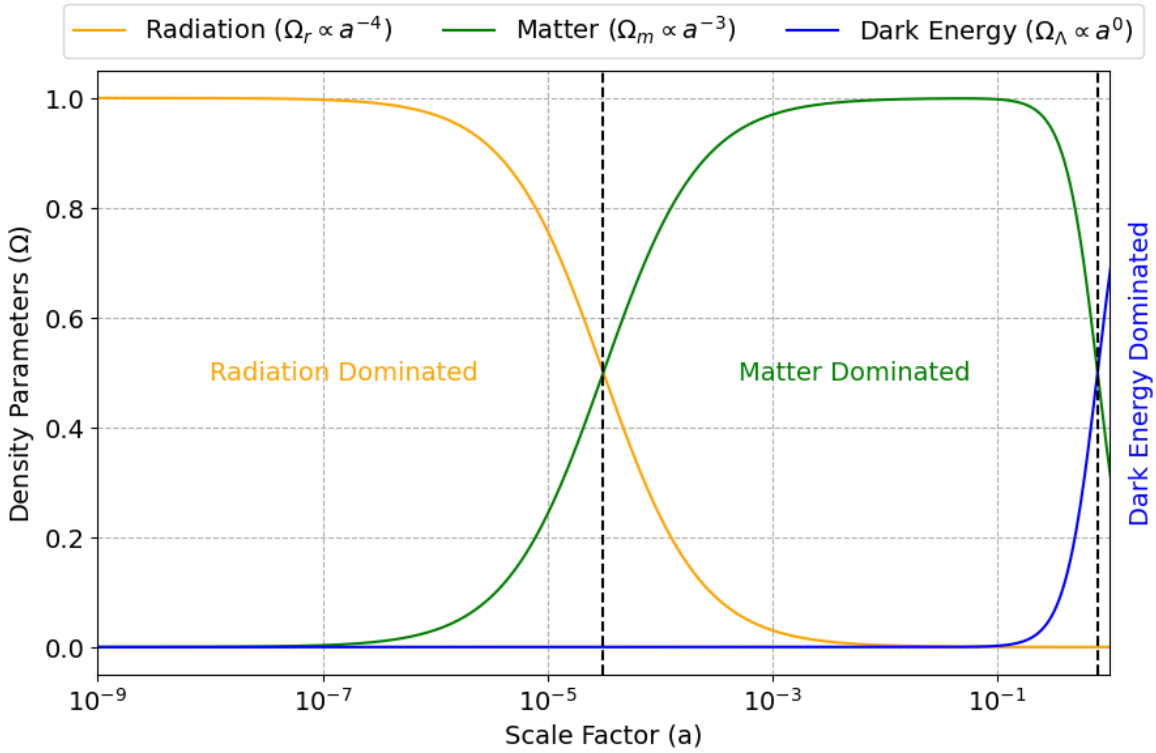

FIGURE 1.2: Evolution of the density parameters throughout the Universe's expansion. The dashed lines indicate the epochs of radiation-matter equality and matter-dark energy equality. The cosmological values used are from the Flagship 2 mock (flat cosmology) with an arbitrary $\Omega_r = 10^{-5}$.

Figure 1.2 illustrates the evolution of different density parameters with the scale factor up to the present epoch. The points where two components have equal densities are referred to as equality (or turnover) scales. For example, the radiation-matter equality can be computed by solving:

$$\rho_{r0} a^{-4} = \rho_{m0} a^{-3} \rightarrow a_{eq} = \frac{\rho_{r0}}{\rho_{m0}} \rightarrow z_{eq} = \frac{\rho_{m0}}{\rho_{r0}} - 1. \tag{1.46}$$

The minimal set of cosmological parameters required to characterize the properties of the Universe's expansion includes: $\{\Omega_i\}, \Omega_k, H_0, w$. Accurate measurements of these parameters are crucial for understanding the Universe's history and future. Observations from the CMB provide precise constraints on these parameters. Current measurements (from Planck + BAO, [7]) indicate that the Universe is nearly flat. Radiation, once dominant, is now a minor component compared to matter and dark energy. Dark matter, more abundant than baryonic matter, is categorized into cold dark matter (CDM), denoted as Ω_c, and baryonic matter, Ω_b, with $\Omega_m = \Omega_b + \Omega_c$.

Current values are approximately [7]:

$$\Omega_k = 0.001 \pm 0.002$$
$$\Omega_r \sim 10^{-5}$$
$$\Omega_m = 0.315 \pm 0.007$$
$$\Omega_b h^2 = 0.0224 \pm 0.0001$$

1.8 Cosmological Distances

As discussed in Section 1.2, the relationship between redshift (an observable quantity) and comoving distance is determined by the Universe's expansion history, characterized by $H(z)$. In cosmology, there are several definitions for distances which can be useful in different situations to extract information about the Universe through the relation between distance and redshift [58].

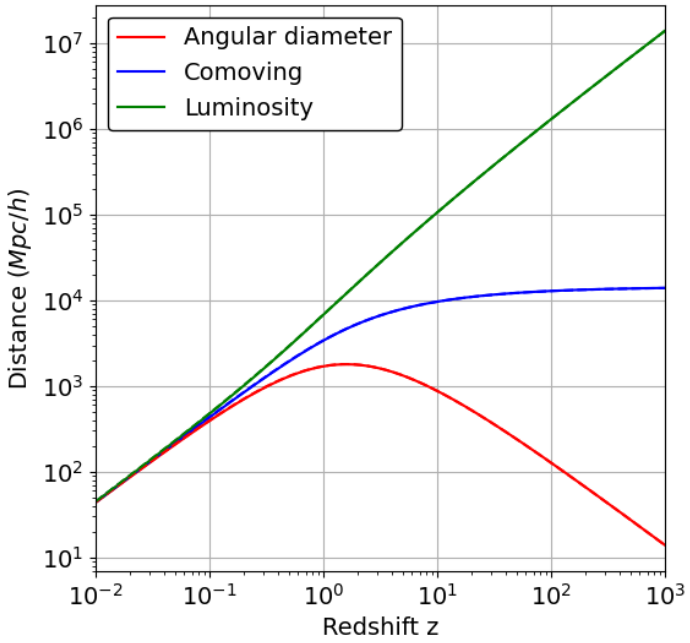

FIGURE 1.3: Plot showing the evolution of different distances with redshift, using the cosmological parameters from the Flagship 2 mock.

1.8.1 Comoving Distance

Using physical distances in an expanding universe is complex. Instead, cosmology often uses comoving distances, which remain constant for objects moving with the Hubble flow.

Consider a source emitting light in the past, arriving to an observer after a certain period. In this time interval, light would have traveled a physical distance of:

$$c\ dt = a(t) d\chi, \tag{1.47}$$

where the comoving distance between the source and the observer is given by $d\chi$. This follows from the metric equation for radially traveling light, where the spacetime interval is zero.

To find the total comoving distance to the observed object, integrate from the time of emission t_e to the time of observation t_0:

$$\chi(t_e) = \int_{t_e}^{t_0} \frac{cdt}{a(t)}. \tag{1.48}$$

Substituting $\dot{a} = \frac{da}{dt}$ and using $H \equiv \frac{\dot{a}(t)}{a(t)}$:

$$\chi(a) = \int_{a_e}^{a_0} \frac{cda}{a\dot{a}} = \int_{a_e}^{1} \frac{cda}{a^2 H(a)}. \tag{1.49}$$

By expressing this equation as function of redshift (Eq. 1.44 and Eq. 1.6), we get:

$$\chi(z) = \int_0^z \frac{cdz}{H(z)}. \tag{1.50}$$

This equation is referred at the distance-redshift relation. The collection of parameters used to calculate cosmic distances is known as the fiducial cosmology: H_0 and Ω_i (Eq. 1.44).

1.8.2 Transverse Comoving Distance

The transverse comoving distance D_M measures the separation between two points at the same redshift but separated by an angle $\Delta\theta$ on the sky. It relates to the line-of-sight comoving distance D_C as follows:

$$D_M(z) = \begin{cases} \frac{d_H}{\sqrt{\Omega_k}} \sinh\left(\frac{\sqrt{\Omega_k} D_C(z)}{d_H}\right) & \Omega_k > 0 \\ D_C(z) & \Omega_k = 0 \\ \frac{d_H}{\sqrt{|\Omega_k|}} \sin\left(\frac{\sqrt{|\Omega_k|} D_C(z)}{d_H}\right) & \Omega_k < 0 \end{cases} \tag{1.51}$$

Here, d_H is the Hubble distance, and Ω_k is the curvature parameter, distinguishing between open, flat, and closed universes.

1.8.3 Angular Diameter Distance

The angular diameter distance D_A allows us to infer the physical size of an astronomical object from the angle its extremes defines on the sky from the observer point of view. Using the small angle approximation, it is given by:

$$D_A = \frac{l}{\theta}, \tag{1.52}$$

where l is the object's physical size and θ is the observed angle. The object has a transversal comoving size of l/a, while the angle can be expressed as $\theta = \frac{l/a}{\chi}$. Then the angular diameter distance in a flat universe is related to the comoving distance by:

$$D_A^{\text{flat}} = \frac{\chi(z)}{1+z}. \tag{1.53}$$

For Universes with curvature, expression 1.53 can be generalized to:

$$D_A = \frac{a}{H_0\sqrt{|\Omega_k|}} \begin{cases} \sinh\left(\sqrt{\Omega_k} H_0 \chi\right) & \Omega_k > 0 \\ \sin\left(\sqrt{|\Omega_k|} H_0 \chi\right) & \Omega_k < 0 \end{cases} \tag{1.54}$$

These expressions recover the flat case when Ω_k approaches zero.

1.8.4 Luminosity Distance

The luminosity distance D_L relates the flux F observed from a source object to its intrinsic luminosity L. In a non-expanding universe, the flux is:

$$F = \frac{L}{4\pi d^2}, \tag{1.55}$$

where d is the physical distance to the object. Both the distance and luminosity evolve over time when the Universe expands. Expressing in terms of the scale factor:

$$F(a) = \frac{L(a)}{4\pi\chi^2(a)}, \tag{1.56}$$

where $L(a)$ is the luminosity passing through a comoving spherical shell of radius $\chi(a)$. Due to expansion, $L(a)$ is reduced by two factors: (1) photon energy is redshifted by a, and (2) the number of photons per unit time is reduced by a. Therefore, the observed luminosity is reduced by a factor of a^2:

$$L(a) = L_{\text{source}} a^2. \tag{1.57}$$

Thus, the observed flux becomes:

$$F = \frac{L_{\text{source}} a^2}{4\pi\chi^2(a)}. \tag{1.58}$$

Defining the luminosity distance D_L as:

$$D_L \equiv \frac{\chi}{a}, \tag{1.59}$$

the flux observed in an expanding universe can be expressed as:

$$F = \frac{L_{\text{source}}}{4\pi D_L^2(a)}. \tag{1.60}$$

This relationship enables cosmologists to infer distances from the observed flux, given the source's intrinsic luminosity.

Chapter 2

Large scale structure in the universe

As mentioned in the introduction, the description of the Universe as homogeneous and isotropic is only valid on large cosmological scales. In the early Universe, everything was tightly packed together, and all components were in equilibrium [99]. In this state, structures could not form because the gravitational potential was uniform, leaving no preferred positions for mass to coalesce. Cosmologists believe that the well-defined structures we see today originated from random quantum fluctuations in the early Universe, which acted as "seeds" for the formation of these structures [118].

2.1 Timeline of the Universe

In this section we will give a brief description of the story of the Universe as an introduction as how structures originated and evolved [58].

2.1.1 The Big Bang

By extrapolating Hubble's Law, we can infer that all the energy of the Universe was once confined to a very small space. In this state, the Universe was extremely hot and dense, with temperatures around 1 MeV/kB. Neutral atoms and bound nuclei could not exist because the intense high-energy radiation would immediately destroy any atom or nucleus that formed.

One of the most crucial insights from studying the CMB is that the early Universe was very smooth, showing no anisotropies initially. However, in 1992, the COBE satellite mission discovered anisotropies in the CMB [58], revealing that the early Universe was not entirely uniform. These small perturbations in the cosmic plasma manifested as fractional temperature fluctuations of about 10^{-5}.

2.1.2 Inflation

The inflationary theory, introduced by Alan Guth in 1981 [78], revolutionizes our understanding of the early Universe by proposing a phase of rapid, exponential expansion. This theory was initially developed to solve two major cosmological puzzles: the flatness problem and the horizon problem.

The flatness problem arises from observations showing that the Universe is extraordinarily flat, far beyond what would be expected by chance alone. This extreme flatness suggests that the Universe's geometry is incredibly close to being perfectly flat, which requires an explanation beyond mere coincidence. The horizon problem involves the uniformity of the Universe on scales that exceed the distance light could have traveled since the Big Bang. This implies that regions of the Universe that seem too homogeneous should not have been in causal contact, as they are separated by distances greater than the cosmological horizon.

Inflationary theory proposes that in the very earliest moments, approximately 10^{-32} seconds after the Big Bang, the Universe underwent a period of exponential expansion [78]. During this brief yet intense phase, the scale factor a of the Universe grew by an enormous factor, at least 10^{26}. This extraordinary expansion stretched any pre-existing quantum fluctuations to cosmic scales, effectively "freezing" them into the fabric of the Universe. These amplified fluctuations laid the groundwork for the tiny variations observed in the Cosmic Microwave Background (CMB) and the large-scale structure (LSS) of the Universe.

By addressing the horizon and the flatness problems, inflationary theory provides a compelling framework for understanding the initial conditions of the Universe and the origins of its observed large-scale structure.

2.1.3 Radiation Dominated Era

Following the end of inflation, the Universe entered a radiation-dominated phase. In this period, the Universe was extremely hot and dense, but the expansion rate slowed compared to the inflationary phase. In a radiation-dominated Universe, the scale factor a evolves as $a \propto t^{1/2}$, based on the first Friedmann equation and the radiation density equation with $\Lambda = 0$.

As the Universe expanded and cooled, key processes unfolded [58]:

- Baryogenesis: Quarks combined to form protons and neutrons, the building blocks of atomic nuclei. This process led to the formation of baryons, including protons and neutrons, which constitute the observable matter in the Universe.

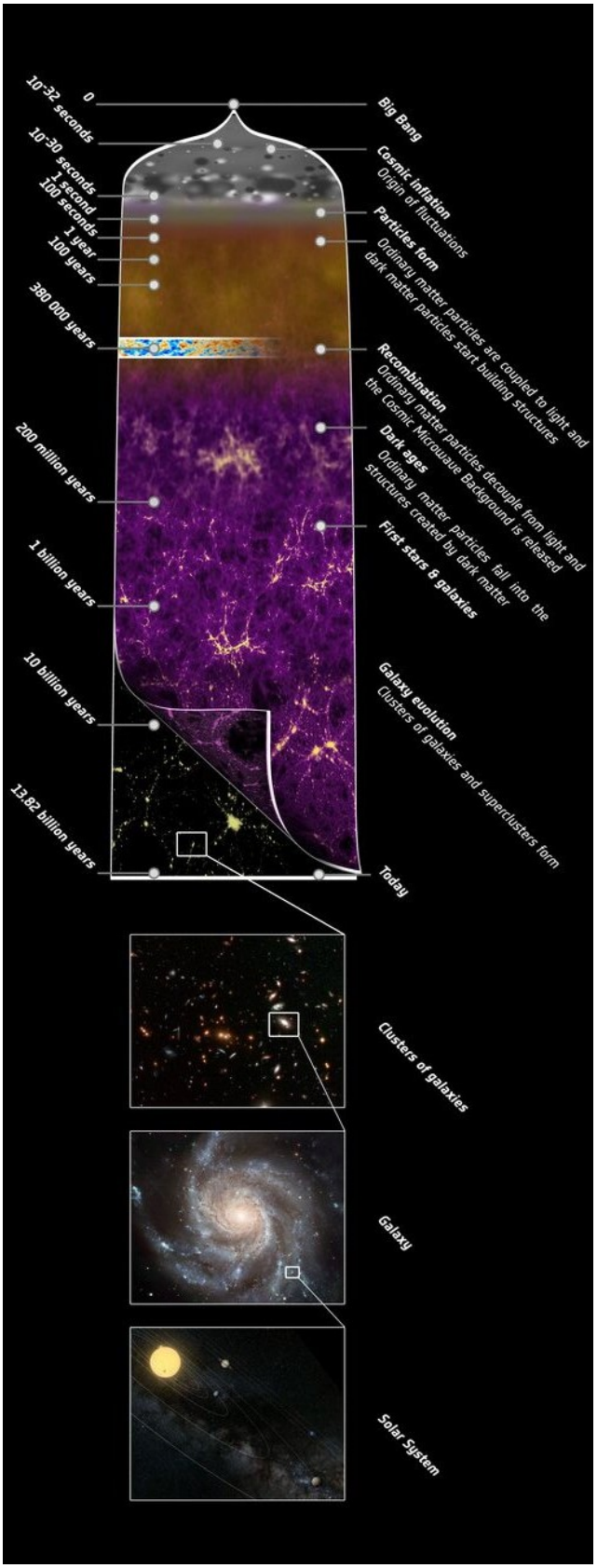

FIGURE 2.1: Diagram showing the timeline of the Universe from the Big Bang to the present day. Source: NASA.

- Neutrino Decoupling: Neutrinos, which interact weakly with other matter and radiation, decoupled from the rest of the particles and began to travel freely. This decoupling suggests the existence of a cosmic neutrino background, though it is challenging to detect.
- Big Bang Nucleosynthesis (BBN): Protons and neutrons combined to form the first atomic nuclei, primarily hydrogen and helium, with trace amounts of lithium. This primordial nucleosynthesis set the initial abundances of these elements, which have been confirmed by observations.

The end of the radiation-dominated era occurred when the energy densities of radiation and matter became comparable. This transition is estimated to have happened at a redshift of approximately $z_{eq} \sim 3600$ [58].

2.1.4 Matter Dominated Era

After the radiation era, matter became the dominant component of the Universe. During this matter-dominated phase, the Universe's expansion rate continued to slow down, with the scale factor evolving as $a \propto t^{2/3}$ when considering only matter density. This change led to the formation of cosmic structures under the influence of gravity, as radiation pressure was no longer significant.

Key events in the matter-dominated era include [58]:

- Photon Decoupling: When the Universe cooled to about $z_{CMB} \sim 1100$, photons decoupled from matter and began to travel freely. This decoupling led to the formation of the Cosmic Microwave Background (CMB) radiation. At the same time, electrons and protons combined to form neutral hydrogen atoms.
- Recombination and Dark Age: Immediately after recombination, the Universe was dark and opaque because neutral hydrogen could absorb radiation. This period, known as the "dark age," lasted until the first stars and galaxies formed.
- Reionization: The formation of the first stars and galaxies led to the ionization of hydrogen, gradually making the Universe more transparent. This process, known as reionization, began around $z \sim 20$ and concluded around $z \sim 6$. After reionization, the Universe became more transparent, and observations of galaxies became possible.

2.1.5 Dark Energy Dominated Era

In more recent times, dark energy has emerged as the dominant force in the Universe. This shift occurred at approximately $z \sim 0.3$, where the energy density of dark energy (ρ_Λ) became greater than that of matter [58]. The presence of dark energy causes the expansion of the Universe to accelerate. According to the ΛCDM model, this accelerated expansion follows an exponential growth pattern, with the scale factor $a \propto e^t$, assuming only the Λ term is considered. This ongoing exponential expansion implies that the observable Universe will continue to shrink relative to distant objects. Eventually, objects not gravitationally bound to our local group will become unreachable.

Figure 2.1 illustrates these different stages of the Universe's evolution, highlighting key events from the end of the CMB era to the present-day dark energy-dominated phase.

2.2 Structure Formation

Following the inflationary period, the Universe began to form structures through the growth of small density fluctuations [58]. These fluctuations, initially tiny, played a crucial role in shaping the cosmic landscape we observe today. After inflation, the Universe was filled with regions of slightly different densities. An overdense region had a stronger gravitational pull than the surrounding average density. This increased its ability to attract more matter, causing further growth of the fluctuation. The density contrast, or overdensity δ, quantifies these variations and is defined as:

$$\delta(\vec{x}, t) \equiv \frac{\rho(\vec{x}, t) - \bar{\rho}(t)}{\bar{\rho}(t)}, \tag{2.1}$$

where $\rho(\vec{x}, t)$ is the matter density at a given location $\vec{x}$ and time t, and $\bar{\rho}(t)$ is the average density of the Universe at that time. Initially, these fluctuations are assumed to be Gaussian. Given the Universe's initial homogeneity and isotropy, the statistical properties of these fluctuations should reflect the same symmetries, implying that the average overdensity across the Universe is zero:

$$\langle \delta(\vec{x}) \rangle = 0. \tag{2.2}$$

To understand the clustering of matter, we use the two-point correlation function ξ. This function measures how density fluctuations at two different points are correlated. It gives the probability of finding an excess density at one point relative to another:

$$\xi(\vec{r}) = \xi(\vec{x}_1, \vec{x}_2) = \equiv \langle \delta(\vec{x}_1)\delta(\vec{x}_2) \rangle, \tag{2.3}$$

where $\vec{r} = \vec{x}_1 - \vec{x}_2$ represents the separation between the points. Due to the Universe's homogeneity and isotropy, ξ depends only on the distance $|\vec{r}|$ between the points, not their absolute positions.

The power spectrum is a more convenient tool for theoretical analysis and observational comparison. It is the Fourier transform of the two-point correlation function and provides a measure of how different scales contribute to the overall structure:

$$P(\vec{k}) = \int \xi(\vec{r}) e^{-i\vec{k}\cdot\vec{r}}\, d^3r, \tag{2.4}$$

where $P(\vec{k})$ represents the power per unit volume at a specific wavenumber k.

To connect the two-point correlation function with the power spectrum, we start with the Fourier transform of the overdensity field:

$$\delta(\vec{x}) = \frac{1}{(2\pi)^3} \int d^3k\, \tilde{\delta}(\vec{k}) e^{i\vec{k}\cdot\vec{x}}, \tag{2.5}$$

where $\tilde{\delta}(\vec{k})$ is the Fourier transform of the overdensity field. Inverting this equation yields:

$$\tilde{\delta}(\vec{k}) = \int \delta(\vec{x}) e^{-i\vec{k}\cdot\vec{x}} d^3x. \tag{2.6}$$

We then calculate the expectation value of $\tilde{\delta}(\vec{k})\tilde{\delta}^*(\vec{k'})$:

$$\langle\tilde{\delta}(\vec{k})\tilde{\delta}^*(\vec{k'})\rangle = \left(\int \delta(\vec{x}_1)e^{-i\vec{k}\cdot\vec{x}_1}\, d^3x_1\right)\left(\int \delta(\vec{x}_2)e^{i\vec{k'}\cdot\vec{x}_2}\, d^3x_2\right). \tag{2.7}$$

Introducing $\vec{R} = \frac{\vec{x}_1+\vec{x}_2}{2}$ and $\vec{r} = \vec{x}_1 - \vec{x}_2$, we obtain:

$$\begin{aligned}\langle\tilde{\delta}(\vec{k})\tilde{\delta}^*(\vec{k'})\rangle &= \int\int \xi(\vec{r})\, e^{-i\vec{k}\cdot\left(\vec{R}+\frac{\vec{r}}{2}\right)} e^{i\vec{k'}\cdot\left(\vec{R}-\frac{\vec{r}}{2}\right)}\, d^3R\, d^3r \\ &= \int\int \xi(\vec{r})\, e^{-i\vec{k}\cdot\vec{R}}\, e^{-i\frac{\vec{k}\cdot\vec{r}}{2}}\, e^{i\vec{k'}\cdot\vec{R}}\, e^{-i\frac{\vec{k'}\cdot\vec{r}}{2}}\, d^3R\, d^3r \\ &= \int e^{-i(\vec{k}-\vec{k'})\cdot\vec{R}}\, d^3R \int \xi(\vec{r})\, e^{-i\frac{\vec{k}+\vec{k'}\cdot\vec{r}}{2}}\, d^3r.\end{aligned} \tag{2.8}$$

The first integral evaluates to a Dirac delta function:

$$\int e^{-i(\vec{k}-\vec{k'})\cdot\vec{R}}\, d^3R = (2\pi)^3\delta_D^3(\vec{k}-\vec{k'}), \tag{2.9}$$

while the second integral is the power spectrum:

$$P(\vec{k}) = \int \xi(\vec{r})e^{-i\vec{k}\cdot\vec{r}}\, d^3r. \tag{2.10}$$

Combining these results, we get:

$$\langle\tilde{\delta}(\vec{k})\tilde{\delta}^*(\vec{k'})\rangle = (2\pi)^3\delta_D^3(\vec{k}-\vec{k'})P(\vec{k}). \tag{2.11}$$

Here, $(2\pi)^3$ is a normalization factor, and the Dirac delta function δ_D^3 signifies that different wavenumbers are uncorrelated. This indicates that the power spectrum represents the variance of density fluctuations on different scales [99]: a larger power spectrum means more pronounced density variations, while a smaller power spectrum indicates a smoother distribution.

The power spectrum and the two-point correlation function are essential tools for analyzing cosmic structure. The power spectrum provides a clear view of the distribution of matter across different scales in Fourier space, while the two-point correlation function offers insights in real space. In this thesis, we will utilize both methods to derive and interpret results related to structure formation.

2.2.1 Baryon Acoustic Oscillations

In the radiation-dominated era, a region of primordial plasma with an overdensity experienced gravitational attraction, drawing in additional matter. At the same time, intense photon-matter interactions generated substantial outward pressure. This interplay led to oscillatory phenomena similar to sound waves in a medium, which propagated over time. As the Universe cooled and matter decoupled from radiation, baryons were no longer influenced by radiation pressure, causing these acoustic oscillations to "freeze" [58]. This freezing left a lasting imprint on the distribution of baryons: locations corresponding to the wave fronts

just before decoupling, representing the maximum distance the waves traveled during the radiation era, exhibit higher than average baryon densities.

This feature in the large-scale structure of the Universe is known as baryon acoustic oscillations (BAO). The BAO distance acts as a standard ruler because the pressure waves "froze" at suficient large scales to be affected by gravitational collapse, remaining constant in comoving space. Consequently, BAO observed in the LOS direction can be used to measure the Hubble parameter at a given redshift. BAO can be detected through clustering statistics, such as the two-point correlation function (2PCF), and the BAO wiggles are included in the transfer function when modeling the power spectrum.

2.2.2 Theoretical evolution of the density field

Another advantage of utilizing the power spectrum is that it simplifies the construction of theoretical models for the evolution of this observable [58]. Accurate theoretical models are essential in cosmology for estimating cosmological parameters through data fitting. These models must account for the varying physical properties of the Universe across different epochs, as well as the independent evolution of each wavenumber mode (k-mode). To simplify the analysis, we initially consider only linear evolution, where matter falls into gravitational wells without any external interactions. However, as the overdensities grow, gravitational interactions between them become significant, leading to non-linear evolution. In this regime, more sophisticated equations are required, which are often too complex to solve analytically. See Fig. 2.2 to observe the impact of the nonlinear corrections on the power spectrum.

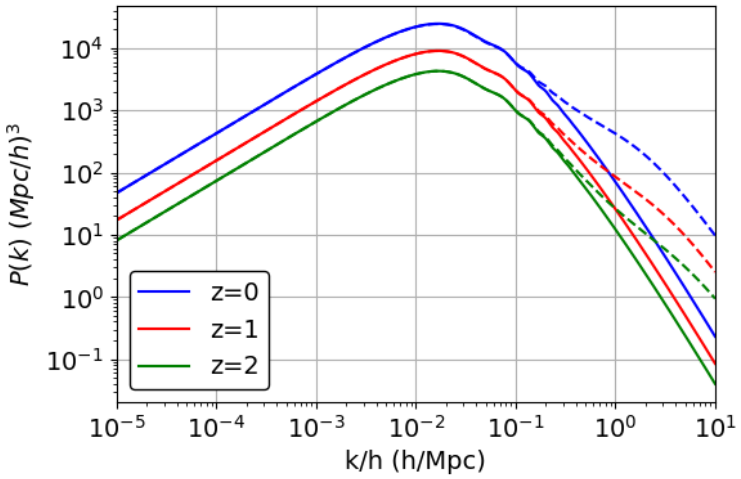

FIGURE 2.2: Predicted matter power spectrum for the linear (smooth line) and non-linear (dashed line) regime for different Redshift. The data was obtained using the code *pyCCL* with the cosmological values for the Flagship 2 mock.

Linear evolution

The initial conditions are set by primordial fluctuations, which gave rise to perturbations that created gravitational potential wells, attracting matter and subsequently forming large-scale structures. This primordial fluctuations are thought to be produced by a Gaussian quantum field [58]. As a result, the primordial power spectrum immediately following inflation is also expected to conform to a Gaussian distribution, characterized by a power-law form:

$$\mathcal{P}(k) = A_s k^{n_s} \tag{2.12}$$

Here, A_s represents the amplitude of the primordial power spectrum, serving as a normalization factor, while n_s denotes the scalar spectral index, which, based on both observational data and theoretical predictions, is close to unity. The most recent results from the Planck Collaboration report a value of $n_s = 0.9649 \pm 0.0044$ [7].

The value of A_s is typically determined by normalizing the power spectrum to match a specific observable quantity [58]. The conventional statistic used for this normalization is σ_8, which represents the standard deviation of the matter overdensity field within a sphere of radius R=8 Mpc/h at redshift $z = 0$:

$$\sigma_R^2 \equiv 4\pi \int_0^\infty dr\, |W_R(r)|^2 r^2 \delta(r)^2 = \frac{1}{2\pi^2} \int_0^\infty dk\, |\widetilde{W_R}(kR)|^2(k) k^2 P(k) \tag{2.13}$$

where $W_k(k)$ and $W_r(r)$ are the window functions that define the range of integration in Fourier and configuration space, respectively:

$$W_R(r) = \begin{cases} 3/(4\pi R^3) & \text{for } r < R \\ 0 & \text{for } r > R \end{cases} \tag{2.14}$$

$$\widetilde{W_R}(kR) = \frac{3j_1(kR)}{kR} \tag{2.15}$$

where $j_1(kR)$ is the spherical Bessel function of the first kind of order one.

It is standard practice to use $R = 8$ Mpc/h when estimating the standard deviation of overdensities, as this scale encompasses a sufficiently large volume for reliable measurements. Distances are expressed in Mpc/h to eliminate dependence on the Hubble parameter, h, particularly given the existing discrepancy, known as the Hubble Tension, between the value of h derived from CMB data ($h \approx 0.67$) and that obtained from local measurements ($h \approx 0.74$).

However, as demonstrated in [128] and [129], when the linear power spectrum is expressed in units of Mpc, all evolution parameters exhibit an exact degeneracy. This implies that their combined influence can be effectively captured by a single parameter. A convenient choice for this parameter is σ_{12}, the root mean square of matter fluctuations within spheres of radius $R = 12$ Mpc, which is equivalent to σ_8 for $h \approx 0.67$.

Transfer function

The change in the initial power spectrum $\mathcal{P}(k)$ over time is described by the transfer function $T(k, z)$, which relates the initial power to the power spectrum at different redshifts:

$$P(k, z) = T^2(k, z)\mathcal{P}(k) \tag{2.16}$$

The transfer function $T(k, z)$ models the evolution of different modes from the radiation era through to the matter era. It is represented as a squared function because it was originally designed to model the gravitational potential power spectrum, which is proportional to the density contrast δ, rather than the matter-matter power spectrum, which is proportional to $\delta\delta$. This transfer function depends on the content distribution of the Universe, making it a function of the cosmological model. Consequently, the power spectrum is sensitive to cosmological parameters.

For instance, the peak observed around $k/h \sim 10^{-2} - 10^{-1}$ h/Mpc in Figure 2.2 is influenced by the epoch of matter-radiation equality, providing a probe of the ratio Ω_γ/Ω_m.

Following the end of inflation, the primordial power spectrum, begins to evolve in response to the physical conditions of the Universe.

Equations of motion

To understand the evolution of large-scale structures, it is essential to quantify how the gravitational field affects fluctuations in the density field. Within the ΛCDM cosmological model, matter is often approximated as an ideal fluid [58]. This approximation allows us to describe the motion of matter using a set of fundamental equations:

- The continuity equation (Eq. 2.17): This equation describes the conservation of mass in the fluid, ensuring that mass is neither created nor destroyed.
- The Euler equation (Eq. 2.18): This equation governs the conservation of momentum, accounting for the forces acting on the fluid, including pressure gradients and gravitational forces.
- The Poisson equation (Eq. 2.19): This equation relates the gravitational potential to the density fluctuations in the fluid, linking the distribution of matter to the gravitational field.

These equations form the basis for analyzing the dynamics of the Universe's matter distribution and understanding the growth of structures under the influence of gravity.

$$\frac{\partial \rho}{\partial t} + \nabla \cdot (\rho \vec{v}) = 0 \tag{2.17}$$

$$\frac{\partial \vec{v}}{\partial t} + (\vec{v} \cdot \nabla)\vec{v} = -\frac{1}{\rho}\nabla_r P - \nabla\Phi \tag{2.18}$$

$$\nabla^2 \Phi = 4\pi G \rho \tag{2.19}$$

where ρ represents the density, P is the pressure (with $P \ll \rho$, indicating that the pressure is negligible compared to the density), $\vec{v}$ denotes the physical velocity, and Φ is the gravitational potential. These equations describe how these quantities vary within the context of physical coordinates.

Since we are interested in comoving coordinates (to describe an expanding universe), we need to convert some quantities starting with the velocity:

$$\vec{v} = \dot{a}\vec{x} + a\dot{\vec{x}} = \dot{a}\vec{x} + \vec{u} \tag{2.20}$$

In this equation, $\vec{u}$ is known as the peculiar velocity, which ignores the movement caused by the expansion of the universe. This velocity is important to consider since it introduces systematic errors when estimating the redshift of an astronomical object. The radial component of the peculiar velocity is added to the radial component of the total velocity in Hubble's Law (Eq. 1.1), modifying the calculated redshift value. We will return to this topic when discussing redshift space distortions (RSD) in sec. 2.3.

To transition to the comoving coordinate system, we need to modify the time derivative as follows:

$$\left(\frac{\partial}{\partial t}\right)_{physical} = \left(\frac{\partial}{\partial t}\right)_{comoving} - H(\vec{x}\cdot\nabla_{comoving}), \tag{2.21}$$

with $\nabla_{comoving} = a\nabla_{physical}$. The gravitational potential Φ can be decomposed into two components relative to the background:

$$\Phi(\vec{d},t) = \varphi(\vec{x},t) + \frac{1}{2}a\ddot{a}x^2. \tag{2.22}$$

where φ represents the perturbation component of Φ, while the second term accounts for the background potential. The perturbation potential does not include dark energy since it is uniformly distributed. In a Universe composed of matter and dark energy, the Poisson equation for the perturbed potential becomes:

$$\nabla^2\varphi = 4\pi G a^2\bar{\rho}\delta(\vec{x},t), \tag{2.23}$$

where the derivatives have been transformed to comoving coordinates, and $\delta(\vec{x},t)$ is the same overdensity defined at (Eq. 2.1).

Lastly, we can obtain the following relation between pressure and density if we consider the conservation of the energy-moment tensor (Eq. 1.17):

$$\dot{\rho} = -3H(\rho + P) \tag{2.24}$$

With all these derivations the continuity and the Euler equations expressed in the comoving coordinate system are given by:

$$\frac{\partial\delta}{\partial t} + \frac{1}{a}\nabla\cdot[(\delta+1)\vec{u}] = 0. \tag{2.25}$$

$$\frac{\partial\vec{u}}{\partial t} + H\vec{u} + (\vec{u}\cdot\nabla)\,\vec{u} = -\frac{1}{a\bar{\rho}(\delta+1)}\nabla P - \frac{1}{a}\nabla\varphi, \tag{2.26}$$

where we have also used $\rho = \bar{\rho}(\delta+1)$ derived from (Eq.2.1).

Linear Regime

Analytical solutions to equations 2.25 and 2.26 are not feasible due to their non-linear nature. To simplify this, we use first-order perturbation theory in δ, which assumes that density and velocity perturbations are minimal ($\delta \ll 1$), applicable only on large scales. By perturbing the variables, we write:

$$x_i = \bar{x}_i + \delta x_i + O(\delta^2 x_i) + \ldots \tag{2.27}$$

Equations 2.25 and 2.26 can then be approximated as follows:

$$\frac{\partial\delta}{\partial t} + \frac{1}{a}\nabla\cdot\vec{u} = 0 \tag{2.28}$$

$$\frac{\partial \vec{u}}{\partial t} + H\vec{u} = -\frac{1}{a\bar{\rho}}\nabla\delta P - \frac{\nabla\varphi}{a} \tag{2.29}$$

$$\nabla^2\varphi = 4\pi G\bar{\rho}^2\delta \tag{2.30}$$

where according to equation 2.27, we have $P = \bar{P} + \delta P$ and $\rho = \bar{\rho} + \delta\rho = \bar{\rho}(1+\delta)$. Now, by differentiating the linearized continuity equation with respect to time, applying a divergence to the linearized Euler equation, subtracting the first to the latter, and substituting in the continuity and Poisson equations while neglecting the pressure term (since $\nabla P \ll \rho\nabla\varphi$), the equation for linear perturbations is derived:

$$\frac{\partial^2\delta}{\partial t^2} + 2H\frac{\partial\delta}{\partial t} = 4\pi G\bar{\rho}\delta \tag{2.31}$$

This is a second-order differential equation for $\delta(\vec{x}, t)$. For a matter-dominated universe (i.e., with $\Lambda = 0$), the first Friedmann equation (Eq. 1.32) simplifies to:

$$H^2 = \frac{8\pi G}{3}\rho_m \tag{2.32}$$

Using the critical density ρ_c (Eq. 1.43) and the density parameter Ω_m (Eq. 1.42), we can rewrite equation 2.31 as:

$$\ddot{\delta_{\rm m}}(\mathrm{k}, z) + 2H(z)\dot{\delta_{\rm m}}(\mathrm{k}, z) - \frac{3}{2a^3}\Omega_{\mathrm{m},0}H_0^2\delta_{\rm m}(\mathrm{k}, z) = 0 \tag{2.33}$$

The linear solution for the evolution of overdensities can be expressed with the growth factor $D(z)$:

$$\delta_{\rm m}(\vec{k}, z) = \delta_{\rm m}(\vec{k}, z_i)\frac{D(z)}{D(z_i)} \tag{2.34}$$

where z_i is a reference redshift in the matter-dominated epoch. The growth factor is typically normalized so that $D(z = 0) = 1$, corresponding to the present time t_0. With this normalization:

$$\delta(\mathbf{k}, z) = D(z)\delta(\mathbf{k}, 0) \tag{2.35}$$

The growth factor, which depends on the universe's composition, describes how density fluctuations evolve with redshift. Thus, the linear perturbation equation can be expressed as:

$$\ddot{D} + 2H(z)\dot{D} - \frac{3}{2}\Omega_{\mathrm{m},0}H_0^2(1+z)^3 D = 0 \tag{2.36}$$

Alternatively, it can be written in terms of the growth rate parameter, defined as [58]:

$$f(\Omega_{\rm m}, a) \equiv \frac{1}{H}\frac{\dot{D}}{D} = -\frac{\mathrm{d}\ln D(z)}{\mathrm{d}\ln(1+z)} \simeq [\Omega_m(z)]^{0.55} \tag{2.37}$$

Linear galaxy bias

Until now when we have considered the matter field we have not distinguished between dark matter and ordinary (baryonic) matter. However, galaxies, which are predominantly composed of ordinary matter, play a unique role in cosmology. Ordinary matter interacts with radiation and can emit light, making galaxies observable. It is expected that ordinary matter tends to accumulate in regions of higher gravitational potential, where astronomical structures such as galaxies form [58]. These regions, which are the evolved overdensities with time, are known as halos, or more specifically, dark matter halos in the context of the ΛCDM model.

Galaxies are therefore considered to be biased tracers of the total underlying matter distribution, residing predominantly at the centers of these dark matter halos. The concept of galaxy bias refers to the relationship between the observed distribution of galaxies and the underlying matter field. In the linear approximation, this relationship can be expressed as:

$$b_1 \equiv \frac{\delta_g}{\delta}, \tag{2.38}$$

where δ_g represents the density fluctuations of the galaxy distribution, and δ represents the density fluctuations of the matter field. The subscript "1" is used to denote the linear bias term, distinguishing it from higher-order, non-linear corrections that will be discussed in the subsequent chapter.

Since direct observation of matter density fluctuations δ is not feasible, galaxy bias is typically inferred using the power spectrum. The observed galaxy power spectrum $P_{gg}(k, z)$ is then related to the matter power spectrum $P_{\delta\delta}(k, z)$ through the linear galaxy bias as:

$$P_{gg}(k, z) = b_1(z)^2 P_{\delta\delta}(k, z) \tag{2.39}$$

This relationship holds true only on linear scales. The value of the linear galaxy bias b_1 is often found to be greater than 1, reflecting the tendency of ordinary matter to be more strongly clustered due to interactions such as collisions and other baryonic processes, which are absent in dark matter. Also, note that different populations of galaxies, obtained with different selection criteria like luminosity cuts, may have a different galaxy bias.

2.2.3 Non-Linear evolution

Once the matter perturbations grow to a considerable size ($\delta \approx 1$), they start to exert gravitational interaction between them [58]. Thus the matter evolution can no longer be considered linear and the equations from the previous section no longer have an analytical solution. In the context of the ΛCDM, dark matter forms these virialized structures that, as presented in the previous section, are called halos. So for dark matter, it is standard to use the Halofit model, which was originally developed by [134] and has since been updated, most notably by [140]. This model assumes that all matter is distributed within dark matter halos, which are considered gravitational bound structures (i.e. the gravitational potential is stronger that the expansion of the Universe).

Due to their great gravitational potential, halos start to attract other halos forming a cosmic web like structure, see Fig. 2.4. In other cases, halos merge forming a bigger halo. In this cases, if both halos contain a central galaxy, and there is no direct collision between the galaxies, one will orbit the one closer to the center of mass. In this cases the one (or ones) further from the center of mass of the new halo are called satellite galaxies.

We usually need to use N-body simulations (Chapter 3) in order to make models of the non-linear interactions and structure formations [58]. These models can be used to make predictions for observational data by fitting a varied amount of parameters specifics to that model. These non-linear parameters are usually non-local since each region will have endure a different non-linear evolution due to the universe no longer being homogeneous.

There are numerous models aimed at predicting the behavior of non-linear scales, a field still under active development due to the significant challenges in modeling small-scale structures. Most of these models are based on the halo model, where the description of the nonlinear matter density field heavily depends on halo statistics. In perturbation theory, halo statistics are expressed in terms of bias parameters, which multiply operators constructed from the matter density field. These operators generally include powers of the matter density, tidal fields, and convective time derivatives of these quantities [105]. Among these, the most well-studied and phenomenologically significant bias parameters on large scales are those related to the powers of the matter density field:

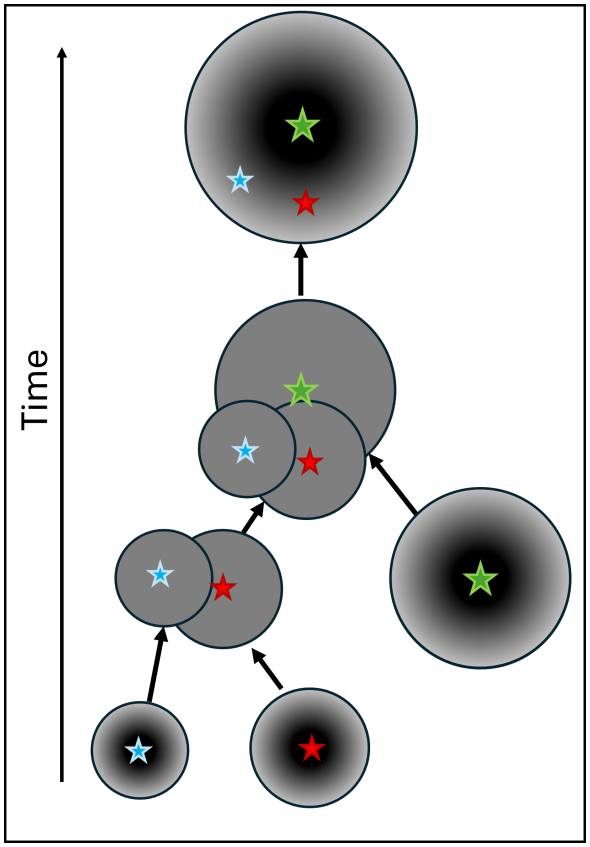

FIGURE 2.3: Diagram showing the merge history of a halo. Central galaxies of the original halos are shown as stars. The final halo contains the central galaxy of the most massive halo (green) merged, which is located close to the center of mass (darker area) of the new halo. The other galaxies (blue and red) are considered satellite galaxies of the halo that may orbit the central one or may collide with the central one at some point.

$$\delta_h \approx b_1 \bar{x}_i + b_2 \delta^2 + b_3 \delta^3 + O(\delta^4) + \dots \quad (2.40)$$

where δ_h represents the fractional number density perturbation of a given halo sample and b_i are different levels of nonlinear biases (except for b_1).

Before diving into the details, it's important to clarify the concepts of Lagrangian and Eulerian halo bias. Lagrangian bias connects the abundance of dark matter halos to the density perturbations in Lagrangian space, describing the relation between protohalos (matter in the process of forming a halo) in the initial conditions and the initial linear density perturbation field. In contrast, Eulerian bias links halos identified at a specific redshift z to the nonlinear density field δ_ρ at the same redshift. For local bias parameters, there is an exact nonlinear mapping between the Lagrangian bias parameters b_n^L and their Eulerian counterparts b_m, a relationship that is utilized in both theoretical predictions and measurements [59, 105]. Describing in detail this two methods is outside of the scope of this thesis so we refer the reader to [29] to expand on the mathematical description. Although we will expand a bit more on the Eulerian model when talking about redshift space distortions on the next section since it will be relevant for one the projects presented on this thesis.

An alternative method for modeling galaxy clustering involves using an approach that is not reliant on specific galaxy formation models [158]. This method operates under the assumption

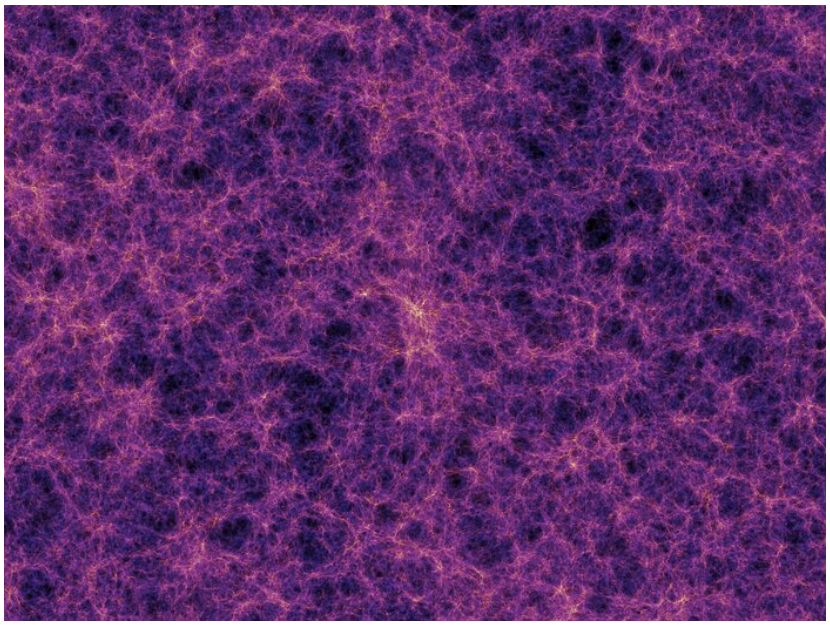

FIGURE 2.4: Artistic interpretation of the cosmic web formed by dark matter in the ΛCDM paradigm. The brighter regions contain more mass, which corresponds to the center of the dark matter halos and where galaxies are supposed to form. Credits: Volker Springel, ESA website.

that the galaxy field depends solely on the underlying matter density and velocity distribution. The model's effectiveness hinges on the accuracy of the matter field description and the robustness of the chosen biasing function. The biasing scheme can be represented in several ways: it may be defined in Eulerian coordinates, which describe the final state of the matter field, or in Lagrangian coordinates, which correspond to the initial state. It may also involve expansions of the density field, incorporate the effects of tidal forces and other nonlocal influences, or include density field derivatives.

While directly modeling galaxy formation can impose specific constraints related to physical processes and necessitate distinct models for different types of biased tracers, the agnostic approach provides greater flexibility. It allows a single model to account for biased tracers with diverse properties. Additionally, hybrid approaches have been developed to address nonlinear galaxy density fields by applying perturbation theory for large scales—thereby circumventing finite-volume issues in simulations—while using numerical N-body simulations to capture smaller, nonlinear scales. The Bacco simulation exemplifies this methodology by employing hybrid Lagrangian modeling in conjunction with simulations to predict galaxy clustering and Redshift space distortions [120].

2.3 Redshift space distortions

In the previous section peculiar velocities were introduced with Eq. 2.20 as the relative radial velocity of an object, with respect to the observer, independent of the universe expansion. This velocity causes a Doppler effect that is equivalent to the cosmological redshift produced by the expansion of space. This introduces an error on the estimated redshift which consequently introduces an incorrect determination of the physical distance to the object through Eq. 1.50. The redshift with the contribution of the peculiar velocities is called observed redshift, $z_{\rm obs}$, since it is the one that we can capture in observations. While when referring to only the

cosmological redshift we usually use the expression true redshift, z_{true}, since it is the one that relates to the true position of the object. The relation between the redshifts is given by [132]:

$$1 + z_{\text{obs}} = (1 + z_{\text{true}}) \left(1 - \frac{u_{\parallel}(\vec{r})}{c}\right)^{-1}, \tag{2.41}$$

where $u_{\parallel}$ denotes the radial velocity also known as the line-of-sight (LOS) component of the peculiar velocity. The conversion from positions in real space[1] "r" to positions in redshift space "s":

$$\vec{s} = \vec{r} + \frac{(1 + z_{\text{true}}) u_{\parallel}(\vec{r})}{H(z_{\text{true}})} \hat{r} \tag{2.42}$$

The second term is often neglected because its relative variation with respect to the comoving distance is minimal. However, the peculiar velocity term disrupts rotational invariance, leading to anisotropy in redshift-space clustering. This anisotropy has significant effects on matter clustering, depending on the scale:

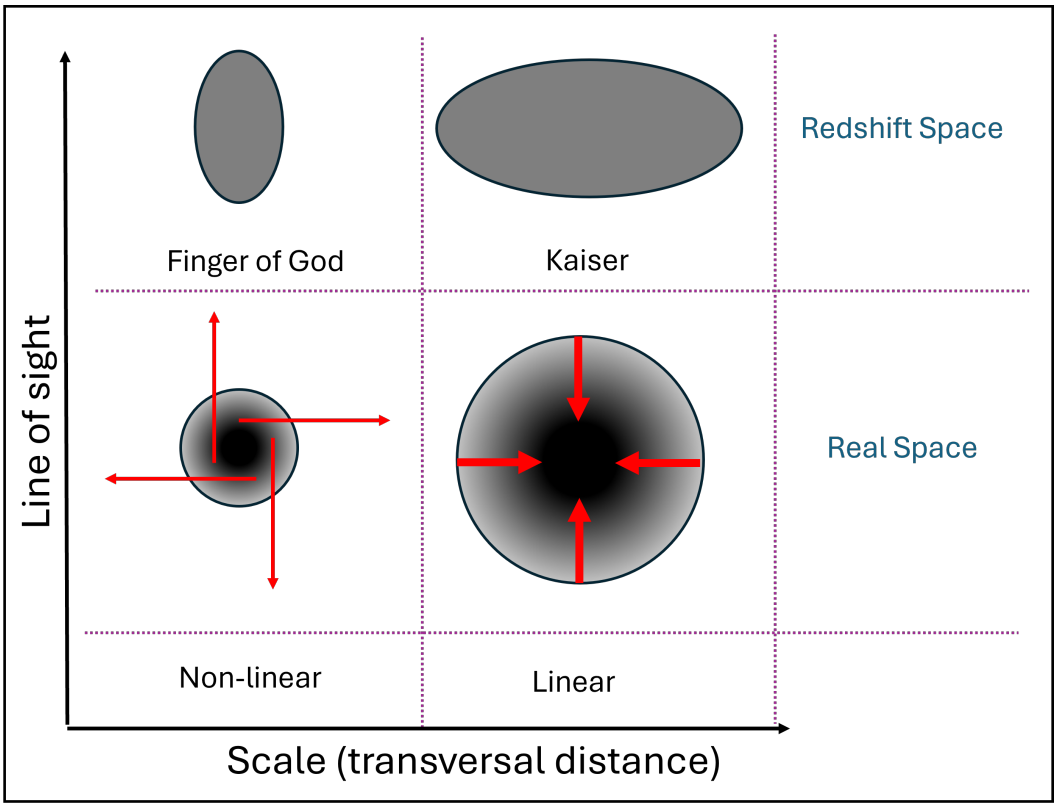

FIGURE 2.5: Diagram showing the effects of the redshift space distortions on the matter clustering on real and redshift space. The red arrows show the direction of the matter.

- Large Scales (Linear Regime): In overdense regions on large scales, galaxies closer to us are moving toward the center of the overdense region, which means they are moving away from us. As a result, these galaxies appear farther from us in redshift space and

[1] From now on, by real space we will refer to the space with true redshifts instead of the one with physicals variables, in contrast to fourier space, to which we will refer as configuration space.

closer to the center of the overdense region than they actually are. This compression of distances in redshift space is known as the Kaiser effect.

- Small Scales (Non-Linear Regime): At smaller scales, velocities are typically higher, and more importantly, the displacement into redshift space becomes significantly larger relative to the distance separating two correlated galaxies. Since clustering on small scales involves galaxies that are close together, this effect results in an elongation of distances in redshift space, known as the Finger of God effect.

This two effects constitute what is known as redshift space distortions (RSD). It is important ot quantify the effect of RSD since in observations we are always inflicted by peculiar velocities which makes obtaining the true redshift of an object unlikely.

2.4 Two dimensional two-point correlation function

Since the RSD breaks down the isotropy of the standard correlation function $\xi^s(\vec{s}) \neq \xi^s(s)$, we need a way to estimate the effects of the anisotropic clustering.

We usually use what is known as the 2D correlation function, $\xi(\sigma, \pi)$ [40], where we separate the radial direction (along the LOS) π from the one parallel to the separation in the plane of the sky σ. We can see then that this variables are related to the distance s as:

$$s = \sqrt{\pi^2 + \sigma^2} \tag{2.43}$$

We can also define the correlation function in terms of μ which is the cosine of the angle between s and the LOS:

$$\mu = \frac{\pi}{\sqrt{\sigma^2 + \pi^2}} \tag{2.44}$$

In Figure 2.6 we show the 2D correlation function for the simulated catalog Flagship 2 mock at z=0.55 with observed redshifts. We can appreciate how the two effects of the RSD distortions are combined on redshift space by looking at the yellow lines. At small scales, $\sigma << 5$ Mpc/h, we appreciate the Finger of God effect elongating the LOS, π, clustering. While, in contrast, at large scales, $\sigma > 5$ Mpc/h, we can see how the Kaiser effect takes place squashing the LOS clustering.

2.4.1 Modeling RSD: Kaiser factor

The Doppler-induced effects on the galaxy power spectrum due to redshift-space distortions (RSD) may initially appear as a complication, but they actually offer a significant advantage. By analyzing these effects, we can directly measure the rate at which structures in the universe grow, since as we will see in the next section it is related to the growth rate f, providing a valuable probe for investigating dark energy and gravity.

In a similar way that in the previous section, we can predict the linear effect (Kaiser) of RSD on the power spectrum by analyzing the velocity divergence field.

On the linear regime we can take the continuity equation that we derived in Eq. 2.17 to obtain [132]:

$$\nabla \cdot \vec{u} = -a \frac{\partial \delta(\vec{x}, t)}{\partial t} \tag{2.45}$$

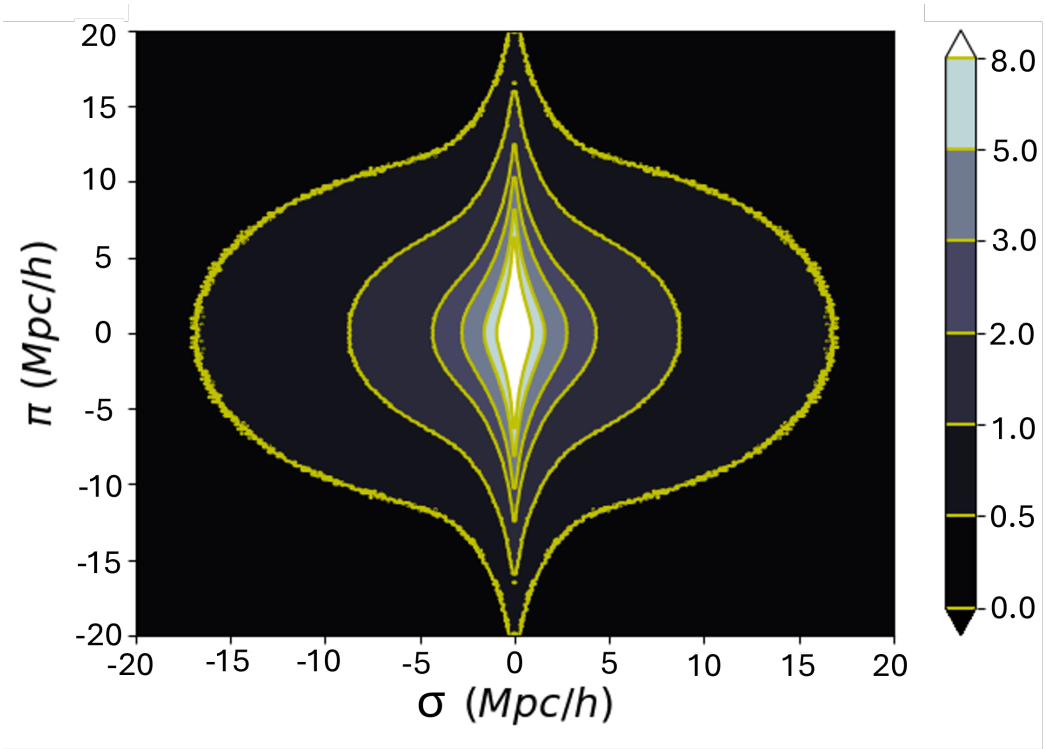

FIGURE 2.6: Heatmap showing the 2D correlation function of the Flagship 2 mock at z=0.55 with a redshift bin of 0.1. The yellow lines show points with the same level of correlation. The values where obtained with the *corrfunc* code using data x 2 number of randoms.

If we apply Eq. 2.35 we obtain:

$$\frac{\partial \delta(\vec{x},t)}{\partial t} = \frac{\partial \delta}{\partial D}\frac{\partial D}{\partial t} = \delta_0 \frac{\dot{D}}{D} = \delta_0(\vec{x})H(z)f(z) \tag{2.46}$$

where we have used the definition of the growth factor (Eq. 2.37). Then we can define the velocity divergence field as [132]:

$$\theta(\vec{x}) \equiv -\frac{\nabla \cdot \vec{u}(\vec{x})}{aHf}, \tag{2.47}$$

So that we have that:

$$\theta(\vec{x}) = \delta_0(\vec{x}) \tag{2.48}$$

The Fourier transform is given by

$$u(\vec{k}) = -iaHf\frac{\vec{k}}{k^2}\theta(\vec{k}). \tag{2.49}$$

Now, considering the density conservation from real to redshift space, we have:

$$\delta^s_{\rm m}(\vec{s}) = \left|\frac{d\vec{s}}{d\vec{r}}\right|^{-1}\{1+\delta_{\rm m}(\vec{r})\} - 1, \tag{2.50}$$

which in Fourier space is given by

$$\delta_{\rm m}^{s}(\vec{k}) = \int d^3x \left\{ \delta_{\rm m}(\vec{x}) - \frac{1}{aH}\frac{\partial u_z(\vec{x})}{\partial z} \right\} e^{i\vec{k}\cdot\vec{x} + ik\mu u_z/(aH)}, \tag{2.51}$$

where the line-of-sight (LOS) direction is fixed as $\hat{z}$, and the directional cosine is defined as

$$\mu \equiv \hat{\vec{k}} \cdot \hat{\vec{z}} \tag{2.52}$$

Note that this expression is exact under the distant observer and global plane-parallel approximations[2].

To derive the redshift-space distortion (RSD) correction at linear order, known as the Kaiser formula, we drop the second term in the exponential factor, yielding:

$$\begin{aligned}
\delta_{\rm m}^{s,L}(\vec{k}) &= \delta_{\rm m}(\vec{k}) - \int d^3x\, e^{i\vec{k}\cdot\vec{x}} \frac{1}{aH}\frac{\partial}{\partial z} \int \frac{d^3k'}{(2\pi)^3} e^{-i\vec{k}'\cdot\vec{x}} {\rm u}_z(\vec{k}') \\
&= \delta_{\rm m}(\vec{k}) + f \int \frac{d^3k'}{(2\pi)^3} \int d^3x\, e^{i(\vec{k}-\vec{k}')\cdot\vec{x}} \frac{k_z k'_z}{k'^2} \theta(\vec{k}') \\
&= \delta_{\rm m}(\vec{k}) + f\mu^2\theta(\vec{k}) \\
&= (1 + f\mu^2)\delta_{\rm m}^{L}(\vec{k}),
\end{aligned} \tag{2.53}$$

resulting in the redshift-space power spectrum at linear order:

$$P_{\rm m}^{s,L}(k) = P_{\rm m}^{s,L}(k,\mu) = (1 + f\mu^2)^2 P_{\rm m}^{L}(k). \tag{2.54}$$

For the galaxy number density, with $\delta_{\rm g} = b_1\delta_{\rm m}$ (Eq. 2.38), the power spectrum similarly becomes:

$$P_{\rm g}^{s,L}(k) = P_{\rm g}^{s,L}(k,\mu) = b^2(1 + \beta\mu^2)^2 P_{\rm m}^{L}(k), \tag{2.55}$$

where we define the quantity β known as the RSD factor:

$$\beta \equiv f/b \tag{2.56}$$

It's important to note that the anisotropic term originates from the velocity field and, therefore, does not depend on bias. This is why RSD measurements are often parameterized by the amplitude of the peculiar velocity field, $f\sigma_8(z_{\rm true})$ [132].

To understand the significance of RSD, we can expand the anisotropic power spectrum using the Legendre polynomials:

$$\begin{aligned}
P^s(k,\mu) &= \sum_\ell P_\ell(k)\mathcal{L}_\ell(\mu), \\
P_\ell(k) &= \frac{2\ell+1}{2}\int_{-1}^{1} d\mu\, P^s(k,\mu)\mathcal{L}_\ell(\mu),
\end{aligned} \tag{2.57}$$

[2]This approximation considers that all pairs of galaxies have the same line-of-sight, which we take to be the $\hat{z}$-direction.

where $\mathcal{L}_\ell(\mu)$ are the Legendre polynomials. The first three even Legendre Polynomials are:

$$\begin{aligned}\mathcal{L}_0(\mu) &= 1 \\ \mathcal{L}_2(\mu) &= \frac{3\mu^2 - 1}{2} \\ \mathcal{L}_4(\mu) &= \frac{35\mu^4 - 30\mu^2 + 3}{8}.\end{aligned} \tag{2.58}$$

The expression derived in Eq. 2.57 are known as the multipoles of the correlation function, and since the Kaiser formula includes terms up to μ^4, only the monopole ($\ell = 0$), quadrupole ($\ell = 2$), and hexadecapole ($\ell = 4$) are non-vanishing:

$$\begin{aligned}P_{\mathrm{g},\ell=0}(k) &= \left(1 + \frac{2}{3}\beta + \frac{1}{5}\beta^2\right) b^2 P_{\mathrm{m}}^L(k), \\ P_{\mathrm{g},\ell=2}(k) &= \left(\frac{4}{3}\beta + \frac{4}{7}\beta^2\right) b^2 P_{\mathrm{m}}^L(k), \\ P_{\mathrm{g},\ell=4}(k) &= \frac{8}{35}\beta^2 b^2 P_{\mathrm{m}}^L(k).\end{aligned} \tag{2.59}$$

Additionally, the multipoles of the correlation function in configuration space is related to the power spectrum multipoles as follows:

$$\xi_\ell^s(s) = i^\ell \int_0^\infty \frac{k^2 dk}{2\pi^2} P_\ell^s(k) j_\ell(ks), \tag{2.60}$$

where $j_\ell(x)$ is the spherical Bessel function of order ℓ. In a similar fashion we can obtain the transformation from configuration to Fourier space:

$$P_l^s(k) = 4\pi(-i)^l \int_0^\infty s^2 ds\ \xi_l^s(s) j_l(ks) \tag{2.61}$$

Similarly to Eq. 2.57 we can express the 2D correlation function in configuration space using Legendre Polynomials as [40]:

$$\xi(\sigma, \pi) = \xi(s, \mu) = \sum_{l=0} \xi_l(s)\mathcal{L}(\mu). \tag{2.62}$$

2.5 Modeling RSD: Non-linear effects

Modeling the Finger of God effect is significantly more complicated than modeling the Kaiser effect due to the complicated nature of non-linear interactions as we have seen in section 2.2.3. As mentioned in that section, there are many models for nonlinear interactions with a different parameter space. Each model presents different considerations when treating nonlinearities and can work better or worse depending on the galaxy sample and the scales considered. Regarding the galaxy power spectrum in redshift space, i.e. including RSD, effective field theory (EFT) [89, 50] has gained popularity recently since it is very versatile. To show this versatility, EFT allows to incorporate several kind of extra parameters to describe models of modified gravity. It also introduces counterterms parameters in order to correct that the energy-momentum tensor (Eq. 1.17) is no longer homogeneous and isotropic at small scales, i.e. off-diagonal elements are no longer 0. Although many models try to incorporate as many

parameters to have more freedom to describe nonlinear processes this is usually not recommended due to the complications of having to evaluate such a substantial parameter space. On top of that, there may be projection effects, where different parameters contribute to the model, or the power spectrum in this case, in a similar manner, i.e. the parameters are degenerated with each other. This could be very prejudicial to the estimation of the cosmological parameters which are the one of interest for cosmologists. The nonlinear parameters are usually considered nuisance parameters since they are local and do not give much information about the composition of our Universe (no particular scientific interest).

In this section we will give an introduction to another perturbative model called the velocity difference generating function (VDG) model [139, 60]. This model will be very relevant for the purposes of this thesis as we will see later when calculating the EG estimator in Chapter 4. The reasons for the selection of this model over others are related to the reported level of accuracy of this model at small scales when comparing results with simulated catalogs. We will discuss the topic with more depth in Chapter 4. So for now we will describe the mathematical description of the model.

2.5.1 The VDG model

This model differ from the EFT approach only on its treatment of redshift-space distortions. While EFT performs a full expansion of the real-to-redshift space mapping, VDG partly retains the non-perturbative nature of this mapping. The model was originally proposed in [139] to describe the matter power spectrum in RSD, in [60] it is referred as VDG due to its relation to the velocity difference generating function to account for the virialized velocity impact via an effective damping function.

In order to describe the VDG model we summarize the key points from [60], so we encourage the reader to check this reference if they want a more detailed explanation.

In redshift space the density perturbations can be expressed as[3]:

$$\delta_s(\vec{k},z) = \int_{\vec{x}} \mathrm{e}^{i\vec{k}\cdot\vec{x}} \mathrm{e}^{-if k_z \mathrm{v}_z(\vec{x})} D_s(\vec{x}) \tag{2.63}$$

where $D_s(\vec{x}) \equiv \delta_g(\vec{x}) + f\nabla_z \mathrm{v}_z(\vec{x})$ is a combination of the galaxy density contrast δ_g and the gradient of v_z along the line-of-sight. The velocity v is related to the normalized divergence field defined in Eq. 2.47:

$$\vec{\mathrm{v}} \equiv -fHa\vec{u} \rightarrow \theta = \nabla\vec{\mathrm{v}} = \delta_0 \tag{2.64}$$

Expanding δ and $\vec{\mathrm{v}}$ in perturbation theory yields the perturbation theory kernels in redshift-space Z_n [131]:

$$\begin{aligned}\delta_s(\vec{k},z) = \sum_{n=1} D^n(z) \int_{\vec{k}_1,\dots,\vec{k}_n} \delta_D(\vec{k}-\vec{k}_{1\dots n})\, Z_n(\vec{k}_1,\dots,\vec{k}_n) \\ \times \delta_L(\vec{k}_1)\cdots\delta_L(\vec{k}_n)\,,\end{aligned} \tag{2.65}$$

This Z_n kernels can be found on appendix A of [60]. Although Z_1 is given by the expression relating the real space and redshift space power spectrum in Eq. 2.54.

[3] For the configuration and Fourier space integrals we use the short-hand notation: respectively $\int_{\vec{x}_1,\dots,\vec{x}_n} \equiv \int d^3x_1 \cdots d^3x_n$ and $\int_{\vec{k}_1,\dots,\vec{k}_n} \equiv \int d^3k_1/(2\pi)^3 \cdots d^3k_n/(2\pi)^3$

$$Z_1(\vec{k}) = b_1(1+\beta\mu^2) \tag{2.66}$$

where the linear galaxy bias appears since this kernels are related to the galaxy power spectrum. In perturbation theory, predicting the clustering of biased tracers like galaxies involves relating their over-densities to various properties of the underlying dark matter field. This process, known as galaxy bias expansion (see Eq. 2.40), involves a series of operators that capture how the large-scale environment affects galaxy formation and evolution, with each operator associated with specific galaxy bias parameters. While these bias parameters cannot be calculated from first principles and depend on the selected tracer population, the relevant operators at each perturbative order can be determined based on symmetry considerations.

Tree and one-loop power spectrum

The galaxy bias expansion relevant for the power spectrum at next-to-leading order is given by:

$$\delta_g = b_1\,\delta + \frac{b_2}{2}\,\delta^2 + \gamma_2\,\mathcal{G}_2(\Phi_v) + \gamma_{21}\,\mathcal{G}_{21}(\varphi_2,\varphi_1) + b_{\nabla^2}\nabla^2\delta + \epsilon_g + \ldots, \tag{2.67}$$

where b_1, b_2 are linear and quadratic bias parameters, γ_2, γ_{21} are parameters for Galileon operators, and b_{∇^2} represents a higher-derivative bias. The operators $\mathcal{G}_2(\Phi_v)$ and $\mathcal{G}_{21}(\varphi_2,\varphi_1)$ measure the effects of large-scale tides at different orders.

Different bases for galaxy bias exist, and their parameters can be transformed into the parameters in the above expansion. The higher-derivative term $b_{\nabla^2}\nabla^2\delta$ accounts for the finite size of galaxy formation regions, becoming relevant on scales comparable to this size. This term is absorbed into a counterterm in some models.

If we want to expand to power spectrum to orders higher than linear theory (which is called the tree level), we usually start by the one-loop power spectrum which contains terms that are quadratic in the initial density perturbations:

$$P^{\rm tree}_{gg,\rm SPT}(\vec{k}) = Z_1(\vec{k})^2\,P_L(k) \tag{2.68}$$

$$P^{1-\rm loop}_{gg,\rm SPT}(\vec{k}) = 2\int_{\vec{q}}\Big[Z_2(\vec{k}-\vec{q},\vec{q})\Big]^2\,P_L(|\vec{k}-\vec{q}|)P_L(q) + 6\,P_L(k)\int_{\vec{q}} Z_3(\vec{k},\vec{q},-\vec{q})P_L(q) \tag{2.69}$$

we are using the plane-parallel approximation, so the wave vector $\vec{k}$ is described by its magnitude k and its cosine μ (Eq. 2.52). $P_L(z)$ represents the linear power spectrum derived in the previous section.

Velocity generating function

To connect the power spectrum in the VDG model with the Standard Perturbation Theory (SPT) computation, we begin with the exact expression for the redshift-space galaxy power spectrum. This can be derived from Eq. 2.42 and involves the pairwise velocity generating function $\mathcal{M}(\lambda,\vec{r})$ [131]:

$$P_{gg}(\vec{k}) = \int_{\vec{r}} \mathrm{e}^{i\vec{k}\cdot\vec{r}}\,\left[\big(1+\xi_{gg}(r)\big)\,\mathcal{M}(\lambda,\vec{r})-1\right], \tag{2.70}$$

where $\xi_{gg}(r)$ is the real-space galaxy correlation function at separation r, and $\lambda = -i\,f k\mu$.

The pairwise velocity generating function can be broken down into components that include connected correlators, which are sensitive to small-scale modes. The VDG model treats the velocity difference generating function non-perturbatively by using an effective damping function $W_\infty(\lambda)$, which accounts for small-scale velocity dispersion. This damping function is defined as:

$$W_\infty(\lambda) = \frac{1}{\sqrt{1-\lambda^2\,a_{\rm vir}^2}}\,\exp\left(\frac{\lambda^2\,\sigma_v^2}{1-\lambda^2\,a_{\rm vir}^2}\right), \tag{2.71}$$

where $a_{\rm vir}$ is a free parameter that controls the non-Gaussianity of velocity differences.

The remaining terms in the expression are treated perturbatively, expanding the exponentials to one-loop order. This involves galaxy bias, stochastic terms, and counterterms from small-scale modes, all evaluated using BAO-damped linear power spectra. The additional terms $\Delta P(\vec{k})$ from this expansion, with respect to EFT, are given by:

$$\Delta P(k,\mu) = \lambda^2\,\sigma_v^2\,P_{D_sD_s}(k,\mu) - \lambda^2\int_{\vec{q}}\frac{q_z^2}{q^4}P_{\theta\theta}(q)\,P_{D_sD_s}(\vec{k}-\vec{q}), \tag{2.72}$$

where $P_{D_sD_s}$ and $P_{\theta\theta}$ are the power spectra of the density and velocity divergence fields, respectively, and σ_v^2 is the linear velocity dispersion given by:

$$\sigma_v^2 = \frac{1}{3}\int_{\vec{k}}\frac{P_{\theta\theta}(k)}{k^2} = \frac{1}{3}\int_{\vec{k}}\frac{P_L(k)}{k^2} \tag{2.73}$$

The stochastic power spectrum

The stochastic field ϵ_g captures highly non-linear effects in galaxy formation that are uncorrelated with large-scale fields and are considered stochastic at large scales. The contribution of this stochasticity to the galaxy power spectrum, $P_{\epsilon_g\epsilon_g}(k)$, can be expanded as:

$$P_{\epsilon_g\epsilon_g}(k) = \frac{1}{\bar{n}}\left(N_0^P + N_{2,0}^P\,k^2 + \ldots\right), \tag{2.74}$$

where $\bar{n}$ is the mean number density of tracers, and $N_0^P, N_{2,0}^P$ are stochastic bias parameters.

Additionally, redshift-space distortions introduce a stochastic term related to the gradient of the line-of-sight velocity field, $P_{\epsilon_g\epsilon_{\nabla_z v_\parallel}}(k,\mu)$, which can be expressed as:

$$P_{\epsilon_g\epsilon_{\nabla_z v_\parallel}}(k,\mu) = \frac{N_{2,2}^P}{\bar{n}}\mathcal{L}_2(\mu)\,k^2, \tag{2.75}$$

where $\mathcal{L}_2(\mu)$ is the second Legendre polynomial.

The total stochastic contribution to the galaxy power spectrum is:

$$P_{gg}^{\rm stoch}(k,\mu) = P_{\epsilon_g\epsilon_g}(k) + P_{\epsilon_g\epsilon_{\nabla_z v_\parallel}}(k,\mu). \tag{2.76}$$

In the VDG model, the impact of small-scale velocities is captured by the effective damping function W_∞, making the contribution from the stochastic velocity term less significant.

Counterterms power spectrum

In perturbation theory, the loop integrals involved in predicting the galaxy power spectrum extend over all scales, including those where the perturbative approach breaks down. To maintain a consistent theoretical framework, it becomes necessary to introduce counterterms. These counterterms have adjustable amplitudes (free parameters) that are designed to absorb any sensitivity to non-linear modes in the large-scale limit. There some studies like [53] that have shown that the leading counterterms for the galaxy power spectrum in redshift space typically scale as $\sim \mu^{2n} k^2 P_L(k)$, with $n = 0, 1, 2$. For simplicity, these are assumed to be local in time.

The first of these counterterms scales identically to the higher-derivative bias term $\nabla^2\delta$ (Eq. 2.67), allowing us to absorb the coefficient $b_{\nabla^2\delta}$ into the corresponding counterterm parameter. This same counterterm also captures the leading effect from deviations in the perfect fluid approximation for the matter field . The other two counterterms, corresponding to $n = 1$ and $n = 2$, can account for relevant velocity bias effects, which have been neglected so far.

Then, three free parameters: c_0, c_2, and c_4, are introduced to define the contribution of leading-order (LO) counterterms to the galaxy power spectrum as follows:

$$P_{gg}^{\rm ctr}(k,\mu) = -2\sum_{n=0}^{2} c_{2n}\,\mathcal{L}_{2n}(\mu)\,k^2\,P_L(k)\,, \tag{2.77}$$

where $\mathcal{L}_{2n}(\mu)$ are the Legendre polynomials of order $2n$. This choice of polynomials instead of μ^{2n} involves a linear transformation of the counterterm parameters, ensuring that each primarily contributes to a single power spectrum multipole. This means that c_i will contribute mostly to $P_{g,l=i}$ for $i = 0, 2, 4$.

Infrared Resummation

Considering all the parts derived in the previous subsections, the VDG model power spectrum is given by:

$$P_{gg,\rm VDG}(k) = W_\infty(k)\left[P_{gg,\rm SPT}^{\rm tree}(k) + P_{gg,\rm SPT}^{1-\rm loop}(k) + P_{gg}^{\rm stoch}(k) + P_{gg}^{\rm ctr}(k) - \Delta P(k)\right]. \tag{2.78}$$

Although this model accurately describes the general behavior of the anisotropic galaxy power spectrum at mildly non-linear scales, it struggles to represent the amplitude of the Baryon Acoustic Oscillation (BAO) wiggles with precision. These wiggles are especially sensitive to large-scale bulk flows, which can blur the BAO signal due to extensive relative displacement fields.

In a perturbative approach, the corrections to the matter power spectrum can be resumed at each wavemode k, accounting for the effects of fluctuations on larger scales. At leading order, this resummation manifests as a damping factor that primarily impacts the BAO wiggles. A common practice is to decompose the linear matter power spectrum into a smooth component and a wiggly component as follows:

$$P_L(k) = P_{nw}(k) + P_w(k), \tag{2.79}$$

Following the leading order approximation, the infrared-resummed matter power spectrum is then expressed as the sum of the smooth component and the damped wiggly component:

$$P_{\rm mm}^{\rm IR-LO}(k) = P_{nw}(k) + e^{-k^2\Sigma^2} P_w(k), \tag{2.80}$$

where the damping factor Σ^2 is given by:

$$\Sigma^2 = \frac{1}{6\pi^2}\int_0^{k_s} P_{nw}(q)\left[1 - j_0\left(\frac{q}{k_{osc}}\right) + 2j_2\left(\frac{q}{k_{osc}}\right)\right]\mathrm{d}q \tag{2.81}$$

Here, j_n represents the n-th order spherical Bessel function, $k_{osc} = 1/\ell_{\rm osc}$ corresponds to the wavemode at the BAO scale $\ell_{\rm osc} = 110\,h^{-1}$Mpc, and k_s denotes the ultraviolet integration limit.

At next-to-leading order, the infrared-resummed matter power spectrum receives further contributions, including standard one-loop corrections sourced by higher powers of the density field. The full expression is then:

$$\begin{aligned} P_{\rm mm}^{\rm IR-NLO}(k) = P_{nw}(k) + \left(1 + k^2\Sigma^2\right)e^{-k^2\Sigma^2}P_w(k) + \\ + P^{\rm 1-loop}\left[P_{\rm mm}^{\rm IR-LO}\right](k), \end{aligned} \tag{2.82}$$

where the square brackets indicate that the one-loop integrals are computed using the leading order IR-resummed power spectrum instead of the linear power spectrum.

When extending this approach to the redshift-space galaxy power spectrum, the most significant change is that the damping factor now depends on the line-of-sight angle μ. At leading order, this can be written as:

$$P_{\rm gg}^{s,\rm IR-LO}(k,\mu) = \left(b_1 + f\mu^2\right)^2\left[P_{nw}(k) + e^{-k^2\Sigma^2_{\rm tot}(\mu)}P_w(k)\right]. \tag{2.83}$$

The angular dependence of the new damping factor $\Sigma^2_{\rm tot}(\mu)$ is given by:

$$\Sigma^2_{\rm tot}(\mu) = \left[1 + f\mu^2(2+f)\right]\Sigma^2 + f^2\mu^2(\mu^2-1)\mathrm{d}\Sigma^2, \tag{2.84}$$

where

$$\mathrm{d}\Sigma^2 = \frac{1}{2\pi^2}\int_0^{k_s} P_{nw}(q)\, j_2\left(\frac{q}{k_{osc}}\right)\mathrm{d}q. \tag{2.85}$$

At next-to-leading order, the expression becomes :

$$\begin{aligned} P_{\rm gg}^{s,\rm IR-NLO}(k,\mu) = \left(b_1 + f\mu^2\right)^2\left[P_{nw}(k) + \left(1 + k^2\Sigma^2_{\rm tot}(\mu)\right)e^{-k^2\Sigma^2_{\rm tot}(\mu)}P_w(k)\right] + \\ + P_{\rm gg}^{s,\rm 1-loop}\left[P_{nw}\right](k) + \\ + e^{-k^2\Sigma^2_{\rm tot}(\mu)}\left(P_{\rm gg}^{s,\rm 1-loop}\left[P_{nw}+P_w\right](k) - P_{\rm gg}^{s,\rm 1-loop}\left[P_{nw}\right](k)\right), \end{aligned} \tag{2.86}$$

where, as before, the square brackets indicate that the one-loop terms are evaluated using either the total linear matter power spectrum ($P_{nw} + P_w$) or just the smooth component (P_{nw}).

Modeling multipoles of the correlation function

When considering the redshift of our galaxy sample we need to consider a fiducial cosmology in order to convert from observed redshfits to redshift space ($\vec{s}$ or $\vec{k}$). If the selected fiducial cosmology deviates from the true cosmology, this results in an incorrect rescaling of both the parallel and perpendicular components relative to the line of sight. Such discrepancies in rescaling can significantly affect the two-point statistics, which are central to the analysis presented in this work.

The anisotropic distortions that arise from an incorrect choice of fiducial cosmology are, to some extent, degenerate with anisotropies induced by the peculiar velocity field. Therefore, to accurately interpret the information contained within the galaxy power spectrum, it is imperative to account for these potential distortions.

To correct for the effects of the chosen fiducial cosmology, a standard approach is to rescale the model power spectrum along the directions parallel and perpendicular to the line of sight. The rescaling is defined as follows:

$$k_{\perp}^{fid} = q_{\perp} k_{\perp}, \quad k_{\parallel}^{fid} = q_{\parallel} k_{\parallel}, \tag{2.87}$$

where $q_{\perp}$ and $q_{\parallel}$ are known as the Alcock-Paczynski parameters. This parameters quantify the ratios of the angular diameter distance $D_M(z)$ and the Hubble distance $D_H(z)$ between the true and fiducial cosmologies, and are given by:

$$q_{\perp}(z) = \frac{D_M(z)}{D_M^{fid}(z)}, \quad q_{\parallel}(z) = \frac{D_H(z)}{D_H^{fid}(z)} = \frac{H^{fid}(z)}{H(z)}. \tag{2.88}$$

With these definitions, the Alcock-Paczynski corrected wavenumber $k(k^{fid}, \mu^{fid})$ and the cosine of the angle to the line of sight $\mu(k^{fid}, \mu^{fid})$ can be expressed as:

$$k(k^{fid}, \mu^{fid}) = k^{fid} \left[\frac{(\mu^{fid})^2}{q_{\parallel}^2} + \frac{1 - (\mu^{fid})^2}{q_{\perp}^2} \right]^{\frac{1}{2}}, \tag{2.89}$$

$$\mu(k^{fid}, \mu^{fid}) = \frac{\mu^{fid}}{q_{\parallel}} \left[\frac{(\mu^{fid})^2}{q_{\parallel}^2} + \frac{1 - (\mu^{fid})^2}{q_{\perp}^2} \right]^{-\frac{1}{2}}. \tag{2.90}$$

Finally, the corrected galaxy power spectrum multipoles $P_{\ell}(k^{fid})$ are evaluated as:

$$P_{\ell}(k^{fid}) = \frac{2\ell + 1}{2 q_{\perp}^2 q_{\parallel}} \int_{-1}^{+1} P_{gg}^{s} \left(k(k^{fid}, \mu^{fid}), \mu(k^{fid}, \mu^{fid}) \right) \mathcal{L}_{\ell} \left(\mu(k^{fid}, \mu^{fid}) \right) d\mu^{fid}, \tag{2.91}$$

where $\mathcal{L}_{\ell}$ represents the Legendre polynomial of order ℓ. This approach ensures that the derived power spectrum is correctly interpreted within the context of the selected fiducial cosmology, thereby allowing for accurate cosmological inferences from observational data.

2.6 Weak Gravitational Lensing

All observed light from distant galaxies undergoes some degree of gravitational lensing due to the inhomogeneous nature of the universe, which is filled with density fluctuations on smaller scales. These fluctuations generate a tidal gravitational field that causes light to bend at various angles [58]. Consequently, the images of light-emitting galaxies we observe are distorted. The degree and direction of this distortion are directly related to the size and shape of the matter distribution projected along the line of sight.

Lensing can be categorized into two regimes based on the deflection angle: strong lensing and weak lensing. Strong lensing occurs when the lensing object lies between the source and

the observer along the line of sight. This regime can produce multiple images of point-like sources or create rings around the lensing object for extended sources. In contrast, weak lensing, which is less pronounced, results in subtle distortions such as isotropic magnification (convergence) and anisotropic stretching (shear) [58]. Strong lensing is less common as it requires lenses with very high masses, like black holes, while weak lensing is more prevalent. Although weak lensing effects are subtle and challenging to detect, statistical methods applied across many galaxies can reveal trends caused by weak lensing. This will be explored in more detail later when discussing shear and convergence. For now, we will focus on calculating the deflection angle in the weak lensing regime using the metric defined in General Relativity and Fermat's principle, as described by equation (2.92).

2.6.1 Deflection angle

Going back to Eq. (1.9), which represents the line element of the homogeneous expanding universe, and adding first-order perturbations to homogeneity with the potentials Ψ and Φ for time and space respectively, the line element is given by [58]:

$$ds^2 = -\left(1+\frac{2\Psi}{c^2}\right)c^2dt^2 + a^2(t)\left(1-\frac{2\Phi}{c^2}\right)(d\chi^2 + S_k^2(\chi)d\Omega^2), \tag{2.92}$$

The potentials Φ and Ψ describe weak gravitational fields, as long as $\Psi, \Phi \ll c^2$. This potentials are equal in GR.

Introducing the propagation condition for light, ds=0, we obtain:

$$c' = \frac{dl}{dt} = c\sqrt{\frac{1+2\Phi/c^2}{1-2\Phi/c^2}} \approx c\left(1+\frac{2\Phi}{c^2}\right) \tag{2.93}$$

Where we have used a first-order Taylor expansion using that for weak lensing $\Phi/c^2 << 1$. The upper index in c' represents the speed of a light ray in a weak gravitational field. So we can define an effective index of refraction as:

$$n = \frac{c}{c'} = 1 - \frac{2\Phi}{c^2} \tag{2.94}$$

Where $n > 1$ as Φ is always negative. We can now apply Fermat's principle [58], which asserts that a light ray follows the path between two fixed points along which it takes the least time to traverse.

$$\delta t = \frac{1}{c}\int n(r)dr = \frac{1}{c}\int\left(1-\frac{2\Phi}{c^2}\right)dr = 0 \tag{2.95}$$

From here we can get the Euler-Lagrange equations for the refractive index. Integrating these equations along the light path results in the deflection angle between the directions of emitted and received light rays:

$$\hat{\vec{\alpha}} = -\frac{2}{c^2}\int \vec{\nabla}_\perp \Phi(r)dr \tag{2.96}$$

The gradient of the potential is taken perpendicular to the light path, with respect to physical coordinates. This integral is hard to calculate over the actual light path. Since for weak

lensing deflection angles are on the order of arc seconds or smaller, the integration path can be approximated by a straight line. Doing the integral this way, over the unperturbed ray, is called the Born approximation [57].

In Figure (2.7) is showed a thin lens approximation of a gravitational lensing system. In this approximation the deflection occurs in the plane of the lens, considered much thinner than the overall extent of the system D_S. Then the path light from the observer to the source can be approximated by straight lines from the observer to the lens impact parameter ξ and from there to the source. The D parameters in Figure 2.7 represents angular diameter distances (sec. 1.8.3) so we can derive a relation between the angles that holds true for any curvature of the Universe:

$$D_S\vec{\beta} = D_S\vec{\theta} - D_{LS}\hat{\vec{\alpha}} \tag{2.97}$$

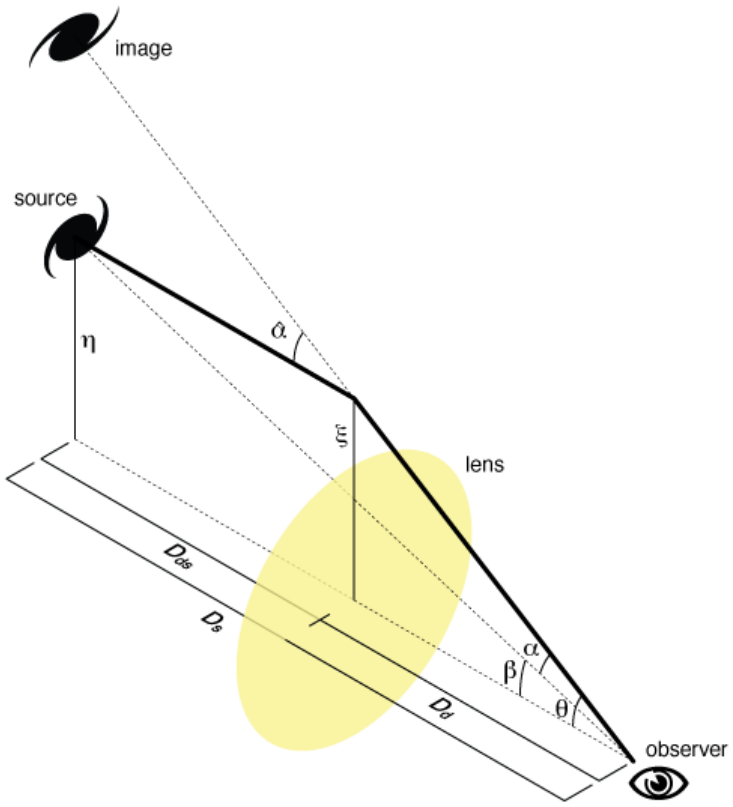

FIGURE 2.7: Sketch of a gravitational lens system. The angle between the source and the optical axis is β, the angle between the image and the optical axis is θ, while the deflection angle caused by the lens is $\hat{\alpha}$. The deflection angle traced from the observer is α. Credit: Michael Sachs, Wikimedia commons.

The angle α which represents the deflection angle from the observer is given by:

$$\vec{\alpha} = \frac{D_{LS}}{D_S}\hat{\vec{\alpha}} \tag{2.98}$$

Which is useful to trace back a light ray from the observer since we can express the position to the source as:

$$\vec{\beta} = \vec{\theta} - \vec{\alpha} \tag{2.99}$$

If we express the gradient in Eq. (2.96) with respect the angular position $\vec{\theta}$ instead of using perpendicular distances we obtain:

$$\vec{\alpha} = \vec{\nabla}_\theta \psi \tag{2.100}$$

Where $\vec{\nabla}_\theta = D_L \vec{\nabla}_\perp$ and ψ is the lensing potential defined as [57]:

$$\psi = \frac{2}{c^2} \frac{D_{LS}}{D_L D_S} \int \Phi(r) dr \tag{2.101}$$

The lensing potential is a 2D potential, the gravitational potential projected into the sky, that contains all imaging properties of a gravitational lens. So is convenient to express all the others lensing observables as a function of this potential.

To obtain Eq. (2.101) we were still assuming the thin lens approximation which is not appropriate for gravitational lensing by the large scale structures. To obtain the expression for extended lenses we just need to incorporate the distance factor $D_{LS}/D_L D_S$ inside the integral over the line of sight as comoving distances (Born approximation).

$$\psi(\vec{\theta}) = \frac{2}{c^2} \int_0^{\chi_S} \frac{\chi_S - \chi}{\chi_S \chi} \Phi(\chi_{\vec{\theta}}, \chi) d\chi \tag{2.102}$$

Where χ_S is the comoving distance to the source. The expression $(\chi_S - \chi)/\chi_S\chi$ is the extended form of the expression $D_{LS}/D_L D_S$ from Eq. (2.101).

2.6.2 Convergence and shear

We can linearize the lens equation (2.99) with the Jacobian matrix A=$\partial\beta/\partial\theta$ that relates the lensed coordinates θ to the the unlensed coordinates β. The matrix elements are given by:

$$A_{ij} = \frac{\partial \beta_i}{\partial \theta_j} = \delta_{ij} - \frac{\partial \alpha_i}{\partial \theta_j} = \delta_{ij} - \frac{\partial^2 \psi}{\partial \theta_i \partial \theta_j} \tag{2.103}$$

The matrix A is then symmetrical. If we parametrize its components with the scalar term convergence κ and the two-component spin-two term shear γ we get:

$$A = \begin{bmatrix} 1 - \kappa - \gamma_1 & -\gamma_2 \\ -\gamma_2 & 1 - \kappa + \gamma_1 \end{bmatrix} \tag{2.104}$$

Where $\gamma = \gamma_1 + i\gamma_2$. With this parametrization the definitions of convergence and shear are given as second derivatives of the lensing potential [57]:

$$\kappa = \frac{1}{2}\nabla^2 \psi \; ; \quad \gamma_1 = \frac{1}{2}\left(\frac{\partial^2 \psi}{\partial \theta_1^2} - \frac{\partial^2 \psi}{\partial \theta_2^2} \right) \; ; \quad \gamma_2 = \frac{\partial^2 \psi}{\partial \theta_1 \partial \theta_2} \tag{2.105}$$

We can separate the matrix A from Eq. (2.104) into two parts:

$$A = (1-\kappa)\begin{bmatrix} 1 & 0 \\ 0 & 1 \end{bmatrix} + \gamma \begin{bmatrix} cos(2\phi) & sin(2\phi) \\ sin(2\phi) & -cos(2\phi) \end{bmatrix} \tag{2.106}$$

Where ϕ is the angle between $\vec{\alpha}$ and the optical axis (see Figure 2.7). This shows more clearly that the convergence, the diagonal part, is an isotropic increase or decrease of the observed size of a source image. While the shear, the trace-free part, is an anisotropic stretching turning the light distribution into an ellipse.

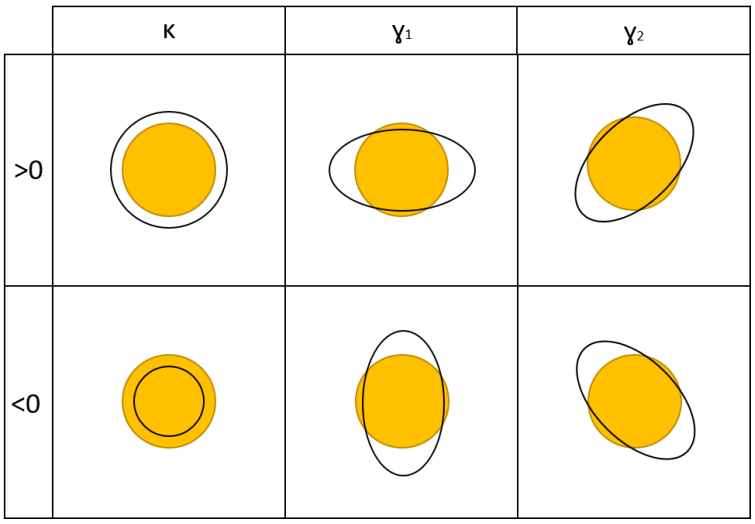

FIGURE 2.8: Effects of a negative/positive convergence and shear over the image (black line) of a source object (yellow area).

Looking back at equation (2.105) we see that the convergence is related to the lensing potential ψ via a 2D Poisson equation so it represents a projected surface density. The gravitational potential Φ is related to the density fluctuations δ, Eq. (1.11), by a 3D Poisson equation:

$$\nabla^2\Phi = \frac{3}{2}\frac{\Omega_m H_0^2}{a}\delta \tag{2.107}$$

Then we can re-express the convergence in terms of the density fluctuations combining Eq. (2.102), (2.105) and (2.107):

$$\kappa(\theta,\chi) = \frac{3\Omega_m H_0^2}{2c^2}\int_0^{\chi}\frac{1}{a(\chi')}\frac{\chi-\chi'}{\chi}\chi'\delta(\chi'_{\vec{\theta}},\chi')d\chi' \tag{2.108}$$

We had to replace the 2D Laplacian of the convergence of Eq. (2.105) with the 3D Laplacian for the gravitational potential. So we would have had to add a second-order derivative along the comoving coordinate but this term vanishes in average while integrating along the line of sight [57].

The weight factor $(\chi-\chi')/\chi'$ represents a parabola centered at half the distance of the source, i.e $\chi' = \chi_S/2$, which is an analogy to the lens efficiency from standard optics.

So expression (2.108) corresponds to the convergence of a thin lens whose effects are equivalent to those caused by the actual extended matter distribution. Since it is related to the density fluctuations we can use the convergence to estimate the matter distribution at different redshift. But obtaining the convergence directly is very complicated since we cannot know

how much the image of a galaxy is enlarged (or reduced) as we cannot observe the unaltered object. The only thing we can observe and distinguish is the shear. Actually we observe the reduced shear g, Eq. (2.109) [57]. But given that for the weak lensing regime the distortions are small we have that $\kappa \sim 0$ and $g \sim \gamma$.

$$g = \frac{\gamma}{1-\kappa} \tag{2.109}$$

The shear of an individual galaxy is also hard to measure. This is because galaxies have an intrinsic ellipticity ϵ^s so is hard to determine if the ellipticity is caused by shear or not. Besides shear is usually very small in the weak regime, the typical cosmic shear is around 0.01, while galaxies have an intrinsic ellipticity dispersion of about 0.4. Then we need to use an statistical approach by averaging the ellipticity of several nearby galaxies in the sky. Since we would expected that intrinsic ellipticities are oriented at random then the average of this term should be close to 0 [57].

$$< \epsilon > \approx < \epsilon^s > + < \gamma > \approx < \gamma > \tag{2.110}$$

The mean value of the shear does not vanish since nearby galaxies are affected by almost the same lens distribution so there is a correlation between the ellipticity direction given by shear. Although some systematic effects or tidal effects caused by gravity can produce intrinsic galaxy alignments that can be detected and corrected using high-order statistical functions.

So the typical approach for obtaining information from weak lensing starts by estimating the reduced shear by averaging the ellipticity over a small patch of the sky. Then using the relations of Eq. (2.105) we can obtain the lensing potential and from there estimate the convergence related to the density fluctuations. We can 3D map the mass distribution by obtaining the shear distribution at different redshift. This technique is called cosmic shear and in practice has many more complications not discussed in this thesis related to higher redshift estimations, shear estimations, high order corrections to statistical functions or approximations (like Bors). Although we will have a little more of insight on some of these issues when we talk about the power spectrum. Despite all these complications, the phenomenon of weak lensing is a continuous research field since its results look very promising in theory [57]. We hope to solve some of this problems by using analytical simulations (sec. 3.3) that allow us to study the predictions of weak lensing and test possible solutions to the issues listed above.

In the next section we will introduce the magnification which is an estimator of the convergence, as an alternative to the reduced shear as estimator of the shear.

2.6.3 Magnification

We have seen that the convergence and shear change the size of the image of a galaxy. This causes the total flux received from the galaxy to change too. Gravitational lensing also conserves surface brightness as a consequence from the Liouville's theorem for optical systems [57]. These effects are produced by what is known as gravitational magnification.

The magnification is defined as the ratio of the lensed to the unlensed flux or, since surface brightness is conserved, the ratio of total size between image and original source. So going back to the lens equation (2.99) we can see that we can define the magnification μ as the determinant of the Jacobian matrix A [57]:

$$\mu = \frac{\text{image size}}{\text{actual size}} = |A| = \frac{1}{(1-\kappa)^2 - |\gamma|^2} \approx 1 + 2\kappa \tag{2.111}$$

Where the approximation is only valid for the weak lensing regime. We see that the magnification is a direct estimator of the convergence as an alternative to use the shear to obtain the 2D potential. Although it is much harder to measure since we cannot know if the flux of a galaxy is altered by magnification. In this case we cannot average the intrinsic (or unaltered) flux over many galaxies since it cannot cancel out. Besides there are other effects like dust absorption that can alter the observed flux of a galaxy. Despite these hardships we can obtain some information from magnification.

In real cosmological observations the measuring instrument has a flux limit below which it cannot detect the light of a galaxy. But cosmological surveys with a given flux limit can detect galaxies below the flux threshold due to magnification. While some galaxies above the threshold may not be detect for $\mu < 1$. This produces a change in the density of source galaxies [57]. On the other hand, lensing not only changes the object sizes but stretches (or compresses for $\mu < 1$) the region of sky behind a lens changing also the density of sources. So for a given value of μ these two magnification effects compete always in opposite directions by reducing and raising the local density of background sources, see Figure 2.9. The net effect of this alteration of the source density counts is called magnification bias.

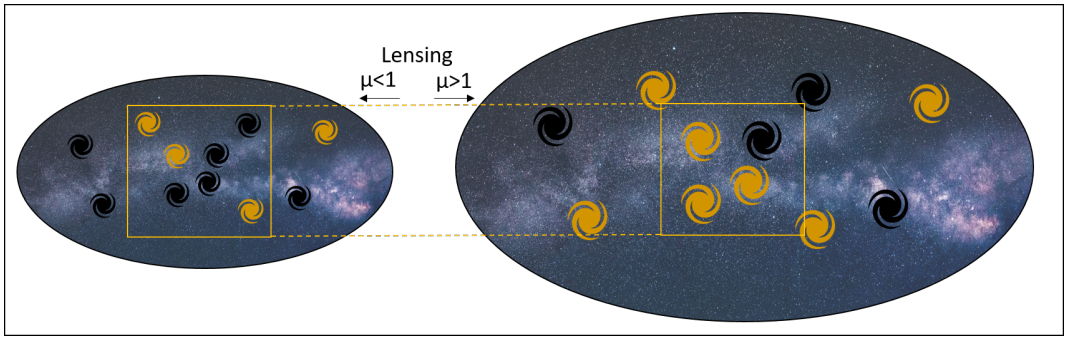

FIGURE 2.9: Effects of magnification bias. The observed area is the yellow square and the galaxies above the flux limit are marked as yellow. The lensed case is determined by the value of μ following the convention written in the figure.

To quantify the magnification bias we can start by considering that the cumulative number of galaxies, for a magnitude limited survey of area A, above a flux limit f scales as $N_o(>) \sim Af^{-\alpha}$. Where α is the power-law slope of the cumulative apparent magnitude m function of the background sources at flux limit f [65]. Then the magnification μ modifies the flux limit as $f \to f/\mu$ and the observed survey area as $A \to A/\mu$. Note that for a $\mu > 1$ the flux limit is reduced because galaxies increase their shape and flux. The survey area is stretched so the observed area is a portion of the original area then the value A is also reduced by magnification for $\mu > 1$ (see right image of Figure 2.9). Then we have that the magnified number count is given by:

$$N(> f) \sim \frac{A}{\mu}\left(\frac{f}{\mu}\right)^{-\alpha} = \mu^{\alpha-1} N_o(> f) \tag{2.112}$$

So the net effect of magnification bias depends on the magnification value μ and the slope of the cumulative apparent magnitude function of background sources α at flux limit f. Then if

$\mu > 1$ the number counts increase as the value of α raises. We can interpret this as follows, a higher value of α means that at the magnitude limit there are more galaxies with a magnitude a bit higher (flux a bit lower) than the limit. This galaxies are the most probable to enter the flux limit by magnification increasing the number count. The same argument can be done for $\mu < 1$ for low values of α.

From Eq. (2.111) we know that $\mu = 1 + 2\kappa$ where $|\kappa| << 1$ so we can Taylor expand the magnification bias term as:

$$\mu^{\alpha-1} \approx 1 + 2(\alpha - 1)\kappa \tag{2.113}$$

Therefore the magnified overdensity of background sources is given by:

$$\delta_{all} = \frac{N - N_o}{N_o} = \delta_m + \delta_p = 2(\alpha - 1)\kappa = (5s - 2)\kappa \tag{2.114}$$

Where $\delta_m = 2\alpha\kappa$ is the contribution to counts from magnified magnitudes (flux limit) and $\delta_p = -2\kappa$ is the contribution to counts from lensed positions (area distortion). These two contributions cannot be distinguished observationally [65]. The value s is the the logarithmic slope of the background number counts for a magnitude limit m at redshift z:

$$s = 2\alpha/5 \equiv \frac{dLog_{10}N(< m, z)}{dm}\bigg|_{m=m_{lim}} \tag{2.115}$$

In sec. 3.6.3 we describe the steps we take to calculate this parameter in simulations.

2.6.4 The lensing angular power spectrum

The 2 point correlation function (2PCF) defined in Eq. 2.3, $< x(r)x(r + dr) >$, corresponds to the average of a certain quantity (galaxy counts, convergence, shear, etc...) over many distances. Until now we have limited this function to study overdensities, but in observations the real observable tracers are galaxies. So we can use this function to study the correlation of other properties like the shear or the magnification. Since lensing correlations are only affected on the sky position of the objects (no effect on the radial component) we can use the angular correlation function defined as:

$$\xi_{\gamma\nu}(\theta) \equiv \langle \gamma(\vec{\theta'})\, \nu(\vec{\theta'} + \vec{\theta}) \rangle, \tag{2.116}$$

where $\vec{\theta}$ is the angular separation on the sky, γ and ν are the quantities being correlated. If $\gamma = \nu$ we refer to an autocorrelation, otherwise we use the term cross-correlation. An advantage of using angular correlations is that we do not need to calculate the redshifts which can be expensive and inaccurate on galaxy surveys.

In a similar fashion we can express this correlations functions in Fourier space to obtain the power spectrum of different quantities. This function contains a lot of information of density fluctuations at different scales. We have already explained in sec. 1.4 that the CMB angular power spectrum was used to determine the composition percentages of our Universe.

We can define the angular power spectrum C_ℓ, which is analogous to the 3D power spectrum but projected onto the sky, where it is expressed in terms of the 2D wave number ℓ (multipoles) [58]. This function is determined using spherical harmonics $Y_{\ell m}(\theta, \phi)$, which form a complete

set of orthogonal functions on the sphere and satisfy Laplace's equation (see Figure 2.10). Similar to how any 1D function can be represented by a Fourier series, any function on a sphere can be expanded as a sum of spherical harmonics. Each spherical harmonic is characterized by two integer indices: ℓ, which relates to the scale k, and m, which ranges from $-\ell$ to ℓ.

The angular power spectrum C_ℓ is defined as:

$$C_\ell \equiv \frac{1}{2\ell+1}\sum_m \langle |a_{\ell m}|^2 \rangle, \tag{2.117}$$

where $a_{\ell m}$ are the coefficients of the spherical harmonic expansion, related to the corresponding $Y_{\ell m}$ and the density perturbations. This expression is particularly useful in cosmology because it accounts for the isotropy of the universe, making C_ℓ independent of the orientation on the sky.

The angular power spectrum can also be understood as the Fourier transform of the angular correlation function $\xi(\theta)$:

$$C_\ell(\ell) = \int d^2\theta\, \xi(\theta)\, e^{-i\vec{\ell}\cdot\vec{\theta}}, \tag{2.118}$$

where $\vec{\ell}$ is the 2D wave vector conjugate to the angular separation $\vec{\theta}$ and with module ℓ.

We can express the angular power spectrum for two quantities γ and ν as [61]:

$$C_\ell^{\gamma\nu} = 4\pi \int \frac{dk}{k}\, \mathcal{P}(k)\, \Delta_\ell^\gamma(k)\, \Delta_\ell^\nu(k) \tag{2.119}$$

where $\mathcal{P}$ is the primordial power spectrum, Δ_ℓ are the transfer functions of the tracers. For example for the galaxy density fluctuations (without including RSD distortions or magnification effects):

$$\Delta_\ell^{\mathrm{D}} = \int dz\, n_z(z) b(z) T_\delta(k,z) j_\ell(k\chi(z)), \tag{2.120}$$

where T_δ is the matter density transfer function and j_ℓ is the spherical Bessel function of order ℓ. Calculating the angular power spectrum this way is computational expensive due to having to integrate two spherical functions.

To simplify the computation of lensing power spectra, the Limber approximation is often used. In this approximation the Bessel functions are given by $j_\ell(x) \simeq \sqrt{\pi/(2\ell+1)}\delta(\ell+1/2-x)$ which are much faster to evaluate. This approximation is valid when the quantities $\gamma(\vec{\theta})$ and $\nu(\vec{\theta})$, which are projected onto the sky, originate from 3D quantities $\gamma(\vec{r})$ and $\nu(\vec{r})$ via a window function $W(\chi)$, where χ represents the comoving distance. Specifically, the projections are given by:

$$\gamma(\vec{\theta}) = \int_0^{\chi_{\mathrm{lim}}} d\chi\, W_\gamma(\chi)\, \gamma(\chi\vec{\theta},\chi), \qquad \nu(\vec{\theta}) = \int_0^{\chi_{\mathrm{lim}}} d\chi\, W_\nu(\chi)\, \nu(\chi\vec{\theta},\chi). \tag{2.121}$$

Under the Limber approximation, the angular cross-power spectrum of γ and ν is expressed as:

$$\mathcal{C}_{\gamma\nu}(\ell) = \int_0^{\chi_{\mathrm{lim}}} d\chi \frac{W_\gamma(\chi) W_\nu(\chi)}{\chi^2} P_{\gamma\nu}\left(\frac{\ell}{\chi}\right), \tag{2.122}$$

where $P_{\gamma\nu}(k)$ is the 3D cross-power spectrum of the fields γ and ν, evaluated at the 3D wave number $k \approx \ell/\chi$. This relation between k and ℓ is an approximation given by the projection of a 3D-dimensional fluctuations onto the 2D-dimensional sky. We can also relate the multipole ℓ to the angular scale by the following approximation:

$$\ell \approx \frac{\pi}{\theta}, \quad \text{with } \theta \text{ in radians} \tag{2.123}$$

The Limber approximation holds when the fields γ and ν vary over length scales much smaller than the characteristic scale of the window functions W_γ and W_ν [61]. This means that at large scales this approximation breaks down, so an alternative is to use limber after a certain ℓ. With Limber we can compute the statistics of any projected quantity as an integral over the 3D statistics.

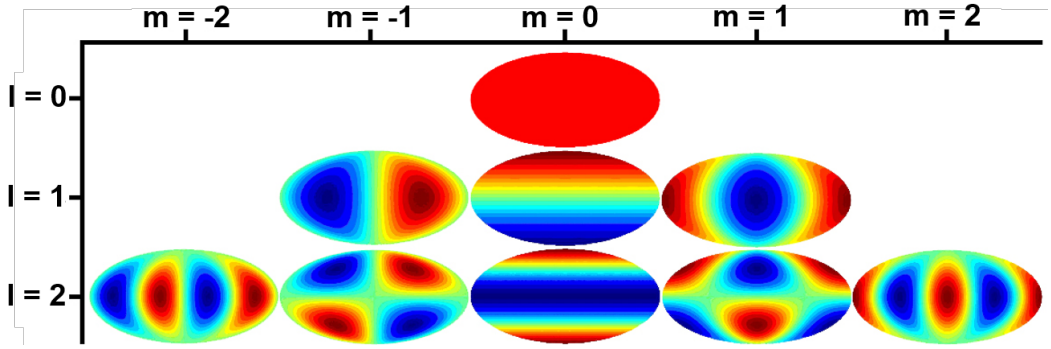

FIGURE 2.10: Firsts low order spherical harmonics plotted in the sphere. Note as ℓ increases the harmonics show amplitude variations over smaller scales. For $\ell = 0$ the function represents an amplitude normalization factor. Credits: Ville Heikkilä.

Going back to Eq. (2.108) we can express the converge C_ℓ^κ under the Born and Limber approximation as:

$$C_\ell^{\kappa\kappa}(z) = \frac{9H_o^4\Omega_m^2}{4c^4}\int P(k,z)\frac{(\chi_s-\chi)^2}{\chi_s^2 a^2}d\chi \tag{2.124}$$

Where $P(k,z)$ is the 3D density power spectrum at redshift z.

The $C_\ell s$, due to its analogy to the correlation function, also contains statistical information about the density fluctuations at different scales. Besides it is very useful to calculate since it relates all the lensing observables, Eq. (2.105), by a linear transformation with the multipole ℓ [65].

$$\kappa_{\ell m} = -\frac{1}{2}\ell(\ell+1)\phi_{\ell m}\ ; \quad \alpha_{\ell m} = -\sqrt{\ell(\ell+1)}\phi_{\ell m}; \tag{2.125}$$
$$\gamma_{\ell m} = \frac{1}{2}\sqrt{(\ell+2)(\ell^2-1)}\phi_{\ell m}$$

So we can save a lot of time and resources by calculating the angular power spectrum of one of this quantities and obtaining all the other observables from the 2D gravitational potential in spherical harmonics.

2.6.5 Shear correlations

The shear components γ_1 and γ_2 are initially defined with respect to a Cartesian coordinate frame [58]. However, when considering the distortion of background galaxies by a foreground mass, it is often more useful to evaluate these components in a rotated reference frame centered on the lens object. The shear is oriented tangentially to the center of mass of a nearby (in angular coordinates) a lens object since the part closer to the center of the lens is more deflected than the part further from the center as shown in Fig. 2.11.

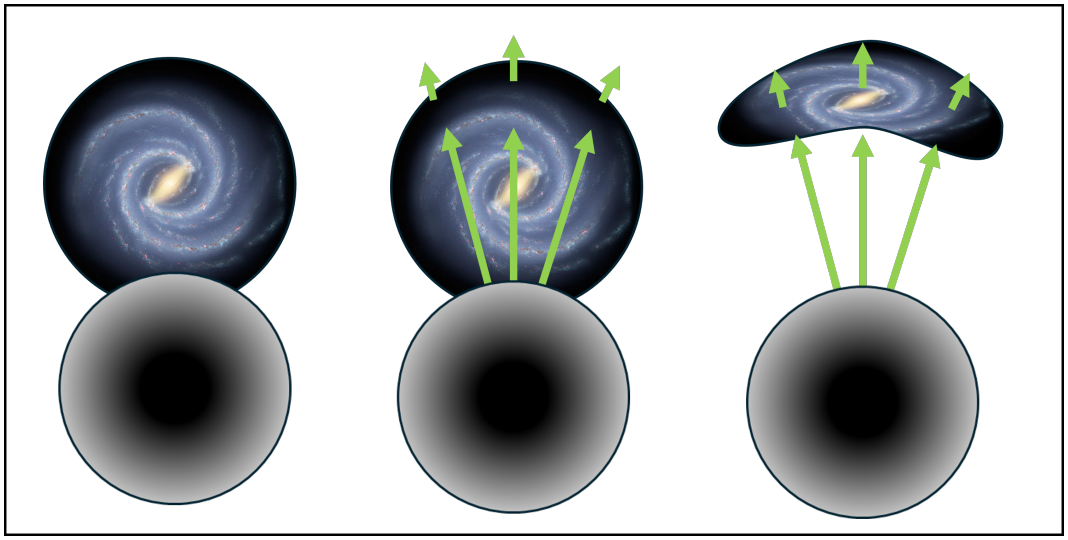

FIGURE 2.11: Effects of the shear on a galaxy close to foreground object. The green lines represent the angular deflection that the light from the background galaxy experiences due to gravitational potential of the lens object. The parts closer to the lens experience a higher deflection distortion than the outer regions. The results is that the original image on the left is distorted becoming the elongated image tangential to the lens object on the right.

For any given lens-source galaxy pair, it is useful to define the tangential and cross components of the shear as:

$$\gamma_t = -\mathrm{Re}\left[\gamma e^{-2i\beta}\right], \quad \gamma_\times = -\mathrm{Im}\left[\gamma e^{-2i\beta}\right], \tag{2.126}$$

where the minus sign is a convention to ensure that γ_t is positive for tangential alignment around a mass overdensity, β is the position angle of the source galaxy with respect to the horizontal axis of the Cartesian coordinate system centered on the lens galaxy (as shown in Fig. 2.12). The reason for the angle to be multiply by 2 is that the direction of the shear is irrelevant since it is expressed as a symmetric quantity around the component axis. So if we rotate the shear components 180^{o} we obtain the same values. This means that the shear field is considered a spin-2 field. If we expand Eq. 2.126:

$$\begin{aligned} \gamma_t &= -\gamma_1 \cos(2\beta) - \gamma_2 \sin(2\beta), \\ \gamma_\times &= \gamma_1 \sin(2\beta) - \gamma_2 \cos(2\beta). \end{aligned} \tag{2.127}$$

The tangential component γ_t captures the gravitational lensing signal for a spherically symmetric mass distribution, while the cross-component $\gamma_\times$ vanishes in such a case. The cross-component has a curl pattern, which cannot be produced by a scalar field like the convergence κ [57]. Consequently, $\gamma_\times$ serves as a null test to ensure the measurement is free from systematic errors.

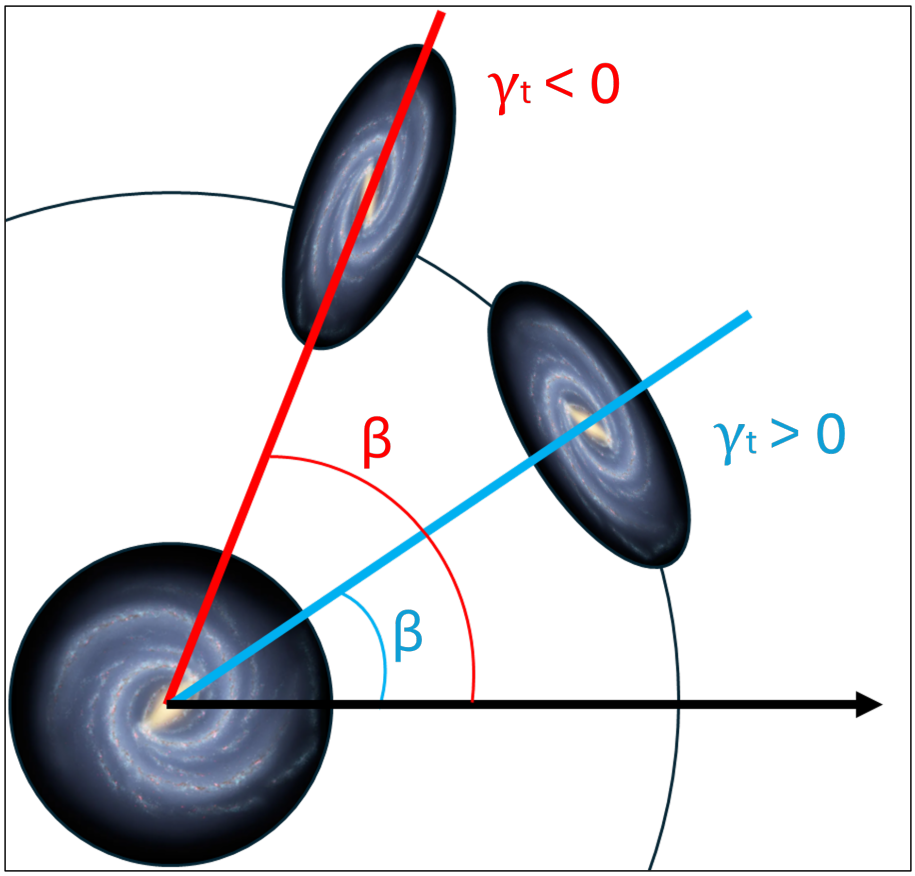

FIGURE 2.12: Representation of tangential and cross component of a lens-source pair system. The angle β is defined with respect to the lens object as a origin on the Cartesian system chosen and the separation line between the lens-source pair. If the shear is mostly perpendicular to the separation line the tangential component is positive (positive correlation), while if it is mostly parallel, the tangential component is negative (negative correlation).

The benefit of using the shear two-point correlation function, as opposed to its Fourier transform, lies in the fact that it can be computed by simply multiplying the ellipticities of galaxy pairs and then averaging the results. Three distinct two-point correlators can be derived from the shear components: $\langle\gamma_t\gamma_t\rangle$, $\langle\gamma_\times\gamma_\times\rangle$, and $\langle\gamma_t\gamma_\times\rangle$. In a Universe that is parity-symmetric, the last correlator disappears, while the first two are combined to form the two components of the shear two-point correlation function [57]:

$$\begin{aligned}\xi_+(\theta) &= \langle\gamma\gamma^*\rangle(\theta) = \langle\gamma_t\gamma_t\rangle(\theta) + \langle\gamma_\times\gamma_\times\rangle(\theta),\\ \xi_-(\theta) &= \mathrm{Re}\left[\langle\gamma\gamma\rangle(\theta)e^{-4i\beta}\right] = \langle\gamma_t\gamma_t\rangle(\theta) - \langle\gamma_\times\gamma_\times\rangle(\theta).\end{aligned} \tag{2.128}$$

As shown in Fig. 2.13, the cosmic shear field form distinctive patterns that like in electromagnetism can be classified as E-modes and B-modes. The tangential shear should reproduce a E-mode which can be positive in over-dense regions and negative in under-dense regions. The so called B-modes are not originated by cosmic shear and have these vortex/curl like patterns. Cosmologist are trying to find the presence of B-modes in the CMB signal since they may correspond to artifacts of inflation and gravitational waves in the CMB signal. Although the presence of B-modes can also be related to a systematic on the signal.

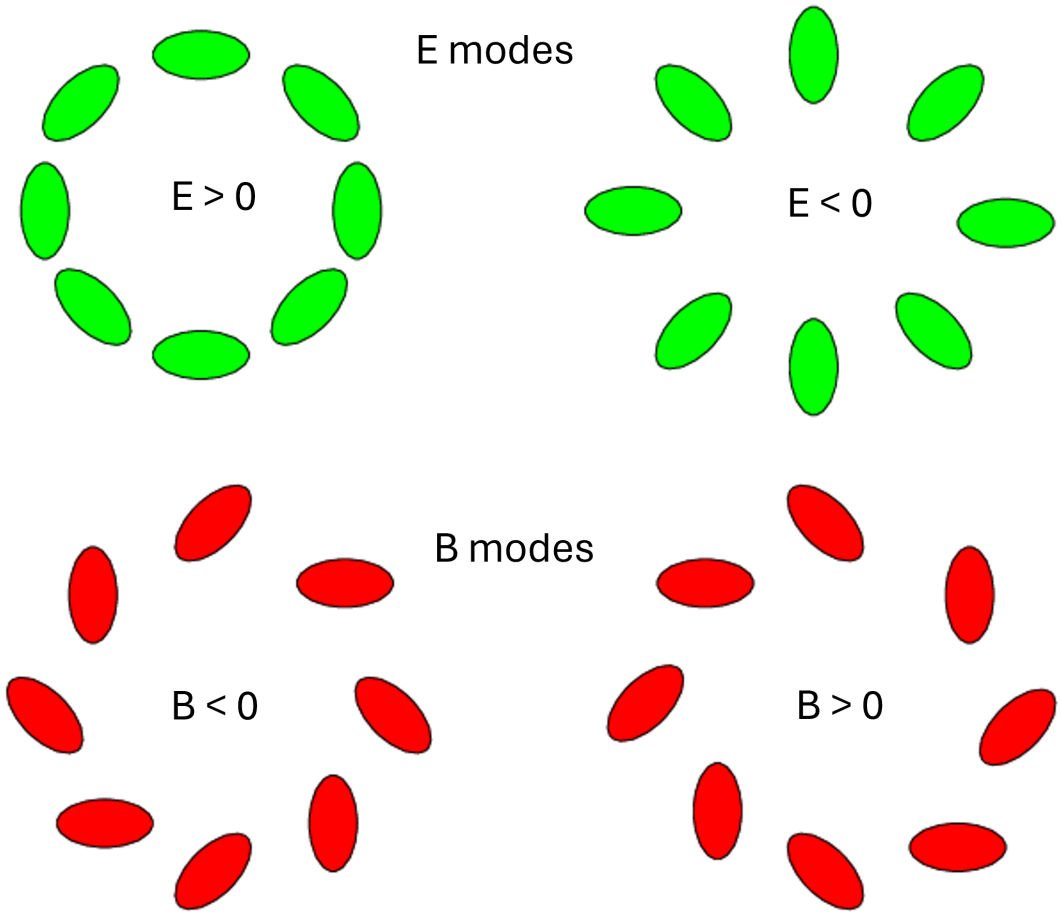

FIGURE 2.13: Polarization modes of light (shear). Top figures show the E-modes corresponding to the pattern that cosmological shear should follow around over-dense (E>0) and under-dense (E<0) regions. The B-modes represent the curl pattern which should not be presented in shear measurement or at very least not caused by shear. Credits: [148]

Chapter 3

Clustering in Galaxy surveys

3.1 Galaxy Surveys

In real cosmological observations, cosmologists use telescopes to capture the radiation (mostly in the form of light) from source objects. Since cosmology aims to discover the contents and formation of the Universe, we need to obtain information from far away objects to trace the full history of the Universe. At such large distances the objects cosmologists can capture and resolve are mainly galaxies (or galaxy clusters) since they are the most massive bound objects that emit light, i.e. the brightest objects. In the previous chapter we talked that galaxies are tracers of the underlying matter distribution so they are a good analysis tool. Galaxy surveys capture the image of an area of the sky which corresponds to a vast volume of the Universe depending on the depth, i.e. flux limit of the survey. The surveys collect an extensive dataset of galaxies using telescopes, providing key physical properties such as position and redshift. In the following section we will see that galaxy surveys can be spectroscopic, photometric or both depending on the instrument used.

Several major galaxy surveys are currently shaping our understanding of cosmology. The **Sloan Digital Sky Survey (SDSS)**[1] [109], a combined photometric and spectroscopic survey, has produced detailed 3D maps of the universe and contributed significantly to studies of galaxy evolution and large-scale structure. The **Dark Energy Survey (DES)**[2] [42], a photometric survey, has mapped over 5,000 square degrees of the sky, offering crucial data on galaxy clusters and weak gravitational lensing to study dark energy. **Kilo-Degree Survey (KiDS-1000)**[3] [93], another photometric survey, focuses on weak lensing to map dark matter distribution, while the **Dark Energy Spectroscopic Instrument (DESI)**[4] [43], a purely spectroscopic survey, aims to map 35 million galaxies and quasars, providing precise measurements of the universe's expansion. The **Vera C. Rubin Observatory's LSST**[5] [159] is a photometric survey expected to revolutionize cosmology with its deep, repeated imaging of the southern sky. The **Hyper Suprime-Cam Survey (HSC)**[6] [8] provides deep photometric imaging for galaxy formation and dark matter studies. Lastly, the **Euclid Space Mission**[7] [44], which will be discussed later in section 3.2 due to its relevance to this thesis, is a space-based survey combining photometric and spectroscopic data that will map the Universe to study dark matter and dark energy.

[1] https://www.sdss.org/
[2] https://www.darkenergysurvey.org/
[3] https://kids.strw.leidenuniv.nl/
[4] https://www.desi.lbl.gov/
[5] https://rubinobservatory.org/
[6] https://hsc.mtk.nao.ac.jp/ssp/
[7] https://www.cosmos.esa.int/web/euclid

3.1.1 Redshift estimation

While galaxy redshift surveys are rich in information, they are also expensive and time-consuming because measuring redshifts is much more difficult than simply determining the angular positions of galaxies. For this reason, cosmological surveys are generally classified as either spectroscopic or photometric, depending on how they estimate galaxy redshifts [99].

Spectroscopic surveys

Spectroscopic surveys provide precise redshift measurements by sampling the full energy spectrum of galaxies with high resolution. Using a spectrograph the full spectrum is extracted from each individual galaxy and the redshift is determined with Eq. 1.5 by using a standard absorption or emission line as reference. Since the individual spectrum of each galaxy is needed, this process is very slow and expensive.

Photometric surveys

Photometric surveys use multi-band filters to observe galaxies, allowing them to trace many more objects in a shorter time, though at the expense of reduced redshift accuracy. A standard set of filters is used, each of which blocking a certain part of the spectrum. By comparing the intensity received from each filter we can estimate the redshift and the galaxy color classification (blue, red, green) using some fitting functions. The redshift obtained through this technique is called photo-z which usually contains a Gaussian error with respect to the true redshift. In current surveys [44, 109], telescopes are equipped with both an spectrograph and a photometer in order to use the spectroscopic redshift as a reference to improve the photo-z using machine learning techniques.

3.1.2 Magnitudes

Every observable object in the Universe emits light that can be capture by survey telescopes as a surface density of photons per unit of time (brightness). Cosmologists quantify the brightness, or more commonly known in cosmology as flux, of an object using the magnitude.

The flux was already defined when talking about the luminosity distance in sec. 1.8.4 via Eq. 1.55, although the expression for an expanding universe is given by Eq. 1.58. The flux decreases the farther the source object is from the observer since the radiation is spread over a larger area (concentrically to the source). This means that farther objects have a lower flux on average making them harder to detect since telescopes have a minimum flux under which can no longer detect the source. In this regard, galaxy surveys have a specific survey depth (in redshift or Mpc) depending the limit of flux that the survey instrument can capture.

Flux are captured on passbands (optical filters) to select or filter out specific ranges of frequencies (bands) of light as explained when talking about photometric surveys. Telescopes usually only capture the intensity of the light, so passbands are used to block certain wavelengths of the light spectrum to determine the intensity of the color that the filter lets through. For this reason fluxes and magnitudes are usually given on a specific band to express the flux that passes through that filter. Each galaxy surveys use different sets of filters and calibrations so the flux for the same band on different surveys may differ significantly. In any case, in most cases the importance of the flux comes from the relative comparison between objects in the same survey, e.i in order to determine the galaxy color classification or the magnified fluxes due to magnification. In this aspect, the magnitude is used to quantify the flux from a source adimensionaly in two ways.

Apparent magnitude

The apparent, or relative, magnitude (m) is the one that describes the brightness of an object as seen from an observer at any given distance. On a given α-band is defined as [58]:

$$m_\alpha = -2.5 \log_{10}\left(\frac{F_\alpha}{F_{\alpha,0}}\right), \tag{3.1}$$

where $F_{\alpha,0}$ is a reference flux for the α-band of the photometric filter for a given observational instrument.

Due to the minus sign on the definition, a brighter object will have a lower magnitude, which can be anti-intuitive but this nomenclature is given by historical reasons [58]. The log helps when comparing huge differences in fluxes which are common in galaxy surveys since a 5 point decrease in apparent magnitude corresponds to an object with 100 more brightness.

Absolute magnitude

The problem with fluxes and consequently apparent magnitudes it is that the value is relative to the observer, for these reason the apparent magnitude can also be called relative magnitudes. Knowing the luminosity of an object can be useful since it is an intrinsic value so it can be related to other intrinsic properties. For example, more massive galaxies are thought to be more luminous since they may contain more stars or luminous objects. For this reason cosmologist have defined the quantity known as the absolute magnitude (M) which is just the apparent magnitude of an object if it were observed from a distances of 10 parsecs ($3.0857 \cdot 10^{17}$ meters).

$$M_\alpha = m_\alpha - 5 \log_{10} \frac{D_L}{10\,\mathrm{pc}}, \tag{3.2}$$

where D_L is the luminosity distance (Eq. 1.59) to the object in parsecs (pc) and m_α is the apparent magnitude of the object in a given α-band.

Evidently, the absolute magnitude cannot be calculated directly since the distance to the object is needed which means that information about the cosmological parameters is also needed (Eq. 1.50).

3.1.3 Error estimation

A crucial part of any observation is the estimation of the accuracy of our results. In cosmology, we already have to deal with instrumental errors when making observations, but in this section we focus only on the systematics errors due to the variance of the data.

Jackknife resampling

Jackknife resampling is a way to check how much a statistic can change when you remove one data point at a time. Leaving out one observation, calculating your statistic without it, then repeating this for every single data point in your set. By comparing how much the statistic changes with each leave-out, you can get a sense of how reliable or stable your result is. It is really good technique to estimate the error in cosmology directly from the data accounting for all the possible systematics [113]. This is mostly useful for large scales where we do not have enough different "iterations" to predict the error since we only have one Universe so the variance tend to be higher.

$$\sigma^2_{\rm JK} = \frac{N_{\rm JK}-1}{N_{\rm JK}} \sum_{i=1}^{N_{\rm JK}} (\hat{\theta}_{(k)} - \hat{\theta}_{\rm JK})^2, \tag{3.3}$$

where N_{JK} is the number of Jackknife resampling, $\hat{\theta}_{JK}$ is the average over all the Jackknife resamples, and $\hat{\theta}_{(k)}$ is the estimate for the kth-Jackknife resample (which excludes the k-region). Following Eq. 3.3 if we have more than one data point we can generate a Jackknife covariance matrix [113]:

$$C_{{\rm JK},ij} = \frac{N_{\rm JK}-1}{N_{\rm JK}} \sum_{k=1}^{N_{\rm JK}} \left(\hat{\theta}_{i,(k)} - \hat{\theta}_{i,{\rm JK}}\right) \left(\hat{\theta}_{j,(k)} - \hat{\theta}_{j,{\rm JK}}\right), \tag{3.4}$$

The value of N_{JK} should be chosen to ensure that there are enough resamples to provide an unbiased estimate of the variance while avoiding an excessively small subtracted region, which would result in insufficient variation in the data. Typically, there exists an optimal range for N_{JK}, where small adjustments to its value result in convergent errors that do not vary significantly [113].

Theoretical errors

Another way to estimate errors is using theoretical predictions to get an estimate of the variance of the data. Assuming Gaussianity on the random primordial fluctuations we can get an estimate for the cosmic variance at any scale. This allows to generate Gaussian theoretical covariance matrix for different kinds of correlation functions. This can be further expanded with numerical simulations, sec. 3.3, which allow to reproduce the volume and density of the data an allow to calculate more precise covariances. Theoretical errors are not only valuable for estimating uncertainties when no other alternatives are available but also play a crucial role in cross-checking systematic errors derived from the data.

For the purpose of this thesis, we mostly use the theoretical errors for the density autocorrelation angular power spectrum to cross-check our Jackknife errors. For a given C_ℓ the errors are calculated as [58]:

$$\Delta C_\ell = \sqrt{\frac{2}{(2\ell+1) f_{\rm sky}}} (C_\ell^{\rm true} + N_\ell), \tag{3.5}$$

where $f_{\rm sky}$ is the observed fraction of the sky, $C_\ell^{\rm true}$ are the C_ℓs without shot noise, N_ℓ. The shot noise is the error that originates from considering a continuous field like the overdensity field as a discrete quantity. This increases the signal with a constant term that depends on:

$$N_\ell = \frac{4\pi f_{\rm sky}}{n_{\rm data}}, \tag{3.6}$$

where $n_{\rm data}$ represents the number of data points, which in this case refers to galaxies. The shot noise, being constant, has a greater impact on smaller scales, where the signal tends to diminish.

3.2 Euclid mission

The *Euclid* mission[8,9] [44], developed by the European Space Agency[10] (ESA) as part of its *Cosmic Vision 2015–2025* program, was launched on July 1, 2023. The mission addresses some of the most fundamental questions in cosmology, with a focus on the nature of dark matter, dark energy, and the overall geometry of the Universe. Its primary goal is to understand the cause of the Universe's accelerated expansion.

Euclid will map the large-scale structure (LSS) of the Universe by surveying a vast portion of the extragalactic sky, capturing the shapes, positions, and redshifts of billions of galaxies. The mission employs two key cosmological probes: galaxy clustering and weak gravitational lensing to study the distribution of matter and cosmic structures over time. These probes will directly address questions about dark energy's influence on cosmic expansion and dark matter's role in structure formation [44].

The first public data release is anticipated in 2025, with subsequent releases providing more comprehensive datasets, including galaxy shapes, redshift estimates, and spectral data.

3.2.1 Scientific Objectives

The primary scientific goals of Euclid include:

- **Measuring Dark Energy**: Euclid aims to explore whether dark energy behaves as a cosmological constant, as suggested by the Lambda Cold Dark Matter (ΛCDM) model, or whether it evolves over time.
- **Mapping Dark Matter**: Through weak lensing, Euclid will map the distribution of both visible and dark matter, offering insights into cosmic structure formation.
- **Testing General Relativity**: By studying the LSS and the expansion history of the Universe, Euclid will test general relativity on cosmological scales.

The key cosmological probes are:

- **Galaxy Clustering (GC)**: Euclid will map the 3D distribution of galaxies, revealing the underlying dark matter structure. This will allow scientists to study baryon acoustic oscillations (BAO, sec. 2.2.1) and redshift-space distortions (RSD, sec. 2.3), which are critical for understanding cosmic expansion and the growth of structures.
- **Weak Gravitational Lensing (WL)**: Euclid will detect weak lensing, sec. 2.6, by measuring tiny distortions in galaxy shapes caused by the gravitational influence of massive objects. These measurements will provide a map of dark matter distribution, including regions where visible matter is absent.

By combining these two techniques, Euclid will probe both geometrical and dynamical aspects of cosmic expansion, improving our understanding of dark energy's nature and the evolution of cosmic structures.

3.2.2 Instruments and Payload

Euclid is equipped with two primary instruments:

- **Visible Imaging System (VIS)**: VIS captures high-resolution optical images, essential for measuring galaxy shapes and weak lensing effects. It has a field of view (FoV)

[8] https://www.cosmos.esa.int/web/euclid
[9] https://www.euclid-ec.org/
[10] https://www.esa.int/

of 0.53 square degrees and is optimized for detecting minute distortions caused by gravitational lensing.

- **Near-Infrared Spectrometer and Photometer (NISP)**: NISP operates in the near-infrared (NIR) range, providing both photometric and spectroscopic data. The photometric channel is used for redshift measurements, while the spectroscopic channel provides precise measurements of galaxy spectra, enabling 3D mapping of galaxies.

Together, these instruments will survey over 14,000 square degrees of the extragalactic sky, covering approximately 1.5 billion galaxies. This dataset will be crucial for advancing our understanding of dark matter and dark energy [44].

3.2.3 Survey Design and Strategy

Euclid's mission comprises two main surveys:

- **Wide Survey**: Covering around 14,000 square degrees of extragalactic sky, the wide survey focuses on obtaining high-precision measurements of galaxy shapes and redshifts over a large area.
- **Deep Survey**: In addition to the wide survey, Euclid will conduct a deep survey of smaller sky patches, targeting fainter galaxies to explore earlier cosmic epochs and study galaxy formation during the early Universe.

The spacecraft is positioned at the L2 Lagrange point, a stable location where the gravitational forces of the Earth and Sun balance. This environment provides a thermally stable platform, essential for precise observations.

TABLE 3.1: Summary of scientific requirements for weak lensing and galaxy clustering observations in Euclid [104].

Spectroscopic Galaxy Clustering	
Spectroscopic redshift accuracy	$\sigma_z < 0.001(1+z)$
Redshift range	$0.7 < z < 2.05$
Photometric Galaxy Clustering and Weak Lensing	
Photometric redshift accuracy	$\sigma_z < 0.05(1+z)$
Redshift range	$0 < z < 2$
Error in mean redshift in bin	$\Delta\langle z\rangle < 0.002(1+\langle z\rangle)$
Catastrophic failures	10%
Density of galaxies	> 30 galaxies/arcmin^2

Following its launch, Euclid entered a *Performance Verification* phase from August to November 2023, during which it produced over 21 terabytes of raw data—surpassing the data output of the Hubble Space Telescope over its entire operational life. Initial observations confirmed that both VIS and NISP are functioning as expected, although some challenges, such as stray light contamination in VIS, were mitigated through calibration.

The **Euclid Flagship Simulation** ([47], section 3.3.3) models the expected observational data, enabling the refinement of data processing pipelines. These simulations are crucial for ensuring the efficient processing of the large datasets Euclid will collect by performing several forecasts of different observables.

3.2.4 Cosmological Probes and Expected Contributions

Euclid is expected to make significant contributions to several key areas of cosmology:

- **Dark Energy and Dark Matter**: Euclid's measurements of the Universe's expansion rate and the growth of cosmic structures will provide crucial data on dark energy. It will help determine if dark energy behaves as a *cosmological constant* or evolves over time. Weak lensing and galaxy clustering data will map the distribution of dark matter.
- **Testing General Relativity**: Euclid will allow for rigorous tests of general relativity on cosmological scales by comparing observed structure formation with theoretical predictions.
- **Neutrino Mass**: Euclid may provide constraints on the mass of *neutrinos*, which play a critical role in the formation of large-scale structures.

Euclid's observations are complemented by ground-based surveys that provide additional photometric bands, improving the accuracy of photometric redshift estimates. Key collaborations include the *Legacy Survey of Space and Time (LSST)*, the *Dark Energy Survey (DES)* and the *Dark Energy Spectroscopic Instrument (DESI)*. These ground-based surveys provide essential data for enhancing redshift estimates and deepening the understanding of faint galaxies.

3.2.5 Impact on Cosmology and Astrophysics

Over its six-year mission, Euclid will significantly enhance our understanding of dark matter, dark energy, and cosmic structures. The mission will:

- Constrain models of dark energy and test if it evolves over time by providing precise measurements of the cosmic expansion rate across different epochs. Second, it will offer unprecedented insights into the distribution of dark matter through weak lensing observations.
- Map the distribution of dark matter with high precision, improving our understanding of its role in structure formation. It will complement surveys like the Dark Energy Survey and the Hyper Suprime-Cam [26].
- In addition to its focus on dark energy, Euclid will also contribute to our understanding of galaxy evolution and the distribution of dark matter. Comparing Euclid's observations with theoretical models of structure formation will help refine our understanding of how galaxies and galaxy clusters form and evolve over cosmic time [94].
- Provide data to test general relativity on cosmological scales. In particular, Euclid's data will be used to test alternative theories of cosmic acceleration, such as modified gravity theories. Studies like those by [41] and [94] propose modifications to general relativity as an alternative to dark energy (see Chapter 4 and 5). Euclid's precision measurements will help determine whether these theories provide a better explanation for cosmic acceleration than dark energy models.
- The mission is expected to significantly improve constraints on key cosmological parameters, building on results from previous missions like *Planck*, which mapped the cosmic microwave background (CMB). While *Planck* offered insights into the early Universe, Euclid will extend these observations to more recent epochs when dark energy began to dominate [119, 10].

Euclid is a collaborative project involving over 1,500 scientists from Europe, the United States, and other countries, reflecting the global interest in understanding dark energy and dark matter. This large-scale collaboration draws on the expertise and resources of the ESA and NASA, among others [10].

The data collected by Euclid will be made publicly available, ensuring that the scientific community can continue to analyze the results long after the mission's operations end. Euclid's survey will serve as a reference for future cosmological studies and will likely inform the design of next-generation observatories and telescopes.

3.3 Numerical simulations

In section 2.2.3 it was mentioned the need for non analytical models to describe the non-linear regime at smaller scales due to the complications of the equations that describes these regions. In section 2.6.2 it was mentioned that obtaining information from weak lensing is still in development due to some hardships so we can use simulations to study and test predictions. In both cases it was referring to the so called numerical simulations. These simulations are generated by powerful computers that can operate with many particles at the same time in order to reproduce a system like our Universe as similar as possible [147].

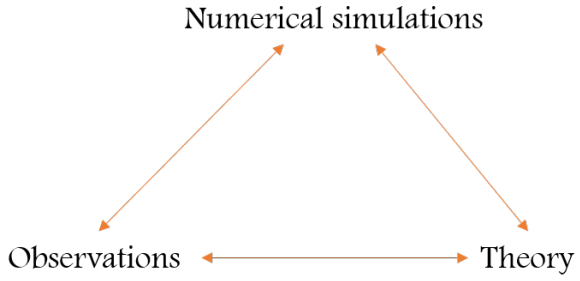

FIGURE 3.1: "Cosmic triangle" that shows the interconnected relation between the numerical simulations to the standard paradigm of theory-observation.

As briefly showed in Figure 3.1 numerical simulations are very useful to complement the lack of information from an observable, like weak lensing, or for obtaining a theoretical approach for an observable difficult to observe/predict (non-linear regime/ matter distribution). At the same time numerical simulations are built to follow the theory and reproduce the observable. If the simulation is in good agreement with the observable, then we can test if the theory is valid comparing the obtained statistical functions, like the power spectrum, to the predictions from the same theory. The most popular numerical simulation is the N-body.

3.3.1 N-body simulations

N-body simulations consist of a cube of side L in the order of Gpc/h that contain billions of dark-matter particles [51]. These particles are given a random initial condition with a position and velocity. Additional cosmological parameter are also included as initial conditions for the simulation. Then the system is evolved under only the presence of gravity between the particles as a collisionless system. So by taking discrete time steps the acceleration of each particle is calculated from the gravitational potential for each step. The system evolves during the time interval until the acceleration has to be recalculated, due to the new positions of the particles. A softening length is defined in order to establish a distance until which particles are affected by the gravitational potential of other particles to avoid infinite accelerations.

Eventually the particles in the N-body simulation collapse to form the dark matter halos structures and filaments between them, Figure 3.2. This is in good agreement with the theory about dark matter halos formation, as mentioned in sec. 2.2.3, and allows the study of the matter distribution and inhomogeneities at small scales. At this point a halo catalog is generated by running diverse algorithm, like friends of friends (FoF) [142, 126], to find and

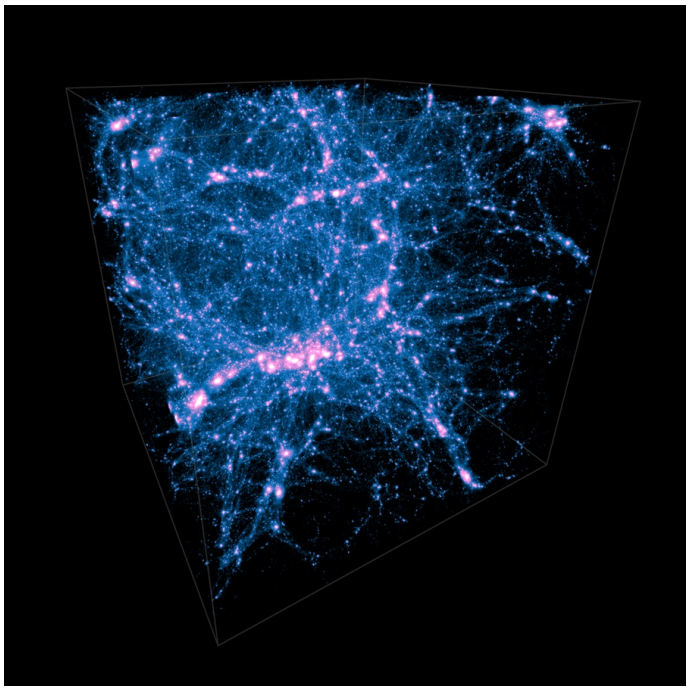

FIGURE 3.2: Simulation box for a N-body after many steps where filaments and halos (brighter compacted regions) can be seen. Source: UC Riverside

label the halos. This algorithms are usually purely based on the proximity among particles, i.e. two particles are linked if their metric (usually Euclidean distance) is less than a predefined "linking length". For example a FoF group corresponds to a set of particles linked to each other, although several improvements are being performed to this algorithms to attribute other considerations like the shape of the halos [126]. The next step is to place the galaxies in the halos simulation by using several techniques related to some properties of the halos. The most typical approach is the halo occupation distribution (HOD) [23], where more massive halos contain more galaxies, and the halo abundance matching (HAM) [98], where more luminous galaxies occupy more massive halos. Once the galaxies are placed inside halos a simulated galaxy mock has been generated that can we used to test observables for future real surveys.

All the simulations that we use in this thesis have lensing data for all their galaxies (deflection angle, shear, convergence). For simulated catalogs obtaining this information is quite different than in real surveys. Since in simulations we start with different conditions: we know the mass distribution (positions of the N-body dark matter particles) but we cannot "observe" (know the position of) the image of the galaxies as there is no actual light coming from them. Theoretical modeling of weak-lensing observables is challenging because the lensing correlations on small angular scales are described by the non-linear regime of gravitational clustering. There are methods that use ray-tracing technique in which light rays are propagated from the observer to the source by computing the distortion and magnification effects from multiple (from tens to a hundred) of equally spaced projected-mass lens planes. Back-tracing the weak lensing observables for each galaxy is very demanding in CPU time and memory usage so it is only used in small patches [67].

In this thesis, the galaxies in all the simulations are distributed over a large region (at least an octant of the full sky). Therefore, a different method is used to calculate weak lensing observables. All the simulations use a technique called the "onion" Universe [67] by constructing a lightcone simulation by replicating the simulation box (and translating it) around the observer. The dark-matter lightcone is then decompose into a set of all-sky concentric

spherical shell of width dz= 0.003(1+z) around the observer until z=1.4. Each dark matter "onion shell" is then projected onto a 2D pixelized map using the Healpix (see section 3.4.1) tessellation. In this way, maps of the matter distribution at different redshift (from the observer) are obtained. Then we can obtain convergence maps at different redshift by summing the maps of lower redshift multiplied by the appropriate lensing weights as in Eq. (2.108). In this approach (all-sky limit) we can take spherical transforms to represent the maps and obtain the other observables with relations to Eq. (2.125). The $C_\ell(\kappa)$ are given by:

$$C_\ell^\kappa(z) = \frac{9H_o^4\Omega_m^2}{4c^4}\sum_j P(\ell/\chi_j, z_j)\frac{(\chi_s-\chi_j)^2}{\chi_s^2 a_j^2}d\chi_j \tag{3.7}$$

Which is the discrete expression of Eq. (2.124) since we are integrating over a finite number of "onion shells". As the convergence is calculated from Eq. (2.108) then the method uses the Born approximation by projecting the matter in the light of sight.

With the convergence angular spectrum calculated we can use Eq. (2.125) to obtain the shear and deflection angle angular power spectrum. With Healpix (sec. 3.4.1) we can generate the all-sky shear and deflection angle maps from the angular spectrum. Then each galaxy receives the corresponding shear and deflection value depending the values of the lensing maps at the position of the galaxy. The deflection position is calculated from the deflection angle using Eq. (2.99) where the components of α are given by:

$$\vec{\alpha} = \alpha\cos\delta\ \vec{e_\theta} + \alpha\sin\delta\ \vec{e_\phi} \tag{3.8}$$

Where δ is the angle between the deflection vector and the polar basis vector $\vec{e_\theta}$.

In the following sections we introduce two of the simulated catalogs relevant for the projects presented in this chapter: MICE and *Flagship*.

3.3.2 MICE Grand Challenge

The Marenostrum Institut de Ciències de l'Espai (MICE) galaxy mock simulations [66, 49, 65] are aimed to reproduce with unprecedented detail the history of the universe, from much before the first stars formed up to nowadays. In order to determine how well future astronomical surveys, such as the DES, PAU, EUCLID, VHS, and PLANCK can answer these fundamental open questions [65].

MICECAT is a simulated galaxy mock originated from the parent MICE-Grand Challenge (MICE-GC) lightcone N-body simulation containing about 70 billion dark-matter particles in a (3 Gpc h^{-1})^3 comoving volume [66, 49]. To build the galaxy mock a combination of the HOD and HAM technique were used to place galaxies inside halos. Assumes a flat concordance LCDM model with $\Omega_m = 0.25$, $\Omega_\Lambda = 0.75$, $\Omega_b = 0.044$, $n_s = 0.95$, $\sigma_8 = 0.8$ and $h = 0.7$ [65]. The mass resolution is $m_p = 2.93{\cdot}10^{10}h^{-1}M_\odot$ and has a softening length $l_{\rm soft} = 50$ kpc/h.

The catalog incorporates lensing properties by assigning a magnified position and shear to all its 200 millions galaxies, as explained in the previous section, which cover around an octant of the full sky [65].

3.3.3 Euclid Flagship 2 Galaxy mock

The Euclid's Flagship 2 (FS2) Simulation is a comprehensive mock galaxy catalog developed to support the scientific exploitation of the Euclid space mission (see sec. 3.2). The Flagship simulation plays a key role in optimizing the mission's observational strategies and testing its scientific output [47].

Technical Specifications

The Flagship simulation is based on a large-scale N-body simulation, involving approximately 4 trillion dark matter particles. The simulation generates a lightcone extending up to a redshift of $z = 3$, covering a cosmological volume that spans more than 10 billion years of cosmic history. The lightcone covers one octant of the sky, or one-eighth of the celestial sphere, and is designed to approximate the survey volume of Euclid.

The simulation mimics with very high precision large-scale structure of the Universe as it incorporates around 4.8 billion galaxies (20 times more galaxies than MICE-GC) up to z=3. It is based on the Flagship N-body simulation halo catalog with two trillion dark matter particles in a 3.6 Gpc/h box with a mass resolution of $m_p = 10^9\ h^{-1}\ M_\odot$. The cosmological parameters are [47]: $\Omega_m = 0.319$, $\Omega_b = 0.049$, $\Omega_\Lambda = 0.681$, $\sigma_8 = 0.83$, $A_s = 2.1 \cdot 10^{-9}$, $n_s = 0.96$ and $h = 0.67$.

N-body Simulation

The N-body simulation was performed using the `PKDGRAV3` code on the Piz Daint supercomputer at the Swiss National Supercomputing Centre (CSCS). It features a simulation box with a size of 3600 h^{-1} Mpc per side, containing $16{,}000^3$ particles, corresponding to a particle mass resolution of $10^9 h^{-1} M_\odot$. This resolution allows the simulation to resolve halos hosting the faint galaxies that Euclid will observe, down to a limiting magnitude of $H_E < 26$.

Halo Catalog

The simulation identified $\sim$ 16 billion dark matter halos using the ROCKSTAR halo finder [22]. These halos were populated with galaxies using the Halo Occupation Distribution (HOD) and Halo Abundance Matching (HAM) techniques. These methods ensure that the galaxy population in the mock catalogue follows observed correlations between halo mass and galaxy properties. This process was calibrated using real-world data from surveys such as the Sloan Digital Sky Survey (SDSS) [157], the Dark Energy Survey (DES) [2], and the Kilo-Degree Survey (KiDS) [102].

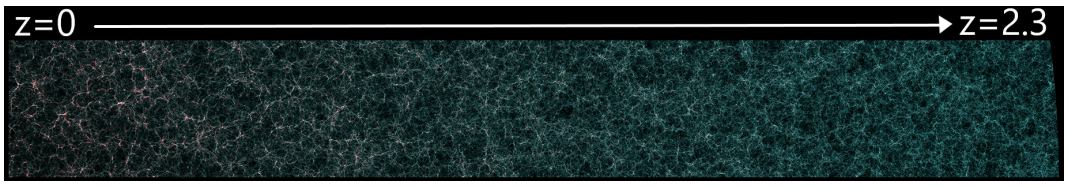

FIGURE 3.3: An excerpt of the Flagship v1 galaxy mock simulation. In the left we can see today's Universe at z=0 with dense halo structures (red dots) formed while at the right we can see the early Universe (3 billion years old) where the matter distribution is more homogeneous. Credits: J. Carretero (PIC), P. Tallada (PIC), S. Serrano (ICE) and the Euclid Consortium Cosmological Simulations SWG

Galaxy Properties

The final catalog contains about 3.4 billion galaxies, selected with a magnitude limit of $H_E < 26$, to match Euclid's observational capabilities. Each mock galaxy is assigned properties such as positions, velocities, redshifts, stellar masses, star formation rates, and spectral energy distributions (SEDs). These properties are consistent with observations, ensuring that the mock catalog realistically reproduces key features of galaxy clustering and weak lensing signals. The galaxies are assigned to halos following HOD while luminosities are assigned following HAM.

Lensing Properties

Weak gravitational lensing, one of Euclid's primary scientific probes, requires highly accurate measurements of galaxy shapes and their distortions due to the gravitational field of intervening large-scale structures. The Flagship simulation includes detailed lensing properties for each galaxy, allowing scientists to model the weak lensing signal observed by Euclid. This is critical for constraining cosmological parameters, particularly the nature of dark energy [9, 151].

The lensing properties are assigned using the same method than for MICE-GC.

Improvements from Flagship 1 to Flagship 2

The current version of the simulation, Flagship 2 (FS2), includes several important improvements over its predecessor, Flagship 1 (FS1):

- **Increased Mass Resolution**: FS2 has twice the mass resolution of FS1, with a particle mass of $10^9 h^{-1} M_\odot$. This allows the simulation to resolve galaxies one magnitude fainter at all redshifts.
- **Extended Redshift Coverage**: The lightcone in FS2 extends to $z = 3$, compared to $z = 2.3$ in FS1, covering a larger cosmological volume.
- **Improved Spectral Energy Distributions**: The method for assigning SEDs to galaxies was revised to match observed photometric properties more closely.

Applications of the Flagship Simulation

The Flagship simulation is instrumental in optimizing Euclid's mission design. Simulated mock data are used to test how well the mission can measure galaxy clustering and weak lensing, which in turn helps minimize systematic errors and refine observational strategies.

The simulation plays a crucial role in developing and validating Euclid's data processing pipelines, which handle large volumes of data from the mission. This includes algorithms for detecting and measuring galaxy shapes, estimating redshifts, and analyzing weak lensing data.

The Flagship simulation helps scientists measure cosmological parameters, such as the equation of state of dark energy, and test different cosmological models. It is particularly useful for comparing General Relativity and alternative dark energy theories [68, 7].

While the simulation was developed for Euclid, it is valuable for a wide range of other cosmological studies and surveys, including the Dark Energy Spectroscopic Instrument (DESI) [55] and the Vera C. Rubin Observatory's Legacy Survey of Space and Time (LSST) [90]

3.3.4 Accessing simulated data: Cosmohub

Cosmohub[11] [33, 141], is an interactive data analysis tool which contains data from observed and mostly simulated galaxy catalogs. It has a very simple to use interface where the desired properties are selected by marking them (halo mass, positions, shear, etc...) as shown in Figure 3.4. It also allows filtering the data by adding conditions by properties or by selecting random subsets of the total galaxy population. All the selected options for the query are showed in a programming window, the expert mode, which can also be edited manually.

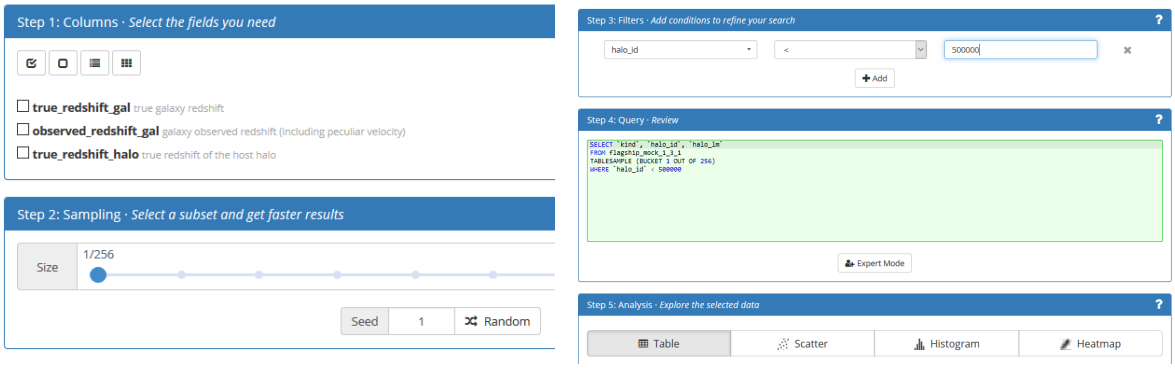

FIGURE 3.4: Cosmohub's interface: Left) shows some of the properties to mark for selecting data and the random subset selector, Right) shows the filter option, the expert mode, and the data plot analysis tool. Source: Cosmohub

Once the query is finished, Cosmohub has the option to show the selected data as a table, scatter plot, histogram or heatmap. The x/y limits and scale and the number of bins for the heatmap/histogram can be customized inside the same interface. The selected query's data (as the data from any generated plot) can also be generated as a *Parquet*, CSV, FITS or ASDF file format.

All the data for each one of the simulations that we use in this thesis can be accessed from Cosmohub. Only the data for MICECAT is public to anyone, while the others need special permission to access the data, e.g. Flagship (1 and 2) is only accessible for Euclid members or collaborators. The name of the properties for each catalog can be different (e.g. the selection field for the true redshift for MICECAT is simply called "z" while for Flagship is called "true_redshift_gal") so it is important to read the small description at the end of each field to make sure the correct property has been selected.

3.4 Tools for analyzing clustering statistics in simulated data

In this section, we described the most essential and important packages needed to achieve the majority of the results in this chapter and the ones that follow.

3.4.1 Healpy: Generating clustering maps

In order to obtain the angular power spectrum of the lensing observable we need first to generate all-sky maps from the Cosmohub's data. In order to do this we used the HEALPix[12] Software [76], or more specifically the python implementation of this package *healpy*[13]. This code allows the subdivision of a spherical surface in pixels all covering the same area. This is very convenient to make density maps since this way there is no need to divide each pixel by

[11] https://cosmohub.pic.es/home
[12] https://HEALPix.sourceforge.io/
[13] https://github.com/healpy/healpy

its area since it is the same everywhere. Then the map can be obtained by simply counting the galaxies in each pixel. This tool, following its original purpose, has been very useful to study CMB anisotropies as it also allows obtaining the angular spectrum from its own maps.

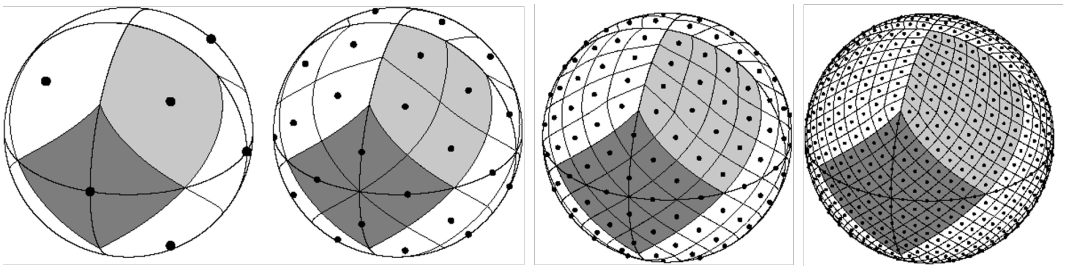

FIGURE 3.5: Orthographic view of HEALPix partition of the sphere at different number of pixels (from left to right): 12, 48, 192, 768. Source: HEALPix documentation

Maps are simply numpy arrays where each array element refers to a location in the sky as defined by the HEALPix pixelization schemes[14]. The number of pixels is defined by the N_{side} parameter whose value must be a power of 2, then the total number of pixels is given by $N_{pix} = 12 \cdot N_{side}^2$. In order to use the spherical harmonics transform functions we had to use the RING pixelization scheme as shown in Figure 3.6. Then to produce the maps we wrote a Python code to obtain the maps directly from reading the Cosmohub data as *parquet* files. HEALPix has a python module to use its main functions directly from python called *healpy* that we used. While to read the *parquet* files we used the *pandas* library.

The general procedure to generate the maps was the following: First we download a query from Cosmohub with the right ascension (RA) and declination (DEC) positions, which are given usually in degrees, for a given observable (more properties were added depending on the purpose of the map that we will specify latter). Then we obtain the corresponding pixel order number of the RING pixelization for the RA/DEC positions with healpy functions. We count the number of galaxies in each pixel to establish its frequency value. We generate a python list with the frequency value of each pixel at the proper list RING order value of the pixel.

3.4.2 PolSpice: Calculating angular power spectrum

The *healpy* package already has a way to directly calculate the angular power spectrum from maps with the *anafast* module, but it does not allow to use masks. Masks are important to define regions of the sky that are not observed or not considered for the analysis. In the case of *Flagship* and *MICE* we want to mask the regions of the sky that the simulations do not cover, i.e. 7/8 regions of the sky. In the case of *anafast*, even if you apply a mask with a package like *numpy*, the code will treat the masked regions as 0 which is not correct since in reality we do not know, or we do not want to consider, the value in this region. Masks are equally important in observations since surveys have a limited sky observation range (usually smaller than simulations), in the same regard than in simulations cosmologists may want to excluded certain regions due contamination or noise in the observed area.

For this reason in this thesis we use the package *PolSpice*[15] to calculate any kind of angular power spectrum. This package is specifically designed to compute the correlation function, and its Fourier transform (i.e. the angular power spectra), of astronomical maps (including

[14] https://HEALPix.sourceforge.io/pdf/intro.pdf
[15] https://www2.iap.fr/users/hivon/software/PolSpice/

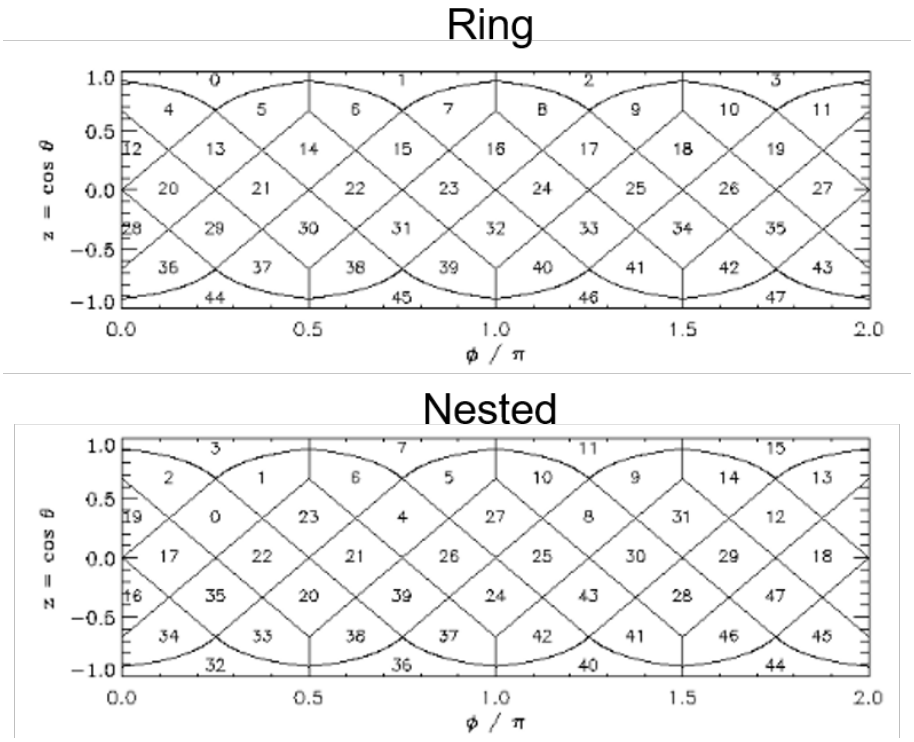

FIGURE 3.6: Comparison between the RING and NESTED scheme for pixel numbering with $N_{side} = 2$ HEALPix cylindrical projection. Source: HEALPix documentation

HEALPix maps), particularly those related to CMB data. It also allows to use masks in order to take into account incomplete sky coverage.

The mask is simply another HEALPix map in which masked (hidden) pixels are assigned a value of 0, while non-masked pixels are given a value of 1[16]. This code enables us to compute the angular power spectrum from one or more HEALPix maps (for cross-spectra), with the option to apply a mask to each map along with other parameters. Additionally, the code provides options to limit certain correlation parameters, such as *thetamax*, to avoid calculating correlations at angular distances larger than the region or mask boundary. For instance, when using an octant mask, it is recommended to set $thetamax < 90°$, as exceeding this value could introduce large, unwanted fluctuations into the angular spectrum. The parameter *apodizesigma* controls how the correlation function transitions into the masked region, where the amplitude rapidly diminishes, and should generally be close to the value of *thetamax*. Essentially, this parameter governs the width (standard deviation) of the Gaussian smoothing applied during apodization (gradual tapering to zero).

The package outputs the C_ℓ values to a text file, along with the corresponding multipoles. If the correlation is polarized, the C_ℓ values are organized into different rows corresponding to the TxT, ExE, BxB, TxE, TxB, and ExB components, where T is the scalar (amplitude) value and E/B are the modes defined in Fig. 2.13.

3.4.3 pyCCL & CAMB: Theoretical predictions for clustering

In the previous chapter we have introduced linear theory, and even some non-linear models, to predict observables in clustering like the power spectrum. As mentioned there, it is important

[16] When working with *numpy*, the 1/0 values are inverted.

to have a precise and accurate modeling of the observables in order to estimate cosmological parameters in order to understand the Universe better. In that regard, two of the most utilized codes in cosmology nowadays to make predictions of 2pt correlations in configuration and Fourier space, are CAMB sources[17] and *pyCCL*[18] [39].

Both codes allow to calculate the matter power spectrum at any redshift for user defined flat ΛCDM cosmologies which accounts for: Ω_m, Ω_b, σ_8, A_s, n_s and H_0. They also have several advance options to account for neutrino mass, non-flat cosmologies or RSD. Both codes also can input several models for the transfer function and the nonlinear matter power spectrum. In this thesis we always use the *Boltzmann CAMB* transfer function, which is based on the Boltzmann solver implemented on CAMB, and the *Halofit* matter power spectrum from [140] (already mentioned in sec. 2.2.3). In the previous chapter we have already shown the matter power spectrum calculated with this codes using Halofit in Fig. 2.2. In this section, we will work with the angular power spectrum since as we explained in the previous chapter it is more efficient to obtain clustering information since it is less sensitive to redshift determination. Both CAMB and *pyCCL* have a module to directly calculate the angular power spectrum by integrating the power spectrum at different z depending the input redshift distribution (or n(z)). They allow to use different tracers to perform the C_ℓ calculation, using Eq. 2.119, like the shear, convergence or density fluctuations.

CAMB has been the standard code for different clustering emulations for several years, while *pyCCL* is more recent and have some advantages and extra options like nonlinear biases or MG models implemented. In this thesis we started using both codes in order to crosscheck the predictions, which as seen in Fig. 3.7 they are quite similar differing not more than a 1%. Also, *pyCCL* until recently only allowed Limber calculations (the non-Limber calculation it is still only implemented in the developer version), so until then we were using CAMB when non-Limber was needed to get better results. Once we were able to use the *pyCCL*'s non-Limber calculation we mostly used this code since it is usually more efficient, easier to use and as discussed previously it has some extra features.

3.4.4 MultiNest & emcee: Fitting cosmological parameters

In cosmology, the parameter space is typically extensive because it encompasses a wide range of cosmological parameters that need to be simultaneously fit to a given dataset. Alongside these cosmological parameters, there are additional parameters known as *nuisance parameters*. These parameters are not of direct scientific interest but must be included because they can significantly influence the model's predictions or likelihood. To isolate the cosmological parameters of interest, nuisance parameters are typically marginalized by integrating over their likelihood, effectively removing their influence on the results.

Nuisance parameters often account for uncertainties, systematic effects, or background processes, ensuring the robustness of the analysis. In cosmology, they frequently describe more complex nonlinear interactions or noise terms. As highlighted in Sec. 2.5, nuisance parameters are generally local in nature, meaning they do not provide meaningful insights into the Universe's global properties. Nevertheless, they are crucial for achieving an accurate and consistent description of the model, as demonstrated in the treatment of the VDG model in Sec. 2.5.1.

[17] https://camb.info/sources/
[18] https://github.com/LSSTDESC/CCL

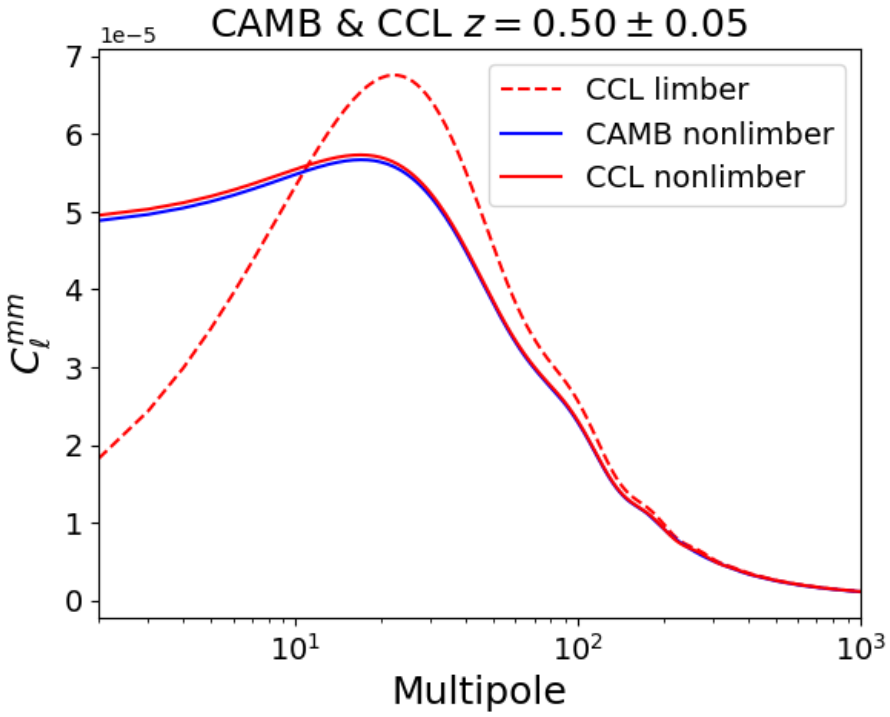

FIGURE 3.7: Comparison of matter angular power spectrum between the emulators pyCCL (red) and CAMB (blue) sources for the same cosmology (FS2) and same redshift. The dashed line corresponds to the Limber approximation used for CCL.

Due to the typically large and complex parameter spaces in cosmological models, advanced techniques such as Markov Chain Monte Carlo (MCMC) sampling or other specialized samplers are widely employed for parameter fitting. In the following sections, we introduce two of the most commonly used software tools for performing these fits.

MultiNest[19] is a Bayesian inference tool used for sampling from complex posterior distributions, especially those that may have multimodal distributions (i.e., multiple peaks or regions of high probability) or strong degeneracies [62]. It is based on the nested sampling algorithm [133] which focuses on finding high-likelihood regions, with tester points called live-points, and then progressively shrinking the parameter space to that region. This method is particularly well-suited for computing the Bayesian evidence (marginal likelihood), a key quantity in Bayesian model comparison.

Conversely, *emcee*[20] is a highly efficient and popular Python library for Markov Chain Monte Carlo (MCMC) sampling [64]. It uses an affine-invariant ensemble sampler, a variant of MCMC particularly effective in high-dimensional parameter spaces, especially when parameters exhibit complex correlations or significant degeneracies. The user can initialize multiple random walkers, which will explore the parameter space, increasing the likelihood of moving towards higher-likelihood regions until eventually converging at a local maximum.

In general, we have found that *emcee* is more convenient when the parameters are not multimodal, meaning they lack multiple local maxima or significant degeneracies with other parameters. Additionally, *emcee* requires an initial starting point, which can be adjusted to favor a particular solution, helping the code to converge more quickly. In contrast, MultiNest

[19] https://github.com/JohannesBuchner/MultiNest
[20] https://github.com/dfm/emcee

is more suited to explore the entire parameter space, especially when priors or fiducial values are uncertain, or when there are expected degeneracies between many parameters.

3.5 Results for galaxy clustering

With the main tools and theory explained we can start presenting our results. In this section, we present the methodology and some results for galaxy clustering, which are mostly related to the linear galaxy bias. We have calculated this parameter in simulated catalogs for several projects, that we will describe in Chapter 6. This is a rather simple parameter to obtain, when you assume a fiducial cosmology like we will do here since we are always dealing with simulations, so we consider this to be the most suitable starting point for the methodology used in this thesis. We will detail how we continuously implemented improvements to the determination of this parameter which was adapted later in more complex projects. In this chapter we work only with linear regime, while the projects that use more complex (nonlinear) models are presented in the next chapter since despite dealing with clustering observables their main focus relay in modified gravity.

3.5.1 Calculating the linear galaxy bias

The most simple observable in galaxy clustering is the linear galaxy bias (b_1) since as described in Eq. 2.38 it represents a global amplitude factor between the matter and galaxy power spectrum. The linear galaxy bias is typically regarded as a nonlocal quantity because, under the assumption of a homogeneous and isotropic Universe, it should remain constant across different regions for a given redshift. However, the value can vary depending on different galaxy sample cuts, as the relationship between various galaxy populations and dark matter may differ.

The most straightforward way to estimate the linear galaxy bias is directly from its definition, using any type of clustering observable. In this thesis, we primarily use the angular power spectrum, as discussed in Sec. 3.4.3, since it helps mitigate redshift errors, especially when employing a wide redshift bin to also suppress RSD effects. Another advantage of the angular power spectrum is that it allows for faster correlation calculations, as it works in a 2D plane rather than using 3D positions required for the power spectrum. We opt for Fourier space instead of configuration space because in Fourier space, the errors—discussed later—are easier to estimate, and it becomes simpler to separate scales (as described in Sec. 2.2, where different wavenumbers $\vec{k}$ are uncorrelated). This is crucial for us, as we aim to distinguish between linear and nonlinear scales, since as right now we only want to consider linear scales to estimate the linear bias.

In angular power spectrum notation, we have that the matter-matter and galaxy-galaxy C_ℓ are given by:

$$C_\ell^{mm} = \int \mathrm{d}z \, \frac{H(z)}{c} \frac{n(z)^2(z)}{\chi^2(z)} P_{mm}\left(k = \frac{\ell + 1/2}{\chi(z)}, z\right), \tag{3.9}$$

$$C_\ell^{gg} = \int \mathrm{d}z \, \frac{H(z)}{c} \frac{n(z)^2(z)}{\chi^2(z)} P_{gg}\left(k = \frac{\ell + 1/2}{\chi(z)}, z\right), \tag{3.10}$$

where we use the Limber notation for simplification, $\chi(z)$ is the comoving distance and the term $n(z)$ is the redshift distribution of objects dN/dz.

Since we have Eq. 2.39 related the linear bias between power spectrums we have that:

$$b_1 = \sqrt{\frac{C_\ell^{gg}}{C_\ell^{mm}}} \tag{3.11}$$

So the estimation will require the calculation of C_ℓ^{gg}, corresponding to the data, and C_ℓ^{mm}, corresponding the to theoretical prediction (since the underlying matter distribution cannot be directly observed).

Obtaining the theoretical prediction

As discussed in sec. 3.4.3 we will use the emulators *pyCCL* and CAMB to obtain predictions for this part. We have already mentioned that both codes allow to integrate the power spectrum given a $n(z)$ to obtain the angular power spectrum.

We adopt the same redshift distribution as the data to define $n(z)$, which we use to compute C_ℓ. To work with the emulators, $n(z)$ must be discretized into bins. Increasing the number of bins generally improves accuracy, though we must avoid setting it so high that considerable fluctuations occur between adjacent bins due to a low galaxy count per bin. Given the high resolution and large number of galaxies in the simulations used for this thesis, we can use a substantial number of bins. We select a consistent value of 200 bins for each redshift width of $\Delta z = 0.1$.

In Fig. 3.8, we see the shape of the $n(z)$ distribution for the full octant sky FS2 sample, with $z_{\rm true} = 0.50 \pm 0.05$ and $m_{\rm VIS} < 23$. Since we are using true redshift values for both galaxy cuts and $n(z)$ data, the distribution appears flat or shows a slight increase or decrease depending on the magnitude cut. As redshift increases, the lightcone volume expands to include more galaxies, although fainter galaxies become unobservable at greater distances. Thus, $n(z)$ serves as a window function, filtering out redshifts that are not used in the C_ℓ integration.

Both *pyCCL*[21] and CAMB accept $n(z)$ defined from any minimum and maximum z (as long as all the relevant z are included).

The next step is to configure the cosmology for the emulator. In *pyCCL*, this involves setting the parameters Ω_c, Ω_b, h, A_s, and n_s. Next, we define the tracer type, which in this case is the *NumberCountsTracer* module, used to account for density fluctuations. This module requires the galaxy redshift distribution $n(z)$ along with the linear galaxy bias and magnification bias for each bin. We set the galaxy bias to 1 as a reference, and since we are excluding weak lensing effects, we turn off magnification by choosing an s value of 0.4 (as seen in Eq. 2.114). With the tracer defined, we can use the *angular_cl* function to compute the theoretical C_ℓ, inputting the tracer twice for autocorrelation. We also specify the multipoles ℓ where we want to calculate C_ℓs and set ℓ_{lim} as the limit up to which non-Limber integration is used. Typically, ℓ_{lim} is set to 1000, which is a very conservative choice though calculations are almost instantaneous regardless.

In Fig. 3.9 we show the corresponding prediction for the case defined in this section. *pyCCL* allows to calculate the C_ℓs with linear or nonlinear theory so we show the difference in the figure. We can see that when not considering nonlinear corrections we have a decrease in power due to not taking into account the irregularities (variance) that nonlinear interactions introduce. The y-axis is usually multiplied by $\ell(\ell+1)/2\pi$ in order to have a better visualization of the fluctuations at small scales since the amplitude drops significantly there.

[21] The developer version of *pyCCL* right now has a bug where if the $n(z)$ is not defined from z=0 (up to the maximum z) the predictions are not correctly calculated.

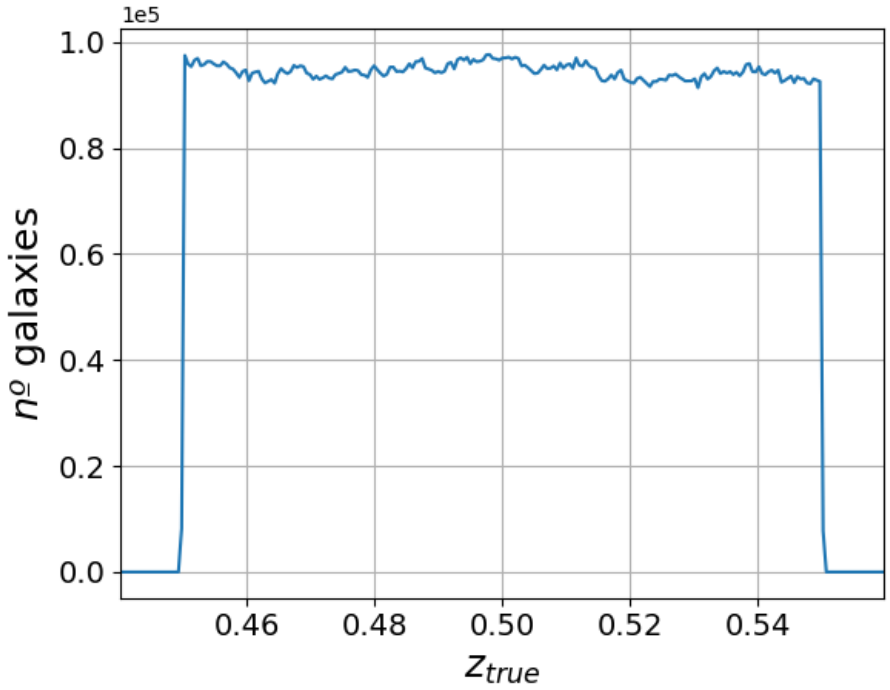

FIGURE 3.8: Redshift distribution, $n(z)$, for a full octant FS2 sample with $z_{true} = 0.50 \pm 0.05$ and m_{VIS}<23.

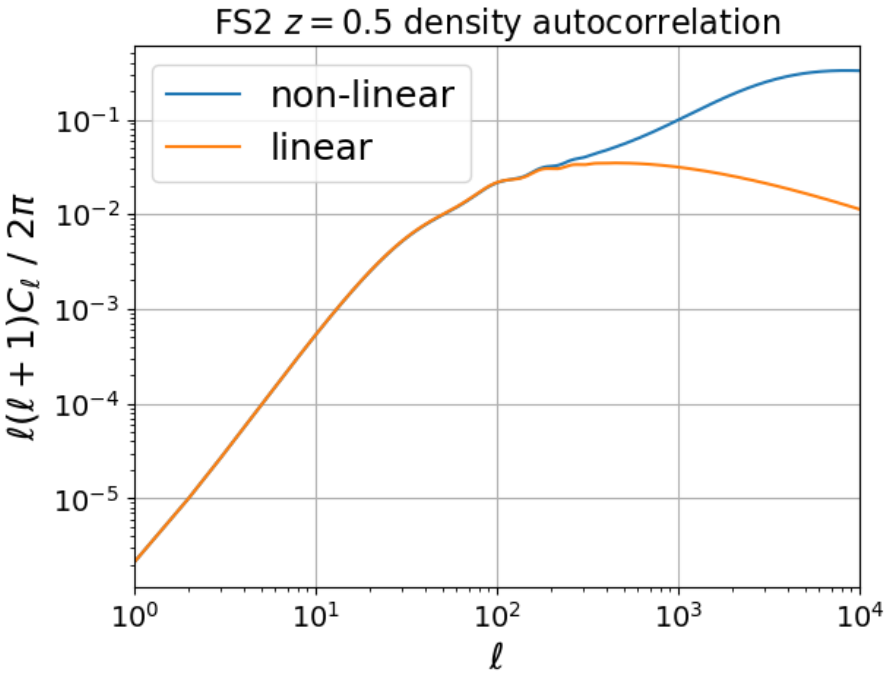

FIGURE 3.9: *pyCCL* theoretical predictions for the FS2 sample $z_{true} = 0.50 \pm 0.05$. The orange line shows prediction only applying linear theory while the blue line shows the prediction with the nonlinear boost from Halofit.

Generating the masks

The first step is to generate the mask, which, as stated in sec. 3.4.2 , are HEALPix maps with 0 and 1 values. For masks we want to consider all the regions that we do not observe,

either because they are outside the observation range or regions that we purposely want to avoid due to systematics. For simulated catalogs we usually ignore systematics so we generate masks to specify the observed area. In our case, we usually want to consider the maximum area in order to have the highest amount of galaxies (signal). So in the case of the FS2 and MICE catalogs we generate 7/8 octant masks to cover the regions outside the octant of the sky these catalogs cover. In Fig. 3.10 we show how the octant mask, 145° <RA< 235° and 0° <DEC< 90°, looks using the HEALPix visualization module. Since *PolSpice* multiplies the data map by the mask map, the 1 values (red) correspond to the unmasked regions, and the other way around for 0.

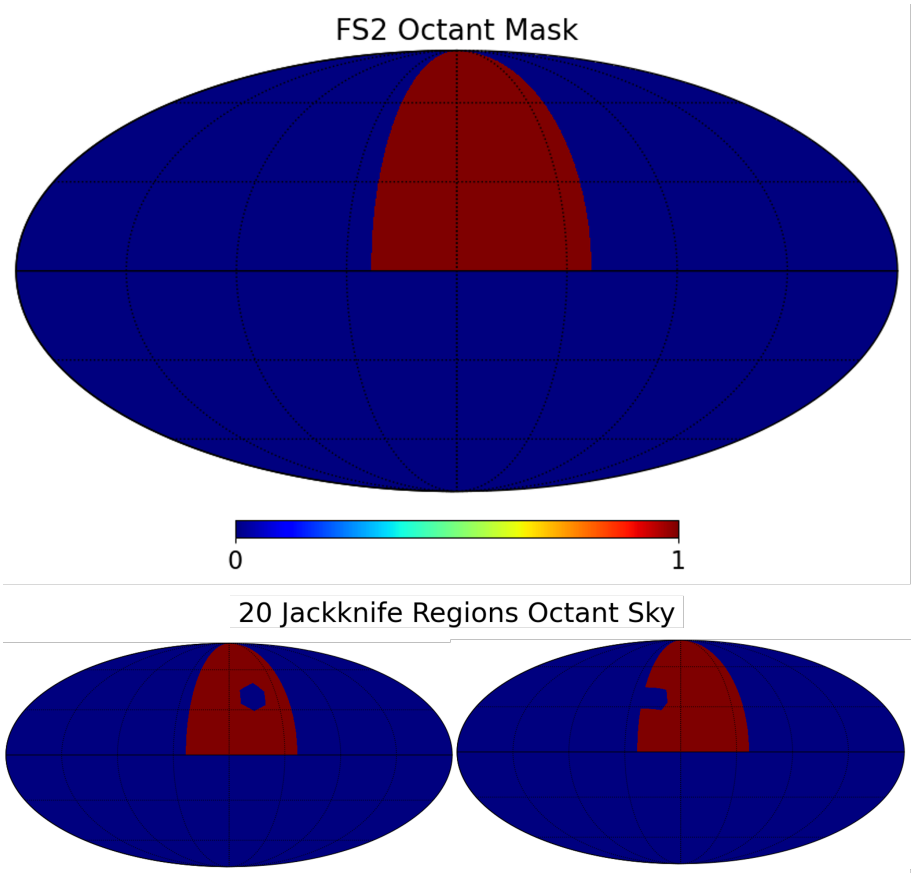

FIGURE 3.10: Top: HEALPix visualization of the octant mask used for the FS2 mock. Bottom: Two of the Jackknife resampling regions for an octant of the sky for $N_{JK} = 20$. The blue (0) regions are masked, following *PolSpice* convention, while the red (1) regions are unmasked (observed). The center of the maps correspond to (180°,0°) in RA, DEC.

We aim to incorporate error estimation into our results, which is why we employ the Jackknife resampling technique outlined in section 3.1.3. To achieve this, we need to generate the Jackknife regions as masks since they will be excluded during each resampling. We use the code *kmeans_radec*[22], to generate same size regions on the sphere. This code applies the k-means clustering algorithm to separate positional data en n_{cen} groups (clusters) where each data point is closer to the nearest mean (cluster center). We use a totally random dataset on the sphere, which can be generated with:

$$\mathrm{RA}_{\mathrm{ran}} = (\mathrm{RA}_{\mathrm{max}} - \mathrm{RA}_{\mathrm{min}}) \cdot r + \mathrm{RA}_{\mathrm{min}}, \quad r \sim U(0,1) \tag{3.12}$$

[22] https://github.com/esheldon/kmeans_radec

$$\mathrm{DEC_{ran}} = \arcsin\left([\sin(\mathrm{DEC_{max}}) - \sin(\mathrm{DEC_{min}})] \cdot r + \sin(\mathrm{DEC_{min}})\right), \quad r \sim U(0,1), \quad (3.13)$$

where r is a uniform random generator function between 0 and 1, the suffixes *max* and *min* represent the respective maximum and minimum value of DEC and RA for the given region. These randoms are only valid for a well defined and uniform mask which is our case for the mock catalogs. Since the randoms do not have a preferred positions the k-means clusters will be equally spaced. So the Jackknife regions, the ones that we will extract in each resampling, are generated by labeling the pixels of the mask to the nearest k-means cluster. So we simply generate N_{JK} masks where in each one we subtract a different Jackknife region to the full mask of our dataset. The bottom plots of Fig. 3.10 show two arbitrary Jackknife masks for the octant of the sky using $N_{\mathrm{JK}} = 20$, the same we can observe in the top maps of Fig. 3.11 for the full sky using $N_{\mathrm{JK}} = 100$. The bottom map show all the Jackknife regions for the full sky where we can observe that they represent different same size regions that cover the full observation area without repetitions. We select $N_{\mathrm{JK}} = 20$ and $N_{\mathrm{JK}} = 100$ for octant and full sky respectively, which represent similar Jackknife areas, after checking that the covariance matrix of the final results is stable as discussed in 3.1.3.

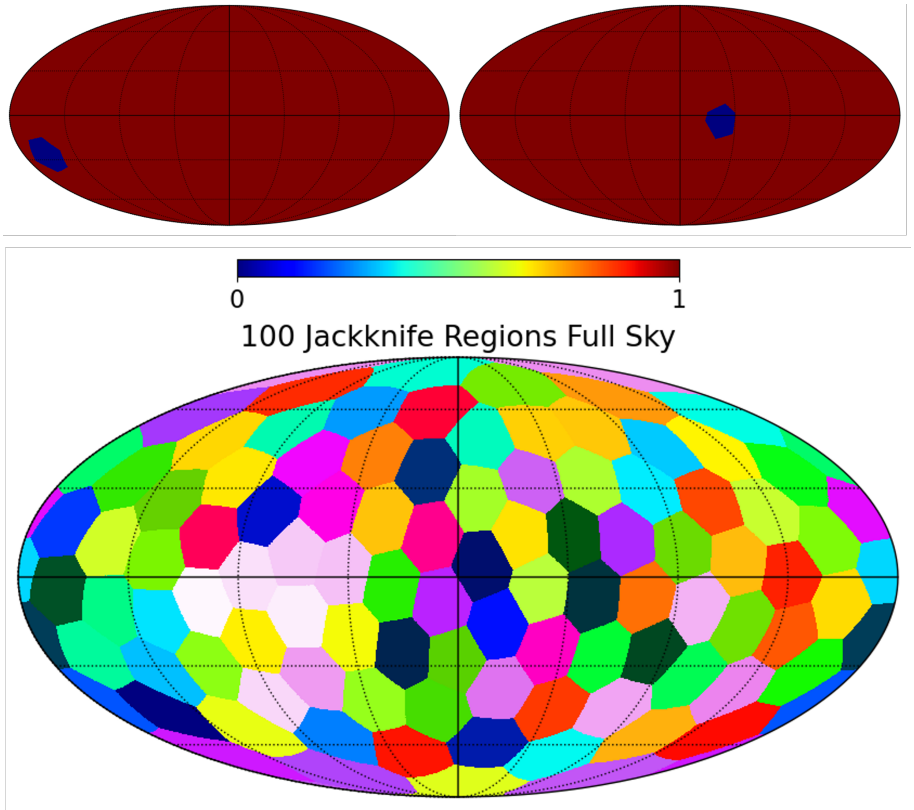

FIGURE 3.11: Top: Two of the Jackknife resampling regions for the full sky using $N_{JK} = 100$. The blue (0) regions are masked, following *PolSpice* convention, while the red (1) regions are unmasked (observed). Bottom: Map showing the 100 Jackknife regions for the full sky in different arbitrary colors. The center of the maps correspond to (180°,0°) in RA, DEC.

Calculating the data vectors

To calculate the observed C_ℓs from data we will use the code *PolSpice* (sec. 3.4.2) which needs the data into a HEALPix map. The specifics to converted the galaxy positional data into

HEALPix maps were already established in sec. 3.4.1. We wrote a simple and efficient python code that uses healpy modules to convert RA and DEC positions in degrees from the mocks data to HEALPix pixel positions. With the number of galaxies per pixel we can generate the density fluctuation per pixel, $\delta_{\rm pix}$, following the definition in 2.1 as:

$$\delta_{\rm pix} = \frac{n_{\rm pix} - \bar{n}_{\rm pix}}{\bar{n}_{\rm pix}}, \tag{3.14}$$

where $n_{\rm pix}$ is the number of galaxies in that given pixel and $\bar{n}_{\rm pix}$ is the mean number of galaxies per pixel over all the unmasked pixels. In Fig 3.12 we show the density map for the sample case described in this section. We can see that due to the definition of overdensity, the values can go to negative which represents a region with an underdensity. For galaxy bias determination, we usually use a nside of 1024 that roughly corresponds up to an accurate $\ell_{max} = 2 * nside + 1$, which is more than enough to capture the linear scales at any z. At practice, we found that $\ell_{max} \approx nside$, which is the reason why we choose 1024 instead of a lower value like 512 that would speed up considerable the calculations.

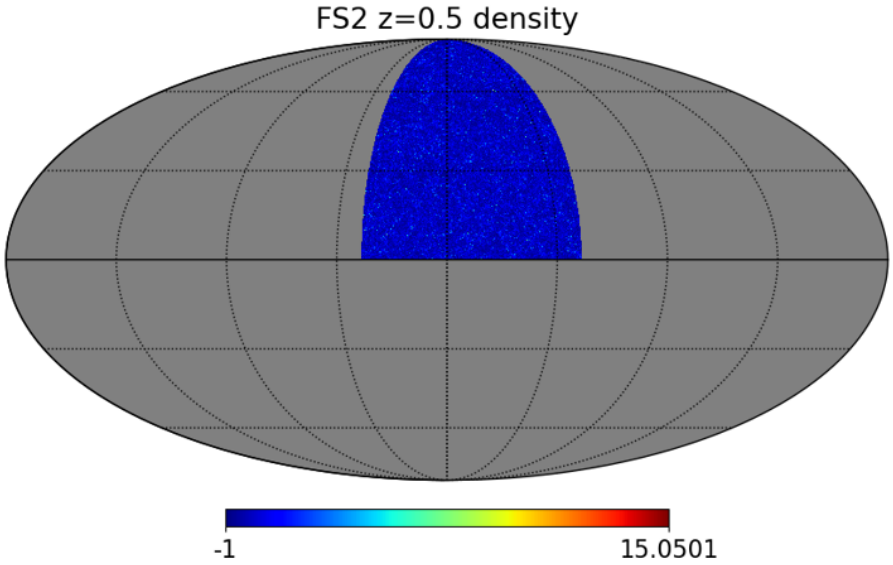

FIGURE 3.12: HEALPix density, δ, map for FS2 at $z = 0.50 \pm 0.05$. The gray area is unseen (masked).

Now, we can use the density maps and masks as input in *PolSpice*. Since we are dealing with an auto-correlation there is no need to input a second pair of data map and mask. We activate the option to correct the finals C_ℓs by the window function of the pixels and run the software for each one of the Jackknife masks. In each iteration the C_ℓs, for each $\ell \in$[0, 2 x nside+1], for each Jackknife resampling are generated and saved into a file. The values produced for each ℓ by *PolSpice* tend to be very noisy so we need to bin the results by averaging all the C_ℓs inside each bin. We usually take equidistant bins of $\Delta\ell$ =20, although in cases when we include smaller scales is more convenient to take log-spaced bins. Before binning the results we subtract the shot noise using Eq. 3.6, which for this particular case $f_{\rm sky} = 1/8$. After binning we can obtain the final values averaging all the C_ℓs for each Jackknife resampling and calculate the covariance matrix using Eq. 3.4. Note that for calculating the covariance we include the shot noise in the C_ℓs since it is a source of error.

In Fig. 3.13 we show the results for the case described here. We can see how the raw results from *PolSpice* (light green solid line) are very noisy and how binning reduces the noise. We

can also check how the shot noise becomes more significant at smaller scales. In this case we have around 19M galaxies on an octant of the sky so the shot noise is relatively small. The *pyCCL* theoretical prediction is below the galaxy C_ℓs as expected ($b_1 > 1$). In the plot below we show the calculation of the linear galaxy bias where we calculate the squared root ratio of the galaxy C_ℓs over the predicted matter C_ℓs. The linear scales are chosen by checking the maximum multipole at which the ratio is somewhat constant. In this case, we can tell that after $\ell = 600$ the ratio decreases which marks the maximum multipole. We also ignore the smallest multipoles since they tend to very noisy. We can also check that the theoretical errors (shaded area) are similar to the Jackknife errors in the ratio. The Jackknife errors tend to slightly over-estimate the error as is the case here.

With the scales selected we can calculate the linear galaxy bias with a χ^2:

$$\chi^2 = (R - b)C^{-1}(R - b)^T, \tag{3.15}$$

where R is the square root ratio and b is a specific value of the linear bias that we want ot test. The most probable value of b will be given by the one that minimizes the χ^2. We can also calculate the 1σ error, as the b value corresponding to $min(\chi^2) + 1$.

The value for the linear galaxy bias as shown in Fig. 3.13 for FS2 z=0.5 is $b_1 = 1.27 \pm 0.01$. This is the methodology that we apply to every calculation of the galaxy bias on this thesis, with the major contributions to projects listed in the next chapter.

3.6 Results for galaxy lensing

Now it is turn to present the methodology and results regarding weak lensing. The most important result in this section is the validation of the Flagship v1 magnification bias. We originally found an issue while testing this observable on the mock which led to identify an error while producing the mock. This was later corrected on the production of the Flagship v2 mock. Many of the other validations that we perform here are actually tests to check and identify the source of the issue with FS1. Nevertheless, these tests are perfectly useful on its own and that's why we are presenting them separately from the magnification bias results.

3.6.1 RMS of magnified positions

One of the initial steps to validate lensing observables is to verify whether the lensed (or magnified) positions are accurately generated. For this purpose, we conducted our first test directly on Cosmohub using its heatmap tool. By selecting both unmagnified and magnified positions, we created two heatmaps showing galaxy counts in the same patch of the sky at $z = 1$. We focused on a region of the sky with a pronounced lensing effect, identified by first locating areas with more massive halos at $z = 0.5$[23]. To achieve this, we generated another heatmap on Cosmohub, filtering galaxies associated with halos of mass $M_{\rm halo} > 10^{14} M_\odot/h$ within the redshift range $z = 0.45$ to $z = 0.55$ using Cosmohub's query tools.

Fig. 3.14 shows the heatmaps for the magnified and unmagnified positions. While subtle, there is a discernible trend where the galaxies appear slightly shifted upward and to the left due to the deflection angle. This effect becomes more noticeable when the number of bins is increased, although comparing the heatmaps side by side remains challenging. To better

[23]This selection follows the lens efficiency factor described in Eq. 2.108, where z is related to distances via its connection to the scale factor in Eq. 1.6.

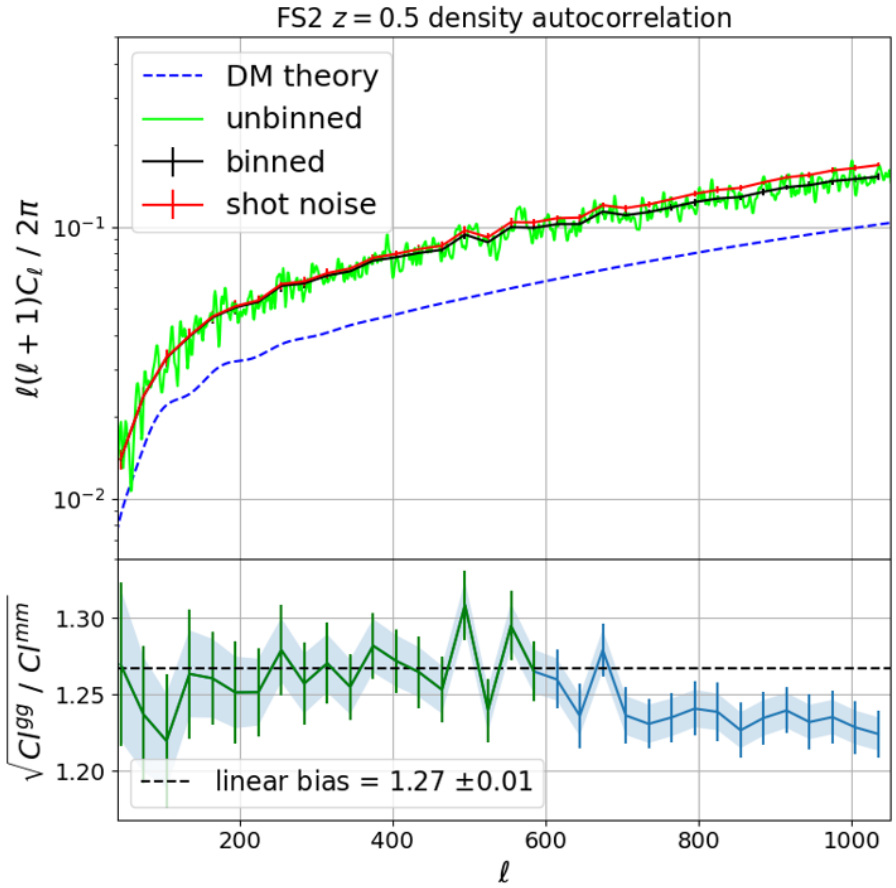

FIGURE 3.13: Top: Shows the density autocorrelation angular power spectrum for FS2 z=0.5. The light green solid line shows the values without any binning, while the black solid line show the binned results with $\Delta\ell = 20$ and Jackknife errors. The red solid line is the same as the black but without the shot noise subtraction. The dashed blue line is the theoretical prediction for the dark matter. Bottom: The solid blue line show the squared root ratio of the calculated C_ℓs over the predicted C_ℓs. The solid green line shows the regions used to fit the linear galaxy bias, whose mean value is shown by the black dashed line. The shaded area represents the theoretical errors for the calculated C_ℓs.

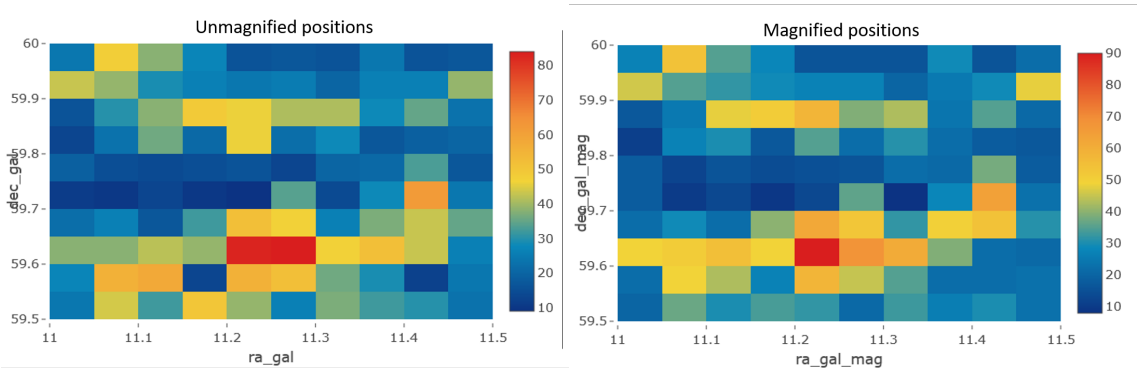

FIGURE 3.14: Heatmaps of galaxy counts at z=0.95-1.05 for a 0.5x0.5 deg patch of the sky obtained with Cosmohub's interface. At left it shows the unlensed positions and at right the lensed positions. RA/DEC axis values are in degrees.

visualize the shift, we conducted the test using 100 bins and overlaid one heatmap on top of the other. By toggling rapidly between the two heatmaps, we confirmed that the lensed positions are correlated, as nearby sources are influenced by the same lenses.

Following a more statistical approach we can calculate the RMS of unmagnified to magnified positions. The RMS stands for the Root Mean Square and is calculated in the following way:

$$\theta_{RMS} \equiv \sqrt{\frac{1}{N}\sum_{i}^{N}\theta_i^2}, \tag{3.16}$$

where the sum is extended over all the N galaxies in the query. In this case the θ variable of Eq. (3.16) represents the angular distance between the unmagnified and the magnified position. The angular distance is given by:

$$\theta = \arccos(\sin(\delta_1)\sin(\delta_2) + \cos(\delta_1)\cos(\delta_2)\cos(\alpha_1 - \alpha_2)), \tag{3.17}$$

where $\alpha \in [0°, 360°]$ corresponds to RA and $\delta \in [-90°, 90°]$ corresponds to DEC. The subscript 1 and 2 indicates indifferently the lensed or unlensed position.

Using Eq. 3.17 within the definition of Eq. 3.16, we compute an RMS of 1.082 arcminutes for Flagship v1, considering all galaxies at $z = 1.00 \pm 0.05$. For now, we can compare this result to that obtained from MICECAT, which gives an RMS of 0.959 arcminutes at $z = 1$. We use MICE as a reference catalog in these section since this catalog has already been correctly validated [65]. The lower RMS for MICECAT is reasonable, as its Ω_m value (0.25) is smaller than Flagship's (0.319). Since Ω_m is directly related to the matter density, it influences the average lensing strength (see Eq. 2.108).

3.6.2 Lensing angular power spectrum

In this section, we will evaluate whether the convergence and shear spectra (see Sec. 2.6.2) agree with the theoretical predictions provided by the revised Halofit model [140]. Following a similar approach to our analysis of the density angular power spectrum, we generate `HEALPix` maps for the shear and convergence.

The shear and convergence information is obtained from the galaxy catalogs in Cosmohub, with the shear represented by its two components, γ_1 and γ_2. The assigned values correspond to those in the original convergence and shear maps, with $N_{side} = 8192$, derived from the final particle distribution of the simulations. Each galaxy inherits the pixel value of the map corresponding to its location.

The convergence and shear maps are generated differently since the pixel values no longer represent the galaxy counts within that pixel. Instead, they reflect the mean shear or convergence values of the galaxies inside each pixel. Given that lensing studies focus primarily on interactions at small scales, we create maps with higher resolution, using $N_{\rm side} = 4096$. While $N_{\rm side} = 8192$ would provide a closer 1:1 match with the original map values, this resolution is computationally prohibitive for us when generating the maps and calculating the C_ℓ values. Since the information is derived from the galaxy distribution, we must address pixels without galaxies, which are effectively unobserved. To account for this, we generate a

mask tailored to each galaxy sample by marking empty pixels and incorporating regions not observed by default in the mock/sample. Figure 3.15 illustrates the appearance of the mask with the empty masked pixels. Additionally, the Jackknife and survey masks are included to demonstrate the final combined mask. For observables like deflection and shear, which have two components, we generate a TQU (or TEB) map by combining three `HEALPix` maps. The first map corresponds to the amplitude (a scalar, left empty in this case), while the other two represent the first and second components of the observable. Next, we use *PolSpice* to compute the C_ℓ values, enabling the polarization mode when dealing with two-component observables. For shear, our primary focus is on the E × E C_ℓ values (see sec.3.4.1), as the shear only has an E-mode component.

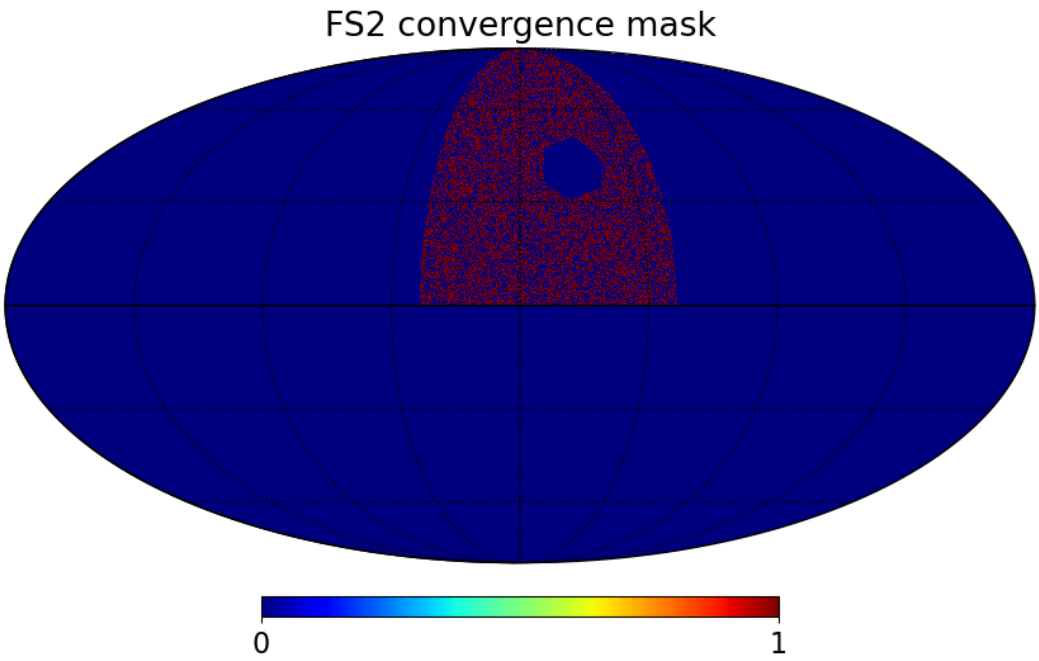

FIGURE 3.15: Mask for the convergence where the pixels without information (galaxies) are masked since we cannot predict the convergence or shear. We also combine the observational mask and Jackknife mask.

Using relations in Eq. 2.125 we can convert the shear C_ℓs into C_ℓ^κs for comparison.

$$C_\ell^\kappa = \frac{l^2(l+1)^2}{(l+2)(l^2-1)} C_\ell^s \tag{3.18}$$

Figure 3.16 shows that the convergence spectra agrees very well with the dark matter prediction. However, some discrepancies and fluctuations are observed at smaller scales (high ℓ), likely due to resolution effects. Additionally, we compare the shear power spectrum (C_ℓ^s) with the convergence power spectrum (C_ℓ^κ) using Eq. (3.18). Although the shear power spectrum is significantly noisier, its values remain within the 1σ error bounds, indicating that these observables are appropriately applied to the mock data.

3.6.3 Magnification bias factor

As outlined earlier, our goal in this section is to establish the relationship between source density fluctuations caused by magnification and the convergence responsible for such magnification. Referring to equation (2.114), we see that the key step is to calculate the magnification

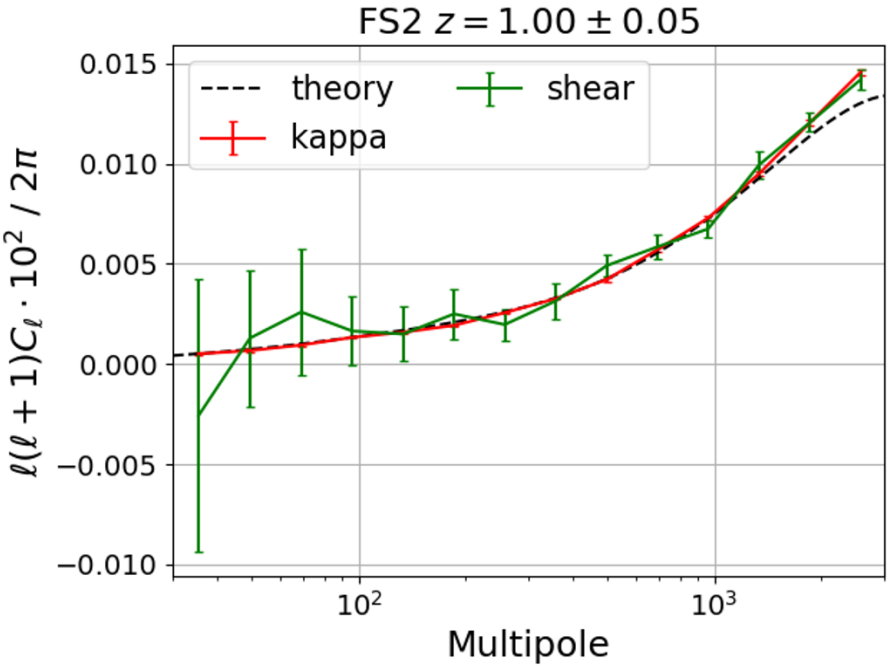

FIGURE 3.16: Flagship convergence angular spectrum at z=1 for the DM and galaxies with $N_{side} = 4096$. The theoretical prediction from the revised Halofit model is also included to verify the lensing observables. We also plot the shear C_ℓ^s transformed to C_ℓ^κ by using Eq. (3.18).

bias factor s, which corresponds to the logarithmic slope of the cumulative background number counts at a given redshift and magnitude limit. This term can be derived using equation (2.115).

To calculate the parameter s, we selected a query for a redshift bin $\Delta_z = 0.1$ centered around the desired z value and retrieved data for the Euclid-VIS (or $E_{\rm VIS}$) magnitude band, which is less impacted by non-cosmological signals such as dust extinction. Using Cosmohub's plotting tool, we generated a histogram of magnitude counts for i_{AB} values ranging from 21 to 25, with a bin width of $\Delta_i = 0.1$. The histogram was configured to display a cumulative plot on a logarithmic Y-scale (number counts), as shown in Figure 3.17. Since the function is cumulative for $m < m_{\rm lim}$, it naturally incorporates brighter galaxies for a given $m = m_{\rm lim}$ value. The slope of this cumulative plot at a specific m corresponds to the s-value at $m_{\rm lim} = m$ for the given redshift. To determine this slope, we exported the plot data and processed it using a Python code. The slope at each magnitude bin was approximated by considering the values from the adjacent bins and fitting the function locally to a linear model. This procedure was repeated for various redshifts, and we subsequently plotted the value of $5s - 2$ (as per Eq. (2.114)) against the respective $m_{\rm lim}$, as shown in Figure 3.18.

Figure 3.18 shows that the magnification bias decreases as we move to dimmer magnitude limits. This trend arises because fewer faint galaxies exceed the flux threshold. When $5s - 2$ reaches 0 (corresponding to $\alpha = 1$), the magnification bias is nullified, resulting in no change to the density of background sources. Beyond this point, the competing effect of area dilution becomes more significant, reducing the number counts of sources[24].

[24]These effects are valid under the assumption of $\kappa > 0$ or $\mu > 1$.

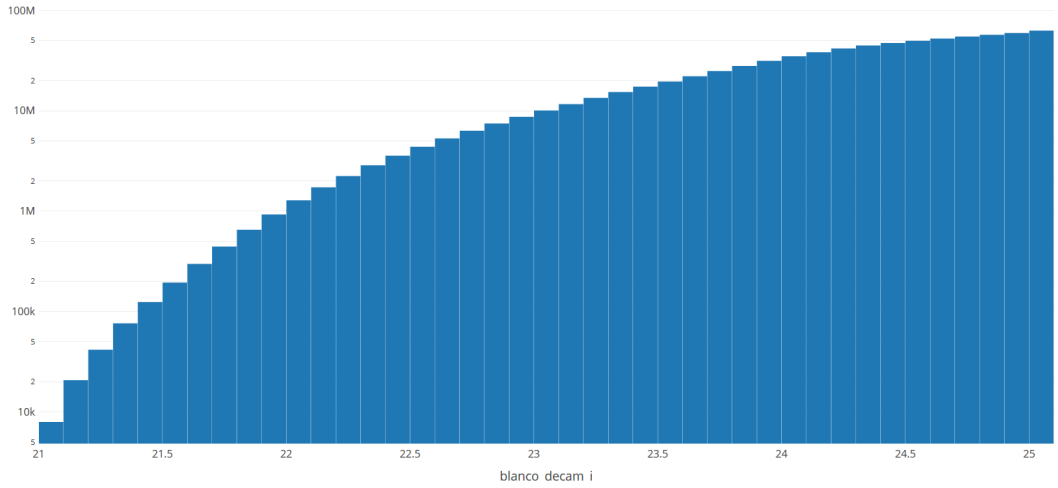

FIGURE 3.17: Cumulative logarithmic histogram for E_{VIS} magnitude for z=1 obtained with the plotting tool of Cosmohub.

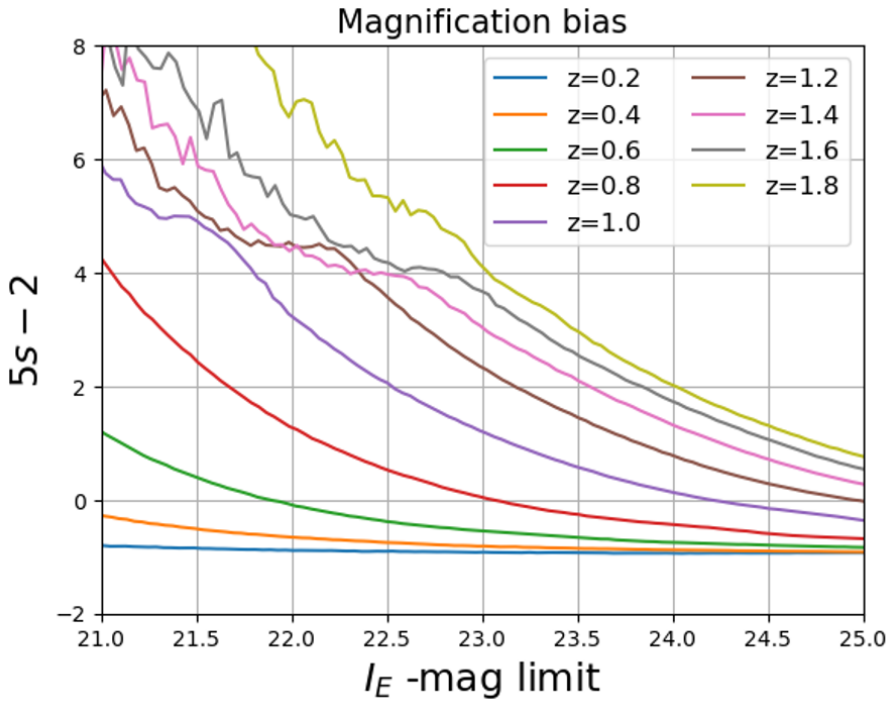

FIGURE 3.18: Magnification bias plot for Flagship at different redshifts using magnitude cuts in E_{VIS}.

With the s-values derived for various magnitude limits and redshifts, we can now make magnification bias predictions for the catalogs. In the next section, we will assess whether the galaxy distributions align with these predictions. This will help determine whether the mock catalogs correctly implement the magnification bias.

3.6.4 Magnification from galaxy cross-correlations

To confirm that the magnification bias induces the expected density variations, we will cross-correlate the density fluctuations of source galaxies with the lens galaxies responsible for these

variations[25]. Specifically, we aim to compute the cross-spectrum of the density fluctuations of sources and lenses, $\langle\delta(z_l)\delta(z_s)\rangle$. The cross-spectrum measures the correlation between the pixel values of two maps: one map for the lenses and another for the sources.

The source maps were generated at $z = 1.00 \pm 0.05$ with a magnitude limit of $E_{\rm VIS} < 23$. For the lens map, we selected galaxies at $z = 0.50 \pm 0.05$, corresponding to the point of maximum lensing efficiency, which occurs approximately halfway between the observer and the source. To separately analyze the two competing effects of magnification bias, we created four different source maps:

- **Nomag**: Contains the galaxies' unlensed positions.
- **Magpos**: Contains the galaxies' lensed positions.
- **Magmag**: Contains the galaxies' magnified magnitudes but with unlensed positions.
- **Magall**: Contains galaxies with both magnified magnitudes and lensed positions.

The term *magnified magnitudes* refers to the modification of flux due to lensing effects (magnification). This is mathematically expressed as:

$$\Delta m = -\frac{5}{2}\log_{10}\mu = -2.5\log_{10}(1+\delta_\mu) \simeq -\frac{5}{\ln 10}\kappa \tag{3.19}$$

To produce these maps, we selected three queries from *Cosmohub*:

- One with the unlensed and lensed positions at $z = 0.5$.
- Another with the unlensed and lensed positions at $z = 1$ and $m_i < 23$.
- A final one with the unlensed and lensed positions at $z = 1$ and $[m_i - (5/\ln 10)\kappa] < 23$[26] to account for magnified magnitudes, as described in Eq. (3.19).

We also checked the total number of galaxies of the maps: 8712473 for Nomag, 8710679 for Magpos, 8731314 for Magmag, 8728530 for Magall and 25352156 for Lens. Since the gain of galaxies is greater than the loss of galaxies, as $(5 - 2s) > 0$ for our conditions, we have more galaxies in Magall than in Nomag. The same mask was applied to all maps to ensure consistency. For the lensed position maps (*Magpos* and *Magall*), the area dilution effect is partially accounted for by removing galaxies that move outside the unmasked region.

The magnification modify the density fluctuation in the following way:

$$\delta = \delta_g + \Delta\delta_{\rm mag} = b\delta_m + (5s-2)\delta_\kappa, \tag{3.20}$$

where δ_g, δ_m, δ_κ are galaxy, matter and convergence fluctuations respectively. Then when we perform a cross-correlation of lenses and sources:

$$\begin{aligned}\left\langle \delta^s\delta^l \right\rangle = b^s b^l \left\langle \delta^s_m \delta^l_m \right\rangle + b^s(5s^l-2)\left\langle \delta^s_m \delta^l_\kappa \right\rangle \\ + b^l(5s^s-2)\left\langle \delta^l_m \delta^s_\kappa \right\rangle + (5s^l-2)\cdot(5s^s-2)\left\langle \delta^l_\kappa \delta^s_\kappa \right\rangle .\end{aligned} \tag{3.21}$$

[25] This methodology is based on the MICE Grand Challenge Lightcone Simulation paper [65].
[26] This can be done using the expert mode in *Cosmohub*.

where the upper-index "s" and "l" correspond to sources and lenses. We observe that four terms appear, but only the second term is relevant. The first term is zero because there is no correlation between arbitrary galaxies without magnification at different redshifts when there is no overlap between sources and lenses. Similarly, the third term, which represents the magnification of lenses due to sources, is zero because the sources do not influence the light propagation of lenses that are closer to the observer. The fourth term is not exactly zero, as there is a slight correlation between the convergence of lenses and sources, since the convergence includes all the matter between the object and the observer. However, this correlation is very small, primarily due to the varying lensing efficiency across different redshifts. Therefore, the final expression simplifies to:

$$\left\langle \delta^s \delta^l \right\rangle \approx b^s (5s^l - 2) \left\langle \delta^s_m \delta^l_\kappa \right\rangle \tag{3.22}$$

Then the predictions for the magnification bias C_ℓs can be calculated as follows:

$$\begin{aligned} C_\ell(\text{Nomag}) &= 0 \\ C_\ell(\text{Magpos}) &= \text{-2b } C_\ell^{\kappa g} \\ C_\ell(\text{Magmag}) &= \text{5b·s } C_\ell^{\kappa g} \\ C_\ell(\text{Magall}) &= \text{b(5s-2)} C_\ell^{\kappa g}, \end{aligned}$$

where $C_\ell^{\kappa g} = \left\langle \delta^s_g \delta^l_\kappa \right\rangle$ represents the cross-spectrum between the convergence at $z = 1$ and the galaxy density fluctuations at $z = 0.5$. The value of s is determined by referring to Figure 3.18 for a magnitude limit < 23 and $z = 1$, yielding a value of $s \sim 0.6$. The parameter $b = \frac{\delta_g}{\delta_{DM}}$ is the bias factor at $z = 0.5$, which was calculated in section 3.5.1 with a value of b_1=1.27.

In Figure 3.19, we present the initial results of the magnification bias cross-spectra for all source maps with the lens map. The C_ℓ values obtained from *PolSpice* exhibited significant noise, with high-frequency oscillations. Additionally, we show the predictions based on the values of b_1 and s. At low ℓ, it is difficult to discern whether the values align with the predictions due to substantial fluctuations caused by sample variance. At higher ℓ, the unlensed terms (Nomag and Magmag) closely match their expected amplitudes. For Magmag, the amplitude is somewhat lower, likely due to resolution effects that dilute the signal, a behavior also observed in the MICE plot from [65]. The lensed terms appear to follow a similar trajectory to their respective un/magnified counterparts. Thus, we are not detecting the lensed position term (area dilution) in the cross-correlation.

We can suppress sample variance to a very good degree by obtaining each term as a subtraction of other terms to cancel out the noise (as all the maps should carry the same sample variance noise). We have that C_ℓ(Magall) = C_ℓ(Magpos) + C_ℓ(Magmag) so we can obtain the sample variance free C_ℓ as:

$$\begin{aligned} C_\ell(\text{Magpos}) &= C_\ell(\text{Magall}) \text{ - } C_\ell(\text{Magmag}) \\ C_\ell(\text{Magmag}) &= C_\ell(\text{Magall}) \text{ - } C_\ell(\text{Magpos}) \\ C_\ell(\text{Magall}) &= 2C_\ell(\text{Magall}) \text{ - } C_\ell(\text{Magmag}) \text{ - } C_\ell(\text{Magpos}) \end{aligned}$$

In Figure 3.20 we can observe the same plot with the suppression of sample variance. The unlensed C_ℓ now follow with perfect agreement the predictions at low ℓ, while at high ℓ we still have the resolution effects that dilutes the signal. Now is clear that the lensed terms (Magpos and Magall) do not trace the prediction at all. This indicates that there is something wrong with the magnified positions since the signal for this term seems to be 0.

In order to crosscheck our methodology we reproduced the magnification bias cross-spectrum for MICECATv1 as found in the paper [65]. So we repeated the procedure for data of MICE using the values of s=0.767 and b=1.35 given in the same paper for the predictions. In Figure

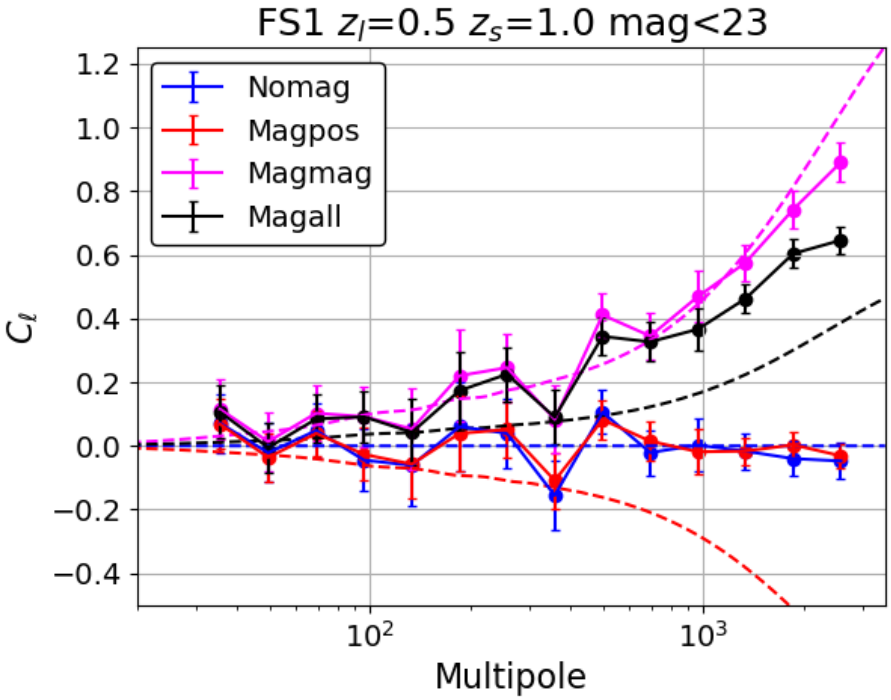

FIGURE 3.19: Magnification bias cross-spectrum for Flagship for lenses at z=0.5 and sources z=1. The corresponding predictions are showed as dashed lines with the same legend color. Jackknife errors with $N_{\rm JK} = 20$ are included.

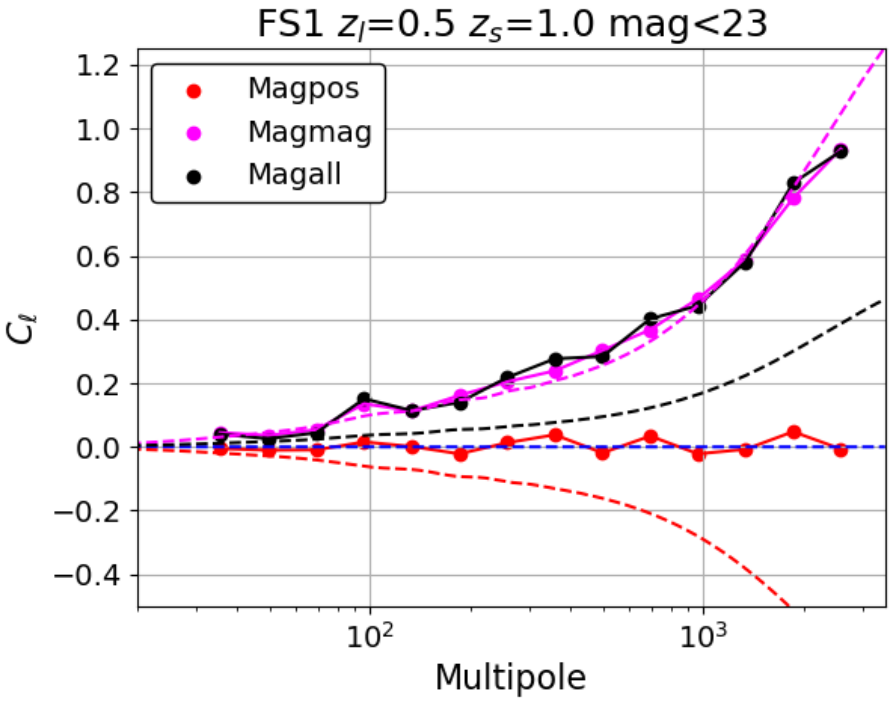

FIGURE 3.20: Magnification bias cross-spectrum for Flagship with suppression of sample variance.

3.21 we can see that all the terms follow the predictions in very good agreement at the plot without sample variance. The expected resolution effect at high ℓ is also present just as in the MICE-GC paper's plot.

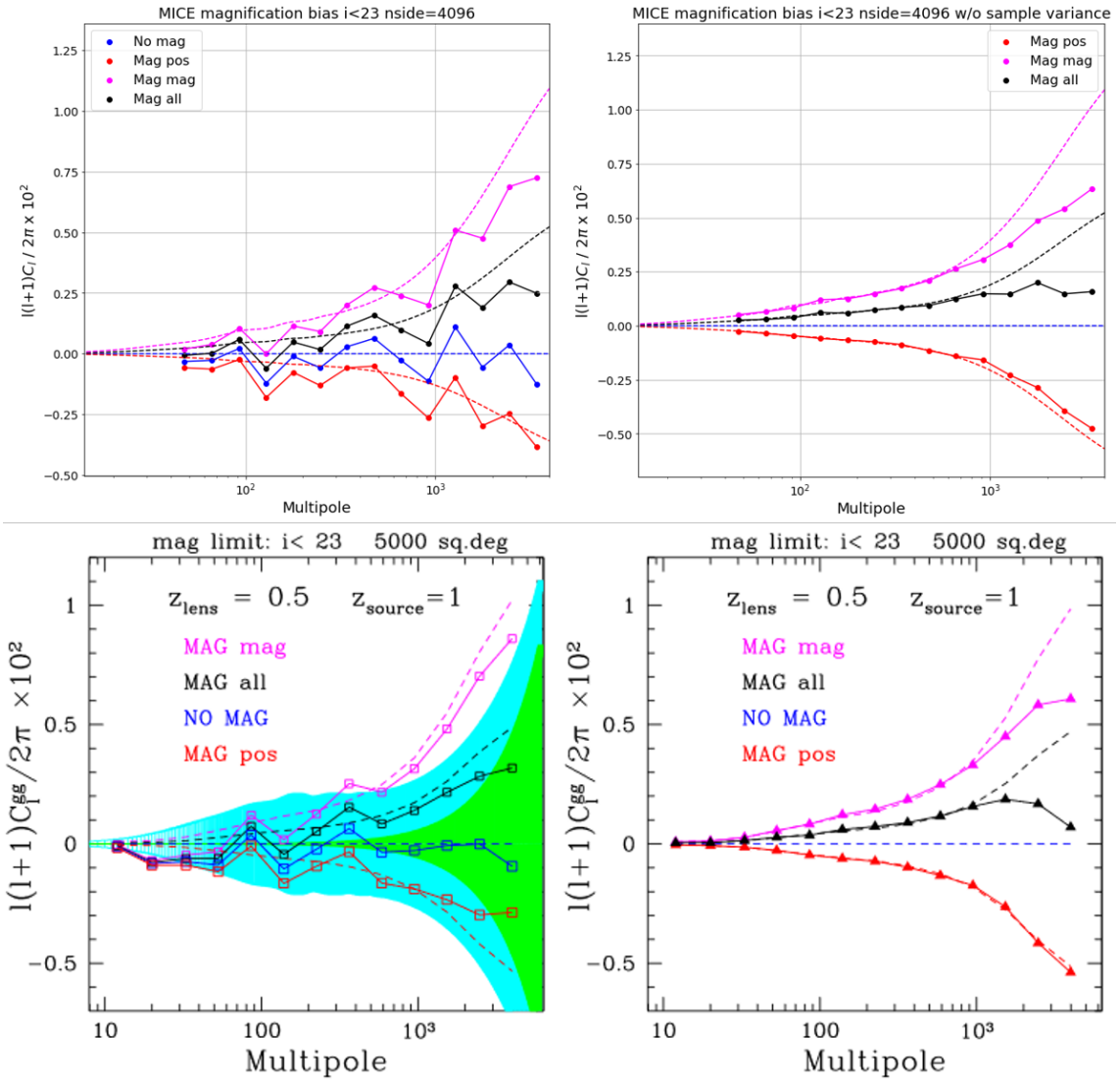

FIGURE 3.21: Magnification bias cross-spectrum for MICE at $i_{AB} < 23$: At top we present our obtained results to compare with the MICE-GC paper's plots below. At right we have the corresponding plot w/o sample variance. Source (bottom plots): [65]

The agreement in the results from Figure 3.21 seem to indicate that our methodology is well executed. Then the disagreement in the lensed term for Flagship may indicate some issue with the catalog data originated from a bad implementation of the lensed position calculation.

We conducted extensive tests with Flagship to identify the source of the issue. In Figure 3.22, we present a Cartesian projection of a small patch from all the Flagship source maps to gain some insight into their validity. From the projection, it appears that the maps themselves are not problematic. For Magpos, we observe the expected correlated displacement of galaxies in the same direction (downward). In the Magmag map, there are small variations in the pixel number density counts. Finally, Magall represents the sum of both effects.

We also performed tests with lenses and sources at different redshift bin widths and attempted to generate the cross-spectrum from maps with lower resolution ($N_{side} = 2048$) without significant changes in the results. Ideally, we would like to increase the resolution further, but as mentioned in a previous section, generating maps at resolutions higher than $N_{side} = 4096$ proved too demanding in terms of RAM and CPU resources. We had already optimized

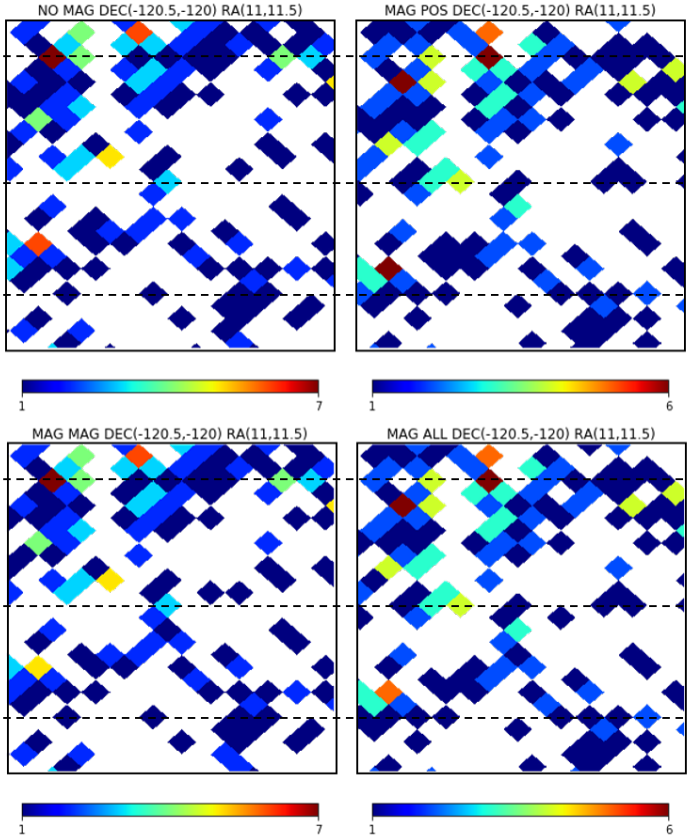

FIGURE 3.22: HEALPix Cartesian projection of the same 0.5x0.5 deg patch for all the 4 Flagship source maps. Horizontal dashed lines are for position reference between maps.

our code to generate maps at $N_{side} = 4096$ without running out of memory, and *PolSpice* took about 30 minutes to produce the four cross-spectra at this resolution, making it time-consuming to test multiple solutions. Looking back at Figure 3.22, it appears that the galaxies shift by one pixel due to lensing, which is expected given that for $N_{side} = 4096$, the pixel size is 0.85 arcminutes, while the θ_{RMS} of the unlensed-lensed distance is 1.08 arcminutes for Flagship. This suggests that many galaxies may have a lensed distance smaller than the pixel size, given the close proximity of the θ_{RMS} value, which could explain why we are not capturing the lensed position in the cross-correlation.

To verify whether Flagship's data from Cosmohub was properly produced, we conducted a final test by re-obtaining the Flagship lensed positions using the SQL query that was originally used to retrieve the lensed positions stored in Cosmohub. We were provided with the SQL code, which we then rewrote in Python to calculate the positions using the unlensed positions from the CSV files and the DM deflection maps. The RMS of the angular distance between the lensed positions from Cosmohub and those obtained with our Python implementation of the SQL query is 1.533 arcminutes for Flagship and 0.025 arcminutes for MICE. This suggests that there may be an issue with Flagship's data, as we would expect this value to be close to zero. For MICE, the discrepancy is small enough, especially considering that the limited accuracy of the *numpy* trigonometric functions may have contributed to the increase in this value.

After several months of testing, we were able to find the origin of this issue which we detail in the following section.

3.6.5 Final validation of the magnification bias

After reviewing the internal data of the halo catalog for the mock by validating the original deflection, convergence, and shear maps, we identified discrepancies in the deflection and shear maps when derived from the convergence map (Eq. 2.125). The issue was traced to the code used for generating these maps, which relied on a deprecated *healpy* function called *alm2map*. This function no longer accounted for the spin of the $a_{\ell m}$ coefficients (see Eq. 2.117). We resolved this issue by updating the code to use the newer *alm2map_spin* function, which explicitly allows setting the spin value for the $a_{\ell m}$: spin 1 for deflection and spin 2 for shear. Despite this error, it did not affect the E-mode of the angular power spectrum, which is why the issue was undetectable in Figure 3.16.

With the corrected maps, we revisited the magnification bias validation. As shown in Figure 3.23, the results now align with predictions. We also tested fainter magnitude limits at $E_{\rm VIS} < 24$, where the magnification bias is nearly nonexistent due to the cancellation of the two contributing effects, $(5s - 2) \sim 0$.

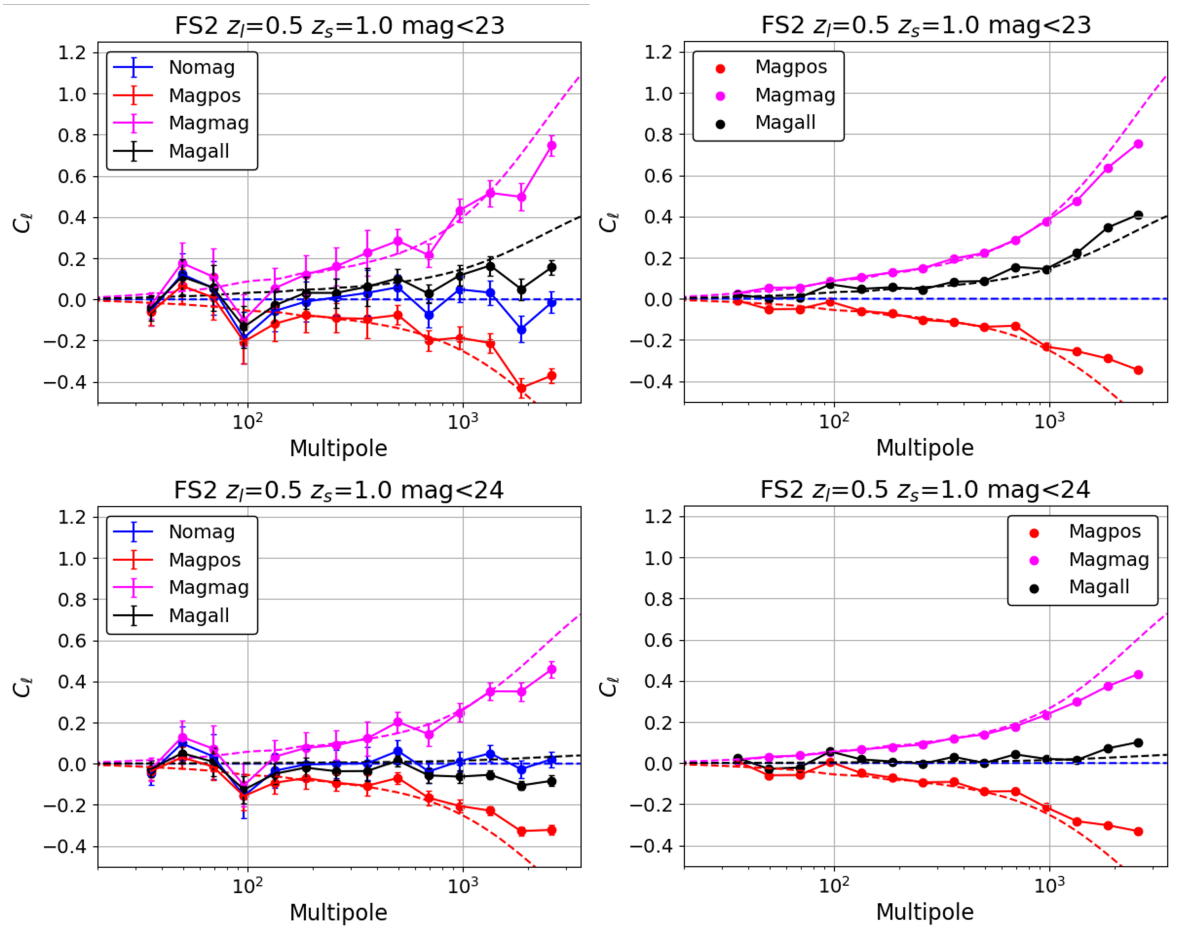

FIGURE 3.23: Final results for the magnification bias validation in FS1. The top plots show the results for $E_{\rm VIS} < 23$ while the bottom for $E_{\rm VIS} < 23$. The right plots show the values with the sample variance subtraction.

This validation was essential for the development of the improved Flagship v2 mock (Sec. 3.3.3), enabling the correct generation of shear and magnified galaxy positions.

Chapter 4

Probing gravity with non-linear clustering in redshift space

Using the primary tools for galaxy clustering and galaxy lensing described in Chapter 3, in the following chapters we present the main projects and contributions made throughout the course of this thesis. The two main projects, for which we are the primary authors, focus on modified gravity models and will be described in detail. In this chapter, we detail the core project of this thesis, which involves the E_G estimator applied to a pair of twin GR and modified gravity $f(R)$ simulated mocks. This chapter is essentially a reproduction of the final paper submitted for publication (Viglione C. et al., 2025). In Chapter 5, we discuss a related project that performs a 3x2pt analysis on the same mocks. A paper for this project is currently in preparation (Viglione C., Alemany M. et al., in preparation). Lastly, in Chapter 6, we present the contributions made to the Euclid mission [44], which are reflected in several published papers where we are listed as co-authors: [107, 46, 108, 47].

In the project presented in this chapter we present the first computation of the gravity model testing parameter E_G on realistic simulated galaxy mocks. The analysis is conducted using two twin simulations presented in [16]: one based on general relativity (GR) and the other on the $f(R)$ Hu & Sawicki model with $f = 10^{-5}$ (F5). Both simulations share an identical fiducial background cosmology and initial conditions, and they are calibrated against low redshift observations. This study aims to measure the E_G estimator in GR and $f(R)$ gravity models using high-fidelity simulated galaxy catalogs. The ultimate goal is to asses to what extent future galaxy surveys can detect deviations with respect to standard gravity using this widely used gravity estimator.

4.1 Introduction

The need of a theoretical explanation for the observed accelerated expansion of the universe has forced the inclusion of the cosmological constant (Λ) as a dark energy component that acts as a negative pressure or effectively "repulsive" gravity on large cosmological scales. Little advances have been achieved in determining the nature of the cosmological constant since its introduction, despite massive recent observational efforts (SDSS [109], DES [42], BOSS [89], DESI [43]). Several alternative gravity models [88] are also able to explain this accelerated expansion without the need of a cosmological constant. So far, the validity of general relativity (GR) has been mainly tested on relatively small scales [91, 101]. However modified gravity models apply corrections to GR that only become important at cosmological scales much larger than the Solar System where screening effects make deviations from standard gravity vanish. In particular, current galaxy surveys are trying to break the degeneracy between modified gravity models and dark energy models in observations by sampling the largest

accessible scales.

The large number of theories of gravity that have been proposed in recent years have motivated the need develop methods to probe the validity of these models. Of particular interest are those approaches that focus on those observables directly related to the underlying theory of gravity. One of the first observables that was put forward, presented in [160], provides a direct test for gravity on larger scales. The E_G estimator corresponds to the ratio between curvature, related to the Φ and Ψ gravitational potentials, with the velocity field, related to the growth rate of structures f. In GR, since these relations follow Einstein's equations this observable takes a scale-independent relation that only depends on the matter density parameter and the growth rate at the given redshift. This is very useful to test the validity of GR since any deviation from this value could indicate that GR breaks down on the largest cosmological scales.

Observationally, the velocity field, related to redshift space distortions, can be estimated with density (galaxy) auto-correlations, while the curvature field can be estimated from the correlation between the weak gravitational lensing (shear) of background galaxies with foreground galaxy positions. In this analysis the correlation functions are calculated in Fourier Space, or rather its curved sky generalization, spherical harmonic space, using a pseudo-$C_\ell s$ estimator in order to have a better separation of large and small scales. Previous analysis [71, 156, 122, 123, 5, 152] have used CMB lensing in order to estimate the convergence field, since this estimator is not affected by systematics related to intrinsic alignments and it has a broad kernel that samples dark-matter clustering at higher redshifts. We instead opt for using galaxy-galaxy lensing since this allows us to be self-consistent with the data as we can extract the galaxy source information directly from the same lightcone simulation. This also gives us the opportunity to select different source sample populations to optimize the gravity estimator. In this context, we leave for future work the potential impact of intrinsic alignments in our analysis.

Estimating the value of the growth rate can be difficult since it suffers from a degeneracy with galaxy clustering bias and the scalar amplitude A_s or σ_8 when parameterized from the power spectrum alone. So working with multipoles of the correlation function have become a common approach to break this degeneracy as each multipole exhibits a different dependence on these clustering amplitude parameters. In this context, several emulators have been proposed to produce fast and accurate predictions of the clustering multipoles for a given cosmology that are also able to reproduce different sources of non linear effects. For this analysis the public code COMET-EMU [60] is used to predict the multipoles of the correlation function which allows to emulate non-linear galaxy clustering in redshift space using different perturbation theory approaches (EFT, VDG). In this study, we incorporate both the monopole and quadrupole in configuration space to adopt a more robust approach [30]. We note others ways to estimate the growth rate not studied here. [48] uses the angular galaxy-galaxy autocorrelation to estimate f, which is further expanded in [70] and [18] by using additional weak lensing cross-correlations between redshift bins. While [81] uses the shape of the reduced three-point correlation and a second method with a combination of third-order one- and two-point cumulants to estimate the linear growth factor D.

Modified gravity models often introduce an additional scalar degree of freedom, which generates a fifth force [45]. In this study, we examine the $f(R)$ gravity model, where the fifth force has a finite range, denoted by λ_c. Within this range, the force strength in the linear regime is equivalent to one-third of the standard gravitational force, effectively modifying G to $\frac{4}{3}G$

on small scales (r « λ_c), while preserving the standard G on larger scales. Such a significant modification would be incompatible with observations if not for the presence of a screening mechanism, which suppresses these changes in regions of high density.

In this paper, we perform the first self-consistent calculation of the E_G estimator from a synthetic galaxy mock that follows an $f(R)$ Hu & Sawicki modified gravity model [16]. Potential deviations from GR are estimated by comparing measurements of the gravity estimator in this mock with respect to a reference galaxy mock that uses the same galaxy assignment pipeline applied to a ΛCDM simulation (i.e, same cosmological parameters and initial conditions, but standard gravity force). The fact that we use simulated data allows us to ignore systematics that affect the estimator in observations, namely the effect of lensing and magnification that can produce errors on the E_G estimation of up to 40% on high redshift photometric samples [156, 71]. Moreover, since we want to assess whether it is possible at all to distinguish gravity models that are consistent with the set of current observational data, we focus as a working case on an ideal all-sky survey, and neglect sources of astrophysical systematics such as intrinsic alignments or photometric errors. We adopt the refined E_G estimator introduced by [152], which builds upon the traditional method of using the angular power spectrum, as presented by [122]. Additionally, [77] proposed a novel, entirely model-independent E_G estimator that combines galaxy velocity measurements from surveys with the Weyl potential. However, this new approach is not explored in this study.

Due to the nature of $f(R)$ in the Hu & Sawicki model the value of the growth rate f is scale dependent. Consequently, we will estimate this parameter across different scales. In GR, this parameter is typically calculated by fitting a model to the multipoles of the correlation function over a broad range of scales, under the assumption of scale independence. Estimating this parameter over limited scales introduces several complexities, which we will address throughout this paper. To the best of our knowledge, such an approach has not been previously attempted in the literature.

This paper is organized as follows: in section 4.2 we introduce the $f(R)$ Hu & Sawicki model and emulators to calculate the dark matter and growth-rate boost, in section 4.3 we explain the theoretical predictions for the E_G estimator for F5 and GR, while in section 4.4, we introduce the COMET emulator and the VDG model that we use to perform the fits to the growth rate. Then we present the GR and F5 simulated catalogs that we use to obtain the data vectors in Section 4.5. A description of the different ingredients that enter in the E_G estimator and how can they be accurately computed is presented in section 4.6. Our main results are discussed in 4.7, and we propose a null test of gravity in 4.8, as a simple alternative test to distinguish between GR and F5 using the 2-point clustering in redshift space. Finally, in sections 4.9 and 4.10 we discuss our main findings in detail, and present our conclusions and future work.

4.2 The $f(R)$ Hu & Sawicki model

The $f(R)$ gravity model, a widely studied modified gravity (MG) framework, extends GR by introducing a scalar function $f(R)$, where R is the Ricci scalar, into the gravitational action:

$$S = \int \mathrm{d}^4x\sqrt{-g}\left[\frac{R + f(R)}{16\pi G} + \mathcal{L}_m\right], \tag{4.1}$$

where g is the determinant of the spacetime metric, $\mathcal{L}_m$ represents the matter field's Lagrangian, and G is the gravitational constant. In this model, $f(R)$ serves as a generalization of the cosmological constant, or, when constant, it represents the cosmological constant itself. From this action, one can derive the modified Einstein equations.

By varying the action with respect to the metric, one derives the field equations, commonly referred to as the Modified Einstein Equations [16]:

$$G_{\mu\nu} + f_R R_{\mu\nu} - \left(\frac{f}{2} - \Box f_R\right) g_{\mu\nu} - \nabla_\mu \nabla_\nu f_R = 8\pi G T_{\mu\nu}, \tag{4.2}$$

where ∇ represents the covariant derivative with respect to the metric, $\Box \equiv \nabla_\nu \nabla^\nu$ is the d'Alembert operator, and $T_{\mu\nu}$ is the energy-momentum tensor for the matter fields. $R_{\mu\nu}$ is the Ricci tensor, and $f_R \equiv \frac{df(R)}{dR}$ is the derivative of the scalar function with respect to the Ricci scalar R.

The form of the $f(R)$ function depends on the specific model chosen. To simulate the observed structure formation, a functional form for $f(R)$ must be selected. According to [87], an appropriate $f(R)$ function should satisfy the following conditions: (1) it should reproduce the ΛCDM model at high redshifts (consistent with CMB observations), (2) at low redshifts, it must behave similarly to a cosmological constant, driving accelerated expansion, (3) it should include free parameters to model various low-redshift phenomena, and (4) it must recover GR results at small scales (e.g., solar system scales) to be consistent with observational constraints. The Hu-Sawicki (HS) model satisfies these criteria and takes the following form:

$$f(R) = -m^2 \frac{C_1 \left(\frac{R}{m^2}\right)^n}{C_2 \left(\frac{R}{m^2}\right)^n + 1}, \tag{4.3}$$

where $m^2 \equiv \Omega_m H_0^2$, and C_1, C_2, and n are model parameters. For this work, $n = 1$ is used.

Additionally, the derivative of $f(R)$ respect the Ricci scalar is given by:

$$f_R = -n \frac{C_1 \left(\frac{R}{m^2}\right)^{n-1}}{\left[C_2 \left(\frac{R}{m^2}\right)^n + 1\right]^2} \tag{4.4}$$

In the high curvature regime ($R \gg m^2$), as shown by [117], Eq. 4.4 becomes:

$$f_R \approx -n \frac{C_1}{C_2^2} \left(\frac{m^2}{R}\right)^{n+1}, \tag{4.5}$$

In [87] was demonstrated that a background resembling the standard ΛCDM model can be recovered by enforcing the condition:

$$\frac{C_1}{C_2} = 6 \frac{\Omega_{\Lambda,0}}{\Omega_{m,0}}, \tag{4.6}$$

where $\Omega_{\Lambda,0}$ and $\Omega_{m,0}$ represent the present-day densities of dark energy and matter, normalized by the critical density. This condition reduces the number of free parameters in the

equation to one: either C_1 or C_2), since as established earlier n=1 for this work.

The remaining free parameter is described by the scalar field's background value at redshift $z = 0$, denoted $\bar{f}_{R0}$, which is treated as a free parameter to constrain the HS $f(R)$ model:

$$\frac{C_1}{C_2^2} = -\frac{1}{n}\bar{f}_{R_0}\left(\frac{R_0}{m^2}\right)^{n+1}. \tag{4.7}$$

By appropriately selecting this parameter, the $f(R)$ model can recover GR in high-density regions, ensuring consistency with solar system tests via the chameleon mechanism [87].

In cosmological simulations based on standard gravity, it is common to use the Newtonian limit of GR, which assumes weak gravitational fields and a quasi-static evolution of matter fields. This approximation is also applied in most modified gravity simulations, including those in this work. The limitations of this approach, specifically in the context of $f(R)$ gravity, are explored in [130].

Under the Newtonian limit, the complex 16-component field equation (Equation 4.2) simplifies to two key equations. The first is the Modified Poisson Equation:

$$\nabla^2\phi = \frac{16\pi G}{3}\delta\rho_m a^2 - \frac{1}{6}\delta R, \tag{4.8}$$

where ϕ represents the total gravitational potential, $\delta\rho_m = \rho_m - \bar{\rho_m}$ is the perturbation from the background matter density $\bar{\rho_m}$, and δR is the perturbation from the background value of the Ricci scalar, i.e., the background curvature. The second equation describes the scalar degree of freedom f_R:

$$\nabla^2 f_R = \frac{1}{3}\left(\delta R - 8\pi G\delta\rho_m\right). \tag{4.9}$$

Combining Eq. 4.8 and Eq. 4.9, the Modified Poisson Equation is expressed as:

$$\nabla^2\phi = \frac{8\pi G}{2}\delta\rho_m a^2 - \frac{1}{2}\nabla^2 f_R, \tag{4.10}$$

where it is more clear that $f_R/2$ acts as the potential for the modified gravity force. The equation approaches the standard GR expression within the Solar System, thanks to the chameleon mechanism [97, 87]. In scenarios with small values of $\bar{f}_{R_0}$, the background expansion remains indistinguishable from that in ΛCDM [100]. In observations, numerous constraints on HS $f(R)$ gravity focus on f_{R_0}. On cosmological scales, constraints have been derived from cluster number counts, CMB, supernovae, and BAO data, with [37] placing $\log|f_{R_0}| < -4.79$, [84] finding $\log|f_{R_0}| < -4.5$, [83] setting $\log|f_{R_0}| < -4.15$ and [100] finds $\log|f_{R_0}| < -4.61$. On more local scales constraints arise from galactic studies, with [114] setting $\log|f_{R_0}| < -6.1$ through galaxy rotation curves, and [54] obtained $\log|f_{R_0}| < -7.85$ based on galaxy morphology. This means that low scale measurements force practically all astrophysical objects to be screened, i.e. behave like GR. In [45] an upper limit of $\log|f_{R_0}| < -5.6$ is constraint with no observational systematics using dark matter simulations with baryonic effects.

Despite these tight bounds, $f(R)$ gravity remains a valuable framework for exploring deviations from GR on cosmological scales. In this study, we explore the $f(R)$ gravity model using a $|\bar{f}_{R_0}| = 10^{-5}$ (also known as F5), which, while slightly conflicting with local observational constraints unless environmental screening is considered, is within the HS constraints on cosmological scales [16]. F5, with its more significant deviation from GR compared to other studied deviations like F6, provides key insights into the effects of gravity modifications on large-scale phenomena such as weak lensing and clustering statistics. Understanding these effects is crucial for upcoming large-scale structure surveys like DESI, Euclid and LSST, which aim at testing GR as one of its main scientific goals.

[34] performs a forecast for precise constraints on $f(R)$ for the Euclid mission. For a fiducial value of $\log|f_{R_0}| = -5.30$, Euclid can constrain $\log_{10}|\bar{f}_{R_0}|$ to 1% accuracy by combining both spectroscopic and photometric observations. Additionally, Euclid is expected to distinguish between larger values such as $\log_{10}|\bar{f}_{R_0}| = -4.30$, smaller values like $\log_{10}|\bar{f}_{R_0}| = -6.30$, and ΛCDM with a confidence level exceeding 3σ.

4.2.1 Dark matter power spectrum boost

The matter power spectrum, despite not being a direct observable, is one of the basic theoretical tools that can be modeled to characterize the growth of cosmic structures. This power spectrum allows the construction of predictions for other observables, like the galaxy power spectrum, which are useful to estimate cosmological parameters. So an accurate estimation of the dark matter spectrum for f(R) is a key ingredient of the EG estimator to calculate the E_G estimator. Perturbation theory (PT) can be used to predict the matter power spectrum on quasi-linear scales [24] with great precision. In the non-linear regime, PT breaks down and one needs to resort to measurements from N-body simulations to achieve accurate predictions. This makes the use of cosmic emulators crucial, as they allow for analytical predictions of non-linear scales by interpolating results from a vast number of N-body simulations covering a wide parameter space. These emulators enable a more complex modeling of matter and galaxy clustering on small scales.

Many emulators exists for ΛCDM, but in the past years some emulators have appear for extended Dark Energy models, including modified gravity theories like f(R). For linear matter power spectrum calculations, Boltzmann codes such as *mgcamb* [163, 82, 164, 150], *MGHalofit* [162] and *MGCLASS* [127] are commonly used for different gravity theories including $f(R)$. Additionally, there are simulation-based emulators that extend into the mildly non-linear regime, like *ELEPHANT* [154], COLA (COmoving Lagrangian Acceleration)) [124]; FORGE [15], E-MANTIS [138] and *Sesame* [111]. Another prominent tool is *ReACT* [28, 27], which applies a halo model reaction framework validated using N-body simulations.

Cosmological simulations for $f(R)$ models require significantly more computational time given that they have to compute the intrinsically non-linear evolution of the scalar field that mediates the modified gravity force. These emulators typically work by comparing the power spectrum results of modified gravity models to those of ΛCDM emulators. In this paper, we use the emulator E-MANTIS [138] (Emulator for Multiple observable ANalysis in extended cosmological TheorIeS), which is specifically designed for the Hu & Sawicki $f(R)$ gravity model. The E-MANTIS emulator provides a boost for the $f(R)$ gravity matter power spectrum, defined as:

$$B(k) = \frac{P_{f(R)}(k)}{P_{\Lambda\mathrm{CDM}}(k)}, \tag{4.11}$$

where $P_{f(R)}(k)$ and $P_{\Lambda\mathrm{CDM}}(k)$ are the matter power spectra for $f(R)$ gravity and ΛCDM, respectively. This boost is less sensitive to statistical and systematic errors and exhibits a smoother dependence on cosmological parameters than the raw power spectrum. Since both $f(R)$ and ΛCDM simulations start from the same initial conditions, the minimal impact of $f(R)$ gravity on large scales preserves the strong cancellation of cosmic variance and large-scale errors. Similarly, small-scale systematic errors due to limited mass resolution also cancel out. By focusing solely on this boost, the emulator significantly reduces computational demands, as less precise simulations are required to achieve the desired accuracy for the boost compared to the raw power spectrum.

The power spectrum boost is mainly influenced by three cosmological parameters: $\bar{f}_{R_0}$, Ω_m, and σ_8. Variations in other parameters, such as h, n_s, and Ω_b, have a negligible impact, with less than 1% variation up to scales of $k = 10h\,\mathrm{Mpc}^{-1}$. The emulator does not account for the effect of baryonic physics on the matter distribution, which affects the matter power spectrum boost in $f(R)$ gravity for scales $k < 2\,h\,\mathrm{Mpc}^{-1}$ [13]. However, [138] anticipates that using a ΛCDM emulator, which incorporates the baryonic impact on the matter power spectrum, to apply the boost will correct for this in the $f(R)$ power spectrum. In this study we will use the Halofit matter power spectrum from [140] which despite no including baryonic impact accounts for accurate nonlinear corrections.

Using simulations with an effective volume of $(560\,h^{-1}\mathrm{Mpc})^3$ and a particle mass resolution of $m_{\mathrm{part}} \sim 2 \times 10^{10}\,h^{-1}M_\odot$, the power spectrum boost can be determined with better than 3% accuracy for the range $0.03\,h\,\mathrm{Mpc}^{-1} < k < 7\,h\,\mathrm{Mpc}^{-1}$ and redshifts $0 < z < 2$. Although the systematic error on the boost varies with $\bar{f}_R$, redshift, and scale, the 3% estimate is conservative, as most cases achieve better than 1% accuracy [138].

4.2.2 Scale dependence in the growth rate

At the linear perturbation level in the comoving gauge, the modified Einstein equations for $f(R)$ gravity lead to the following equations in Fourier space for the evolution of matter overdensities. These describe how perturbations in the matter density evolve over time [144, 112]:

$$\begin{aligned} &\ddot{\delta}_m + \left(2H + \frac{\dot{f}_R}{2f_R}\right)\dot{\delta}_m - \frac{\rho_m}{2f_R}\delta_m \\ &= \frac{1}{2f_R}\left[\left(\frac{k^2}{a^2} - 6H^2\right)\delta f_R + 3H\delta\dot{f}_R + 3\delta\ddot{f}_R\right] \end{aligned} \tag{4.12}$$

$$\delta\ddot{f}_R + 3H\delta\dot{f}_R + \left(\frac{k^2}{a^2} + \frac{f_R}{3f_{RR}} - \frac{R}{3}\right)\delta f_R = \frac{1}{3}\rho_m\delta_m + \dot{f}_R\dot{\delta}_m. \tag{4.13}$$

In these equations, k is the comoving wavenumber, $a = (1+z)^{-1}$ is the scale factor (normalized to unity today), ρ_m is the matter density, and $\delta_m(a) = \delta\rho_m/\rho_m$ is the matter density contrast.

The Hubble parameter H is given by $H = \dot{a}/a$, and dots represent derivatives with respect to cosmic time. Lastly, f_{RR} is the derivative of f_R respect to R.

$$f_{RR} \equiv \frac{df_R}{dR} \approx \frac{n(n+1)}{m^2}\frac{c_1}{c_2^2}\left(\frac{m^2}{R}\right)^{n+2}, \tag{4.14}$$

where we take the approximation from Eq. 4.5

For cosmologically viable $f(R)$ models, f_R changes slowly, meaning $|\dot{f_R}| \ll H f_R$. Under this approximation, for f_R, the time derivatives can be neglected and the oscillatory modes are insignificant compared to those driven by matter perturbations. Additionally, for modes well inside the Hubble radius, $k^2/a^2 \gg H^2$, further simplifying the equations. These approximations lead to the following equation for the evolution of the matter density contrast:

$$\ddot{\delta}_m + 2H\dot{\delta}_m - 4\pi G_{\rm eff}\rho_m\delta_m \simeq 0, \tag{4.15}$$

where $G_{\rm eff}$ replaces the standard gravitational constant G from ΛCDM cosmology. $G_{\rm eff}$ is the effective gravitational constant, defined as:

$$G_{\rm eff}(k,z) = \frac{G}{f_R}\left[1 + \frac{1}{3}\left(\frac{k^2}{a^2M^2/f_R + k^2}\right)\right], \tag{4.16}$$

The dependence of $G_{\rm eff}$ on scale introduces scale-dependent effects in the formation of cosmic structures, distinguishing $f(R)$ models from standard cosmology. From Eq. 4.15 the growth rate is usually calculated. The growth rate f is typically defined as:

$$f(a) = \frac{d\ln D}{d\ln a} = \frac{a}{D}\frac{dD}{da} \tag{4.17}$$

where D(t) is the growth factor corresponding to the time factorization of the linear growth of matter perturbations. We assume that the growth of perturbations can be factored into a time-dependent part and a spatially dependent part:

$$\delta(\mathbf{x}, t) = \delta_0(\mathbf{x})D(t) \tag{4.18}$$

The growth factor can be calculated as solution to the linear perturbation theory differential equation:

$$\ddot{D}(t) + 2H(t)\dot{D}(t) - 4\pi G_{\rm eff}\rho_m(t)D(t) = 0 \tag{4.19}$$

which happens to be the same than in ΛCDM but using $G_{\rm eff}$ instead of G. This means than since $G_{\rm eff}$ now depends on the scale k, the growth rate in $f(R)$ will also depend on k.

In this work we use the public code MGrowth[1] which allows to obtain the value of the growth rate for several models of gravity. One of the gravity models is HS f(R) for any value of redshift, wavenumber and $\bar{f}_{R_0}$ between 10^{-9} and 10^{-2}. This code basically works by solving

[1] https://github.com/MariaTsedrik/MGrowth/blob/main/docs/MGrowth.rst

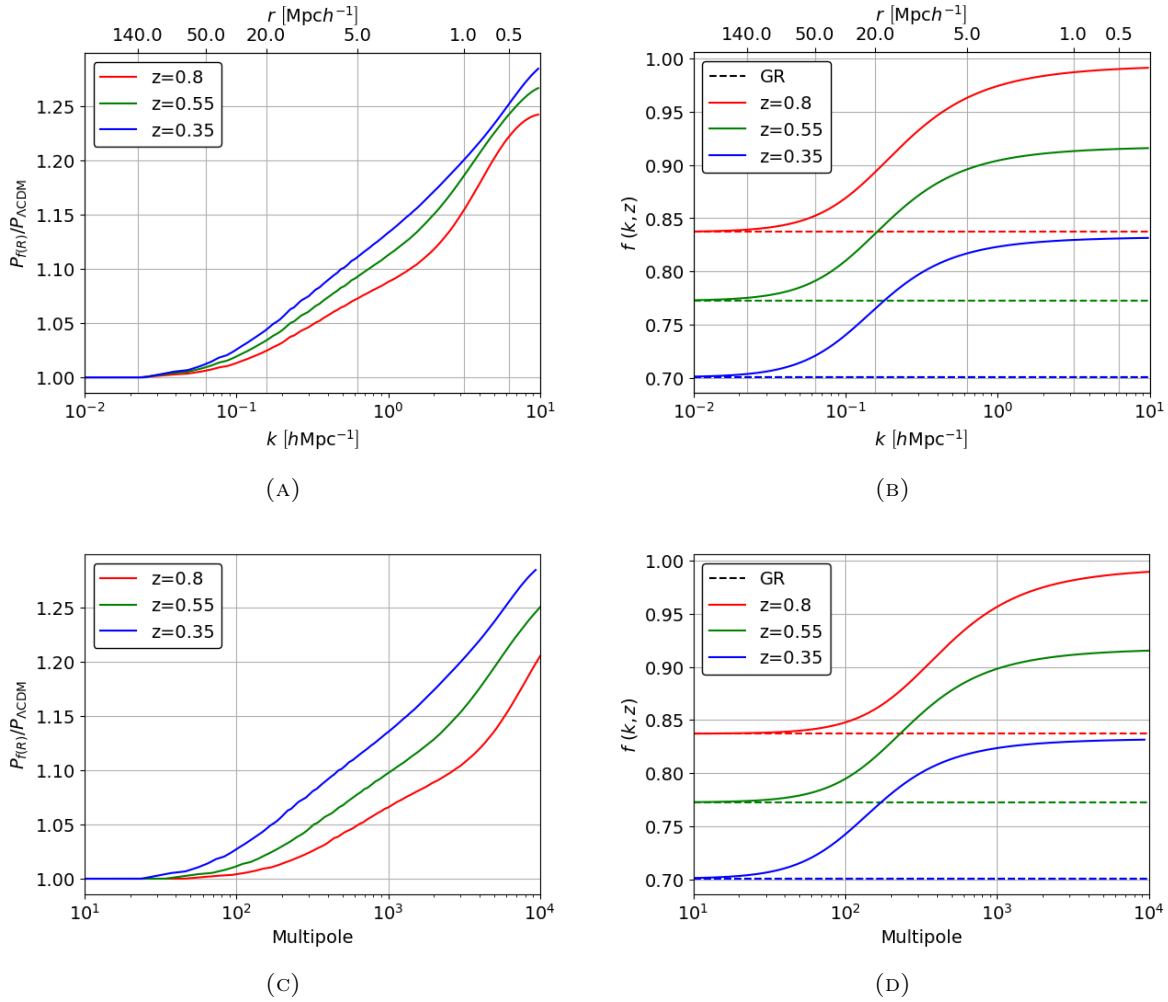

FIGURE 4.1: Comparison of the effects of $f(R)$ gravity on the dark matter power spectrum (Left plots) and the growth rate (Right plots) for the three redshifts used in this analysis. We show the results on k-wavenumbers and the corresponding commoving distance separation (Top plots). On a separate plot (Bottom plots), due to the dependence on a different projected commoving transversal distance for each z, we show the equivalent multipoles. Note that for the DM spectrum, we show the ratio (boost), while for the growth rate we show the values for GR and MG separately since the ratio is quite similar for each z.

Eq. 4.19 numerically using the $G_{\rm eff}$ defined in this section. In Figure 4.1 we plot the values of the growth rate for the three redshifts bins that we will use for GR and MG. Within the limber and small angle approximation, we can obtain a simple approximate relation between Fourier wavemodes and projected scales:

$$\ell \approx \frac{\pi}{\theta} \tag{4.20}$$

$$\theta \approx \frac{s}{\chi(z)} \tag{4.21}$$

$$k \approx \frac{\ell}{\chi(z)} \sim \frac{\pi}{s} \tag{4.22}$$

where $\chi(z)$ is the commoving distance and θ the angular scale. The final relation between k and s (Eq. 4.22) should be taken as a reference only since it comes from combining three approximations between variables.

4.3 The E_G estimator

The original definition of the E_G estimator in harmonic space as introduced in [160] is the following:

$$E_G(k,z) \equiv \frac{c^2k^2(\phi-\psi)}{3H_0^2(1+z)\theta(k)}\,, \tag{4.23}$$

where θ is the divergence of the peculiar velocity field. The potentials ψ and ϕ are, respectively, the time and spatial component of the perturbation fields of the metric. For a flat universe governed by the Friedmann-Robertson-Walker (FRW) metric and under the assumption of negligible anisotropic stress and non-relativistic matter species, the Einstein field equations for time-time and momentum components in GR can be expressed in Fourier space as follows [82]:

$$\begin{aligned} k^2\psi &= -4\pi G a^2 \rho_m(a)\delta \\ \phi &= -\psi, \end{aligned} \tag{4.24}$$

ρ_m represents the background matter density, a is the scale factor and δ denotes the matter density perturbation. In modified gravity models, these equations are usually generalized to:

$$\begin{aligned} k^2\psi &= -4\pi G a^2 \mu(k,a)\rho_m(a)\delta \\ \phi &= -\gamma(k,a)\psi, \end{aligned} \tag{4.25}$$

where $\mu(k,a)$ and $\gamma(k,a)$ are arbitrary functions of k and a. The μ function parametrizes the effective strength of gravity, and γ is the gravitational slip that quantifies the difference in the gravitational perturbation fields. These functions reduce to $\mu=\gamma=1$ in the GR case in order to recover Eq. 4.24.

Combining the equations in 4.25 we can then rewrite the numerator of E_G in Eq. 4.23 as [122]:

$$k^2(\phi-\psi) = \frac{3}{2}H_0^2\Omega_{m,0}(1+z)\mu(k,a)[\gamma(k,a)+1]\delta \tag{4.26}$$

where $\Omega_{m,0} = \frac{8\pi G\rho_0}{3H_0^2}$ with $\rho_m(a) = \rho_{m0}a^{-3}$. The velocity perturbation θ is given by $\theta = f\delta$ at linear scales. Combining this relation with Eq. 4.26, the expression for E_G becomes:

$$E_G(k,z) = \frac{\Omega_{m,0}\mu(k,a)[\gamma(k,a)+1]}{2f} = \frac{\Omega_{m,0}\Sigma(k,a)}{f}, \tag{4.27}$$

where we have re-parameterized as $\Sigma \equiv \frac{1}{2}\mu(1+\gamma)$ [152], which represents the lensing parameter. This is the parameter that the E_G more directly measures, which is 1 for GR. From this equation we can clearly see that for GR, the value of E_G is given by:

$$E_G^{GR} = \frac{\Omega_{m,0}}{f(z)}, \tag{4.28}$$

which can be readily computed using that, since f in GR can be approximated as $f(z) \approx \Omega_m(z)^{0.55}$. This means that for GR the value of E_G is predicted from the background expansion only using a constraint on $\Omega_{m,0}$ and it is thus independent of sample-specific parameters like the galaxy bias and its potential systematic effects. This value is predicted to be scale independent for GR at linear scales. In contrast, for $f(R)$ and other MG theories this estimator depends on scale, what is a potential smoking gun for detecting deviations with respect to GR.

Returning to the $f(R)$ model the functions μ and γ can be parameterized as [122]:

$$\mu^{f(R)}(k,a,) = \frac{1}{1 - B_0 a^{s-1}/6} \left[\frac{1 + (2/3) B_0 \bar{k}^2 a^s}{1 + (1/2) B_0 \bar{k}^2 a^s} \right] \tag{4.29}$$

$$\gamma^{f(R)}(k,a) = \frac{1 + (1/3) B_0 \bar{k}^2 a^s}{1 + (2/3) B_0 \bar{k}^2 a^s}, \tag{4.30}$$

Where $\bar{k} = k \cdot [2997.9\,\mathrm{Mpc}/h]$, and $h = H_0/[100\,\mathrm{km/s/Mpc}]$, with $s = 4$ for models that follow the Λ-CDM expansion history. The parameter B_0 is a free variable associated with the Compton wavelength of an additional scalar degree of freedom, and it is also proportional to the curvature of $f(R)$ at present times. Current observational constraints place a limit of $B_0 < 5.6 \times 10^{-5}$ at a 1σ confidence level [122]. Implementing this parametrization into the general expression from Eq. 4.27 one gets:

$$E_G^{f(R)}(k,z) = \frac{1}{1 - B_0 a^{s-1}/6} \frac{\Omega_{m,0}}{f^{f(R)}(k,z)}. \tag{4.31}$$

Since the constraints establish that $B_0 a^3 << 1$ then we can simply the expression to:

$$E_G^{f(R)}(k,z) = \frac{\Omega_{m,0}}{f^{f(R)}(k,z)}. \tag{4.32}$$

Therefore, in the large scale limit, the E_G estimator in $f(R)$ will only differ from the one in GR through the scale and redshift dependence of the growth rate. Since as we have seen in the previous section, the growth rate depends on the scale for $f(R)$ so the value $EG^{f(R)}$ will do so. Going back to the Σ parameter defined in Eq. 4.27, we have that just like GR $\Sigma = 1$ for the HS $f(R)$ model. The reason behind this is that, unlike other modified gravity theories, HS $f(R)$ has negligible impact on the propagation of light in the weak-field limit [83], since $f(R)$ models have a conformal coupling. The actual value of Σ in $f(R)$ is given by [45]:

$$\Sigma(z) = \frac{1}{1 + f_R(z)} \tag{4.33}$$

Since the maximum value of $|f_R(z)|$ is given by $|f_{R0}|$ we can ignore this effect in this study.

In summary, in order to differentiate HS $f(R)$ from GR we shall need to accurately estimate the linear growth rate of perturbations. In Figure 4.2 we plot the predictions of E_G for F5

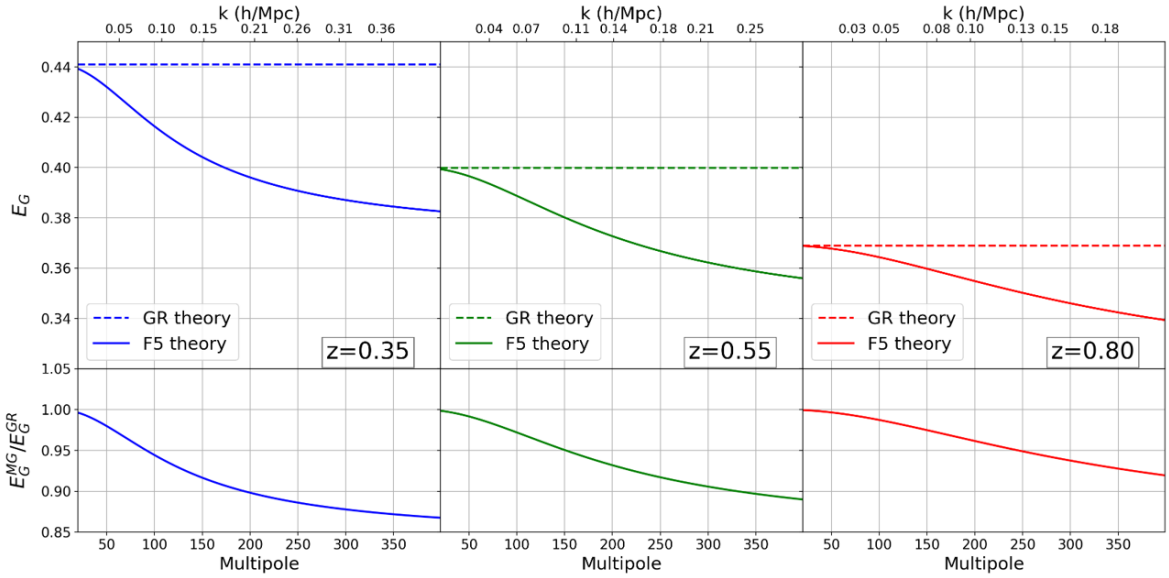

FIGURE 4.2: Plots showing the difference between the prediction of E_G for GR (dashed line) and F5 (solid line) at the three redshift bins. The lower plots show the respective ratio of the prediction for F5 over GR.

and GR with the respective ratio of the former over the latter. We can see that contrary to the growth rate prediction, since E_G is inverse to this parameter now the prediction for F5 decreases with the scale and it is always lower than the one for GR which is scale independent. We also note that the ratio between both predictions increases as we move to lower redshifts. This suggests that attempting to identify differences at these lower redshifts could be beneficial. However, as we will later demonstrate, nonlinear effects at smaller scales significantly complicate matters, thereby increasing the error.

4.4 Modelling RSD: Non-linear effects

The impact of (peculiar) velocities of galaxies away from the Hubble flow introduce a perturbation in the estimation of distances to galaxies as expected from the Hubble law. This systematic effect distorts the pattern of galaxy clustering in a way that depends on the growth rate. Therefore one can exploit the so-called redshift space distortions (RSD) as a powerful probe of dark-energy and gravity. By analyzing these effects, we can directly measure the rate at which structures in the universe grow, since it is related to the growth rate f, providing a valuable probe for investigating dark energy and gravity.

In the linear regime, the galaxy clustering patter suffers a characteristic squashing distortion along the line of sight, known as the Kaiser effect. In this limit, one can obtain a rather simple expression that relates the linear power spectrum with the RSD power spectrum using the growth rate. But modeling also the nonlinear contribution, known as the Finger of God effect, is significantly more complicated due to the complicated nature of non-linear interactions. There are numerous models, each with its own parameter space. These models address nonlinearities in different ways and may perform better or worse depending on the galaxy sample and the scales being analyzed. Regarding the galaxy power spectrum in redshift space, i.e. including RSD, effective field theory (EFT) [89, 50] has gained popularity recently since it is very versatile.

The versatility of EFT allows to incorporate several kind of extra parameters to describe models of modified gravity. It also introduces counterterms parameters in order to correct that the energy-momentum tensor is no longer homogeneous and isotropic at small scales, i.e. off-diagonal elements no longer vanish. Although many models try to incorporate as many parameters to have more freedom to describe nonlinear processes this is usually not recommended due to the complications of having to evaluate such a substantial parameter space. On top of that, there may be prior volume effects in the language of Bayesian statistics, also called "projection effects", where different parameters contribute to the model, or the power spectrum in this case, in a similar manner, i.e. the parameters are degenerated with each other. This can significantly bias the estimation of the cosmological parameters. The non-linear parameters are usually considered nuisance parameters since they describe systematics and do not give much information about the composition of our Universe.

In this section we will give an introduction to another perturbative model called the velocity difference generating function (VDG) model [139, 60]. We will use this model in this paper to estimate the β parameter for the calculation of the E_G estimator. We choose this model over others due to the reported level of accuracy at small scales when comparing results with simulated catalogs. The reason behind this is related to the better description of the PDF of "pairwise velocities" [31] (compared to the EFT model), which primarily captures the Fingers of God (FoG) effect. The COMET emulator [60] implements the VDG model, alongside an EFT implementation with a similar parameter space. We will use this emulator for the purposes of this paper.

4.4.1 COMET-EMU

The emulator contains a reduced parameter space thanks to the *evolution mapping* approach from [129] which separates the parameter space in: shape parameters, which determine the shape of the liner power spectrum (physical densities Ω_i and the spectral index n_s) and evolution parameters, which determine the amplitude and evolve with redshift (the scalar amplitude of the primordial power spectrum A_s and the parameters defining the curvature and the dark energy model).

The emulator also works with the parameter σ_{12} as the RMS of matter fluctuations in spheres of radius R=12 Mpc. This parameter is determined from the evolution and shape parameters when emulating a ΛCDM model, but it becomes a free parameter (in which case A_s is no longer needed) when selecting a *None* cosmology. The emulator uses σ_{12} instead of the most conventional σ_8 (RMS of matter fluctuations in spheres of radius R=8 Mpc/h) since as shown in [128] is better to express the power spectrum in Mpc instead of Mpc/h to have the correct scaling. The hubble parameter h and A_s are completely (perfect) degenerated with respect the amplitude of the power spectrum. So using Mpc units breaks the dependency of h in the normalization parameter σ. In any case, with a standard value of h=0.67 σ_{12} and σ_8 represent the same scale. The predictions of COMET are limited to the range of scales $k \in [6.95 \cdot 10^{-4}, 0.35028]\ Mpc^{-1}$, although it can make power-law extrapolations on both sides.

4.4.2 The VDG model

This model differ from the EFT approach only on its treatment of redshift-space distortions. While EFT performs a full expansion of the real-to-redshift space mapping, VDG partly retains the non-perturbative nature of this mapping including the exponential-type

PDF (damping factor) for the pairwise velocities. The model was originally proposed in [139] to describe the matter power spectrum in RSD, in [60] it is referred as VDG due to its relation to the velocity difference generating function to account for the virialized velocity impact via an effective damping function.

The VDG model implemented in COMET is very complex so in sec. 2.5.1 we summarize the key points from [60], we encourage the reader to check this reference if they want a even more detailed explanation. In sec. 4.6.3 we present and give a brief description of the space of COMET's parameters that we will use to perform the MCMC chains with MultiNest.

4.5 Simulations

4.5.1 Nbody simulations

We take our data from the General Relativity and f(R) Modified Gravity mock presented in [16]. The $f(R)$ simulation was obtained using the cosmological simulation code MG-GADGET3, which is a modification of the code P-GADGET3 that allows to run collisionless simulations in the Hu-Sawicki $f(R)$-gravity model. Four collisionless cosmological simulations were conducted. Each simulation was run twice: once using the $f(R)$ model and once with a ΛCDM cosmology, both utilizing identical initial conditions. In this paper we use the pair of simulations with the higher resolution placing 2048^3 particles in a 768 Mpc/h sidelength box, which give a mass resolution of $M_{part} = 3.6 \cdot 10^9\ M_\odot/h$. The mocks have a fiducial cosmology following [6] cosmology of $\Omega_m = 0.3089$, $\Omega_\Lambda = 0.6911$, $\Omega_b = 0.0486$, $h = 0.6774$, $\sigma_8 = 0.8159$ and $n_s = 0.9667$.

To solve the equation for the scalar degree of freedom in modified gravity (Eq. 4.2), MG-GADGET applies an iterative Newton-Raphson method combined with multigrid acceleration on an adaptive mesh refinement (AMR) grid. Instead of solving directly for f_R, the code solves for $u = \log(f_R/f_{R0})$ to avoid unphysical positive values of f_R in the simulation, a technique first introduced by [117]. Once f_R is determined, it is used to calculate an effective mass density, incorporating all $f(R)$ effects, including the chameleon mechanism:

$$\delta\rho_{\text{eff}} = \frac{1}{3}\delta\rho - \frac{1}{24\pi G}\delta R. \tag{4.34}$$

The total gravitational acceleration can then be computed by adding this effective density to the real mass density and using the standard Tree-PM Poisson solver implemented in P-GADGET3.

Each simulation includes a 2D lightcone output, consisting of 400 HEALPIX maps [76] between redshifts $z = 80$ and $z = 0$. These maps, spaced evenly in lookback time, have a resolution of 805,306,368 pixels. They are constructed using the 'Onion Universe' method [67], where the simulation box is repeated in all directions to cover the volume up to a given redshift z_i, and particles within a thin spherical shell at z_i are binned onto a HEALPIX map. The shell thickness is chosen to ensure space-filling lightcone output. From this lightcone HEALPix maps, the convergence maps are generated for each redshift bin from which all the lensing properties for all the galaxies of the catalog are extracted, like the deflection angle and the cosmic shear [85].

For the simulations a 3D halo catalog is generated on the fly. Halos are identified using a shrinking sphere method applied to objects found by the Friends-of-Friends (FOF) halo finder in P-GADGET3. The catalog stores properties such as the halo's mass, velocity, center of mass, and tensor of inertia, along with their positions. The simulations also produce time-slice outputs and halo catalogs generated using the SUBFIND algorithm [135].

4.5.2 Galaxy mocks

The galaxy assignment method used for the simulations of this paper are described in detail in Tutusaus et al. (in preparation). Below we summarize the main steps in the galaxy mock production and calibration. Following [63], the galaxy population is added to these halos based on a combination of models: the Halo Occupation Distribution (HOD) and Halo Abundance Matching (HAM), following recipes and strategies from [32] and [19]. In this setup, the model includes two key parameters for populating galaxies within each halo. The first parameter, M_1, establishes a mass threshold that controls the presence of central galaxies in the halos. For each halo that surpasses this mass threshold, a central galaxy is assigned. The second parameter, ΔL_M, introduces scatter in the pseudo-luminosity assigned to galaxies, which helps match the observed galaxy distribution and luminosity scatter seen in the survey data. Satellite galaxies are then assigned to each halo following a Poisson distribution, and they are positioned according to a Navarro-Frenk-White (NFW) profile within each halo to approximate the realistic clustering patterns.

After generating this initial galaxy catalog, calibration is applied to ensure that the mock galaxy catalog closely mirrors observed galaxy clustering statistics [63]. This calibration involves optimizing the M_1 and ΔL_M parameters across tomographic bins that represent different redshift intervals. An automated calibration process is used, employing a differential evolution algorithm to find parameter values that minimize the difference between the angular correlation function measured from the mock catalog and that from the real data. This angular correlation function is computed over three specific angular scales, chosen to best capture the clustering signal.

Due to computational constraints, the calibration is initially performed using a subset of five mock datasets. The differential evolution algorithm refines the parameter values iteratively, adjusting the clustering pattern in the simulated catalog to achieve a close match with the actual survey data. Once this process achieves satisfactory accuracy across the redshift bins, the calibrated parameters are applied to the entire set of simulations, yielding a galaxy catalog that faithfully represents the spatial distribution and clustering properties observed in the universe.

The F5 and the GR mock data are found on separated datasets with identical structure. As shown in [13], most of the differences in dark-matter clustering between $f(R)$ and GR models appear at low redshift. Therefore in our analysis we study the E_G estimator in 3 redshift bins at $z < 1$. In particular we choose bins centered at $z = 0.35,\ 0.55$ and 0.8, each one with bin-width of $\Delta_z = 0.1$. The lensing source sample is selected at $z = 1.0$ with a bin-width of $\Delta_z = 0.2$. We always select all the galaxies over the full sky within each case, imposing a relative magnitude cut on the SDSS r-band of $r < 24$.

In order to test the robustness of our results to sample selection, we select six different galaxy samples: 1) the full sample of galaxies, which is our baseline or reference case, 2)

		GR			MG		
Sample	**Observed Redshift**	**Nº galaxies**	**Nº density** (h/Mpc)^3	**Angular density** (sr^{-1})	**Nº galaxies**	**Nº density** (h/Mpc)^3	**Angular density** (sr^{-1})
All galaxies	$\mathbf{0.35 \pm 0.05}$	125,758,470	4.35×10^{-2}	1.00×10^{7}	119,326,008	4.13×10^{-2}	9.50×10^{6}
	$\mathbf{0.55 \pm 0.05}$	171,038,806	3.01×10^{-2}	1.36×10^{7}	182,214,423	3.21×10^{-2}	1.45×10^{7}
	$\mathbf{0.80 \pm 0.05}$	71,500,296	7.94×10^{-3}	5.69×10^{6}	75,675,455	8.41×10^{-3}	6.02×10^{6}
Central galaxies	$\mathbf{0.35 \pm 0.05}$	73,832,083	2.55×10^{-2}	5.88×10^{6}	76,231,335	2.64×10^{-2}	6.07×10^{6}
	$\mathbf{0.55 \pm 0.05}$	117,723,717	2.07×10^{-2}	9.37×10^{6}	124,580,224	2.19×10^{-2}	9.91×10^{6}
	$\mathbf{0.80 \pm 0.05}$	55,051,493	6.12×10^{-3}	4.38×10^{6}	61,317,982	6.81×10^{-3}	4.88×10^{6}
Red galaxies	$\mathbf{0.35 \pm 0.05}$	42,963,500	1.49×10^{-2}	3.42×10^{6}	31,651,738	1.09×10^{-2}	2.52×10^{6}
	$\mathbf{0.55 \pm 0.05}$	47,592,520	8.38×10^{-3}	3.79×10^{6}	46,889,007	8.26×10^{-3}	3.73×10^{6}
	$\mathbf{0.80 \pm 0.05}$	15,828,156	1.76×10^{-3}	1.26×10^{6}	16,745,570	1.86×10^{-3}	1.33×10^{6}
Blue galaxies	$\mathbf{0.35 \pm 0.05}$	67,289,748	2.33×10^{-2}	5.35×10^{6}	70,419,462	2.44×10^{-2}	5.60×10^{6}
	$\mathbf{0.55 \pm 0.05}$	105,853,959	1.86×10^{-2}	8.42×10^{6}	115,424,023	2.03×10^{-2}	9.19×10^{6}
	$\mathbf{0.80 \pm 0.05}$	52,725,554	5.86×10^{-3}	4.20×10^{6}	56,066,342	6.23×10^{-3}	4.46×10^{6}
Bright galaxies	$\mathbf{0.35 \pm 0.05}$	84,652,259	2.93×10^{-2}	6.74×10^{6}	87,599,150	3.03×10^{-2}	6.97×10^{6}
	$\mathbf{0.55 \pm 0.05}$	51,431,683	9.06×10^{-3}	4.09×10^{6}	53,406,408	9.41×10^{-3}	4.25×10^{6}
	$\mathbf{0.80 \pm 0.05}$	3,302,610	3.67×10^{-4}	2.63×10^{5}	3,581,404	3.98×10^{-4}	2.85×10^{5}
Faint galaxies	$\mathbf{0.35 \pm 0.05}$	19,848,022	6.86×10^{-3}	1.58×10^{6}	10,869,529	3.76×10^{-3}	8.65×10^{5}
	$\mathbf{0.55 \pm 0.05}$	84,989,583	1.50×10^{-2}	6.76×10^{6}	93,461,750	1.65×10^{-2}	7.44×10^{6}
	$\mathbf{0.80 \pm 0.05}$	58,350,416	6.48×10^{-3}	4.64×10^{6}	61,392,659	6.82×10^{-3}	4.89×10^{6}
Source galaxies	$\mathbf{1.0 \pm 0.1}$	58,903,889	3.28×10^{-3}	4.69×10^{6}	64,311,850	3.58×10^{-3}	5.12×10^{6}

TABLE 4.1: Table with all the galaxy: count number, number density and angular density; for each sample and gravity simulation.

only the central galaxies of the halos, 3) a red galaxy sample, 4) a blue galaxy sample, 5) a faint sample, selected by imposing a magnitude cut, $23 < r < 24$, 6) a bright sample, obtained with a relative magnitude cut of $r < 22.5$. For the color and central/satellite classification, *CosmoHub* already has this information for each galaxy for both catalogs. The color classification is defined using a $g - r$ cut [47]. In table 4.1 we present the number of galaxies and number densities for both catalogs for each galaxy sample and redshift bin.

4.6 Methodology

In this section we specify how we calculated the E_G estimator for both catalogs (F5 y GR). The expression in Eq. 4.23 cannot be directly calculated since the quantities involved correspond to fields. A good alternative is to use the 3D power spectrums to estimate E_G with observables [122, 152]:

$$\hat{E}_G(k,z) = \frac{c^2 \hat{P}_{\nabla^2(\psi-\phi)g}(k,z)}{3H_0^2(1+z)\hat{P}_{\theta g}(k,z)}, \tag{4.35}$$

where $P_{\nabla^2(\psi-\phi)g}$ is the galaxy and gravitational potential perturbations cross-power spectrum, $\nabla^2(\psi-\phi)$, and $P_{\theta g}$ is the galaxy-peculiar velocity cross-power spectrum, while the hats denote estimates based on observable quantities. We can already tell that the estimator does not depend on the galaxy bias since $\hat{P}_{\theta g} \propto b_g$ and $\hat{P}_{\nabla^2(\psi-\phi)g} \propto b_g$ as well. From Eq. 4.26 we get that:

$$\nabla^2(\psi - \phi) = \frac{3}{2} H_0^2 \Omega_{m,0}(1+z)\mu(k,a)[\gamma(k,a)+1]\delta \tag{4.36}$$

which fortunately is true for both GR and $f(R)$ so we can change the divergence velocity-galaxy correlation by: $\langle \nabla^2(\psi-\phi)g \rangle \propto \langle \delta g \rangle \propto \langle \kappa g \rangle$, where κ is the convergence, which is an actual observable unlike δ. Later we will perform the connection between this two properties when building the final expression for the E_G. Projecting 3D power spectra into angular quantities, we can estimate E_G as:

$$\hat{E}_G^{\ell}(z) = \frac{2c^2\hat{C}_{\ell}^{\nabla^2(\psi-\phi)g}}{3H_0^2\beta\hat{C}_{\ell}^{gg}}, \tag{4.37}$$

where $\hat{C}_{\ell}^{gg}$ is the angular auto-power spectrum of the galaxy sample, while $\hat{C}_{\ell}^{\nabla^2(\psi-\phi)g}$ is gravitational potential perturbations-galaxy cross-spectrum and $\beta = f/b_1$ (since this is the continuity equation to linear order $\theta = -\beta\delta_g$) is derived from a RSD analysis at the same effective redshift as the auto-correlation. The correlation in the denominator comes from the approximation $\hat{P}_{\theta g}(k,z) = \beta\hat{P}_{gg}(k,z)$. Under the limber approximation, the angular power spectra can be expressed as:

$$\hat{C}_{\ell}^{\nabla^2(\psi-\phi)g} = \frac{1}{2}\int \mathrm{d}z \frac{H(z)}{c(1+z)}\frac{W_g^2(z)}{\chi^2(z)}\hat{P}_{\nabla^2(\psi-\phi)g}(k,z). \tag{4.38}$$

$$C_{\ell}^{gg} = \int \mathrm{d}z\, \frac{H(z)}{c}\frac{W_g^2(z)}{\chi^2(z)}P_{gg}\left(k = \frac{\ell+1/2}{\chi(z)}, z\right), \tag{4.39}$$

$$C_{\ell}^{\kappa g} = \int \mathrm{d}z\, \frac{W_\kappa(z)W_g(z)}{\chi^2(z)}P_{\delta g}\left(k = \frac{\ell+1/2}{\chi(z)}, z\right), \tag{4.40}$$

the last term is the convergence-galaxy or lensing angular power spectrum. The terms $W_g(z)$ and $W_\kappa(z)$ are the window function for the galaxy sample and lensing respectively and $\chi(z)$ is the comoving distance. These kernels are given by:

$$W_g(z) = \frac{\mathrm{d}N}{\mathrm{d}z}. \tag{4.41}$$

$$W_\kappa(z, z_\mathrm{S}) = \frac{3H_0^2\Omega_{\mathrm{m},0}}{2c^2}\hat{W}_\kappa(z, z_\mathrm{S}) \tag{4.42}$$

$$\hat{W}_\kappa(z, z_\mathrm{S}) \equiv (1+z)\chi(z)\left(1 - \frac{\chi(z)}{\chi(z_\mathrm{S})}\right). \tag{4.43}$$

From Eqs. 4.40 and 4.39 we can tell that the dependence on the galaxy bias still cancel out in angular notation. We have that $\hat{P}_{gg} \propto b_g^2$ and $\hat{P}_{\delta g} \propto b_g$, while the β term adds an extra galaxy bias on the numerator. This bias needs to estimated in such a way that is consistent with the C_ℓ's. The effective redshifts of auto- and cross-correlations for the same galaxy sample generally differ, which may introduce a bias in the estimation of E_G. The effective redshifts for the auto and cross-correlation are given by the following expression [38, 152]:

$$z_{\mathrm{eff}}^{\mathrm{cross}} = \frac{\int \mathrm{d}z\, \chi^{-2}\hat{W}_\kappa(z)W_g(z)z}{\int \mathrm{d}z\, \chi^{-2}\hat{W}_\kappa(z)W_g(z)}, \tag{4.44}$$

$$z_{\mathrm{eff}}^{\mathrm{auto}} = \frac{\int \mathrm{d}z\, \chi^{-2}(z)H(z)c^{-1}W_g^2(z)z}{\int \mathrm{d}z\, \chi^{-2}(z)H(z)c^{-1}W_g^2(z)}. \tag{4.45}$$

We follow the same methodology than in [152] and we equate the effective redshift by weighting the galaxy sample of the cross-correlation using:

$$W_g^* \equiv \frac{\mathrm{d}N^*}{\mathrm{d}z} = \frac{\mathrm{d}N}{\mathrm{d}z} w_\times(z) \tag{4.46}$$

with:

$$w_\times(z) = W_g \frac{1}{\hat{W}_\kappa(z) I}, \tag{25}$$

where:

$$I = \int \mathrm{d}z \frac{W_g^2(z)}{\hat{W}_\kappa(z)}, \tag{4.47}$$

where I is selected to normalize the weighted galaxy distribution $\int W_g^* dz = 1$. Following still the steps in [152] , we use this re-weighting and get express Eq. 4.37 as,

$$\begin{aligned} \hat{C}_\ell^{\nabla^2(\psi-\phi)g} &\approx \frac{H(z_{\rm eff})I}{c} \left[\int \mathrm{d}z \frac{\hat{W}_\kappa(z) W_g^*(z)}{\chi^2(z)} \hat{P}_{\kappa g}(k,z) \right] \\ &= \frac{H(z_{\rm eff})I}{c} C_\ell^{\kappa g *}, \end{aligned} \tag{4.48}$$

where we have used that $W_g^*(z) = W_g(z) w_\times(z)$ and $\hat{P}_{\nabla^2(\psi-\phi)g} \approx \hat{P}_{\kappa g}$, which holds for both GR and $f(R)$ (Eq. 4.36). Here, the term $C_\ell^{\kappa g *}$, equivalent to the expression in brackets in Eq. 4.48, represents the cross-correlation measurement using the reweighted galaxy sample. The term $H(z)$ is moved outside the integral as it varies slowly over the redshift sample.

The final estimator for E_G is given by [152]:

$$\hat{E}_G^\ell(z_{\rm eff}) \approx \Gamma(z_{\rm eff}) \frac{C_\ell^{\kappa g *}}{\beta C_\ell^{gg}}, \tag{4.49}$$

where:

$$\Gamma(z_{\rm eff}) \equiv \frac{2cH(z_{\rm eff})}{3H_0^2} \int \mathrm{d}z \frac{W_g^2(z)}{\hat{W}_\kappa(z)}, \tag{4.50}$$

and $z_{\rm eff}$ is the effective redshift of the observables as defined by Eq. 4.45.

In Figure 4.3 we can appreciate how the $f(R)$ boost on C_ℓ^{gg} is the same than in $C_\ell^{\kappa g}$ for any redshift. This confirms the theoretical prediction from Eq. 4.32 since the MG boost will cancel out on Eq. 4.49 leaving all the discrepancy with GR on the growth rate. For the $f(R)$ model however, re-weighting the C_ℓs does not change the fact that the E_G estimator is only sensitive to the underlying gravity model through the growth rate (i.e, is not sensitive to the ratio between the galaxy-lensing cross-correlation over the galaxy auto-correlation).

This definition of the E_G estimator is the one considered more accurate until now as claimed by [152] when taking observable quantities. Previous to this work, most analysis were using the expressions found by [122] and [123], where they average the redshift instead of using the

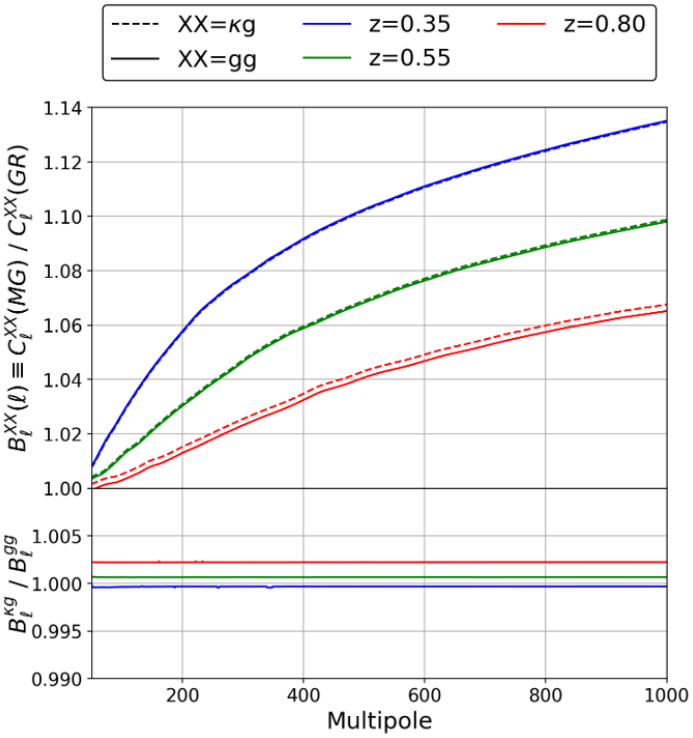

FIGURE 4.3: F5 boost (B_ℓ ratio, analogous to Eq. 4.11 impact on the C_ℓs for auto-galaxy correlation (continuous line) and convergence-galaxy cross-correlations (dashed line) for the 3 redshifts bins. In the plot below, we have the ratio between the dashed and continuous line above for each z. We can appreciate how the boost is practically the same for each case. The theoretical C_ℓs from the plots are obtained with *pyCCL*. The F5 boost, implemented on the 3D matter power spectrum, is calculated with *e-mantis* using a F5 gravity

more accurate effective redshift. [123] proposes a correction term but it can only be obtained numerically using N-body simulations. Without this correction the estimated value was differing a 5% from the predicted value for E_G.

[152] already compared the accuracy of Pullen and their own estimator and showed that their estimator has an accuracy better than 3% on all scales. We also calculate the relative difference between the analytic value calculated with Eq. 4.27 and the value obtained with theoretical predictions from *pyCCL* using Eq. 4.49. To calculate the C_ℓs and Γ, Eq. 4.50, we use the fiducial values of the simulations, the n(z) from our full sample for GR and F5 respectively and, since the linear galaxy bias is irrelevant for E_G, we leave the default value of 1. For the F5 calculation we use *e-mantis* [138] to estimate the C_ℓs boost, although as shown in Figure 4.3 this is also irrelevant when doing the ratio, and *MGrowth* to estimate the scale dependent growth rate. The Pullen estimator is calculated following Eq.(16) from [123] where they use $C_\ell^{\kappa g}$ instead of $C_\ell^{\kappa g *}$ and a different Γ which does not take into account the effective redshift. In Figure C.1 we show the accuracy results and we find that evidently, the Wenzl estimator is more accurate than the one by Pullen. It depends on the redshift, but in the two extreme cases the relative difference for the Pullen estimator is doubled over the relative difference of the Wenzl estimator. One thing that we notice is that the accuracy gets worse as we go to higher redshifts, although for the Wenzl estimator the difference does not surpass the 2%.

In the following sections we detail the calculation of all the components needed to calculate the E_G from expression 4.49.

4.6.1 Linear galaxy bias

The linear galaxy bias $b_g \equiv b_1$, can be obtained from the RSD analysis using clustering multipoles. But since we want to break as much as possible the degeneracy of the parameters on the RSD analysis we estimate the linear galaxy bias in a separate step in order to obtain an estimate of b_1 that we can use to constraint the values on the RSD analysis.

In order to estimate the galaxy bias, we calculate the galaxy angular auto-correlation and compare with theory predictions from the public code *pyCCL*[2].

The calculation of the galaxy angular auto-correlation is performed with the routine *anafast* from the HEALPY[3] package. For each sample (case, redshift, catalog) we generate a HEALPix map with an nside=1024 where each pixel corresponds to:

$$\delta = \frac{n_{pix} - \bar{n}}{\bar{n}} \tag{4.51}$$

where n_{pix} is the number of galaxies that fall inside that pixel, while $\bar{n}$ is the mean galaxy value of all the pixels. Although we are working with full sky, which would indicate that we do not need any mask, we still generate 100 masks to define Jackknife regions. Each Jackknife mask extracts a different 1/100 same size region of the sky for which we use a k-means algorithm called *kmeans-radec*[4] to select the regions. The C_ℓs are calculated with the software POLSPICE[5] for each Jackknife region using a corresponding *pixelwindow* for the given nside. POLSPICE calculates the C_ℓs for each individual ℓ, but this is normally very noisy so we average the signal by binning the results in equidistant bins of $\Delta\ell = 20$ between $\ell_{min} = 30$ and $\ell_{max} = 1024$. We subtract the shot noise to the binned values using:

$$n_{shot} = \frac{4\pi}{n_{gal}} \cdot \frac{1}{\text{pixelwindow}(\ell)^2}, \tag{4.52}$$

which is the standard definition of area/n_{gal}, with n_{gal} being the total number of galaxies (see Table 4.1) and the area is given by the full sky (4π radians) with a correction by the pixel window to be consistent with the correction done to the C_ℓs.

The binned values are then averaged over each Jackknife region to obtain the final $C_\ell^{gg}s$, while the Jackknife covariance matrix is given by:

$$\sigma^2_{ij}(C_\ell^{gg}) = \frac{N_{JK} - 1}{N_{JK}} \sum_{i,j=1}^{N_{JK}} [C_\ell(\ell)_i - \bar{C}_\ell(\ell)][C_\ell(\ell)_j - \bar{C}_\ell(\ell)] \tag{4.53}$$

[2] https://github.com/LSSTDESC/CCL/blob/master/readthedocs/index.rst
[3] https://healpy.readthedocs.io/
[4] https://github.com/esheldon/kmeans_radec
[5] https://www2.iap.fr/users/hivon/software/PolSpice/

where the top bar indicates the mean value over all the Jackknife regions while the suffix i, j indicates i, j-region calculated C_ℓ.

Using the code *pyCCL* we obtain the prediction using the fiducial cosmology of the mocks since we wish to only estimate the galaxy bias in this step to have the best constraints possible. We use the CAMB code to compute the transfer function and the non-linear power spectrum given by Halofit [140]. The n(z) for the prediction are obtained from the same sample and it is binned in 15000 equidistant z-bins in order to have a precise definition of the n(z). We integrate the C_ℓs exactly, ie, without the Limber approximation in order to have a more accurate estimation on linear scales.

The linear galaxy bias is estimated as:

$$b_1 = \sqrt{\frac{C_\ell^{gg}}{C_\ell^{\delta\delta}}} \tag{4.54}$$

where $C_\ell^{\delta\delta}$ is the matter angular power spectrum. We can obtain the covariance matrix of b_1 directly since we do not assign any error to $C_\ell^{\delta\delta}$. With the covariance matrix we can estimate the bias as the E value that minimizes the following χ^2 since we assume the Jackknife errors to be Gaussian:

$$\chi^2 = (\bar{b_1} - E)^T(\sigma_{ij}^2(b_1)[\ell_{min} : \ell_{max}])^{-1}(\bar{b_1} - E) \tag{4.55}$$

where $\bar{b_1}$ is the mean value of b_1 given by Eq. 4.54 in the region $[\ell_{min} : \ell_{max}]$ considered. The ℓ_{min} is fixed at $\ell = 50$ while ℓ_{max} will depend on the redshift since we need to consider only linear scales. For z=0.8 we estimate the ratio between C_ℓ^{gg} and $C_\ell^{\delta\delta}$ deviates significantly from the linear model at $\ell \approx 500$ from which we extract that the wave-number $k_{lin} < 0.119h^{-1}$Mpc by using the small-angle approximation $k \approx \ell/\chi_d(z)$ where χ_d is the commoving distance. Similarly, at z=0.35 and z=0.55 we obtain a l_{max} of 250 and 372 respectively. The values of b_1 obtained for each sample are shown in Table 4.2, while the individual ratios for the Full Sample are shown in Figure 4.4. The errors are given by the 1-σ error, i.e. $\mathcal{O}(b_1) = |b_1(\chi^2_{\rm min}) - b_1(\chi^2_{\rm min} \pm 1)|$

For the F5 mock data, we use the emulator *e-mantis* to apply the $f(R)$ boost, with $|\bar{f_{R0}}| = 10^{-5}$, to the matter power spectrum at each n(z) bin from which the C_ℓs are calculated. We also perform an extra case were we assume that the F5 mock follows GR and we estimate b_1 without using the boost for this mock. As we can see in 4.2 this does not apply any change on the linear galaxy bias which makes sense since the boost is only noticeable at smaller non-linear scales (see Figure 4.1 or Figure 4.3). We also notice that the galaxy bias on GR is usually significant larger than F5. The clustering is stronger in F5 so the galaxy bias is lower to compensate in order to get a similar amplitude consistent with the simulation calibration.

4.6.2 Multipoles of the correlation function

The growth rate is completely degenerated with σ_8 when only taking into account the angular power spectrum [152]. The multipoles of the correlation function can break this degeneracy. Using only the monopole ($\ell = 0$) and the quadrapule ($\ell = 2$) is enough to break the degeneracy with the linear galaxy bias. Although the hexadecapole ($\ell = 4$) further breaks this

Case	z=0.35	z=0.55	z=0.8
All F5	1.047 ± 0.004	1.104 ± 0.003	1.305 ± 0.002
All GR	1.077 ± 0.004	1.147 ± 0.003	1.353 ± 0.002
Central F5	0.778 ± 0.003	0.856 ± 0.002	1.185 ± 0.002
Central GR	0.815 ± 0.004	0.895 ± 0.002	1.213 ± 0.002
Red F5	1.246 ± 0.006	1.342 ± 0.004	1.393 ± 0.003
Red GR	1.282 ± 0.006	1.441 ± 0.004	1.639 ± 0.003
Blue F5	0.830 ± 0.004	0.888 ± 0.002	1.140 ± 0.002
Blue GR	0.825 ± 0.004	0.900 ± 0.002	1.158 ± 0.002
Bright F5	1.057 ± 0.004	1.196 ± 0.003	1.705 ± 0.004
Bright GR	1.090 ± 0.004	1.233 ± 0.003	1.780 ± 0.004
Faint F5	1.047 ± 0.004	1.041 ± 0.003	1.232 ± 0.002
Faint GR	1.067 ± 0.004	1.086 ± 0.003	1.278 ± 0.002
All (F5 assumed as GR)	1.047 ± 0.004	1.104 ± 0.003	1.305 ± 0.002

TABLE 4.2: Linear galaxy bias values and standard deviation for all the different cases studied.

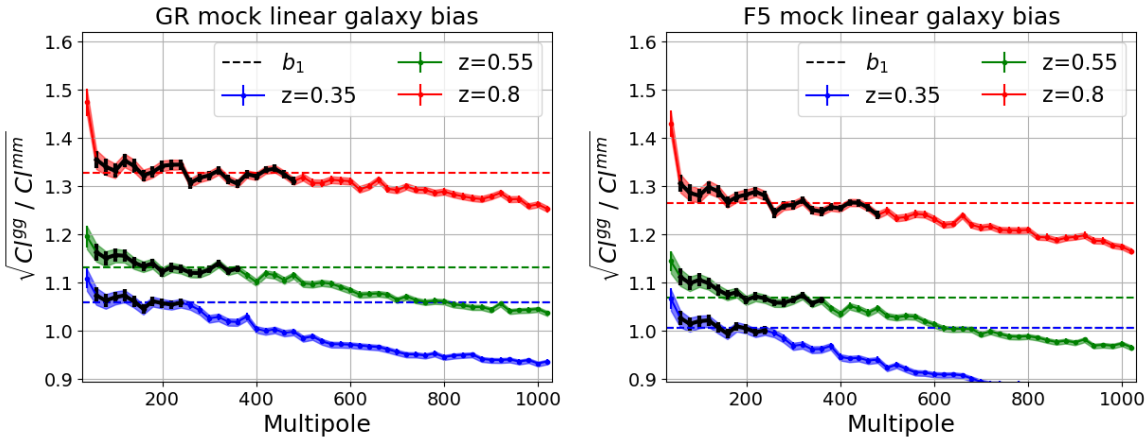

FIGURE 4.4: Linear galaxy bias estimated as root squared ratio of of the galaxy-galaxy and matter-matter C_ℓs, the latter obtained with *pyCCL* (and also *e-mantis* for F5) for the three redshifts bins using the full sample. The black lines show the linear regions we have considered to estimate the linear galaxy bias. The dashed lines show the value of the estimated linear galaxy bias for each redshift using χ^2 minimization. The left plot shows the results for the GR mock while the right plot for the F5 mock. The errorbars are given by 100 Jackknife regions. The shaded areas correspond to the theoretical Gaussian error.

degeneracy with additional information, we have decided to leave this contribution out of the analysis as its measurement in our mocks turns out to be very noisy in practice.

We calculate the multipoles using the recent code Fast-Correlation-Function-Calculator [161] due to its high calculation speed. Even though the code allows the direct calculation of the even multipoles we decide to calculate the 2D anisotropic correlation function $\xi(r, \mu)$ since this will be useful to calculate the Jackknife error. The parameter μ represents the cosine of the angle between the line of sight direction and the direction between the galaxy pairs.

We use 20 radial projected bins with a $s_{min} = 0.5\ Mpc/h$ and a $s_{max} = 200\ Mpc/h$. We use 200 bins on the μ parameter which goes from [0, 1] since the code only calculates even multipoles which are symmetric, which means that Eq. 2.91 should be multiplied by 2.

Similarly to the linear galaxy bias, the errors are calculated using $N_{jk} = 100$ Jackknife resampling of the data. We use once again the code *kmeans-radec* to generate 100 equidistant regions on the sky and we assign each galaxy to a region. In order to speed up the calculation instead of performing the calculation of each individual Jackknife region we take a different approach. We calculate the $\xi(r, \mu)$ correlation of the full dataset with each individual region, i.e. each region that is subtracted from each Jackknife region, we then subtract the pair count of this crosscorrelation from the full dataset auto-correlation. We also have to do the same for the random dataset, which we generate with a quantity of 2 times the data. Since we are using the full Landy-Szalay estimator [103] we also need to subtract the cases for the DR terms, where D corresponds to the data and R to the randoms. The final estimator for each Jackknife region would be given by:

$$\xi(r,\mu)_{N_i} = \frac{(DD - DD_i) - (2DR - DR_i - D_iR) + (RR - RR_i)}{(RR - RR_i)} \tag{4.56}$$

where the suffix on D_i (and R_i) correspond to the data (random data) of the region i not included on Jackknife region N_i. Each set of pairs in expression 4.56 are normalized by dividing individually the total number of pairs for the total number of data points, in this case galaxies, of each dataset that compose the pair. This method has allow us to calculate the Jackknife errors fairly quick by not having to repeat several common pairs in each region.

Since calculation are done in configuration space the definition of the multipoles is given by:

$$\xi_\ell(r) = \frac{(2\ell + 1)}{2} \int_{-1}^{1} \xi(r,\mu) P_\ell(\mu) d\mu \tag{4.57}$$

where P_ℓ is the Legendre polynomial of degree ℓ. The Jackknife covariance matrix is obtained in a similar fashion than in the previous section.

In Figure 4.5 we show the Jackknife covariance matrix for the GR mock at z=0.55 for the joint monopole and quadrupole. We will also fit the results using a Gaussian theoretical covariance matrix, also shown in the same figure, obtained with the code BeXiCov[6] with the same simulation volume and particle density. We can check that both matrices are similar, specially when considering the global amplitude, which is a good indicator that the Jackknife resampling was correctly generated. Both matrices are very close to be singular which may complicate the inversion for likelihood determination. We find that despite this, both matrices can be properly inverted using the python module *mpmath*[7]. Although we find that the theoretical covariance, which is more close to singular than the Jackknife one, have complications to correctly estimate the likelihood of the chains so we needed to apply a negligibly perturbation of a 0.1% increase to the diagonal elements. We have checked that using the SVD and Cholesky decompositions does not improve this, and we need to add this same small perturbation to the diagonal elements to be able to invert the covariance matrix.

[6] https://gitlab.com/esarpa1/BeXiCov/-/tree/main
[7] https://mpmath.org/

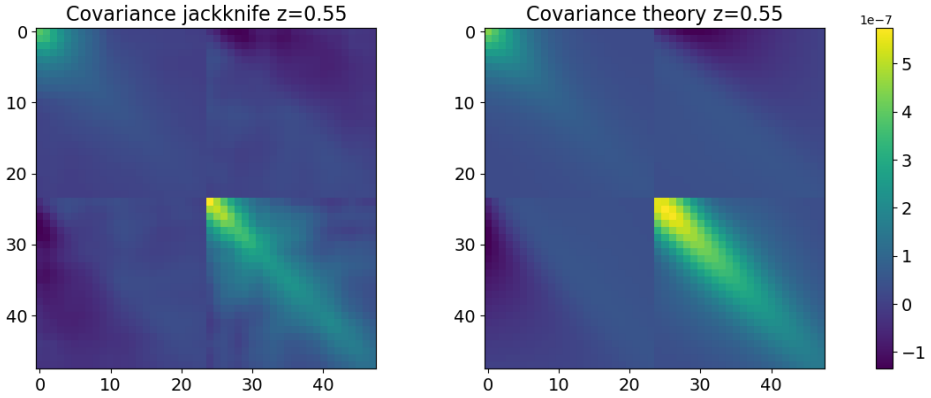

FIGURE 4.5: Monopole-quadrupole joint covariance matrix of the multipoles of the correlation function for the GR mock z=0.55 all galaxies case. The values are in configuration space and the bins represent the 24 linear s-bins chosen for the full range $[20, 140]$Mpc/h. Left figure shows the Jackknife covariance obtained from the data while the right plot shows the theoretical Gaussian covariance obtained with BeXiCov.

4.6.3 Estimating the growth rate using MCMC

With the multipoles calculated, we need a method to compare them to theoretical predictions in order to parametrize the growth rate and the galaxy bias. As previously mentioned, we use the VDG model implemented in COMET-EMU [60] to obtain a reliable estimate of nonlinear effects. Our goal is to calculate the growth rate at both large and small scales to test for scale dependence in $f(R)$ gravity. We also perform the calculation on both scales on GR in order to check that there is no scale dependence in this case as expected which would validate our methodology. For F5, we simply multiply the final multipoles by the boost provided by *e-mantis* at the respective redshift z. However, since *e-mantis* only calculates the boost for the dark matter power spectrum, we are uncertain whether it can be directly applied to the final multipoles, which account for galaxies and RSD effects. Unfortunately, COMET does not allow the input of a custom matter power spectrum outside of those already incorporated into the code, which limits our ability to modify this aspect of the analysis. However, we expect the approach to perform well as an approximation. Looking at appendix 2.5.1 and the final expression for the multipoles wedges, Eq. 2.86, it appears that the relationship remains linear with the matter power spectrum, as the galaxy power spectrum terms, Eq. 2.78, are also linear with the matter power spectrum. The final expression for the multipoles, Eq. 2.91, integrates the wedges over the angle μ, but since the boost is independent of μ, we can simply exclude it from the integral.

Estimating the growth rate at small scales can be quite challenging since we do not have many data points to work with and there are more parameter degeneracy due to the higher amount of non-linear parameters on top of linear ones that affect all scales. For this reason we try to constraint as many parameter as we can like the linear galaxy bias in the previous section. Fortunately COMET-EMU let us work with a reduced parameter space from which we select the following:

- $\mathbf{b_1}$: We will use a Gaussian prior centered on the value of the linear galaxy bias calculated with the C_ℓs and with a deviation given by the obtained standard deviation of the measurements. Although we also tried to set it as a free parameter between [0.5,2] which did not produce significant changes on the posteriors.

- **f** : Since the growth rate is the parameter of interest, we leave this parameter as completely free between the broad limits of the emulator ([0.5, 2]).
- σ_{12} : Since we are not assuming a cosmological model with COMET-EMU for any of the mocks we can leave this parameter as a free parameter. Although in the final setup we ended up fixing this value to the fiducial value of the mocks, which is similar to what [30, 152] did in order to avoid degeneracies between f, b_1 and σ_8. For $f(R)$ this should not be a problem as mentioned in a footnote in [138] the σ_8 (and consequently σ_{12}) are considered the same for both ΛCDM and $f(R)$.
- $\mathbf{b_2}$: The second order bias can be estimated from the C_ℓs using non-linear models like Eulerian or Lagrangian Perturbation theory. In some other analysis, is set with a Gaussian prior centered at 0 with a variance of 1. We tried some of these approaches, but we decided to leave it as a free parameter (between [-2, 2]) since we have checked our analysis are robust to different choices for the prior range used.
- γ_2, γ_{21} : The tidal biases are highly non-linear parameters, that in most cases are completely degenerated with b_2 and between themselves. In GR exists a empirical relation with the linear galaxy bias [139]: $\gamma_2 = 0.524 - 0.547 b_1 + 0.046 b_1^2$ and $\gamma_{21} = (2/21)(b_1 - 1) + (6/7)\gamma_2 2$, which helps break the degeneracy. Originally, we tested that fixing the values of the tidal biases with the galaxy bias helped when using only the monopole and quadrupole, since otherwise the degrees of freedom (when not using the hexadecapole) seemed to be very small for the amount of parameters and we obtained many projection effects between the biases. Although when we fixed the value of σ_{12}, the degeneracies with or without fixing the values of the tidal bias disappeared so we opted to leave them as free parameters since it is unclear whether these relations are valid for our MG model.
- $\mathbf{c_0}, \mathbf{c_2}, \mathbf{c_4}$: The counterterms are implemented to correct the assumption of a zero energy-stress tensor. So these parameters are defined as non-linear parameters but they actually affect significantly all scales depending on their value. Each c_i parameter affects mostly the corresponding $\ell = i$ multipole, while its effect on the other multipoles is negligible unless its value is extremely high. Since we opt to leave the hexadecapole out of the analysis we do not consider c_4, otherwise we add degeneracy to the other parameters.
- $\mathbf{a_{vir}}$: This parameter is exclusive to the VDG model and it is related to the virialized velocities. Since it only appears on Eq. 2.71 as a squared quantity, we define so we need only take positive values. We set the limits given by the emulator of [0, 8].
- $\mathbf{q_{lo}}, \mathbf{q_{tr}}$: The AP parameters quantify how well we recover the fiducial or input cosmological parameters used in our simulations.

We use the code MULTINEST to perform the MCMC fitting with 1200 live points, a sampling efficiency of 0.8 and an evidence tolerance of 0.01 (this settings are guided from previous analysis like [4]). As mentioned above, we do not use the hexadecapole since we considered to be very noisy so it would not bring much more additional information to our analysis. Although one last consideration is that COMET-EMU obtains predictions in Fourier scale (k-wavenumbers) and our data is in configuration space. Then we use the algorithm *hankl*[8] to convert the comet multipoles from Fourier space to configuration space using a Fast Fourier Transform for each evaluation:

[8] https://github.com/minaskar/hankl/blob/master/docs/source/index.rst

$$\xi_l(r) = i^l \int_0^\infty k^2 dk/(2\pi^2) P_l(k) j_l(kr) \tag{4.58}$$

where j_l are the Spherical Bessel function of order l. To avoid numerical instabilities in the above integral, the COMET multipoles are first smoothed by multiplying by the factor $\exp\left(-(k \cdot r_{\rm smooth})^2\right)$, where $r_{\rm smooth} = 0.25$ Mpc/h.

The reason behind using configuration space instead of Fourier space to compare directly with COMET are the stochastic terms (see sec. 2.5.1). In configuration space these terms disappear since they average out. This helps reducing the parameter space eliminating three terms: N_0^P, $N_{2,2}^P$, $N_{2,0}^P$. The first term N_0^P is completely degenerated with parameters like b_1 that control the full amplitude of the multipoles while the other two are partially degenerated with parameters that depend on the scale. We performed a quick test using *pypower*[9] to calculate the multipoles in Fourier space, but parameter fitting was unsuccessful due to the high amount of parameters. On top of that the multipoles in Fourier space that were obtained were very noisy at large scales which made parameter fitting more difficult. So we decided to continue our analysis only on configuration space despite other potential issues that this choice may bring, as we shall comment below.

For the small scale we select the data points from [20, 50] Mpc/h, while for the large scales we select the data points from [50, 140] Mpc/h for all redshifts. This leaves us with 6 data points for small scales and 18 data points for large scales. We performed some several tests by fitting the COMET parameters with a data vector (DV) generated with the COMET itself. We deduced that for small scales 6 data points were not enough, even in an idealized case like this, to correctly estimate and converge so many parameters. For this reason we came up with the following methodology: 1) We first perform a fit on the full range of scales [20, 140] Mpc/h with everything as a free parameter but b_1, which contains a Gaussian prior from the C_ℓs as detailed earlier, and s_{12} which is fixed to the fiducial value, 2) then we use the obtained values for b_1, b_2, γ_2, γ_{21}, c_0 and c_2 as Gaussian priors, with their corresponding standard deviation as the variance of the Gaussian, for the parameters of large and small scale fits. Using the COMET DV we obtained good results using this methodology so it is the one we use for the final setup.

4.6.4 Calculating the lensing power spectrum

Having C_ℓ^{gg} already calculated when estimating the linear galaxy bias, the last ingredient to calculate the E_G estimator is the $C_\ell^{\kappa g*}$ corresponding to the weighted lensing angular power spectrum defined in Eq. 4.48.

The procedure is the same than when calculating the C_ℓ^{gg}, with similar HEALPix maps and Jackknife regions. In this case we are dealing with a cross-correlation of the source sample at z=1.0 (see Table 4.1) with a $\Delta z = 0.2$. We have chosen this particular source z-bin as a working example, but we do not expect our main results to change significantly by selecting another source sample. The convergence κ is directly obtained from the catalog for each galaxy and it is averaged on each pixel as the average convergence value of all the galaxies inside that pixel.

[9] https://github.com/cosmodesi/pypower

Since we are using the weighted estimator $C_\ell^{\kappa g*}$ from [152] Eq. 4.48 we have to account for re-weighting of the galaxy sample. For that we just calculate $w_\times(z)$ using Eq. 25 and we assign to each source galaxy a weight corresponding to $w_\times$ (since it is already normalized by definition) at its respective z. Then we proceed as in sec. 4.6.1 where n_{pix} Eq. 4.51 is given by the average value of the weight of all the galaxies inside that pixel, the same goes to $\bar{n}$.

Since we are dealing with a cross correlation this time we need not subtracting any kind of shot noise.

4.6.5 Calculating the E_G estimator

In order to combine the previous observables that comprise the E_G estimator we use a similar approach than in [152] with the ratio distribution. As mentioned in that reference, the ratio between Gaussian values (Jackknife resampling, which mostly contains Gaussian sample variance directly from the data) it is not guaranteed to be also Gaussian so it is convenient to do the ratio distribution. They perform a double ratio distribution by first combing the angular power spectra as:

$$R \equiv \Gamma C_\ell^{\kappa g*}/C_\ell^{gg}, \tag{4.59}$$

which includes the Γ parameter, Eq. 4.50, which we treat as factor without attributed error, just like [152]. Then the second ratio distribution is perform by combining R with the RSD parameter as $R/\beta \equiv \hat{E_G}$. We instead perform only one ratio distribution since we directly combine the observables $C_\ell^{\kappa g*}/C_\ell^{gg}$ given that we use the same collection of Jackknife masks for each kind of C_ℓ. In this regard, we are actually doing the ratio in each Jackknife region and then obtaining directly the Jackknife variance for this ratio. This a luxury that [152] could not afford since they did not have enough area to calculate the Jackknife properly they had to resort to the theoretical Gaussian covariance estimate. Then the probability distribution of the E_G estimator is given by the ratio distribution of $\beta \equiv f/b_1$ and $R \equiv \Gamma C_\ell^{\kappa g*}/C_\ell^{gg}$. The ratio distribution is then:

$$p_{\hat{E}_G}(\hat{E}_G|\hat{C}_\ell^{\kappa g}, \hat{C}_\ell^{gg}, \beta) = \int \mathrm{d}\beta' |\beta'| p_R(\hat{E}_G \cdot \beta') p_\beta(\beta'), \tag{4.60}$$

where p_R is considered a multivariate Gaussian distribution with mean given by $\overline{\left(\frac{C_{\ell,i}^{\kappa g}}{C_{\ell,i}^{gg}}\right)}$ calculated with the $N_{\rm JK} = 100$ regions for each of the i ℓ-bins. The variance of this distribution is given by:

$$\sigma_{ij}^2 = \frac{N_{\rm JK}-1}{N_{\rm JK}} \sum_{i,j=1}^{N_{\rm JK}} \left[\frac{C_{\ell,i}^{\kappa g}}{C_{\ell,i}^{gg}} - \overline{\left(\frac{C_{\ell,i}^{\kappa g}}{C_{\ell,i}^{gg}}\right)}\right] \left[\frac{C_{\ell,j}^{\kappa g}}{C_{\ell,j}^{gg}} - \overline{\left(\frac{C_{\ell,j}^{\kappa g}}{C_{\ell,j}^{gg}}\right)}\right] \tag{4.61}$$

4.7 Results

In this section, we provide the final results for the E_G estimator and the observables that comprise it for each sample analyzed in this study.

4.7.1 Angular power spectrum ratio

Below we discuss how we compute the parameter R, defined in Eq. 4.59. The Γ parameter, Eq. 4.50, uses the n(z) computed from the mock catalogs, that enters in the calculation of W_g. For the rest of parameters we use the fiducial values of the simulation to set H_0, $H(z_{\rm eff})$ and to calculate the comoving distances needed for W_κ. The mean effective redshifts for the samples at $z = [0.35, 0.55, 0.8]$, are, respectively, $z_{\rm eff} = [0.353, 0.546, 0.791]$. We obtain the same results using Eqs. 4.44 and 4.45. In view of this, we do not assign any additional theoretical error to the value of Γ in relation to the total error budget of E_G.

In order to build the E_G estimator, we decompose it in two different contributions. The first involves the ratio of (real space) angular power spectra, as given by Eq. 4.59, and a second term given by the linear growth rate. Focusing on the first of these contributions, we have already shown above the results for the galaxy auto-correlation, C_ℓ^{gg}, when calculating the linear galaxy bias in Figure 4.4. We then include the cross-correlation between source shears and lens galaxy positions, $C_\ell^{\kappa g}$, to estimate the ratio estimator, R. More interestingly, we can define a (linear) galaxy-bias independent estimator, $R_b \equiv b_1 R$, where the linear galaxy bias, b_1, is estimated using the full range of scales (within the scale-cuts used, see Fig 4.4). Within the approximation that the galaxy bias is linear (for the range of scales considered here) R_b does not depend on scale for both gravity models used (F5 and GR). This is shown in Figure 4.6 where most measurements of R_b are within errors for all redshift bins explored, and thus consistent with the theory prediction. At larger scales the values fluctuate more due to the sample variance which in turn increases the error-bars.

On the other hand, using our small-scale cut set in configuration space, $s_{min} = 20$ Mpc/h, we can define the corresponding largest multipole at each redshift bin. Using Eqs. 4.20 and 4.21, we get $\ell \approx [150, 225, 300]$ at z=[0.35, 0.55, 0.8]), respectively. We assume that within the resulting multipoles ranges (see Figure 4.4), the galaxy bias is approximately linear, what is in agreement with the fact that we observe no deviation from a scale-independent behavior for the ratio estimator, R_b (see Figure 4.6). We note that this is consistent with our assumption that our E_G gravity estimator is also defined on linear scales. The observed multipole bin-to-bin fluctuations largely cancel out when taking the average over the range of scales of interest (i.e., for the used split in the so-called" large" or "small" scales in the plot). In fact, the statistical average for R_b follows a ratio distribution (see Eq. 4.60) with $\beta = 1/b_1$. Although we see that for F5, in the low redshift bins, some small-scale values tend to be above the theory prediction beyond the 1-σ errors, overall the measurements agree with theory.

The errors attributed to R_b come mostly from the C_ℓ^{kg}, since b_1 and C_ℓ^{gg} have negligibly small uncertainties. In particular, the statistical errors scale with the lensing efficiency (see Eq. 4.43), i.e, the larger the lensing signal, the smaller the errors in C_ℓ^{kg}, and vice versa. Given that we choose our source sample at $z = 1.2$, i.e, at a distance ≈ 2600 Mpc/h, the lensing efficiency peaks at half this distance, ≈ 1300 Mpc/h. Therefore, given that the lens planes for the three redshift bins ($z = [0.35, 0.55, 0.8]$) are located at $\approx [960, 1430, 1940]$Mpc/h respectively, the highest z-bin has about a factor of 2 lower signal and correspondingly larger statistical error in its measurement of the C_ℓ^{kg}. In turn this reflects in a larger error in R_b, as shown in Fig 4.6.

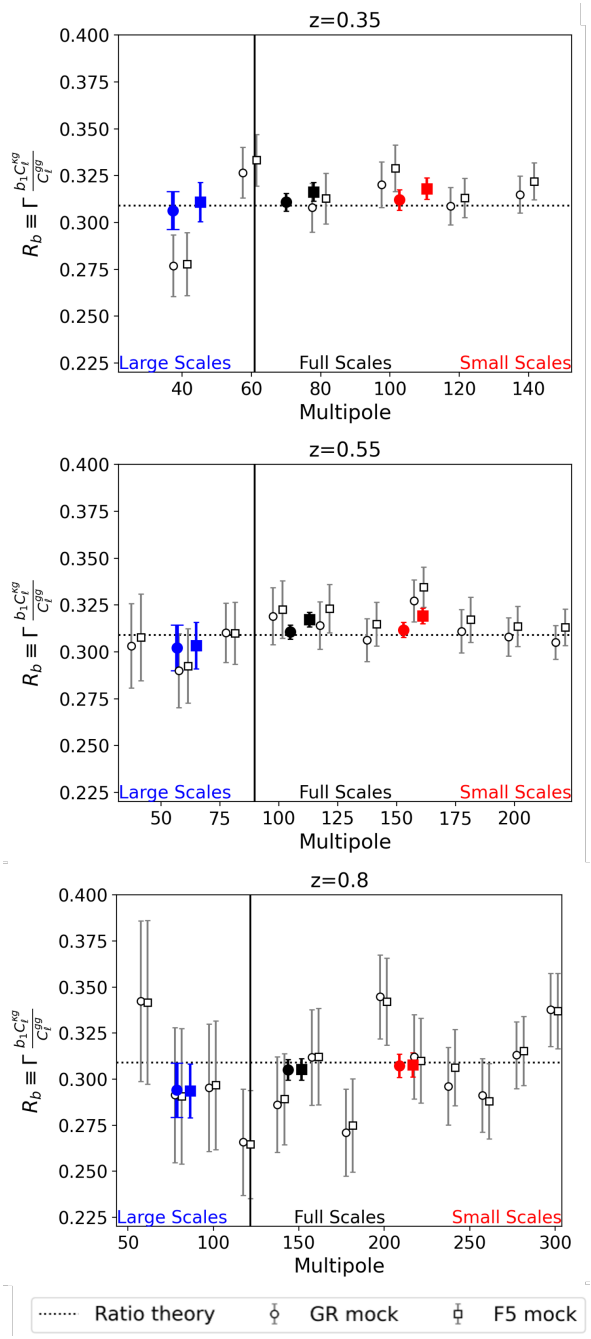

FIGURE 4.6: Results for the growth rate independent part of the E_G estimator for the all galaxies case. The white filled data points show the values at which the C_ℓs are binned. The black, blue, and red data points represent the full, large and small scales mean result, respectively. The solid vertical black line represents the scale at which we separate the small and large scales.

4.7.2 RSD β parameter fitting results

The redshift space contribution to the E_G estimator is given by the linear growth rate-related quantity, β, see Eq. 4.49, which is a derived parameter. It is calculated from the fitted posterior distributions for the linear galaxy bias, b_1, and the linear growth rate, f, using an Markov chain Monte Carlo (MCMC) approach with the MultiNest sampler [62]. In the upper plots of Figure 4.7 we show the marginalized posterior profiles (over the full parameter space) for b_1 and f, for both catalogs at $z = 0.55$ (for the equivalent plots for the other two redshifts

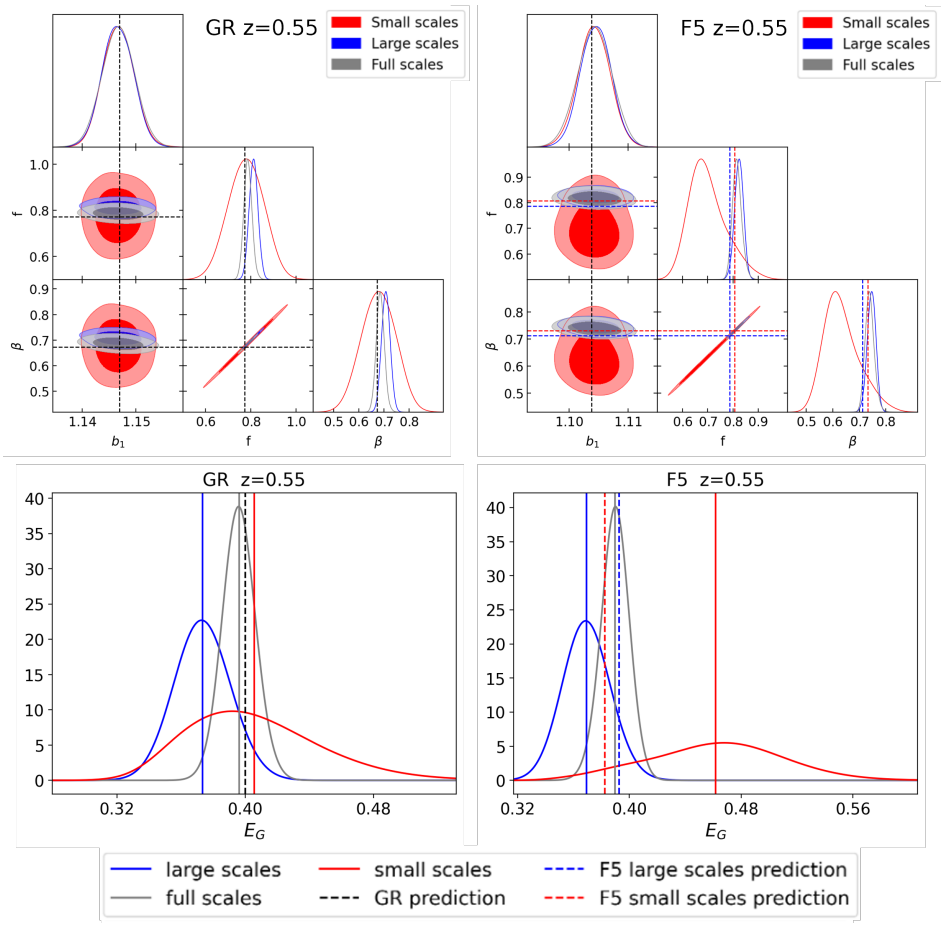

FIGURE 4.7: Top plots show the contours results for b_1 and f and the corresponding derived β parameter for small, large and full scales for GR (Left) and F5 (Right). The dashed lines show the predictions for f and b_1 (estimated from the C_ℓs) for GR (black), and F5 small (red) and large (blue) scales. The bottom plots show the PDF for the EG estimator for the respective scales, the solid lines show the mean of the respective same color PDF while the dashed lines represent the predictions of the respective same color solid lines.

check the appendix for Figures C.2 and C.3). We also show the density profile for β which is derived from the posterior distributions of the other two parameters. We can see in these plots that the growth rate at small scales has a variance around 3 times bigger than the other two cases, which is expected, since there are much fewer (uncorrelated) modes available for measurements on such small (non-linear) scales.

For completeness, in Figure C.4 and C.5 we show the posterior distribution of the full 10-dimensional parameter space of the VDG model for the intermediate redshift bin, $z = 0.55$. As shown in Figures C.4 and C.5, most of the model parameters seem to converge well although we observed a double peak on the local quadratic bias parameter, b_2, for GR when constrained to large scales only. We note that this is not the case for the F5 model, where even this parameter exhibits a well defined peak, and away from zero, at variance with the large-scale fit. The fact that this non-linear parameter shows this double peak at large scales could be the result that these particular scales do not have enough non-linear information to properly fit this parameter. For the rest of parameters, they seem to follow the expected behavior. The counterterms (c_0, c_2, g_2, g_{21}) are consistent with zero and the AP parameters

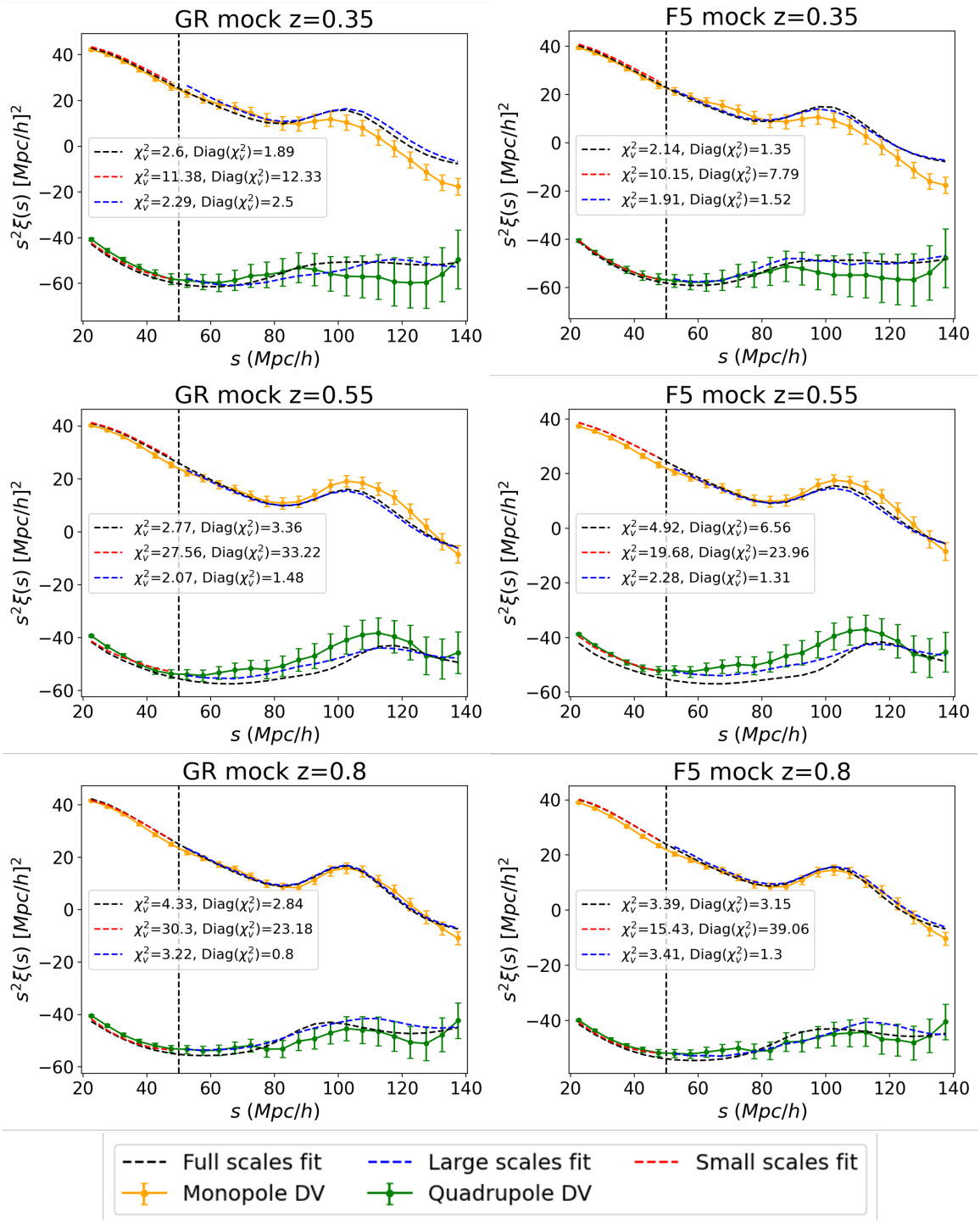

FIGURE 4.8: Multipole data vectors values for the F5 and GR mock using the all galaxy sample. The monopole is the yellow line and the quadrupole is the green line. The best fit to the VDG model using the Jackknife covariance matrix is plot as dashed lines for the full (black), small (red) and large (blue) scales. The respective reduced χ^2_ν of the best fit is shown in the legend, while Diag(χ^2_ν) is calculated with only the diagonal terms of the covariance matrix.

are consistent with 1 (although only when considering 2-sigma contours for the full scales case) since the data vectors are using the fiducial cosmology of the mock.

As mentioned before, for small scales we can appreciate how the contours are much bigger for parameters such as the growth rate or the AP parameter. This is arguably caused by the few data points included in the "small scales" range, and the large correlation between them induced by the non-linear clustering, which results in very few effectively independent modes to constrain the model parameters. This is usually called "projection effects" from the prior volume of the multi-dimensional parameter space that is intrinsically largely degenerate and, thus, it needs many independent modes to break such degeneracies. In order to alleviate this, we first derive Gaussian priors for the counterterms of the VDG model by first running a MCMC chain using the full scales with fix cosmology. Then we use the derived constraints on these counterterms to run the full MCMC chains letting both the cosmology and contermterms parameter change for the small and large scales cases. in particular, we have observed that this prior step is crucial to avoid a large amount of projection effects in our constraints on the growth rate.

In Figure 4.8 we show the results for the multipoles of the correlation function alongside the COMET theoretical data vectors using the corresponding best-fit parameters. The best-fit shown reproduces overall the measurements, although there are discrepancies specially on large-scales. We note however that the large covariance between scales makes the fit appear worse than it is in practice. We can see that the quadrupole is quite noisy in comparison with the monopole, specially at large scales. This is induced by the higher error-bars at this scales due to sample variance. It seems that COMET can hardly fit both the monopole and the quadrupole simultaneously. Since the monopole have smaller error-bars the MCMC chains seem to favor fitting the monopole over the quadrupole. This is illustrated by the fact that the monopole exhibits a good fit overall, with only a poorer model fitting around the baryon acoustic oscillation feature at 100 Mpc/h scales. Similarly, the quadrupole is well described by the non-linear theory model overall, except for the redshift bin at $z = 0.55$ where the theory deviates from the simulation on large scales.

In order to quantify the model fitting we define a reduced χ^2_ν test as,

$$\chi^2_\nu = \frac{\chi^2}{n_d - n_p} \tag{4.62}$$

where n_d is the number of data points combined between monopole and quadrupole (48 for the standard case) and n_p the number of free parameters ($\approx$10 for most cases), while χ^2 has the same definition as in Eq. 4.55.

Overall the results for all redshift bins and scales yield large χ^2_ν values (see legends of the different panels in Figure 4.8). This, at face value, suggest a poor fit to the theory model. There might be several reasons for this. On one hand, the particularly small error-bars, specially at small scales, exacerbate this excess in the resulting χ^2_ν value. But this is also true, although with somewhat lower values, for the full and large scales. This is specially surprising for the case at $z = 0.8$, where the mock data vectors seem to be in very good agreement with the best-fit, at least visually (i.e, in chi-by-eye). In fact, one would expect to obtain better fits as we go to higher redshift where clustering has a lower degree of non-linearity. However, one thing that seems to artificially increase the value of χ^2_ν is that the Jackknife covariance is close to singular. Moreover if we only take the diagonal elements of the covariance

matrix the value of χ^2_ν drops by a factor of 2 or more at large scales, yielding a value consistent with unity in all cases, except for the GR model in the lowest redshift bin (see Figure 4.8).

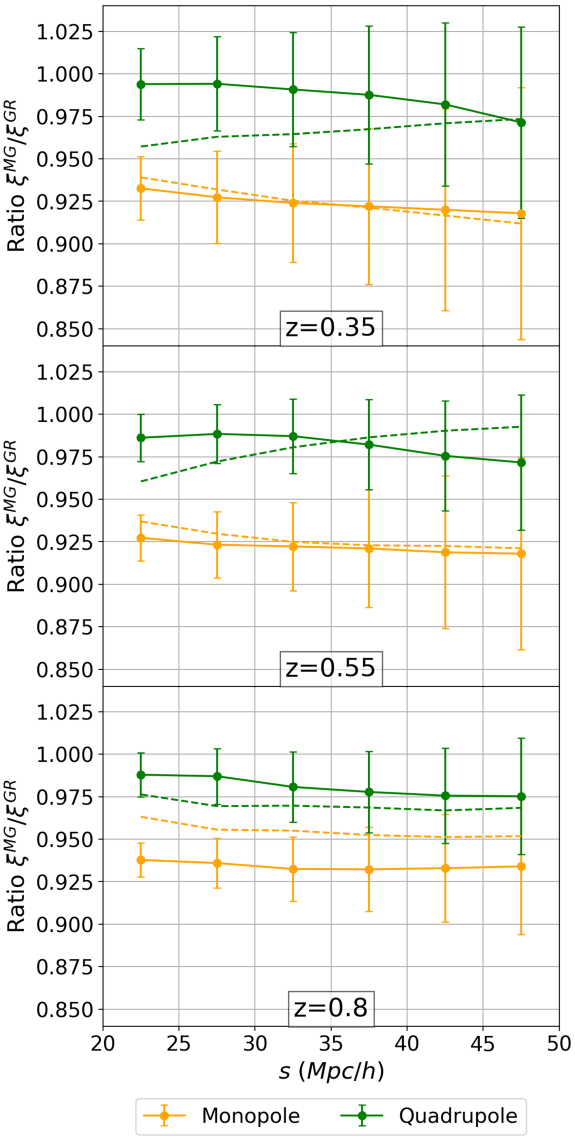

FIGURE 4.9: Comparison of the multipoles: monopole (orange) and quadrupole (green) at small scales for GR and F5. The solid lines represent the ratio of the data vectors while the dashed line is the ratio of the best fit of each case (for both the ratio is defined as F5 over GR). The errors represent the propagated Jackknife errors of each data vector.

Since it is on the smallest scales that we expect the specific gravity theory has larger impact on the clustering (related to the non-linear power boost in the matter power spectrum in MG with respect to GR), we further investigate in Figure 4.9, where we plot the ratio of the data vectors and the corresponding ratio of the best fits of F5 over GR. This provides a direct way to see to what extent is possible to distinguish between the two models. Note that the errors, obtained with the Jackknife method applied to each catalog, are big enough as compared to any small numerical perturbation in the ratio of the data vectors. Looking at the correlation function multipoles ratios We find that the theory prediction for the monopole ratios closely follow the ratio of data vectors. For the quadrupole there is some degree of

discrepancy between theory and simulations, although not significant, given the errors. This puts into perspective that, despite the small errors, they are still large enough to shadow possible deviations with respect to standard gravity even for (ideal, i.e, systematics free) all sky surveys as we model in this paper. In section 4.8 we further quantify our results from the small-scale clustering in redshift space in terms of a null test of gravity.

4.7.3 Results for the E_G estimator

Having estimated all the ingredients of the gravity estimator, i.e, the RSD β parameter[10], as discussed in the previous section, and the real-space clustering ratio, R_b (see Eq. 4.59), we are ready to compute the E_G statistic. In order to derive the posterior for this estimator, we shall apply the ratio distribution, as given by Eq. 4.60.

In the plots below Figure 4.7 (and C.2 and C.3), we show the posterior PDF obtained for the E_G estimator using the ratio distribution given by Eq. 4.60. We simultaneously plot the results for the small and large scales alongside the full range of scales. The E_G estimator seems to follow a Gaussian distribution as obtained in [152]. The corresponding best-fit values with error-bars are provided in Figure 4.10 what provides a more direct comparison of the marginal differences between the gravity theories fitted to the simulations. Given that the E_G estimator is inversely proportional to the growth rate its value decreases when going to smaller scales at a given redshift. Taking into account that the clustering ratio R, Eq. 4.59, is not expected to change in F5 with respect to GR the (see 4.7.1), the E_G estimator is only sensitive to the underlying gravity theory through the linear growth rate parameter. This is illustrated in detail in Figure 4.10 which summarizes the main results of this paper and tests the robustness of them with respect to the analysis choices used, as we shall discuss in more detail below.

Overall, as shown in Figures 4.7, C.2 and C.3, the values of the gravity estimator for the full scales of GR and F5 seem to agree with the respective prediction within 1-σ errors. However, for F5 at $z = 0.8$, the estimated value of the growth rate is biased low at around 2-σ, but since the value of R_b for F5 is slightly biased high, this tends to compensate for the estimated E_G value. Moreover, for this case, the GR and F5 simulation results can not be distinguished given the statistical errors. For the other redshift bins, $z = 0.35$ and $z = 0.55$, the values for both simulations appear to align closely with the best-fit models. While for small scales the values are vastly over-predicted despite the larger errors, contrary to the F5 prediction. For the redshift bin at z=0.35, it follows the opposite trend, making the estimated F5 values agree better with the theory prediction. For completeness, we have also included the case where we try to fit an F5 simulated data vector with a GR model. This is a direct way of testing (sort of a "null test") how well the estimator is able to distinguish between close gravity theories such as F5 and GR. Our results yield best-fit values to GR and F5 theory that are statistically consistent, suggesting that assuming the wrong theory might not significantly bias our results. We have checked that even at higher redshifts (e.g, using a mock sample at $z = 1$ with lensing sources at $z = 1.2$), where the clustering is closer to the linear regime, we find that the F5 results are biased high at all scales, while for GR results are unbiased except on large scales.

The results in all the previous plots were for the all galaxies case, where we consider the full sample of galaxies in a given redshift bin and the relative magnitude cut on the r-band of $r < 24$. As stated in the sec. 4.5, we also perform the same calculations on several different

[10] As described in [38] we can ensure that we can combine all our results since the correlations have the same effective redshift. The same goes for the β parameter which is estimated from a 3D distribution at the same effective redshift.

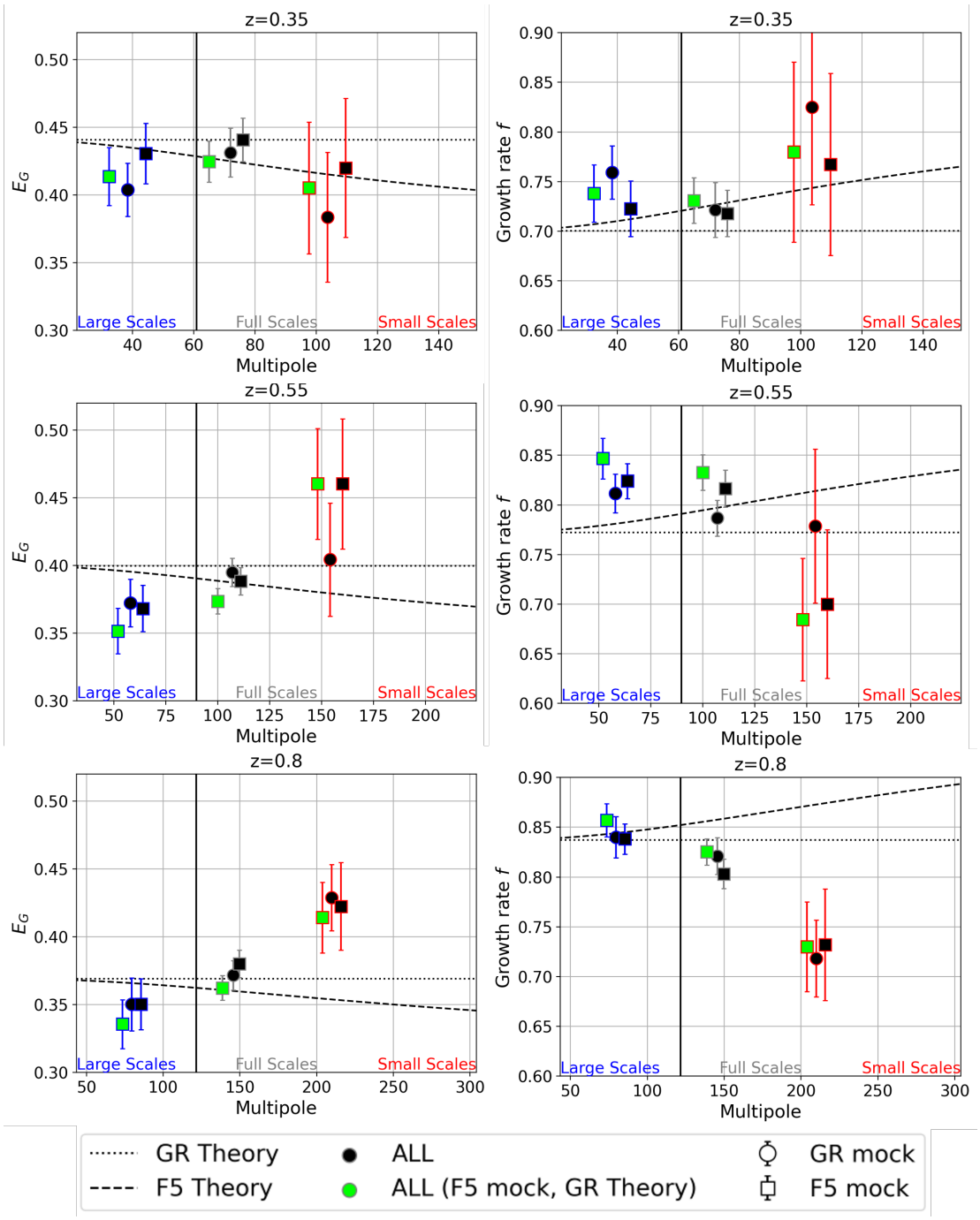

FIGURE 4.10: Final results for the E_G parameter (left plots) and the growth rate f (right plots) for the GR (circles) and F5 (squares) mocks at the three redshift bins studied. The results are split according to the various scales considered: small (red symbols and errors), large (blue) and full range (gray). The vertical solid line separates the small and the large scales. The black filling of the data points represent the baseline case (All) for both GR and F5 (using the corresponding gravity for the theory model), while the green one represent the case that uses the F5 mock data but assumes the GR theory to perform the fits (GR theo). The dot (dashed) line represent the theoretical prediction for E_G for GR (F5). The values are centered around the mean ℓ of the respective range of scales (large, small or full scales), although they are slightly shifted to the left and right to avoid to clutter.

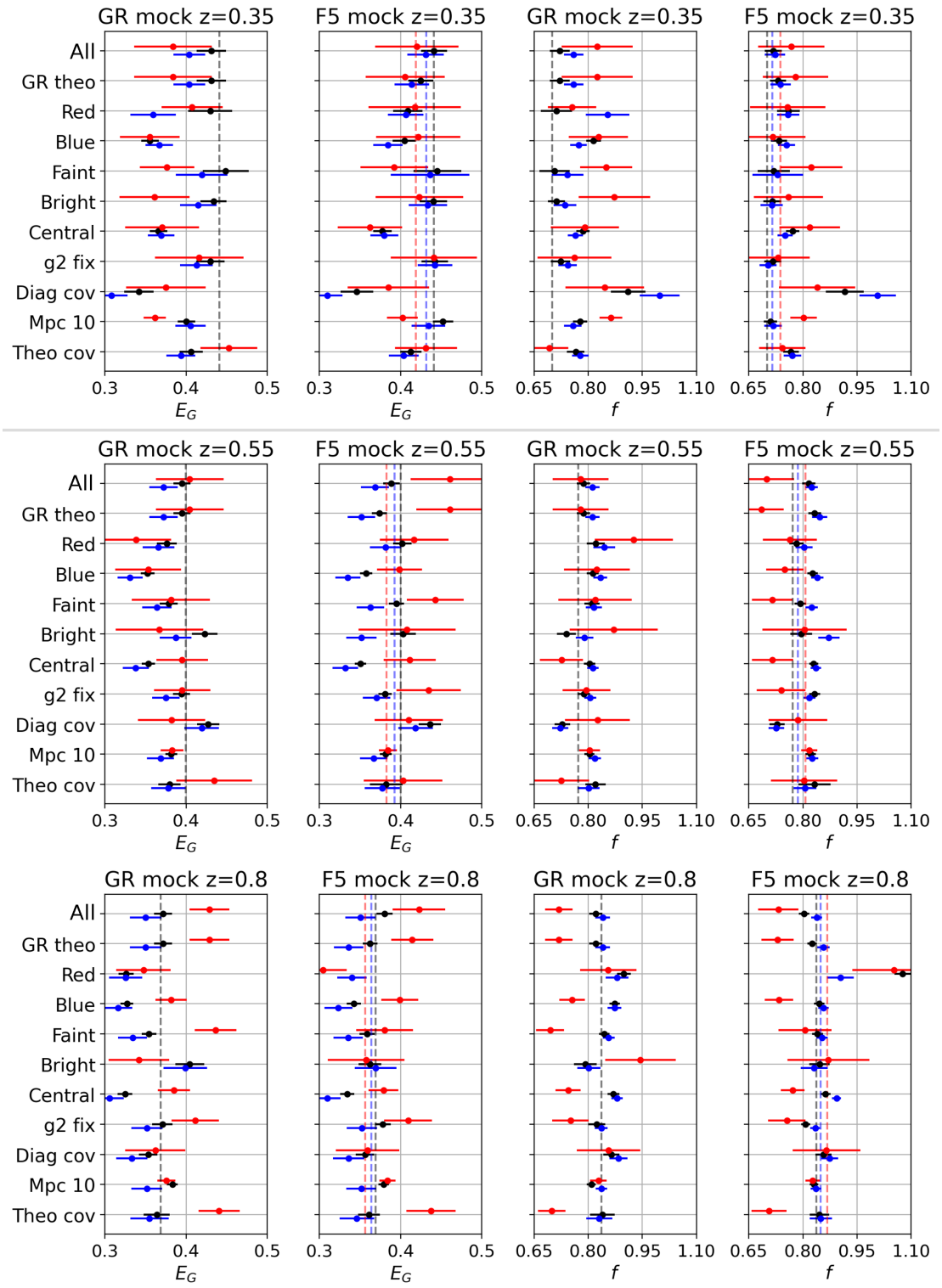

FIGURE 4.11: Summary of the main results for the various cases analyzed in this paper. The black, blue, red points and error-bars represent the full, large and small scales result, respectively. Results displayed are for both gravity theories, with the left plots showing the EG estimator and the right plots showing the growth rate results. The dashed lines show the fiducial values where the F5 have the respective values for small and large scales.

samples and analysis choices. In Figure 4.11, we present the mean and standard deviation for the gravity estimator for all the cases considered. Below we summarize the cases explored,

- 1) **All**: reference case used in this. It uses the full-sky mock, all galaxies sample, with a cut in relative for $r < 24$ for the SDSS r-band. The rest of sample-specific cases 3)-7) are derived from this one by applying additional selecting criteria.
- 2) **GR theo**: same as above but using a best-fit GR theory to analyze the F5 simulated data.
- 3) **Red**: same as reference, but for red-color galaxies classified using a $g-r$ cut following [32].
- 4) **Blue**: same as reference, but for a blue galaxy sample, following [32].
- 5) **Faint**: same as reference sample, but for faint galaxies, obtained by imposing a relative magnitude bin, $23 < r < 24$.
- 6) **Bright**: same as reference, but for a bright galaxy sample defined by imposing a relative magnitude cut $r < 22.5$.
- 7) **Central**: same as reference case, but only selecting the central galaxy of each halo.
- 8) **g_2 fix**: same as reference case, but setting the tidal bias parameters, g_2 and g_{21} as derived parameters from the linear galaxy bias b_1, using the relations: $g_2 = 0.524 - 0.547b_1 + 0.046b_1^2$ and $g_{21} = (2/21)(b_1 - 1) + (6/7)g_2$ [139].
- 9) **Diag cov**: same as the reference case but using only the diagonal elements of the Jackknife covariance matrix.
- 10) **Mpc**: same as the reference case but extending the minimum scale to 10 Mpc/h. The full range is now defined as $[10, 140]$ Mpc/h and the small scale goes from $[10, 40]$ Mpc/h, while the large scale range remains the same.
- 11) **Theo cov**: same as the reference case but using the theoretical Gaussian covariance matrix to calculate the likelihood.

In summary, our extended analysis shows that our results are robust to changes in the galaxy sample selection and analysis choices made. The general trend is usually the same as the reference "All" galaxies case, where at small scales the values for E_G are over-predicted and for large scales are under-predicted. The same behavior is observed for the F5 simulation, with a larger tension with respect to the theory than for the GR case. In particular, the recovered scale dependence goes in the opposite direction to that predicted by theory. In the cases where we put specific cuts on the sample such as for the red, blue, faint, bright and central samples, the values deviate more from the prediction than the "All" galaxies case. This is mostly notorious with the full scales since for the reference case the results are no longer consistent with the prediction at 1-σ. The rest of cases depict different analysis choices relative to the reference case. When we fix the tidal biases (g_2, g_{21}), it does not seem to have significant impact on the growth rate posteriors. The tidal biases obtained are slightly different, e.g. for $z = 0.55$ the estimated value for g_{21} turn out positive instead of the negative value we find in Figures C.4 and C.5. It seems that these parameters are highly nonlinear and are not largely degenerate with a linear parameter like the growth rate. In addition, we have also tested the impact of the choice of covariance matrix in our results. For this purpose we have compared the case when using the theoretical (Gaussian) and diagonal matrix and they seem to produce similar results to the Jackknife covariance with the exception at $z = 0.35$ where results worsen significantly. A possible explanation for this is that at lower redshifts the off-diagonal terms of the covariance become larger, and the accuracy in the computation of these may have

a larger impact in our results. Lastly, we have tested how including even smaller scales in the analysis may impact our findings. This is specially relevant since we expect these small non-linear scales to be the ones most sensitive to the underlying gravity model. With this in mind we have extended the range of the "small scales" case from 20 Mpc/h (in the reference case) to 10 Mpc/h. However, including these smaller scales does not appear to significantly reduce the estimator biases; in fact, it worsens the fit in certain cases. This suggests that the non-linear model used is already breaking down at the minimum scale used, for all the redshifts explored.

4.8 A null test of gravity from small scales clustering in z-space

From the comprehensive analysis presented in section 4.7.3 above, we conclude that the E_G has clear limitations to constrain gravity, mainly due to projection effects coming from the multi-dimensional parameter space of the non-linear model used. Besides, most of the deviations in the clustering statistics are expected to show up on small (non-linear) scales, where the perturbative model we have used (VDG model) is expected to break-down. In Fourier space, the limiting scale of the model is at $k > 0.35$h/Mpc, see [60], what should translate, according to Eq. 4.22, into projected scales of about 10 Mpc/h. In particular, we have also checked that this conclusion is robust to the specific perturbative model used (EFT or VDG), although we have found that the VDG model outperforms the EFT for the RSD modeling, what has been our criteria to select the former as our reference model for the analysis.

All things considered, we find that, with the current state-of-the-art modeling tools, the E_G estimator is not well suited to differentiate between both gravity theories, even for an ideal survey set-up. Alternatively, in this section we explore whether one can set constraints on gravity using all the information contained in the basic 2-point clustering statistics in redshift space. In order to quantify the expected differences in RSD clustering, we compute the ratio of the 2D correlation function $\xi(\pi, r_p)$ between the F5 and the GR mocks, where π is the line of sight (LOS) distance and r_p is the project distance on the plane of the sky. Figure 4.12 shows this projected clustering ratio, where we factor out the dependence on the linear galaxy bias of both mocks by multiplying by $(b_1^{GR}/b_1^{MG})^2$. Our results show the only significant ($> 10\%$) differences show up at rather small projected scales < 10 Mpc/h, where the Finger of God effect becomes prominent, what renders the widely-used perturbative models (VDG or EFT) largely inaccurate. This is a good indicator that properly modeling even smaller scales than those investigated in this work would be a critical improvement to detect potential deviations from standard gravity. Unfortunately, current models do not allow to predict these scales with enough accuracy.

In order to quantify the observed differences from the small scales in the projected clustering, we decompose the data vectors into their correlation function multipoles, according to Eq. 4.57, to quantify the differences between both gravity simulations. Specifically, we compute the χ^2 statistic for the difference between the data vectors of GR and F5, as well as for difference between data vectors and the best-fit to theory. The χ^2 estimator thus defined provides a simple "null test" to measure the ability to distinguish between the two theories. Since the simulations were generated using the same cosmology, except for the gravity theory. Once these mocks are calibrated against observations at very low redshifts (see [32]), any observed differences in the clustering at higher redshift are expected to be caused by the different underlying gravity model used to produce each synthetic galaxy catalog.

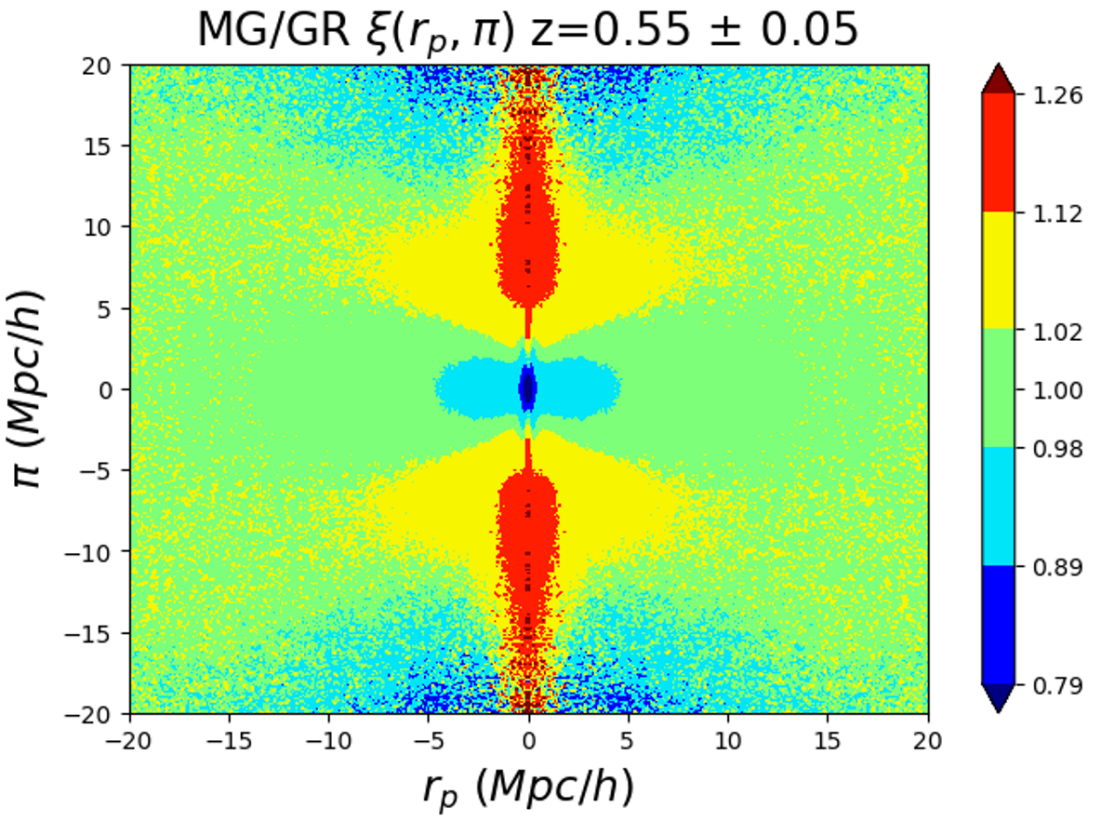

FIGURE 4.12: 2D correlation function in π (LOS distance), r_p (projected distance). The color scale indicates the clustering amplitude ratio of the F5 over the GR mocks, where each correlation is normalized by its corresponding linear galaxy bias, b_1, at $z = 0.55$.

	z=0.35	**z=0.55**	**z=0.8**	
χ^2_D	67.99	129.27	124.46	**Small Scales**
	91.17	203.22	166.39	**Full Scales**
χ^2_T	79.86	119.61	43.54	**Small Scales**
	150.71	149.10	70.88	**Full Scales**
χ^2_{GR}	76.46	131.90	40.73	**Small Scales**
	123.99	180.46	86.31	**Full Scales**

TABLE 4.3: χ^2 values for a comparison between data vectors (MG vs GR, denoted as χ^2_D), for the data vectors vs. each corresponding theory (χ^2_T), and for the data vectors (F5 and GR) against the GR theory (χ^2_{GR}). The values are calculated using the fiducial range for the small scales, $s \in [20, 50]$ Mpc/h, and the Jackknife covariance of the GR catalog.

Table 4.3 summarizes the results for this section, where we define three χ^2 statistics: χ^2_D, representing the difference between the data vectors; χ^2_T, quoting the difference between the data vectors and the corresponding best-fit gravity models; and χ^2_{GR}, giving the difference between each data vector (for both F5 and GR) when assuming standard gravity (i.e, GR) as the theory model. In all cases the χ^2 values are computed using the Jackknife covariance derived from the GR mock data vectors, which closely resemble that of F5. The computation follows the method outlined in Eq. 4.55. The high χ^2_D values demonstrate that the theories can be clearly distinguished, in terms of such null test, despite the associated uncertainties. Dividing the quoted χ^2 values by the number of data points within the scales (6 points for

the small-scales) we get that the data vectors are drawn from distributions that differ at a significance level of 3–4.5σ, for each of the redshift bins studied. If we use the best-fit theory models instead, the null test (χ^2_T, and even χ^2_{GR}) yields similar significances, what suggests that the models seem to describe the correlation function multipoles of the mocks well enough. Additionally, the table includes results for the same test applied to the full scales range. Here the χ^2 values are approximately double those obtained for small scales. Given that the full scale range involves 3 times more data points (24 measurements) the test, normalized to the number of degrees of freedom, suggests that, as expected, most of the discriminating power resides on small scales (< 50 Mpc/h).

The results indicate that the differences between the models are significant enough to distinguish the underlying gravity model. Developing more precise theoretical models that can accurately predict behavior even at small scales would be a valuable step toward improving model differentiation. However, while these findings hold for the idealized case of simulations, it remains essential to test their applicability to real observations, where higher levels of uncertainty and sources of systematic error would degrade the ideal survey case presented in this work.

4.9 Discussion

4.9.1 Novelty and challenges of growth rate estimation at different scales

This paper represents a pioneering effort to model the growth rate and the E_G gravity estimator across multiple scales for modified gravity models. While most previous studies [122, 123, 152] assumed a scale-independent growth rate, calculated from the full range of scales, this approach clearly limits the fundamental purpose of E_G as a general test of gravity models. Probing the scale dependence is crucial since the gravity estimator and the linear growth rate are predicted to vary with scale in most non-standard theories and thus require a proper framework to accurately model from large (linear) to small (quasi-linear or fully non-linear) scales. From the observational standpoint, this is what past analyses have studied, e.g. [123] and [152] measured the value of E_G at different harmonic multipoles, ℓ, in a similar way to what we have done with the clustering ratio, R_b, as shown in Figure 4.6. However these analyses have overlooked the consistent estimation of the scale of the growth rate, specifically the β parameter, and its possible scale dependence, to accurately derive the E_G gravity estimator.

However, this is inherently challenging due to the limited availability of accurate non-linear models in redshift space. The present study develops a well defined framework to address this issue, using state-of-the-art perturbative models, and emphasizing the importance of separating the analysis into large- and small-scale regimes. In practice, small scales are especially difficult to model due to strong non-linear effects related the so-called Fingers-of-God effect, that demand a proper account of the distribution of pairwise velocities and how those impact the 2-point clustering in redshift space.

4.9.2 The Role of priors in the parameter estimation

This study also demonstrates the pivotal role of imposing (Gaussian) priors to the counterterms of the VDG perturbation theory model for improving the robustness of parameter fits, especially when working with small-scale data. Small scales present significant challenges due to the limited amount of uncorrelated information and complex parameter degeneracies within the multi-dimensional model parameter space, the so-called "projection effects". One example

of such degeneracies arise between the growth rate parameter and the clustering amplitude (σ_8 or σ_{12}). The inclusion of Gaussian priors helps to stabilize the fitting procedure, enabling faster convergence and reducing variance in the results. For large scales, the posteriors can still be reasonably accurate without Gaussian priors, particularly if nonlinear biases are not included. However, the large error bars at these scales result in high variance in the posteriors.

Most of the considerations discussed here were analyzed individually, although some may be specific to our dataset. Certain aspects have already been addressed in previous studies, such as fixing the value of σ_{12}, as done in [152] for σ_8. This step was crucial to mitigate the strong degeneracy between f and σ_{12}. The latter parameter can, however, be estimated through alternative analyses, such as a $3x2$pt approach, that combines 2-point statistics of clustering and weak-lensing. This reasoning also underpins our decision to use the fiducial cosmological parameters the simulation for the background cosmology $\{\Omega_m, \Omega_b, H\}$ in COMET, and in the C_ℓ theory predictions. In any case, we incorporate Alcock-Paczynski parameters to account for deviations in cosmological parameters, and these have been observed to align reasonably well with 1 (i.e, unbiased cosmology) within statistical errors.

Regarding the linear galaxy bias, a tight Gaussian prior based on the estimates from the harmonic space galaxy clustering is not strictly necessary in most cases, as fits to the correlation function multipoles tend to yield consistent values. This is further validated in Annex C.4, where we apply a more sophisticated non-linear model to jointly fit the linear (b_1) and quadratic bias (b_2), improving the estimate of b_1 from the C_ℓ. Using this method, we finding consistent values, and thus similar Gaussian priors, for b_1. While the Gaussian prior on b_1 is not critical, it significantly accelerates chain convergence and helps avoid degeneracies with non-linear biases in specific cases. For the rest of non-linear parameters, although these priors could theoretically introduce parameter biases, the analysis confirms they allow sufficient wide sampling of the parameter space. The triangular plots for the derived parameter constraints (Appendix C.3) demonstrate that the priors are not overly constraining (i.e, not too informative), as we can see that the parameters for the small and large scales are able to variate over the values (priors) for the full scales. This particular approach proves particularly important for small scales, where degeneracies and irregular fits are otherwise unavoidable.

4.9.3 Small Scales as the critical testing ground for gravity models

When analyzing the full range of scales, the results are generally robust. This agrees with previous work where β is calculated over an extensive range of scales, such as in [123] and [152]. In our case, the use of all-sky lightcone simulations yield relatively small error bars, with a relative error of approximately 3–5% for E_G, which makes the agreement with theoretical predictions even more remarkable. For comparison, [152] reports a relative error of about 15–25% for E_G using the BOSS survey. It is also important to note that the observable estimate for E_G, based on the method in [152], is biased low by approximately 1–3%, as illustrated in Figure C.1. However, the error bars are not small enough to distinguish between the F5 and GR theory models clearly, as their average predictions differ by only about 5% at these scales. Observational estimates of the gravity estimator are also affected by complex real-world systematics that substantially increase the overall error budget, thus further compromising the power of the estimator to discriminate gravity theories.

We note that this work places particular emphasis on small scales, where deviations between F5 and GR models are expected to be most pronounced. Unfortunately, this is also the regime where fitting challenges are greatest, even under ideal simulation conditions. Specially

at scales below 10 Mpc/h where we seem to find the highest deviations in the RSD (see Figure 4.12). Again, the large non-linearities and limited amount of uncorrelated modes on these scales undermine the ability of the estimator to distinguish between competing models. Despite these challenges, the methodology underscores the potential for enhanced small-scale estimations with novel hybrid approaches that combine perturbative and fully non-linear (N-body) tools such as the BACCO emulator [120], and and higher-quality observational data. This is particularly promising since much of the error budget at these small scales appears to originate from the growth rate-related parameter, β.

Tests like the E_G estimator do not currently provide sufficient constraints to distinguish between models. The results in Section 4.8 suggest that, at least in simulations, the data is robust enough to achieve at least a significant detection (3σ for the F5 model) of deviations from GR at small scales across all the redshifts studied (for $z < 1$). However, in observational contexts, this approach is more limited, as we only have access to a single Universe with an unknown gravity model. This means that we cannot perform such model dependent comparisons, and most of the relevant information will be captured by nuisance parameters, e.g. the linear galaxy bias being higher in GR than F5, that we cannot use to directly distinguish gravity models. A better approach, would be to directly measure model dependent parameters like f_{R0} as they do in [34], although a model of gravity, in this case $f(R)$, needs to be assumed.

4.9.4 Limitations of the theory modeling and future directions

The reliance on GR-based assumptions for estimating certain cosmological parameters (e.g., β) introduces biases into the E_G calculation for F5 models, a limitation acknowledged in the analysis with the "GR theo" case (see sec. 4.7.3). These biases are inherent to the model-dependent nature of parameter fitting and underscore the difficulty of achieving truly model-independent estimates for E_G. In Section 4.4, we highlighted that the emulator has a $k_{max} = 0.3502\text{Mpc}^{-1}$ (or $k_{max} = 0.5171$h/Mpc for the mocks used). Using equation 4.22, this gives a $s_{min} \approx 6$Mpc/h. However, this may not be sufficient for our $s_{min} = 20$Mpc/h, as shown in equation 2.91, where we need to integrate over the entire range of Fourier scales, k. Additionally, our implementation of E-MANTIS's amplitude boost to the final multipoles, rather than applying it to the original matter power spectrum, could introduce a bias in the results at small scales. At these scales, the relationship between the correlation multipoles and the power spectrum is not necessarily linear, which may further affect the accuracy of the model. Nonetheless, the study demonstrates that, despite these limitations, the results remain consistent within acceptable error margins, highlighting the robustness of the methodology. However, the potential impact of using GR theory (e.g, perturbation theory counterterms) to estimate cosmological parameters for the F5 model remains uncertain. A forthcoming paper (Viglione et al., in preparation) will describe a 3x2pt analysis to constrain gravity using the mocks presented in this work.

Moreover, the χ^2_ν test when comparing data to best-fit models are unusually high, even for the full-scale case. We are confident that this is not an issue with the modeling done with COMET, as this emulator has been successfully used to fit other simulated catalogs with good agreement (Camacho et al., in preparation). At small scales, it is evident that the small error-bars (as compared to the large scales) make the χ^2_ν increase, specially considering that the perturbative model seems to start breaking down. On the other hand, for large scales, the off-diagonal terms of the covariance matrix seem to boost the value of χ^2_ν since setting them to zero (i.e, taking only the diagonal part) tends to keep the value close to 1. Typically,

these fits are performed at high redshifts to avoid large non-linear effects, but even at redshifts around $z = 1$, the results do not improve in any significant way.

Another consideration is that the relationship between the wavenumber k and the projected distance s (as given by Eq.4.22) is based on several approximations that are only valid at small scales. This could potentially affect the accuracy of the predictions for the growth rate and the E_G in multipoles, although we have not investigated this in detail. An alternative approach would be to perform the fits in Fourier space, using the power spectrum multipoles, but as previously discussed, this introduces additional complications, such as extra noise parameters and noisy measurements of the multipoles, particularly when trying to split the measurements in small and large scales.

Future improvements may involve employing Fourier-space fits, and state of the art new emulators such as the BACCO emulator [120] that combine perturbative and fully non-linear approaches, for greater accuracy. These advancements could address the current limitations, but this is left for future work.

On the other hand, we note that in the current analyses we have neglected a number of real-world effects that would potentially degrade our constraints, including the finite survey mask (that limits the number of uncorrelated modes available), photometric redshift errors, and astrophysical systematics such as intrinsic alignments of galaxies (not present in alternative analyses that use the CMB lensing instead of the galaxy lensing, see e.g, [122]) or the impact of shape noise.

4.10 Conclusions

In this paper we have presented an end-to-end cosmological analysis pipeline to constrain gravity using one of the largest modified gravity simulations to date (see [13]). In particular, we use a comprehensive galaxy mock built out of a N-body simulation of the Hu & Sawicki f(R) model, with amplitude $f_{R_0} = 10^{-5}$ (denoted as F5), that is still viable given current observational constraints, and a twin LCDM simulation that assumes General Relativity (denoted as GR) with the same cosmological parameters and initial conditions, to investigate whether future surveys (in the limit of an ideal noise-free full-sky survey) can detect deviations from standard gravity using the so-called E_G estimator [160]. This estimator combines 2-point statistics of galaxy clustering in real and redshift space, along with weak-lensing (galaxy-galaxy lensing). A key advantage of this estimator is that it is independent of the galaxy bias on large scales, and it is a direct test of gravity.

We have presented a well defined and comprehensive framework to compute this gravity estimator across distinct scales, including a number of theoretical and modeling improvements with respect to previous studies (see e.g, [122, 123]). Traditional approaches, which assume the scale independence of the estimator on large scales, are potentially biased by the break down of this assumption, in particular related to the linear growth rate estimation in non-standard gravity models. Dropping this assumption, this work investigates the impact of the scale-dependent in the theoretical modeling of the E_G estimator, specially in the context of distinguishing between GR and similar (in terms of expansion rate and clustering) yet alternative models, such as the F5.

Our main results can be summarized as follows:

- Even for ideal all-sky galaxy surveys, the widely used E_G estimator is unable to clearly distinguish between the currently viable, e.g, F5 and GR, gravity theories (see section 4.7.3). This is mainly due to two reasons. First, the large degeneracies between perturbative and cosmological parameters of current state-of-the-art non-linear models for galaxy clustering in redshift space (such as VDG or EFT), that bias the linear growth rate estimation at the low redshifts explored. Secondly, the fact that such perturbative models can not accurately model RSD clustering on small-enough scales (typically < 10 Mpc/h) where most of the constraining power resides.
- We have proposed a simple null-test, based on the correlation function multipoles, to quantify the optimal detection level for deviations with respect to standard gravity, that we illustrate for the working example of the F5 model. We find that detection levels at about $4\,\sigma$ significance can be reached for all the low-redshift (lens) samples we have used. This result holds when using either a purely data-based approach or a model-dependent one (see section 4.8).

Finally, this work identifies several promising directions for future research. The use of Fourier-space fits, combined with advanced emulators such as BACCO, that effectively extend the range of (small) scales that are accurately modeled, could significantly enhance the precision and accuracy of the growth rate and E_G estimations. These emulators offer improved modeling of the galaxy bias parameters in the non-linear regime and allow for direct estimation of noise parameters, potentially addressing many of the limitations identified in this study. Expanding the analysis to include alternative simulations and novel tools for modeling clustering in the non-linear regime will also provide new pathways to constrain gravity using the next generation of galaxy surveys.

In conclusion, this study presents an end-to-end cosmological analysis pipeline to constrain gravity using high-fidelity galaxy mocks. We have used a very large lightcone simulations of one the most popular models (F5) that is still viable given observational constraints, to asses whether a widely used estimator for gravity, the E_G statistic can be effectively used to detect deviations with respect to standard gravity (GR). Our results show the limitations of such estimator even for ideal next generation surveys, what opens the door to alternative approaches that combine multiple observables to break degeneracies between nuisance (e.g, galaxy bias) and cosmological parameters. In particular, we envisage that using the now standard combination of photometric galaxy clustering and weak-lensing observables, known as the 3x2pt analysis, can provide a more optimal way of breaking the observed parameter degeneracies and provide more competitive constraints of gravity. We leave this study for future work (Viglione et al. in preparation).

Chapter 5

Probing gravity with the 3x2pt analysis

In this project, we explore an alternative probe of gravity, alternative to the E_G estimator presented in the previous chapter. The proposed estimator uses a combination of photometric galaxy clustering and weak-lensing from a given galaxy survey (usually know as 3×2pt analysis) on the same pair of twin simulations described in Chapter 4. The primary goal of this work is to investigate potential biases arising from assuming GR theory while analyzing data generated under a $f(R)$ gravity framework. To validate our methodology, we use the GR mock as a benchmark. A paper on this work (Viglione C., Alemany M. et al.) is currently under development, as we are finalizing the results.

5.1 Introduction

Cosmology has entered an era of precision and massive data volumes, driven by stage IV surveys, yet the fundamental nature of the cosmological constant (Λ) and cold dark matter (CDM) in the standard ΛCDM model remains unresolved. Efforts to derive Λ from quantum field theory face the "cosmological constant problem," with theoretical predictions differing from observations by over 50 orders of magnitude [110]. Besides, from the thorough investigation of the huge amount of new high-quality data, a number of "cosmological tensions" have merged when trying to fit the same standard model to data spanning a wide range of scales (from galactic to the cosmological) and cosmic times (from the the CMB last scattering surface to the present), see [56, 137]. This has prompted the development of alternative models, based on modified gravity (MG) models, to explore deviations from standard gravity that can potentially provide a better explanation of all the available observational data.

The new generation of galaxy surveys, such as DESI, Euclid and LSST, will collect a wealth of unprecedented high-quality data, underscoring the need for reliable modeling methods to extend beyond current scale cuts and strengthen constraints on gravity theories [1]. These surveys will map the 3D distribution of galaxies over increasing cosmological volumes, which are crucial for understanding both the physics of the early Universe and the mechanisms that govern structure formation in the later (non-linear) stages. In turn, these galaxy catalogs will provide new and more powerful tests of the standard model.

Interpreting galaxy clustering requires careful modeling of the galaxy bias [95], which describes the relation between the observed galaxy distribution and the underlying matter distribution, predicted by theoretical models. To address potential degeneracies between the galaxy bias and the cosmlogical model parameters, additional observational probes, such as weak gravitational lensing, are needed. Weak lensing, especially cosmic shear, provides a direct, bias-independent measurement of the matter distribution. Additionally, galaxy–galaxy

lensing, which analyzes the correlation between the positions of lens galaxies and the distorted shapes of background galaxies, offers a complementary handle on the nature of galaxy bias.

By combining galaxy clustering, cosmic shear, and galaxy–galaxy lensing, collectively known as the 3×2pt analysis, due to its reliance on three two-point correlation functions, it becomes possible to separate galaxy bias from basic cosmological parameters [86, 25, 92, 116]. This method has long been recognized as a powerful tool for extracting complementary information while minimizing the impact of nuisance parameters, such as systematic errors or non-cosmological factors.

The combination of large-scale structure and weak lensing measurements, specially in tomographic analyses, can strongly constrain how structure formation develops in the late Universe [80, 3]. In observations, by comparing these results with constraints derived from the cosmic microwave background (CMB) [7], we can perform a fundamental test of the ΛCDM model, checking whether cosmological parameters inferred from late-Universe observations match those derived from the early Universe, i.e, whether the model is consistent over three orders of magnitude in the scale factor of the Universe.

Traditionally, testing gravity has spanned over two well-studied regimes: the Solar System scales, validated through parameterized post-Newtonian (PPN) methods [153], and the largest available (linear) cosmological scales, assessed using the quasi-static approximation in perturbation theory [20, 72]. However, the non-linear regime of cosmological structure formation, lying between these two regimes, remains poorly tested. Modeling this regime is computationally demanding, even in ΛCDM, and the lack of robust MG modeling techniques, beyond specific cases like $f(R)$ or DGP gravity, limits our ability to unlock the full power of cosmological observables to probe gravity.

There are numerous studies in the literature that employ Fisher forecasts for phenomenological MG to evaluate the improved constraints achievable with Stage IV surveys [36, 12, 35]. These studies typically parameterize the gravity theory across all cosmological scales using the post-Friedmann formalism [143], which involves a rescaling of the Poisson equation in general relativity (quantified by the parameter μ) and a rescaling of the ratio of gravitational potentials in general relativity (quantified by the parameter η). This particular studies assume specific functional forms for $\mu(z)$ and $\eta(z)$ derived from established models or phenomenology. A more recent study [136] has adopted a model-agnostic binning approach, arguing that it is premature to apply such techniques given that non-linear modeling has not yet been formally validated for multiple $\mu(z)$ bins.

In this study, however, we aim to test deviations from GR using a high-fidelity simulated galaxy catalogs that are based on an underlying $f(R)$ Hu & Sawicki modified gravity theory. We use the two twin simulations presented in [16]. In particular, the pair of simulations used are an $f(R)$ (F5) and a fiducial ΛCDM (GR) gravity with identical fiducial cosmology, initial conditions, and matched calibration against observations at low redshift. We shall use the GR simulation as a reference case to test the validity of our methodology. Our objective is to test what biases arise in the posteriors of the basic set of cosmological parameters when analyzing datavectors from a MG galaxy mock, but assuming the standard GR gravity theory.

5.2 Galaxy mocks

Similar to the work discussed in Chapter 4, our data is taken from the General Relativity and $f(R)$ Modified Gravity mock catalog presented in [16]. These mocks assume the following cosmological parameters: $\Omega_m = 0.3089$, $\Omega_\Lambda = 0.6911$, $\Omega_b = 0.0486$, $h = 0.6774$, $\sigma_8 = 0.8159$, and $n_s = 0.9667$. The catalogs contain consistent information for galaxy clustering (i.e,

angular position and observed redshifts) and weak lensing information (convergence, shear, magnified positions).

For both catalogs, we take 6 photometric redshift bins centered at redshift: 0.3, 0.5, 0.7, 0.9, 1.1 and 1.3. Each bin has a width of $\Delta z = 0.2$. We impose a cut on absolute magnitude in 0.1-r-band of <-18, which effectively removes only the very faintest galaxies in the catalog, and include all galaxies on the full sky (i.e, over a solid angle of 4π radians). In Figure 5.1, we present the n(z) of the true (spectroscopic) redshifts of the 6 z-bins taken for both catalogs. Note that the catalogs are defined up to redshift z=1.4 which explains the sudden cut on the distribution of high-z-bins. In Table 5.1 we summarize the number of galaxies and densities for each z-bin consiedered in the analysis.

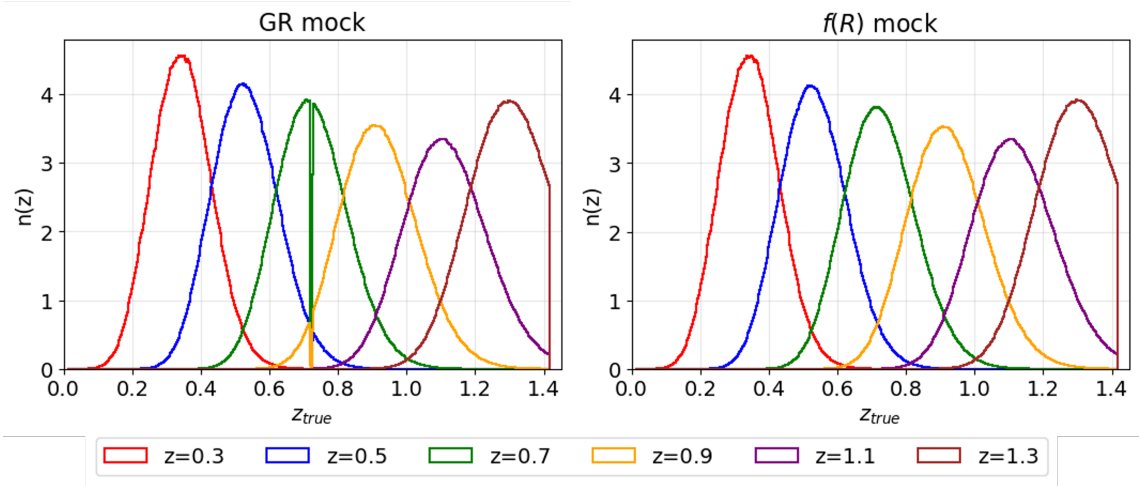

FIGURE 5.1: True redshift distribution normalized, n(z), for the 6 bins taken. The left plot shows the distribution for the GR mock while the right plot shows the distribution for the F5 mock.

	GR			MG		
Photometric Redshift	**Nº galaxies**	**Nº density ((h/Mpc)^3)**	**Angular density (sr^{-1})**	**Nº galaxies**	**Nº density ((h/Mpc)^3)**	**Angular density (sr^{-1})**
0.3 ± 0.1	145,601,195	3.2×10^{-2}	1.16×10^{7}	147,659,571	3.25×10^{-2}	1.18×10^{7}
0.5 ± 0.1	299,222,068	3.01×10^{-2}	2.38×10^{7}	309,071,652	3.11×10^{-2}	2.46×10^{7}
0.7 ± 0.1	436,205,899	2.82×10^{-2}	3.47×10^{7}	466,771,685	3.02×10^{-2}	3.71×10^{7}
0.9 ± 0.1	557,384,860	2.75×10^{-2}	4.44×10^{7}	594,969,701	2.93×10^{-2}	4.73×10^{7}
1.1 ± 0.1	628,732,986	2.59×10^{-2}	5.00×10^{7}	678,940,196	2.80×10^{-2}	5.40×10^{7}
1.3 ± 0.1	533,445,424	1.96×10^{-2}	4.25×10^{7}	583,179,162	2.14×10^{-2}	4.64×10^{7}

TABLE 5.1: Table with all the galaxy: count number, number density and angular density; for each catalog.

5.3 Methodology

Our model testing is based on MCMC analysis that uses a nested sampling algorithm, Polychord [79], as implemented in the CosmoSIS[1] framework [165]. Polychord is a robust nested sampling algorithm that incorporates methods to better sample multi-modal posteriors and high-dimensional models. It has been previously used in leading cosmological surveys, i.e, DES-Y3 [3], KiDS [17]) or Planck [7]. We employ Polychord with the following choices: $n_{live} = 100$ (live points), tolerance=0.1 and default settings for the rest of the configuration. Next we shall describe the 3x2pt observables, that is, the angular power spectra for weak

[1] https://cosmosis.readthedocs.io/

lensing, galaxy-galaxy lensing and galaxy clustering, and the covariance matrix used, along with the metric we use to quantify the statistical significance of a bias with respect to the baseline cosmology.

We aim to perform a harmonic 3×2pt analysis combining all the tomographic information by computing the autocorrelations (A-C) within the same z-bin, and cross-correlations (C-C) across different z-bins. For galaxy clustering (GC), we compute only the six A-Cs within the same bin, generating six data vectors. For weak lensing (WL), we calculate six A-Cs and 15 C-Cs across all combinations of bin pairs, resulting in 21 data vectors. In galaxy-galaxy lensing (GGL), the distinction between lenses (density) and sources (shear) breaks the symmetry of C-Cs, leading to 30 C-Cs and six A-Cs, producing 36 data vectors. Altogether, this yields a total of 63 data vectors for our 3x2pt analysis.

5.3.1 Data Vectors

To compute the C_ℓ data vectors, we use the publicly available code *PolSpice*[2], which requires the data in the form of a HEALPix map. These maps are created by converting the right ascension (RA) and declination (DEC) coordinates into pixel indices using the `healpy` module with `nside=1024`. The galaxy count within each pixel is then used to determine the corresponding frequency value. We construct a list containing the frequency values for each pixel, indexed by their respective pixel numbers. Subsequently, we generate the lens and source galaxy sample maps that are needed for the galaxy clustering (GC), galaxy-galaxy lensing (GGL), and the weak lensing (WL) observables.

- **Lens galaxy density map**: using the number of galaxies per pixel we can generate the density fluctuation per pixel, $\delta_{\rm pix}$, following the definition in 2.1 as:

$$\delta_{\rm pix} = \frac{n_{\rm pix} - \bar{n}_{\rm pix}}{\bar{n}_{\rm pix}}, \tag{5.1}$$

  where $n_{\rm pix}$ is the number of galaxies in that given pixel and $\bar{n}_{\rm pix}$ is the mean number of galaxies per pixel over all the unmasked pixels.

- **Source shear map**: we need to generate two sets of maps: one for γ_1 and another for γ_2, the two components of the (complex) shear field, $\gamma = \gamma_1 + i\,\gamma_2$. The values on each pixel represent the averaged shear component of all the galaxies inside that pixel.

Since the catalogs cover the entire sky, no mask is required to exclude specific regions. However, for shear maps, which derive information from the galaxy distribution, it is necessary to handle pixels without galaxies, as these are effectively unobserved. To address this, we generate a mask specific to each redshift bin leaving out the empty pixels.

To incorporate error estimation into our analysis, we use the Jackknife (JK) resampling technique. This involves generating JK regions within the mask, which are excluded (one JK region at a time) during each resampling iteration. We employ the *kmeans-radec*[3] code to create equal-area regions on the celestial sphere, producing 100 JK regions to estimate the covariance matrix of each data vector. We have checked that increasing/decreasing the number of JK subsamples by a factor of two, does not change our results in any signficant way.

We proceed in the analysis as follows: we run the pseudo-C_ℓ code *PolSpice* for the data maps and corresponding masks[4], computing the angular power spectrum for each JK mask. For the

[2] https://www2.iap.fr/users/hivon/software/PolSpice/
[3] https://github.com/esheldon/kmeans_radec
[4] we deconvolve the raw C_ℓ values by the pixel window function

WL observables, such as the deflection (spin-1) and shear (spin-2) maps with two components, we construct a TQU (or TEB) map array containing the corresponding three `HEALPix` maps: one for the amplitude (a scalar, left empty in this case) and the other two maps are for γ_1 and γ_2.

The individual C_ℓ values computed by *PolSpice* are typically noisy, even for the full-sky mock, so we bin them in band powers. In particular, we use 10 logarithmically spaced bins between $\ell = 30$ and $\ell = 1000$. Before binning, we subtract the shot noise contribution, calculated as:

$$N_{\rm shot} = \frac{4\pi f_{\rm sky}}{n_{\rm gal}} \frac{1}{\text{pixelwindow}(\ell)^2},$$

where $n_{\rm gal}$ is the galaxy number density, and $f_{\rm sky} = 1$, given the full-sky coverage. Note that the pixel window correction is also included here for consistency with the corrections applied to the signal C_ℓ's. Once binned, the final binned angular power spectra are obtained by averaging across all JK resampling iterations.

The covariance matrix is then estimated using:

$$\sigma^2_{ij}(C_\ell) = \frac{N_{\rm JK} - 1}{N_{\rm JK}} \sum_{i,j=1}^{N_{\rm JK}} \big[C_\ell(\ell)_i - \bar{C}_\ell(\ell)\big]\big[C_\ell(\ell)_j - \bar{C}_\ell(\ell)\big],$$

where $N_{\rm JK} = 100$ represents the number of Jackknife regions.

5.3.2 Analysis pipeline

The 3x2pt analysis is a powerful way of constraining cosmology, including the nature of the underlying gravity theory. The derivation of observable predictions from a cosmological model, namely from ΛCDM, involves the modeling of the evolution of matter over-densities in the primordial universe in a statistical sense. A field of matter over-densities in the primordial universe will result in clumps of matter than progressively cluster into structures by the action of gravity and against the expansion of the universe. Give the over-density matter field in the early universe, we derive its spatial correlations in terms of the matter power spectrum.

The matter power spectrum quantifies the distribution of matter density fluctuations $\delta(\mathbf{x})$ across different scales. These fluctuations are defined as the excess of matter density at a given region compared with the mean matter density of the Universe:

$$\delta(\mathbf{x}) = \frac{\rho(\mathbf{x}) - \bar{\rho}}{\bar{\rho}} \tag{5.2}$$

Where $\rho(\mathbf{x})$ is the matter density at position $\mathbf{x}$ and $\bar{\rho}$ is the mean density. The power spectrum $P_m(k)$ is defined as the Fourier transform of the two-point correlation function $\xi(r)$, which measures the clustering strength between two points (in this case, galaxies) separated by a distance r.

$$\big\langle \delta(\mathbf{k})\delta^*(\mathbf{k}')\big\rangle = (2\pi)^3 \delta_D(\mathbf{k} - \mathbf{k}') P_m(k),$$

Where $\delta(\mathbf{k})$ is the Fourier transform of $\delta(\mathbf{x})$, δ_D is the Dirac delta function, and $P_m(k)$ is the

matter power spectrum. This expression defines $P_m(k)$ as the variance of density fluctuations per unit wavenumber.

We generate the matter power spectra using the CAMB implementation in CosmoSIS. In order to include the non-linear evolution of the density field, we make use of the revised Halofit boost [140] to model the the non-linear power spectrum, $P_m^{nl}(k)$, from the linear power spectrum.

We have divided the distribution of galaxies in our catalogs into a series of tomographic bins in which to compute the observables as projected into a flat sky, with the distance measure for our correlation functions in real space being the angular separation in the sky. We compute those observables in harmonic space, with our observables in the analysis thus being the angular power spectra for our set of three datavectors (for GC, GGL and WL, respectively).

Given a cosmological model we then generate theoretical predictions for the angular power spectra of each probe and use those predictions for our pipeline of parameter inference. We compute the angular power spectra for GC, GGL and WL within the Limber approximation. In this formalism the equations for the angular power spectra of the three probes is as follows:

$$C_\ell^{\gamma\gamma} = \int_0^{\chi_H} d\chi, \frac{q_{\gamma\gamma}^2(\chi)}{f_K^2(\chi)} P_{\rm m}\left(\frac{\ell+1/2}{f_K(\chi)}, \chi\right), \tag{5.3}$$

$$C_\ell^{gg} = \int_0^{\chi_H} d\chi, \frac{q_{gg}^2(\chi) b^2(\chi)}{f_K^2(\chi)} P_{\rm m}\left(\frac{\ell+1/2}{f_K(\chi)}, \chi\right), \tag{5.4}$$

$$C_\ell^{\gamma g} = \int_0^{\chi_H} d\chi, \frac{q_{\gamma g}(\chi) b(\chi)}{f_K(\chi)} P_{\rm m}\left(\frac{\ell+1/2}{f_K(\chi)}, \chi\right), \tag{5.5}$$

Where b is the galaxy bias and the kernel for each probe is defined as:

$$q_{gg}(\chi) = n_g(z(\chi))\frac{dn}{dz} \tag{5.6}$$

$$q_{\gamma g,\gamma\gamma}(\chi) = \frac{3\,H_0\,\Omega_m}{2\,c^2}\frac{\chi}{a(\chi)}\int_{chi}^{\infty} d\chi' n_\gamma(z(\chi'))\frac{dz}{d\chi'}\frac{\chi'-\chi}{\chi'} \tag{5.7}$$

Given that the Limber approximation can yield inaccurate results for large scales (low ℓ), we compared predictions from CosmoSIS, which use the Limber approximation, against an independent code, Core Cosmological Library [5] [39], which performs the exact integration. We find that only the GC angular power spectra is inaccurate at $\ell < 200$ when using Limber. Therefore, for this multipole range, we use the exact calculation, which is expressed as follows:

$$C_\ell^{gg} = \frac{2}{\pi}\int_0^{\infty}\frac{dk}{k} k^3 P_m^{nl}(k)\Delta_{\delta g}^2(k,\ell) \tag{5.8}$$

With $\Delta_{\delta g}^2(k,\ell)$ being:

[5] https://ccl.readthedocs.io/en/latest/

$$\Delta_{\delta g}(k,\ell) = \int d\chi b^2(z) q_{gg}\, T_{\delta g}\, j_\ell(k\chi) \tag{5.9}$$

Where $T_{\delta g}$ being the transfer function of the primordial power spectrum and $j_\ell(\chi k)$ is the Bessel function.

In terms of non-cosmological parameters, we consider the galaxy bias in our predictions. The linear galaxy bias parameter, as an overall effective scaling factor for the amplitude of the GC and GGL angular power spectra, is expected to compensate for the excess clustering of matter in an $f(R)$ universe with respect to the GR ΛCDM model. On the other hand, we note that the simulated galaxy catalogs do not contain shape noise or intrinsic alignments and therefore these sources of systematic error are not modeled in our analysis. According to this, our modeling is only limited by the validity of the linear galaxy bias assumption and thus we should only include those scales where this assumption holds. In order to accomplish that we defined a series of scale-cuts to the data vectors to avoid biases in cosmology due to non-linear galaxy bias contributions.

In practice, our criteria to define scale-cuts is based on the agreement between theory and measurement in the GR simulation, discarding the scales in which the measured data vectors deviate from the theoretical prediction generated with the fiducial cosmological parameters of the simulation (and after re-scaling the data-vectors using the fitted galaxy bias parameters in each redshift bin). More in detail, for GGL we discard those scales were theory and simulations disagree by more than $3\,\sigma$. For GC data vectors we use a different criteria since error-bars are significantly smaller than for GGL what is some cases could lead to disregard data-points that are roughly consistent between simulation and theory predictions or, in other words, the criteria used for the GC scale-cuts would be too aggressive. Alternatively, we implement scale cuts for GC data-vectors whenever the deviation of simulations with respect to theory is above 5%. We note however that applying this criteria strictly would lead to somewhat inhomogeneous cuts depending on redshift bin, so we have opted for using homogenized scale-cuts per observable, that work on average for all the redshift bins considererd in the analysis. Lastly, for WL we do not observe any significant deviations between theory and simulations up to $\ell_{max} = 1000$. Therefore, the resulting scale cuts for the different probes are: for GC $\ell_{min} = 50$, $\ell_{max} = 400$, for GGL $\ell_{min} = 50$, $\ell_{max} = 250$, and for WL $\ell_{min} = 30$, $\ell_{max} = 1000$.

We include in the discussion of scale-cuts the removal of the data from two tomographic bins for our final cosmological analysis. The last tomographic bin resulted in unexpected behaviour in the WL shear measurements due to the abrupt cut of the galaxy catalogs at redshift z=1.4, which was not included in the theoretical modelling. We also removed the first redshift bin from the analysis due to the large dominance of non-linearities in the GC and GGL. The inclusion of those tomographic bins in the analysis could lead to biases in the inferred cosmology, so we performed the final analysis with 4 z-bins, centered at z=(0.5, 0.7, 0.9, 1.1). While those bins are removed from the pipeline of cosmological parameter inference we nonetheless include them in our comparative discussions regarding measurements in a GR or $f(R)$ universe.

5.3.3 Covariance matrix estimation

In order to generate our covariance matrix we use the public code OneCovariance[6] [125]. We compute the Gaussian terms of the covariance with the addition of the Super Sample Covariance (SSC) which describes the inherent variance introduced by surveys of limited volume not encapsulating density fluctuation beyond the survey size. We neglect non-Gaussian sources of uncertainty but nonetheless compare with the JK estimated covariance to assess their impact and compare it with our analytic estimates. We defer to [125] for the details on the derivation of the covariance terms.

We can think of our analytic covariances as the sum of a Gaussian covariance and the matrix encapsulating the effects of SSC, mostly present in lensing probes at large scales (low ℓ). Those SSC contributions will mostly be on the off-diagonal terms of the covariance.

$$\mathbf{Cov} = \mathbf{Cov}^{Gaussian} + \mathbf{Cov}^{SSC} \tag{5.10}$$

This is illustrated in Figures 5.2 and 5.3, as well as the comparison with the JK-estimated covariance. We will discuss the validation of our covariance in this section.

The first step in our validation consists in comparing the purely Gaussian CosmoSIS-based analytic covariance with either the OneCovariance-based Gaussian + SSC covariance, or the JK-estimated one. JK covariance estimates are susceptible to numerical fluctuations that result in non-definite positive matrices, which makes them unfit for our parameter inference analysis. However, the JK covariance can inherently capture non-Gaussian contributions to the covariance that are expected to originate from the bispectrum and trispectrum of the data maps, as well as small-scale non-linear behavior that may be not properly characterized in the analytic Gaussian estimate. It does not properly characterize SSC, which means that with our three-way comparison we can discern the impact of the different contributions to the covariance.

In Figure 5.2a we present the ratio between the diagonal elements of the GC submatrix of the covariance of either the OneCovariance Gaussian + SSC or the Jackknife and the CosmoSIS Gaussian covariances. We see that the uncertainty estimates from Jackknife are generally larger than the Gaussian and at the same time we see how the addition of SSC into the covariance does not have a substantial impact for GC, as expected. Similarly in Figure 5.2b the uncertainties are still generally larger for the JK estimate, especially when taking into account that our previously detailed scale-cuts remove the high multipole data points of each data vector where JK yields a lower estimate. This increased uncertainty points at the importance of the contributions not accounted for in the Gaussian estimate.

We briefly tested the use of a rescaled Gaussian matrix in order to account for these effects. The rescaled matrix consists in the CosmoSIS-based Gaussian covariance estimate being multiplied by the diagonal elements of the Jackknife covariance in the following way:

$$\mathrm{Cov}_{ij}^{Resc.} = \mathrm{Cov}_{ij}^{An.} \left(\sqrt{\mathrm{Cov}_{ii}^{JK}} \sqrt{\mathrm{Cov}_{jj}^{JK}} \right) / \left(\sqrt{\mathrm{Cov}_{ii}^{An.}} \sqrt{\mathrm{Cov}_{jj}^{An.}} \right) \tag{5.11}$$

[6] https://github.com/rreischke/OneCovariance

Resulting in a covariance that somewhat accounts for the measured uncertainty in the data with the Jackknife estimate despite still neglecting the contribution from off-diagonal terms. However, since issues related to possible numerical instabilities were still present in our tests we limited our analysis to the purely analytical covariance estimations.

As for WL, in Figure 5.2c we see how the impact of SSC is rather large when compared with the Gaussian estimate, this is expected and especially so at the larger scales (low ℓ) corresponding to the lower indexes for each data vector, as seen in the plot. We also recover substantially lower uncertainties for WL and high multipoles when using the Jackknife estimation, like with the case of GGL, and this result is not fully understood.

In Figure 5.3 we can explicitly see the contribution of SSC to the Gaussian matrix. The SSC effects introduce off-diagonal contributions that are not present in the Gaussian estimate, introducing mostly positive correlations in WL and negative correlations in GGL and, to a lesser extent, GC. The introduction of those terms does not affect the numerical stability of the Gaussian + SSC covariance. The OneCovariance-based Gaussian + SSC was chosen as our covariance for the analysis.

Regarding the JK-based estimate for the covariance matrix, we present the full correlation matrix in Figure 5.4 where we see a large number of off-diagonal terms in all of the submatrices. While those off-diagonal terms do capture the previously mentioned effects that are not characterized in the Gaussian matrix, the noisy nature of the computation and the consequent numerical instability of the matrix prevents its use in the analysis.

5.3.4 Metrics

The quantification of statistical discrepancies for the parameters of a model can become difficult when trying to capture discrepancies that are lost upon the projection of the posteriors into 1-D. We decided to use the Mahalanobis distance as our metric, which is defined as follows:

$$d_M = \sqrt{(\vec{\mu} - \vec{x})^T \, \mathbf{Cov}^{Post} \, (\vec{\mu} - \vec{x})} \tag{5.12}$$

Where $\vec{x}$ is the set of central values on our roughly Gaussian posteriors, $\vec{\mu}$ is the set of fiducial values used in the simulations and $\mathbf{Cov}^{Post}$ is the covariance matrix from the combined 2-D posterior for a pair of variables, defined as:

$$\mathbf{Cov}^{Post} = \begin{bmatrix} \sigma_{x_i,x_i} & \sigma_{x_i,x_j} \\ \sigma_{x_j,x_i} & \sigma_{x_j,x_j} \end{bmatrix}. \tag{5.13}$$

While the discussion of an appropriate metric may need further consideration (see for example [106]), it is enough for our work to consider the present metric to provide an estimate of the strength of the bias from erroneous modeling of gravity is cosmology.

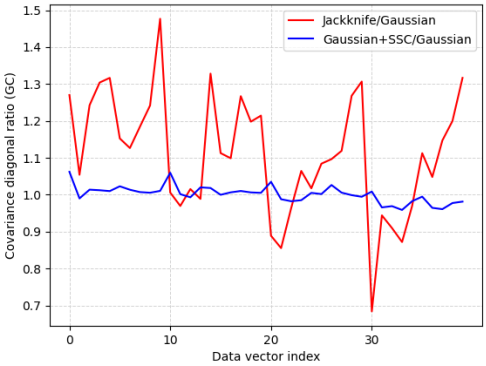

(A) Ratios for the diagonal elements of the covariances corresponding to GC.

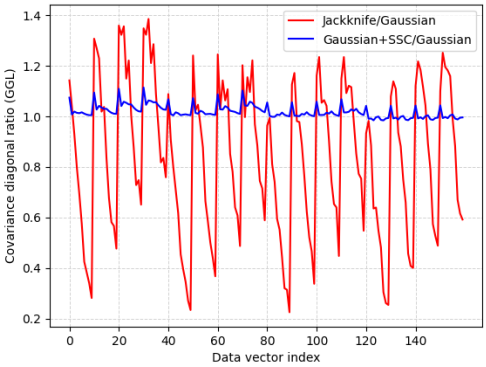

(B) Ratios for the diagonal elements of the covariances corresponding to GGL.

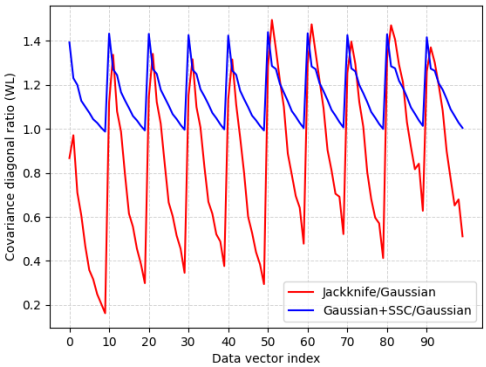

(C) Ratios for the diagonal elements of the covariances corresponding to WL.

FIGURE 5.2: Ratios between CosmoSIS-based (Gaussian) and OneCovariance-based (Gaussian + SSC) analytic and Jackknife covariance matrix diagonals By comparing the CosmoSIS-based Gaussian matrix with the OneCovariance-based we directly see the effect of SSC, present mostly in WL and in GGL to a lesser extent.

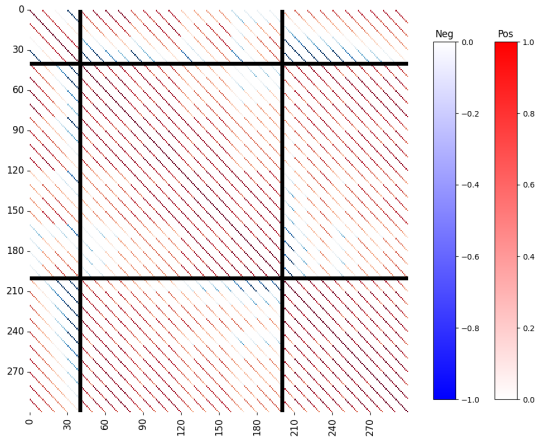

(A) Predicted Gaussian correlation matrix generated with CosmoSIS.

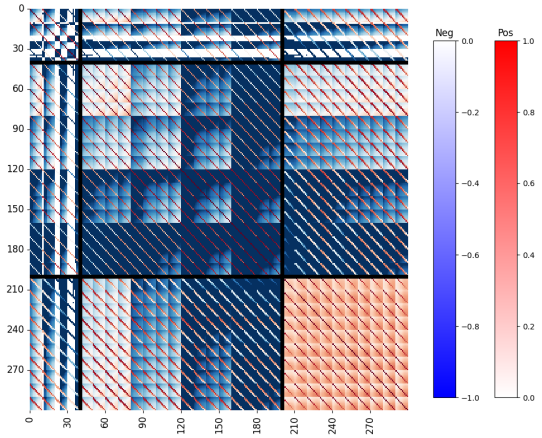

(B) Predicted Gaussian correlation matrix with SSC generated with OneCovariance.

FIGURE 5.3: Analytic correlation matrices for 3x2pt. The CosmoSIS-based Gaussian correlation and the OneCovariance-based Gaussian + SSC correlation. Each matrix is subdivided, from left to right, into GC, GGL and WL. We see how the addition of SSC mostly increases WL uncertainties, as expected.

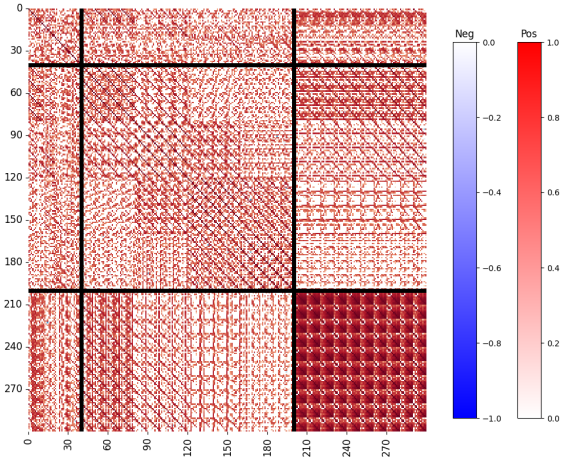

FIGURE 5.4: JackKnife correlation matrix estimate $N_{\rm JK} = 100$ for the 4 tomographic redshift bins used for the GR catalog.

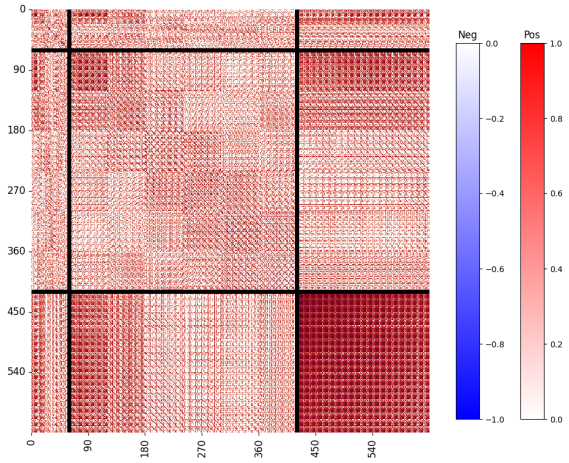

FIGURE 5.5: Full joint Jackknife $N_{\rm JK} = 100$ correlation matrix for the 6 zbins for the $f(R)$ catalog. The order of the data vectors are given by: GC, GGL, WL

5.4 Results

5.4.1 Data Vector Comparison

In this section we present the data vectors by plotting the ratio of the values for $f(R)$ over GR.

In Figure 5.6, we present the galaxy clustering results. The GR mock exhibits a stronger clustering signal compared to $f(R)$. This is based on the fact that the mass function in the F5 model is shifted toward higher masses (at a given redshift) compared to GR. This occurs because the gravitational growth (or rate of structure formation) is enhanced in the F5 model. Thus, at a given z, the abundance of halos at a specific mass (for masses above a certain threshold, roughly corresponding to an absolute magnitude cut) will be higher in F5 than in GR. Consequently, the halo bias will be lower in F5 (since greater abundance leads to lower bias) [16]. This trend should become more pronounced as one moves to lower z. However, in the galaxy mock catalogs, this effect is somewhat masked by the calibration, which enforces the same clustering for F5 and GR, to match observations. In our case, we are using a very faint magnitude cut which corresponds to effectively selecting mostly those galaxies found at the center of the (low-mass) halos. This central galaxies serve as halo proxies and trace a distribution with a lower signal in $f(R)$ than GR due to the reduced halo bias as explained above.

The ratio of clustering remains approximately constant across all redshift bins, with a difference of around 10%, except at $z = 0.3$. At small scales in this redshift bin, the ratio approaches unity, which aligns with expectations since the mocks were calibrated at low redshifts, leading to similar clustering.

In Figure 5.7, we present the weak lensing results. Here, the signal is stronger for $f(R)$ gravity compared to GR, with the difference becoming increasingly significant at smaller scales. Since cosmic shear directly traces the underlying matter distribution, the clustering reflects the enhanced matter spectrum in $f(R)$ gravity relative to GR, as described in [16].

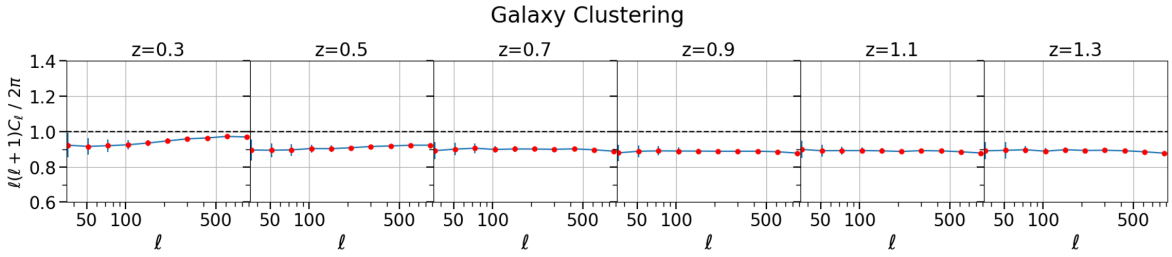

FIGURE 5.6: Ratio of $f(R)$ over GR of all the galaxy clustering data vectors. Note we do not include the cross-correlation between z-bins in the analysis.The errors are given by the error propagation of the JK errors of each catalog.

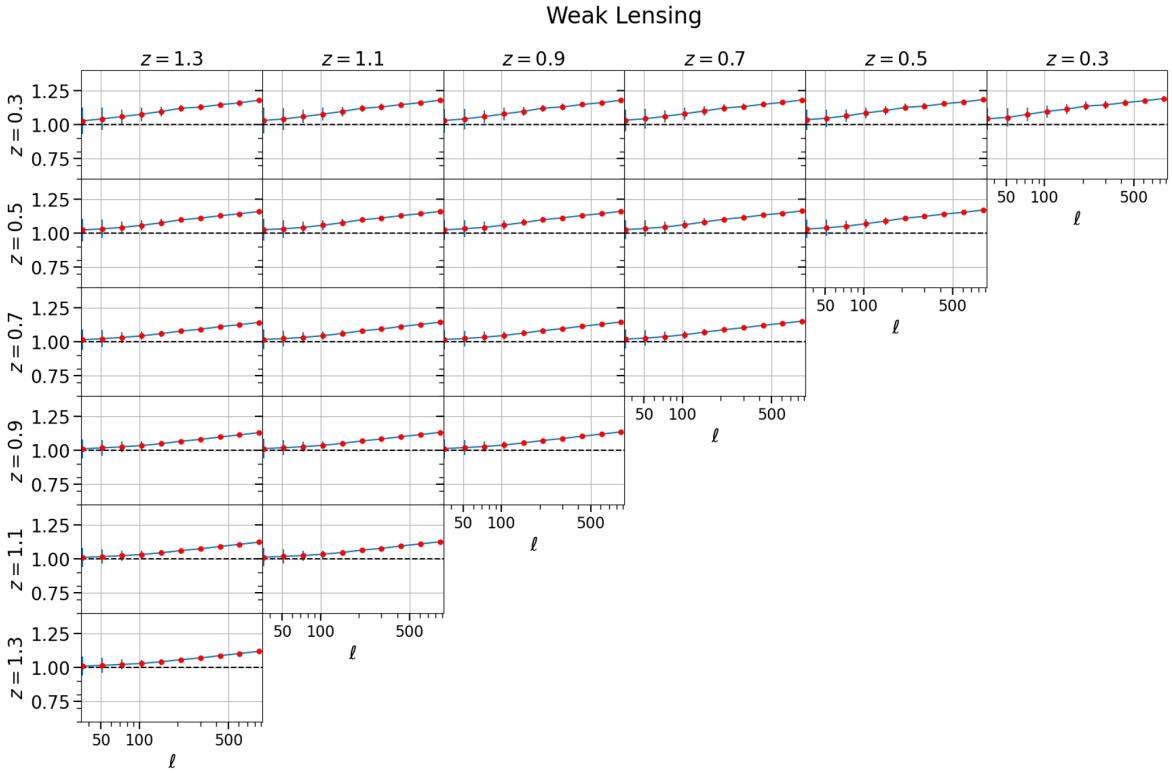

FIGURE 5.7: Ratio of $f(R)$ over GR of all the weak lensing data vectors. The errors are given by the error propagation of the Jackknife errors of each catalog.

Lastly, in Figure 5.8, we present the galaxy-galaxy lensing results. The ratio is consistent with 1 overall, with GR displaying a slightly stronger signal at large scales, whereas the opposite trend is observed at smaller scales. In this scenario, in $f(R)$ gravity, the enhanced weak lensing (matter) signal and the reduced galaxy signal appear to compensate, resulting in a ratio close to unity. For cases where the sources lie behind the lenses, the ratio exhibits fluctuations due to the signal being largely noise-dominated, as indicated by the substantial error bars.

In Figure 5.5, we present the full JK correlation matrix for the joint analysis of all 63 data vectors for $f(R)$. Due to the large size of the 6300x6300 matrix, the covariance matrix is not invertible.

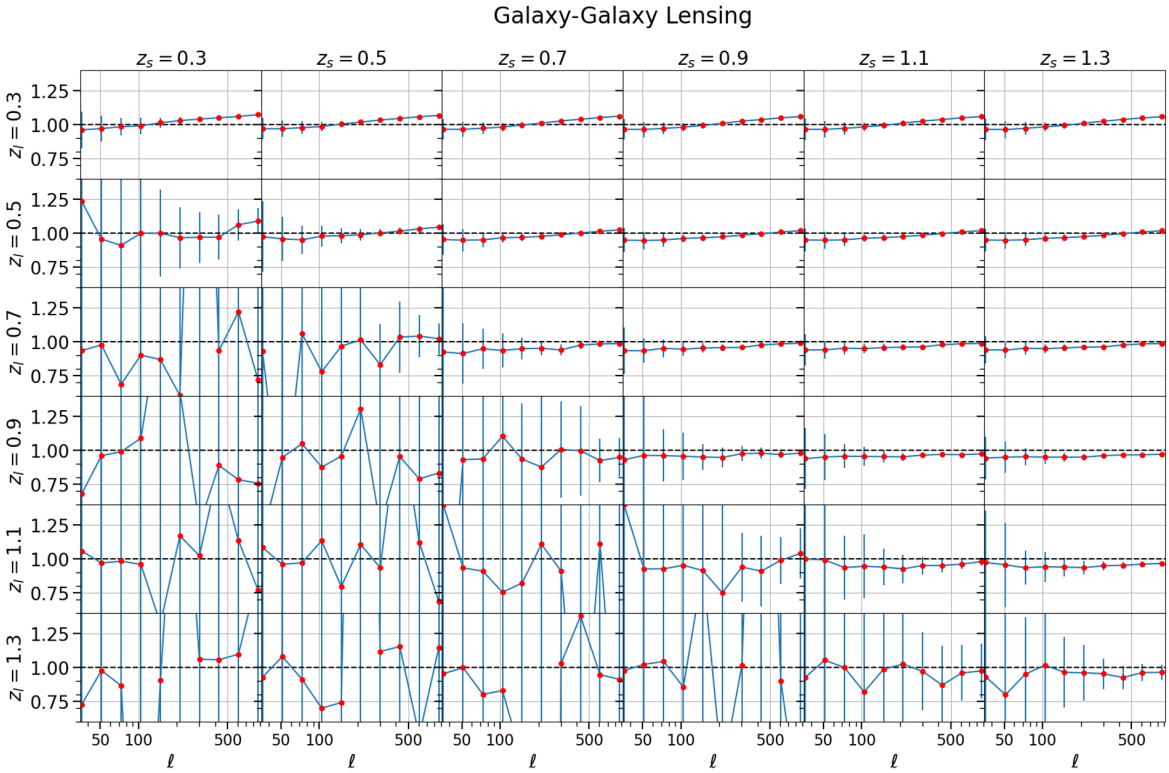

FIGURE 5.8: Ratio of $f(R)$ over GR of all the galaxy-galaxy lensing data vectors. The errors are given by the error propagation of the Jackknife errors of each catalog.

5.4.2 Parameter inference

Our cosmological analysis pipeline was applied to the data vectors measured from the simulations. We perform the parameter inference for different sets of cosmological parameters, namely (Ω_m, A_s) and $(\Omega_m, \Omega_b, A_s, h, n_s)$, the latter still in preparation, applying CMB-based priors in the latter case to account for the reduced constraining power of LSS for certain parameters. Our only systematic present in the measured data vectors, the galaxy bias (for each redshift bin), is included in our sampling. As previously discussed, in an $f(R)$ universe, how baryons trace the underlying dark-matter changes, and thus the galaxy bias would differ from a GR universe. In this section we compare the inferred cosmology when assuming the correct (or not) gravity theory, and quantify the cosmological bias in the inferred parameters for the ΛCDM parameters, for different sub-sets of them.

In Figure 5.9 we see that for Ω_m and A_s, using GR mock measurements one recovers the input cosmological parameters of the simulation, as the true values for the parameters fall within the narrow $2-\sigma$ contour. In contrast, when the data vectors of the $f(R)$ universe are used, the inferred cosmology is significantly biased. This is indeed a detection of Modified Gravity. Using our previously defined Mahalanobis metric the deviation between the true values and the mean values of the posterior is of $\approx 40-\sigma$. The deviation in the 2-D likelihood contours is thus highly significant.

It is interesting to note that, as expected, when fitting the F5 data within the ΛCDM paradigm, one estimates an excess in Ω_m and A_s, since the positive shift in these two parameters mimic the accelerated growth of structure due to the fifth force of the MG model. In

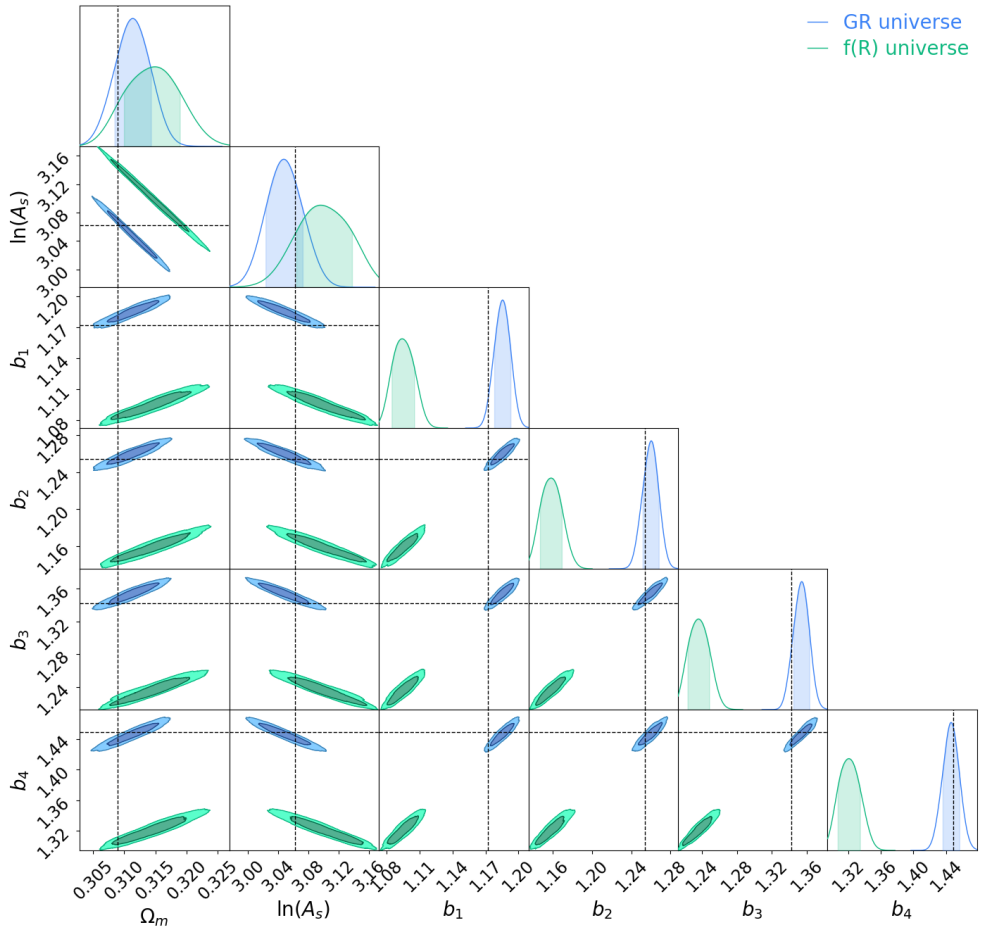

FIGURE 5.9: Constraints on all the sampled parameters in our 3x2pt analysis for our Ω_m and A_s case. Here the galaxy bias constraints are shown explicitly and will be omitted henceforth. The input values of the cosmology of the simulations is shown as a set of black lines.

addition, the galaxy bias parameters are also expected to differ in an $f(R)$ universe as galaxies on average tend to populate smaller mass dark matter halos. This is precisely what we see in the panels for the galaxy bias parameters for each tomographic bin in Figure 5.9, where the inferred galaxy bias in an $f(R)$ universe is smaller than in GR with high statistical significance.

The other parameter of interest in our comparative analysis is S_8, directly related to structure formation in the modern universe and thus heavily impacted by the change in structure formation due to modified gravity. We present in Figure 5.10 the constraints on S_8 along with Ω_m. While the fiducial values of parameters for the simulation are mostly recovered right at the $2-\sigma$ level for the GR universe, we find that the recovered S_8 in the $f(R)$ universe is significantly biased. The deviation for the $f(R)$ case is estimated to be at $\approx 38-\sigma$ using our Mahalanobis distance estimator.

Comparing the biases in Ω_m and A_s to those in S_8, the bias in the first two of them is dependent on the correlation between the two parameters and thus "orthogonal" to the true

value, with the 1-D marginalized posterior for those parameters containing the fiducial values. However, for the latter, the shift is highly statistically significant even in the marginalized 1-D posterior. This result may be of particular interest in the discussion of the observed S_8 tensions, in particular those that arise from probes of the primordial (CMB) and the local universe (galaxy surveys). Given that LSS probes have yielded lower values for S_8 (KiDS: $S_8 = 0.759 \pm 0.02$, DES-Y3: $S_8 = 0.776 \pm 0.017$, HSC: $S_8 = 0.780 \pm 0.03$) while the Planck measurements obtained a higher value ($S_8 = 0.834 \pm 0.016$), our results suggest that a slight deviation in the gravity theory, such as that between F5 and GR, could change the physics of the low redshift universe, thus reconciling the amplitude of clustering (i.e., S_8) in the low and high redshift universe. This idea would be in line with recent measurements of the Weyl potential that hint at Modified Gravity being the origin of the σ_8 tension between LSS and CMB probes [145].

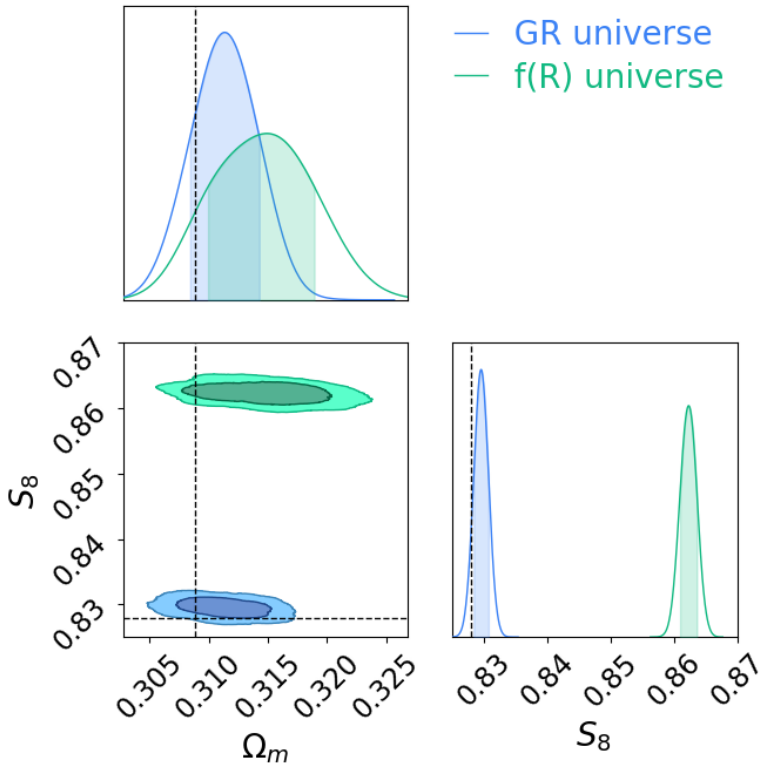

FIGURE 5.10: Constraints on the derived parameter S_8 and Ω_m. The corresponding values for the cosmology of the simulations is shown as the two black lines.

While the best constrained parameters in LSS probes are those most related to structure formation, with photometric clustering being less sensitive to the shape of the primordial power spectrum or to the Hubble parameter, it is important to understand how the bias in Ω_m and A_s changes when the rest of the parameters can vary freely in order to assess the robustness of such a bias in the inferred cosmology.

Chapter 6

Other contributions: scientific preparation of new generation galaxy surveys

In this section, we outline the contributions we made to other collaborations (within Euclid and DESI) during the course of this thesis, applying the methodologies developed throughout the research.

6.1 Euclid mission

6.1.1 Euclid preparation: XIX. Impact of magnification on photometric galaxy clustering

This study, presented in [107], provides a forecast for the Euclid mission, assessing the impact of weak lensing magnification on the cosmological constraints of the Euclid mission derived from the photometric galaxy clustering.

In this work, my contribution was to estimate the linear galaxy bias and magnification bias for the analysis. In detail, we used the Flagship galaxy mock to model galaxy distributions, biases, and luminosity slopes to evaluate the impact of magnification on cosmological parameter estimation using photometric clustering. In order to generate the photometric redshifts, we used the galaxy distributions based on the fiducial selection from [121], where photometric redshift estimates were generated for objects across 400 square degrees of the Flagship catalog. Using the Directional Neighbourhood Fitting (DNF) algorithm, two redshift estimates were provided for each galaxy: $z_{\rm mean}$, the average redshift of galaxies in the neighborhood of similar colors and magnitudes, and $z_{\rm mc}$, a Monte Carlo sampling of the photometric redshift probability density function. The sample used included galaxies with $z_{\rm mean}$ between 0 and 2, divided into 13 equal-width bins. For theory predictions, the final redshift distribution $n(z)$ is derived from the values of $z_{\rm mc}$ in each bin. Despite equal bin widths in $z_{\rm mean}$, non-Gaussianity in $z_{\rm mc}$ causes the mean redshift ($\bar{z}$) of the bins to be unevenly spaced.

The linear galaxy bias is calculated following the same detailed methodology presented in section 3.5.1. This implies obtaining the square-root ratio between the angular galaxy-galaxy power spectrum, $C_\ell^{\rm gg}$, from the different $n(z)$ samples and the angular matter-matter power spectrum, $C_\ell^{\delta\delta}$. The $C_\ell^{\rm gg}$ is obtained from the maps of the fractional overdensity of galaxies, generated using *healpy* with $N_{\rm side} = 4096$ maps. We estimated the angular power spectra using PolSpice. Mask effects for the 400 square degrees photo-z region are also accounted for the harmonic space analysis. The resulting C_ℓ values are corrected for shot noise using $C_\ell^{\rm corr} = C_\ell - 4\pi f_{\rm sky}/n_{\rm gal}$, where $f_{\rm sky}$ is the fraction of the sky covered by the photo-z sample

and $n_{\rm gal}$ is the number of galaxies in the sample. The $C_\ell^{\delta\delta}$ is modeled with the *pyCCL* using the fiducial cosmology of the Flagship simulation. We use Limber's approximation for every multipole, since at the time *pyCCL* did not allow using a non-Limber framework. The linear galaxy bias is calculated as the mean value across the multipoles range $\ell \in [50, 500]$ to avoid non-linear (or higher order) bias effects. While as described in Section 3.6.3, the magnification bias factor is derived from the local count slope.

In terms of galaxy sample selection, we used the observed magnitudes in the Euclid VIS band, incorporating error realizations and assuming a 10σ magnitude limit of 24.6. A cut at magnitude 24.5 was applied for our subsequent analysis. To determine the slope, we computed a binned cumulative magnitude distribution for the photometric redshift sample across different redshifts. The slope at the magnitude cut was then estimated using bins centered at 24.45 and 24.55. In Figure 6.1 and Table 6.1 we show all the results provided and presented on the paper.

TABLE 6.1: Number density (in units of gal/bin/arcmin^2), galaxy bias and local count slope used in each photometric bin. Values extracted from the Flagship simulation.

$\bar{z}$	$n_{\rm gal}(\bar{z})$[gal/bin/arcmin^2]	$b(\bar{z})$	$s(\bar{z})$
0.14	0.758	0.624	0.023
0.26	2.607	0.921	0.135
0.39	4.117	1.116	0.248
0.53	3.837	1.350	0.253
0.69	3.861	1.539	0.227
0.84	3.730	1.597	0.280
1.0	3.000	1.836	0.392
1.14	2.827	1.854	0.481
1.3	1.800	2.096	0.603
1.44	1.078	2.270	0.787
1.62	0.522	2.481	1.057
1.78	0.360	2.193	1.138
1.91	0.251	2.160	1.094

All the values that we provided are later used when analyzing the angular power spectra and their dependence on redshift. They incorporated linear perturbation theory (using the CLASS code) and estimated the uncertainties on the cosmological parameters using a Fisher matrix formalism for clustering and lensing effects.

The linear galaxy bias was obtained by fitting the full sky angular power spectrum of the data to the corresponding fiducial prediction for each n(z). Similarly to what we detailed in sec. 3.5.1 the angular power spectrum was obtained using PolSpice with a mask to generate 100 Jackknife regions that we use to calculate the covariance matrix. We subtract the shot noise of each resample using an analytical expression that accounts for the total number of galaxies in each n(z). The prediction is obtained using CAMB sources with the fiducial cosmological parameters values of the Flagship simulation. The linear scales considered go from power spectrum multipoles $\ell = 80$ to a given ℓ_{max} that increases as we go to higher redshifts (as the effective non-linear galaxy bias scale shifts to larger multipoles, i.e, smaller angular scales), starting at $\ell \sim 300$ for z=0.90 to $\ell \sim 500$ for z=1.8.

The results of this paper demonstrate that, including the magnification consistently in the

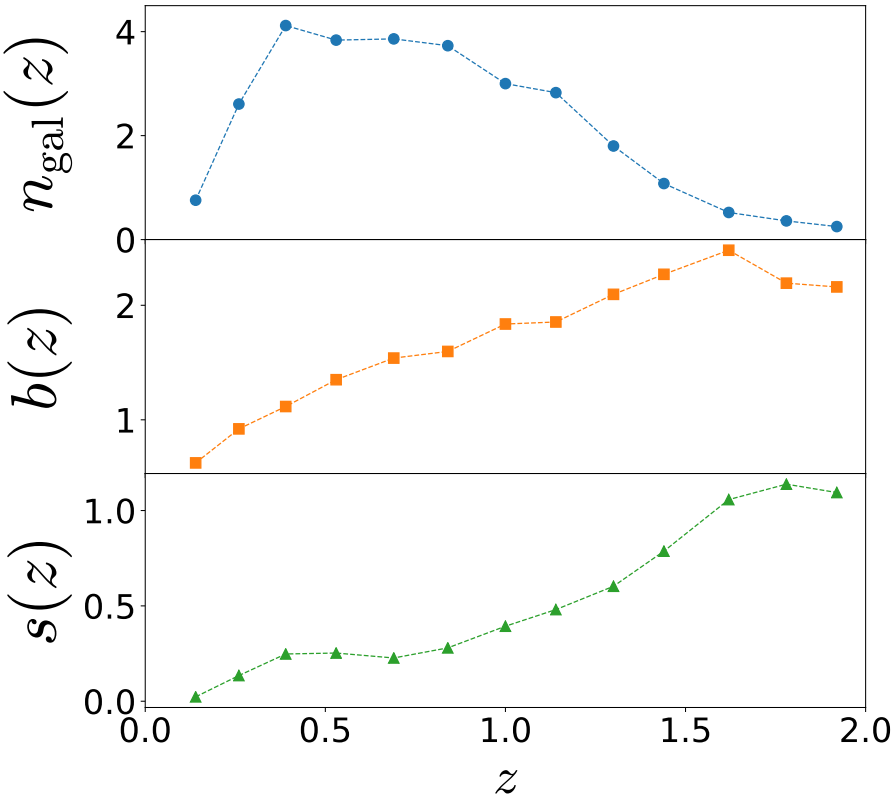

FIGURE 6.1: Values provided for [107] of the galaxy number density in units of gal/bin/arcmin^2 (top panel), galaxy bias (middle panel), and local count slope (bottom panel) as a function of redshift. These results are obtained from the Flagship simulation.

analysis, significantly improves parameter precision and reduces the biases observed when neglecting magnification. Including magnification also reduces uncertainties in basic cosmological parameters such as matter density (Ω_m) and dark energy (w_0, w_a) by 20–35%, depending on the accuracy of the galaxy luminosity slope. Failing to include magnification results in substantial biases, with best-fit parameter shifts up to 1.6σ in galaxy clustering and over 6σ in joint analyses. These effects are most pronounced at large angular scales and when cross-correlating distant redshift bins, where magnification becomes dominant. This means that magnification must be integrated into analyses of the Euclid mission to avoid biases and potentially threaten the overall scientific goals of the mission. In fact, by including magnification, the survey can better test dark energy models, achieve tighter constraints on ΛCDM, and enhance the overall accuracy of parameter estimates. This study sets a precedent for future photometric surveys, emphasizing the necessity of accounting for lensing magnification in cosmological analyses.

6.1.2 Euclid preparation. Impact of magnification on spectroscopic galaxy clustering

In this analysis, presented in [46], we investigate the impact of lensing magnification on the analysis of galaxy clustering using the Euclid spectroscopic survey (in contrast with the photometric surveys used in the previous section). Similarly to the previous contribution, we also provided an estimation of the linear galaxy bias and the magnification bias using the high-fidelity Flagship galaxy mock.

Magnification is often ignored in spectroscopic analyses due to the dominance of other effects like redshift-space distortions. We selected 13 equidistant bins, between z=0.90 and z=1.8, in real space redshift distribution, n(z). We imposed a cut in H_α flux, $\log(F_{H_\alpha}) > -15.7$ $ergs/s/cm^2$.

The linear galaxy bias was analyzed similarly to the previous section, with some modifications. The analysis considered linear scales ranging from $\ell = 50$ to an $\ell_{\max}$ that increases with redshift. This reflects the shift of the effective non-linear galaxy bias scale to higher multipoles (smaller angular scales), starting at $\ell_{\max} \sim 300$ for $z = 0.9$ and reaching $\ell_{\max} \sim 500$ for $z = 1.8$. Due to the limitations in *pyCCL*, the Limber approximation was employed once again. At the scales analyzed, this approximation introduces up to a 4% variation in the predicted angular power spectrum, corresponding to an error of less than 2% in the galaxy bias estimation. Additionally, 100 Jackknife regions were generated to measure the local count slope and calculate the variance of the results. In Figure 6.2 we show the values provided and presented for this paper.

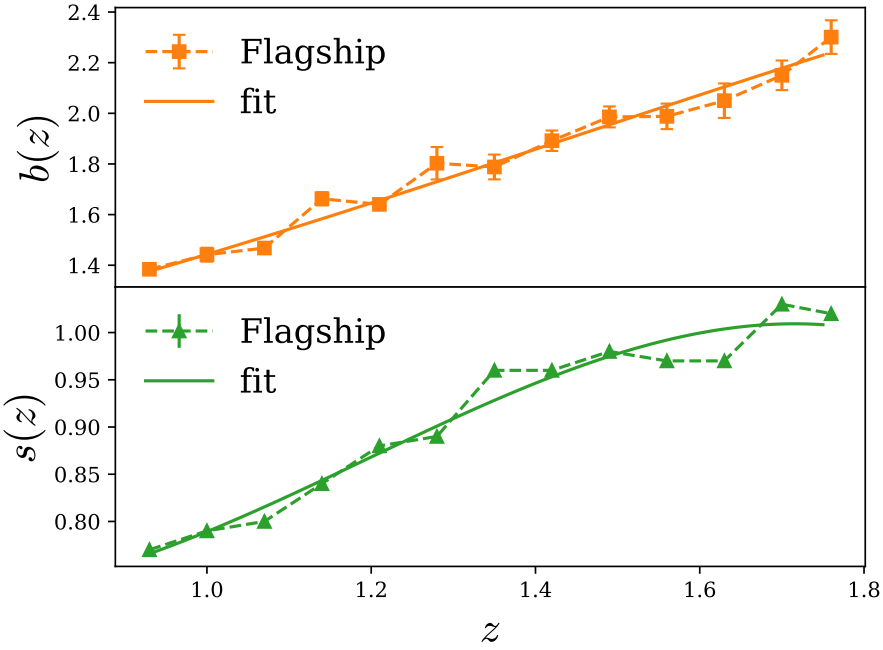

FIGURE 6.2: Values provided for [46] galaxy bias (top panel) and the local count slope (lower panel) with linear interpolation (dashed), as used in our analysis, along with their associated error bars, as well as a polynomial fit (solid).

This study assesses the significance of lensing magnification in two main cosmological analyses: a model-dependent analysis based on ΛCDM and its extension to dynamical dark energy, and a model-independent analysis aimed at measuring the growth rate of structure in redshift bins. Using both Fisher matrix formalism and Markov Chain Monte Carlo (MCMC) techniques, the paper forecasts the shifts in best-fit parameters and changes in parameter constraints caused by neglecting magnification. The results show that ignoring lensing magnification introduces biases of 0.4–0.7 standard deviations in ΛCDM parameters and up to 1.2 standard deviations in growth rate estimates at the highest redshifts. These biases could undermine efforts to test general relativity and alternative gravity models. To mitigate these biases, the paper proposes incorporating a simple template for lensing magnification into the modeling process. This approach, which assumes fixed fiducial cosmological parameters, effectively removes biases while requiring minimal additional computational effort. However, when magnification is

included as part of the analysis with unknown parameters, it slightly increases degeneracies, modestly worsening constraints on some cosmological parameters.

In conclusion, the study finds that in order to get unbiased cosmological constraints from the spectroscopic 2-point galaxy clustering statistics from the Euclid mission lensing one should appropriately include magnification in the modeling.

6.1.3 Euclid: Relativistic effects in the dipole of the 2-point correlation function

We also contributed to the scientific preparation of the Euclid mission in [108]. This paper explores relativistic effects captured in the dipole, or $\ell = 1$, for the multipoles of the correlation function, within the framework of the Euclid spectroscopic galaxy survey. The analysis aims to isolate and measure subtle relativistic effects like gravitational redshift and Doppler effects, which contribute to the odd multipoles of the correlation function.

Relativistic effects in the dipole of the two-point correlation function arise from subtle corrections introduced by general relativity in the observed redshifts and positions of galaxies. These effects include gravitational redshift, Doppler effects (caused by peculiar velocities) and related phenomena, which together contribute an antisymmetric component to the correlation function, manifesting as a dipole.

Gravitational redshift occurs because galaxies are located in gravitational potential wells, and photons escaping these regions lose energy, causing a shift in their wavelength. This effect introduces an asymmetry in the observed redshifts of galaxy pairs, depending on their positions relative to these potential wells. Additionally, the peculiar velocities of galaxies along the line of sight induce Doppler shifts in their observed redshifts, further contributing to the dipole. Galaxies moving towards the observer appear to have a higher clustering amplitude, while those moving away appear less clustered, creating a directional asymmetry.

Another contributing factor is wide-angle effects, which arise when the assumption of parallel lines of sight for a pair of galaxies breaks down. These effects add further asymmetry by accounting for the angular separation between galaxies and the observer. While other relativistic corrections, such as the integrated Sachs-Wolfe effect and Shapiro time delay, play a smaller role in shaping the dipole, they still subtly influence galaxy redshifts by modifying photon travel times and energy along their paths due to evolving gravitational potentials or delays.

The dipole signal emerges prominently when analyzing cross-correlations between two distinct galaxy populations, such as "bright" (more massive) and "faint" (less massive) galaxies. These populations experience gravitational redshift and Doppler effects differently due to variations in their distribution within large-scale structures, leading to an antisymmetric feature in their correlation function. The strength of the dipole is particularly sensitive to the bias contrast between the two populations—greater differences amplify the signal. On smaller scales, typically below $\sim 30\ h^{-1}$ Mpc, the dipole is dominated by nonlinear gravitational potentials, as the deep potential wells of massive halos enhance the gravitational redshift contribution. The detection and analysis of the relativistic dipole have profound implications for cosmology and astrophysics. Since the dipole is closely tied to gravitational potentials, it provides a novel test of general relativity, including the equivalence principle and local position invariance. Furthermore, the dipole offers insights into the nature of dark energy and the interplay between modifications to gravity and new forces in the dark sector. On an astrophysical level, the dipole helps improve our understanding of the distribution of galaxies and the underlying matter that shapes large-scale structures in the Universe. Thus,

while challenging to measure, the relativistic dipole is a subtle yet powerful probe of the fundamental physics governing the cosmos.

This study uses the Flagship mock, simulating galaxy distributions under various relativistic corrections. The methodology involves:

- Splitting Galaxy Populations: Dividing galaxies into "bright" and "faint" categories based on flux to create a differential bias that enhances the dipole signal.
- Modeling Relativistic Effects: Including contributions from nonlinear gravitational potentials using Navarro–Frenk–White profiles for halos and implementing corrections for gravitational redshift in simulated data.
- Statistical Analysis: Estimating the dipole from cross-correlations of galaxy populations in different redshift bins and scales, and calculating the signal-to-noise ratio (S/N) using theoretical and Jackknife-based covariance matrices.

Once again we provided the values for the linear galaxy bias and the magnification bias slope factor for this project in order to model the predictions. Since in this cases the studies relays in performing cross-correlations between two samples of galaxies: one faint and one bright; we needed to generate the samples. We selected the spectroscopic data from the Flagship simulation, version 2.1.10, using the following criteria. Objects are included based on their Hα flux, applying a threshold of $F_{\mathrm{H}\alpha,\,\mathrm{lim}} = 2{\times}10^{-16}\,\mathrm{erg\,cm^{-2}\,s^{-1}}$. Two samples are considered: one containing only central galaxies and another including both central and satellite galaxies. The simulated dataset spans a redshift range from $z_{\mathrm{min}} = 0.9$ to $z_{\mathrm{max}} = 1.8$. This range is divided into four redshift bins centered at $\bar{z} = 1,\ 1.2,\ 1.4,\ 1.65$, with corresponding half-bin widths of $\sigma_{\bar{z}} = 0.1,\ 0.1,\ 0.1,\ 0.15$.

The luminosity distance is influenced by perturbations, which means the measured fluxes are also subject to relativistic effects, including magnification and Doppler corrections. In the Flagship mock, the observed fluxes account for some observational effects, such as dust extinction, but do not include magnification from lensing or Doppler effects. To incorporate these relativistic effects, we adjusted the fluxes using the relation:

$$F_{\mathrm{magn}} = F_{\mathrm{FS}}\ \frac{(1+z)^4}{(1+z_{\mathrm{obs}})^4}\ \mu_{\mathrm{L}}\,, \tag{6.1}$$

where F_{FS} represents the fluxes stored in the mock, F_{magn} denotes the corrected (magnified) fluxes, and μ_{L} is the magnification factor due to gravitational lensing. This magnification factor is expressed in terms of the convergence κ and the shear $\gamma = \gamma_1 + \mathrm{i}\,\gamma_2$ as follows:

$$\mu_{\mathrm{L}} = \frac{1}{(1-\kappa)^2 - \gamma_1^2 - \gamma_2^2}\,. \tag{6.2}$$

Thus, the magnified fluxes F_{magn} are influenced by gravitational lensing through μ_{L} and by Doppler effects and gravitational redshift through z_{obs}.

Using the magnified fluxes, two primary splitting schemes for the samples were proposed: one with an even 50%-50% division into faint and bright galaxies, and another with a 90%-10% split, favoring faint galaxies. To explore other configurations, we calculated the linear galaxy bias and magnification bias for additional split ratios, including 1%-99%, 10%-90%, 20%-80%, 80%-20%, and 99%-1%. From these tests, we determined that the highest signal-to-noise ratio (S/N) was achieved for the two cased selected. The splits were generated by sorting galaxies based on their magnified flux F_{magn} in Hα flux, with the bright sample comprising

galaxies above the corresponding split percentage and the faint sample including those below it. The bright and faint galaxy populations result from two flux thresholds: the one in Hα flux ($F_{\mathrm{H}\alpha,\,\mathrm{lim}}$) and another in Y_{E}-band flux ($F_{Y_{\mathrm{E}},\,\mathrm{lim}}$) to perform the magnification bias calculation. Magnification can alter the population counts in two ways: shifting galaxies across the $F_{\mathrm{H}\alpha,\,\mathrm{lim}}$ threshold and transferring galaxies between the faint and bright populations across $F_{Y_{\mathrm{E}},\,\mathrm{lim}}$. An effective count slope for the bright and faint populations, $s_{\mathrm{B/F,eff}}$, combines contributions from both flux thresholds:

$$s_{\mathrm{B/F,eff}} = s_{\mathrm{B/F,H}\alpha} + s_{\mathrm{B/F},Y_{\mathrm{E}}}\,, \tag{6.3}$$

where each term is defined using the logarithmic derivative of the galaxy counts with respect to the luminosity at the respective flux threshold. The counts of bright ($\bar{N}_{\mathrm{B}}$) and faint ($\bar{N}_{\mathrm{F}}$) galaxies depend on their luminosities in both bands, $\bar{L}_{\mathrm{H}\alpha}$ and $\bar{L}_{Y_{\mathrm{E}}}$. Due to the flux threshold $F_{Y_{\mathrm{E}},\,\mathrm{lim}}$, bright and faint populations are interdependent, leading to a relation between their slopes:

$$s_{\mathrm{F},Y_{\mathrm{E}}} = -\frac{\bar{N}_{\mathrm{B}}}{\bar{N}_{\mathrm{F}}} s_{\mathrm{B},Y_{\mathrm{E}}}\,. \tag{6.4}$$

To estimate these slopes, we used a deeper mock catalog for $F_{\mathrm{H}\alpha,\,\mathrm{lim}}$ and calculated $s_{\mathrm{B/F,H}\alpha}$ with fixed Y_{E}-band flux cuts. For $s_{\mathrm{B},Y_{\mathrm{E}}}$, we analyzed the cumulative luminosity function (LF) of the bright population at $F_{Y_{\mathrm{E}},\,\mathrm{lim}}$, accounting for redshift-dependent Y_{E}-band cuts. The final effective slopes are averaged across sub-bins, weighted by the number of objects in each bin.

In Figure 6.3 we show the provided values for the central galaxies for the galaxy bias and the magnification bias for the two split configurations.

The dipole signal was detected in simulations, particularly on scales smaller than 30 h^{-1} Mpc. The significance of detection varied by redshift. In the two lowest redshift bins, detection significances were $4\,\sigma$ and $3\,\sigma$, respectively. While at higher redshifts, the significance fell below $2\,\sigma$. The overall detection significance across the survey was estimated at approximately $6\,\sigma$. Nonlinear gravitational potentials were identified as the primary contributors to the small-scale dipole.

This paper demonstrates the feasibility of detecting relativistic dipole effects in future Euclid data releases, with implications for understanding the interplay between general relativity and large-scale structure. The findings suggest that Euclid's spectroscopic survey can robustly measure these relativistic signals, enabling tests of fundamental cosmological principles, such as the equivalence principle and local position invariance, and distinguishing between modified gravity theories and dark sector forces.

6.1.4 Euclid. V. The Flagship galaxy mock catalogue: a comprehensive simulation for the Euclid mission

During the realization of this Thesis we used the Flagship mock several times to compute basic 2-point statistics such as the clustering and lensing angular power spectra. By comparing results from this simulation to theory predictions in order to estimate the linear galaxy bias, the growth rate, or the magnification bias factor, we provided several validations of the mock. One of the most important validations was that of the magnification signal in the catalog which, as described in section 3.6.5, resulted in to the estimation of the lensed galaxy positions in the mock catalog.

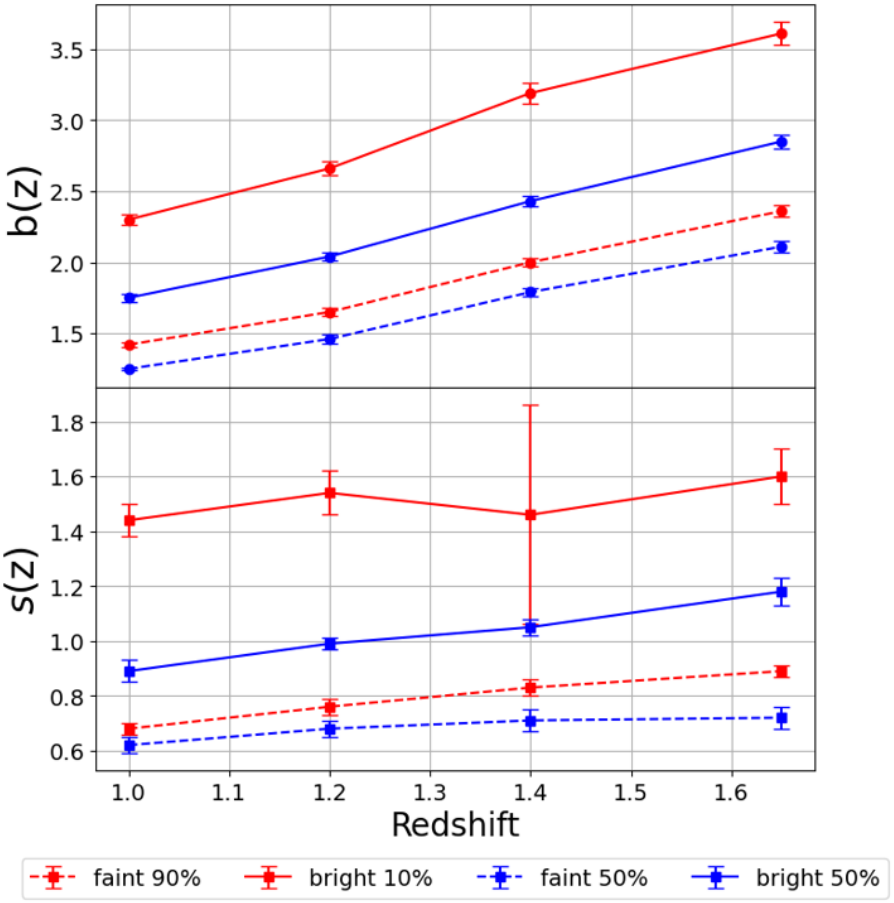

FIGURE 6.3: Values provided for [108] galaxy bias (top panel) and the local count slope (lower panel) for the two split cases studied. The dashed line correspond to the faint sample and the solid line to the bright sample.

In [47]) we presented the Flagship galaxy mock catalog, based on a record-setting Nbody simulation including 4 trillion dark-matter particles, and that is the reference dataset for the scientific preparation and exploitation of the Euclid mission. The paper presents an end-to-end galaxy assignment pipeline to produce a massive simulated galaxy catalog that covers one octant of the sky up to $z = 3$, with about 400 properties per galaxy for several billions of galaxies. This mock consistently models the main probes of Euclid, galaxy clustering and weak lensing, along with many other galaxy formation related properties.

Our contribution to this paper was to provide a set of measurements of the magnification bias factor for the various mock galaxy samples at different redshifts and VIS magnitude cuts, as shown in Figure 6.4. We also provided a polynomial fit up to third order of $f(z, x = \text{VIS mag})$ which are given by:

$$
\begin{aligned}
f(z = 0.2, x) &= -0.00034x^3 + 0.02615x^2 - 0.66765x + 5.87909, \\
f(z = 0.4, x) &= -0.00291x^3 + 0.21117x^2 - 5.11843x + 41.63343, \\
f(z = 0.6, x) &= -0.01126x^3 + 0.81285x^2 - 19.57029x + 157.44804, \\
f(z = 0.8, x) &= -0.02294x^3 + 1.66785x^2 - 40.45909x + 327.83286, \\
f(z = 1.0, x) &= 0.00098x^3 + 0.01326x^2 - 2.48346x + 38.85953,
\end{aligned}
$$

$$f(z = 1.2, x) = 0.00909x^3 - 0.58261x^2 + 12.00675x - 77.66596,$$
$$f(z = 1.4, x) = -0.01782x^3 + 1.28538x^2 - 31.15011x + 254.31386,$$
$$f(z = 1.6, x) = -0.01509x^3 + 1.0987x^2 - 26.92731x + 222.83778,$$
$$f(z = 1.8, x) = -0.01347x^3 + 1.04435x^2 - 27.16381x + 237.44937.$$

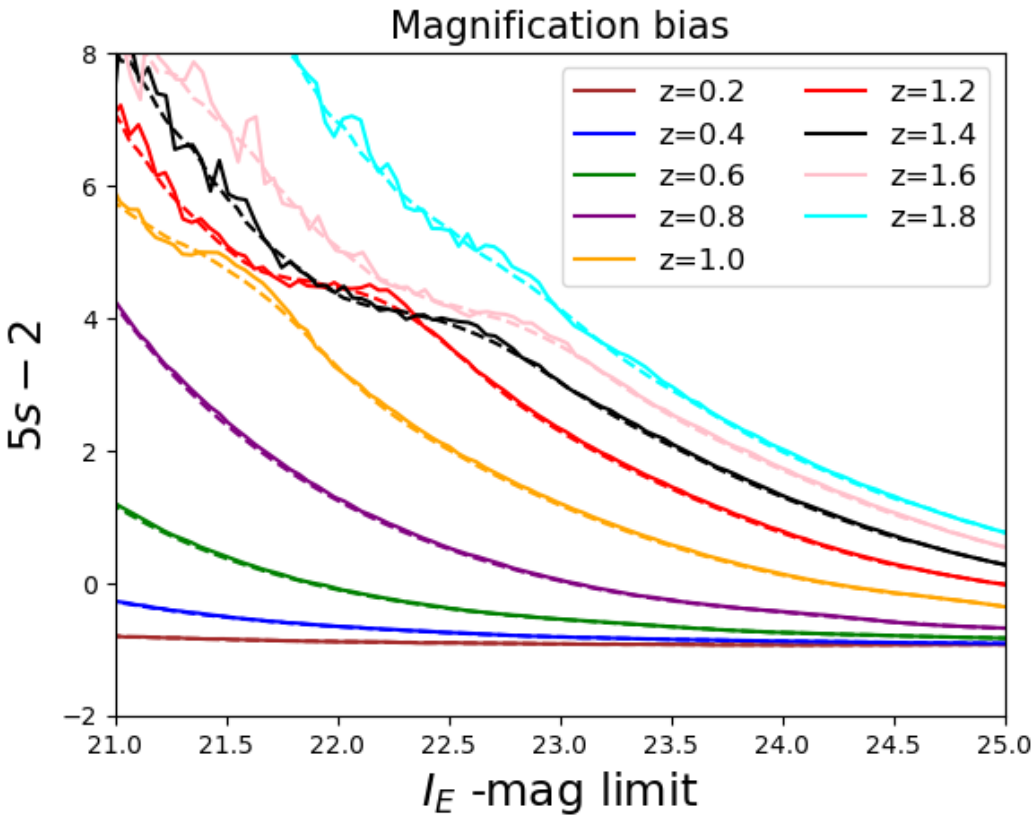

FIGURE 6.4: Values provided for [47] of the magnification bias factor for different z and VIS magnitude cuts. The dashed lines are fitted polynomials up to 3rd order.

This fit is meant to serve as a modeling tool that can be ingested in the theoretical predictions for cosmological analysis pipelines that shall be used by the Euclid collaboration during the scientific exploitation of the mission data.

6.2 DESI mission contributions

Within the DESI mission we collaborated within the galaxy lensing working group in two different aspects.

First, we provided the linear galaxy bias and magnification prediction for the angular correlation function ($\xi(\theta)$) for the Buzzard simulations [52] used for DES forecasts. We did not have access to the simulated data so we were directly provided with the density angular autocorrelation function for 4 redshift bins of the simulation: $0.1 < z < 0.3, 0.3 < z < 0.5, 0.5 < z < 0.7$ and $0.7 < z < 0.9$. We used, as in other analyses presented in this Thesis, the code *pyCCL* to calculate the prediction for this simulations using the fiducial values: $\Omega_m = 0.286$, h $= 0.7$, $\sigma_8 = 0.82$, $n_s = 0.96$ and $\Omega_b = 0.046$. *pyCCL* has a module to calculate the angular correlation function (in configuration space) from the angular power spectrum. We obtained,

on scales lower than 2 deg: $b = 1.24$ for $0.1 < z < 0.3$, $b = 1.65$ for $0.3 < z < 0.5$, $b = 1.89$ for $0.5 < z < 0.7$ and $b = 2.21$ for $0.7 < z < 0.9$. We were later provided with the values for the magnification bias slope, s, and calculated the magnified angular correlation function prediction for each pair of lens and sources bins where $z_l < z_s$.

As a second contribution, we originally started the E_G estimator project within the same working group. We planned to use a set of modified-gravity simulations developed within the DESI collaboration to calculate E_G, but due to time constraints we ended up using the F5 and GR simulations from [13] and presented in this Thesis (see Chapters 4 & 5).

Within the DESI collaboration the E_G gravity estimator was calculated using KiDS-1000 and BOSS data in configuration space. The $E_G(R)$ statistic, in configuration space, is defined as:

$$E_G(R) = \frac{1}{\beta}\frac{\Upsilon_{\rm gm}(R, R_0)}{\Upsilon_{\rm gg}(R, R_0)}, \tag{6.5}$$

where R is the projected distance and R_0 is the reference distance at which $\Upsilon_{\rm gm}(R, R_0) = 0$. The quantities $\Upsilon_{\rm gm}$ and $\Upsilon_{\rm gg}$ are defined as:

$$\Upsilon_{\rm gg}(R, R_0) = \frac{\rho_c}{R^2}\sum_{i=j}^{k} C_i w_p(R_i), \tag{6.6}$$

where (k, j) are the bins containing (R, R_0), and the coefficients C_i are given by:

$$C_i = \begin{cases} R^2_{i,\rm max} - R^2_{i,\rm min} & i = j, \\ R^2_{i,\rm max} - R^2_{i,\rm min} & j < i < k, \\ -R^2_{i,\rm min} & i = k. \end{cases} \tag{6.7}$$

Here, $w_p(R_i)$ is the projected two-point correlation function, and ρ_c is the critical mass density of the Universe.

$$\Upsilon_{\rm gm}(R, R_0) = \Delta\Sigma(R) - \frac{R_0^2}{R^2}\Delta\Sigma(R_0), \tag{6.8}$$

where $\Delta\Sigma(R)$ is the surface mass density contrast:

$$\Delta\Sigma(R) = \frac{\sum_{\rm ls} w_l w_s w_{\rm ls} e_{t,\rm ls}(R/\chi_l)\Sigma_{cr}(\chi_l, \chi_s)}{\sum_{\rm rs} w_r w_s w_{\rm rs}} - \frac{\sum_{\rm rs} w_r w_s w_{\rm rs} e_{t,\rm rs}(R/\chi_r)\Sigma_{cr}(\chi_r, \chi_s)}{\sum_{\rm rs} w_r w_s w_{\rm rs}}, \tag{6.9}$$

w_l, w_s, w_r (χ_l, χ_s, χ_r) are weights (commoving distance) for galaxies in the lenses, sources and random dataset; w_{ls}, w_{rs} are weights for the lens-source pair and the random lens-source pair. The parameter e_t correspond to the transversal shear component of the lens-source pair (see Eq. 2.127). Lastly, $\Sigma_{cr}(\chi_l, \chi_s)$ is defined as:

$$\Sigma_{cr} = \frac{c^2}{4\pi G}\frac{D_s}{D_l D_{ls}}, \tag{6.10}$$

where G is the gravitational constant, c is the speed of light and D_l (D_s) is the angular diameter distance to the lenses (sources), D_{ls} is the angular diameter distance between the

lenses and source sample.

To compute $\Delta\Sigma(R)$, the code *dsigma*[1] was developed for the DESI collaboration. This tool enables the efficient calculation of $\Delta\Sigma(R)$ by using a k-d tree algorithm to rapidly pair lens-source groups. It computes e_t by first determining the projected distances between lens-source pairs and grouping them into concentric bins centered on the lens. Previously, we developed our own code for calculating e_t so we were asked to validate *dsigma* using our own implementation. The details of our code are provided in Appendix B. In brief, it works by preliminarily limiting the potential source pairs for each lens (halo) using an angular cut, which efficiently filters out unrelated sources. However, because our approach processes each halo individually, it is significantly slower when applied to large halo samples.

In contrast, *dsigma* is optimized for any sample size, as its k-d tree structure allows it to simultaneously account for all sources. For validation, we computed $\Delta\Sigma$ (shear profiles) for a sample of 30 Flagship halos at $z = 0.50 \pm 0.01$ and shear for sources at $z = 1.00 \pm 0.01$, focusing on halos with FoF masses between $10^{14.4}$ and $10^{14.5}\,M_\odot$. To enhance the signal, we selected halos with similar masses and combined their signals by averaging the tangential shear values within the same radial bins across all halos. This technique, known as halo stacking, is commonly employed in the literature to amplify weak or noisy lensing signals [146, 21, 73, 74, 75]. As shown in Figure 6.5, the validation was successful, with both codes producing identical shear profiles. We use bootstrap resampling [113] to estimate the error where instead of taking random regions we take random individuals halos to generate a new iteration with the same number of lenses as the original with repetitions.

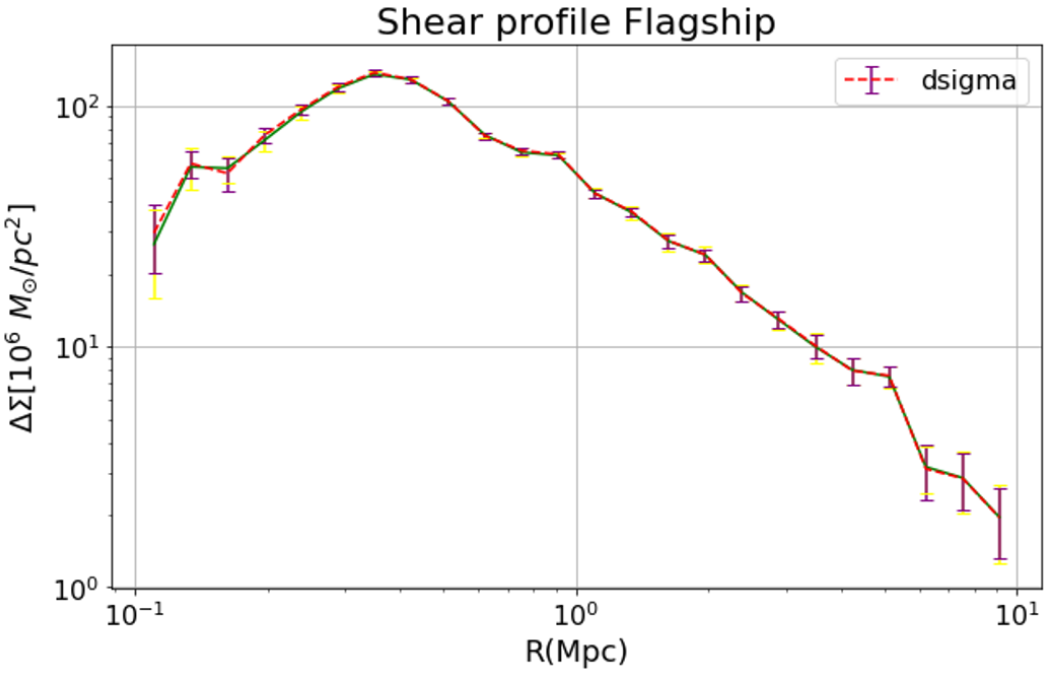

FIGURE 6.5: Shear profile calculated for a Flagship mock sample of 30 stacked halos at $z = 0.50 \pm 0.01$ with a halo mass between $10^{14.4}$ and $10^{14.5}\,M_\odot$. The signal calculated by the code *dsigma* (red dashed line with purple errorbars) and our code (green line with yellow purple errorbars) have errors using 100 samples in the bootstrap resampling.

[1] https://github.com/johannesulf/dsigma

Chapter 7

Future work

In this final chapter, we briefly summarize the work that we plan to pursue following the completion of this thesis.

7.1 New probes of gravity

In Chapter 4 and 5, we have already discussed possible avenues to expand the work presented in them. In particular, we plan to investigate the following points:

- We have outlined our intention to further explore de virtues and limitations of the E_G estimator, expanding the study that forms the main result of this Thesis (Chapter 4). Specifically, we plan to write a follow-up paper using the BACCO hybrid emulator, that combines perturbation theory with Nbody simulations, in Fourier space, targeting smaller scales ($< 10\,\mathrm{Mpc}/h$ or $k > 0.4\mathrm{h/Mpc}$).
- We shall also complete the project on probing gravity using 3x2pt analysis, whose main (preliminary) results are presented in Chapter 5. While our primary contributions are already finalized, we plan to explore the robustness of our main findings and explore additional constraints on dynamic DE cosmologies ($w_o w_a$CDM). We shall also investigate how our gravity constraints degrade when finite survey area and sources of systematic errors (e.g, shape noise, intrinsic alignments, and photo-z errors) are included.

7.2 Magnification Halo Profiles

In this section, we present a side project undertaken during the course of this thesis, that was developed in parallel to the main projects (Chapters 4 and 5 of the Thesis), and that was intended as an application of the code developed in 6.2 in the context of the scientific preparation of the DESI experiment. The ultimate goal is to investigate whether magnification profiles can be used as a new test of gravity, complementary to the shear profiles, that are a much more standard probe of large scale structure. As a first step in this direction, below we present some preliminary results focusing on GR simulations, specifically on the MICE and Flagship mocks.

This project involves the computation of halo profiles, where we fit the density distribution around a halo (or a group of similar halos) to a halo model, such as the Navarro–Frenk–White (NFW) profile [115]. Typically, the density distribution is estimated using the shear signal around the halo. However, in this project, we propose to use the magnification signal as an alternative approach. This approach has already been applied in previous analyses, such as [146, 21], where magnification profiles were successfully calculated, and the halo mass was estimated with good agreement with the ΛCDM model, although partly due to the large

error-bars. In our study, we will use simulated data to attempt to recover the halo mass from the halo catalog using different galaxy samples.

The shear profiles were already introduced in sec. 6.2 which corresponds to the surface mass density $\Delta\Sigma$. The profiles are generated with lenses (halos) and sources nearby to the lenses on the projected sky in order to check how the lensing signal changes around the halo due to its density distribution. This is a good way to estimate the mass distribution of a halo since we can fit this halo profiles to halo models like the NFW profile to obtain important properties of the halo like the average mass over a certain radial distance or the concentration. The surface mass density of a spherical symmetric lens can be expressed as [21]:

$$\Sigma(R) = 2\int_0^\infty \rho(R,z)dz, \tag{7.1}$$

where $R = D_d\sqrt{\theta_1^2+\theta_2^2}$ is the projected radius relative to the center of the lens.

The convergence can be expressed in terms of the surface mass density as:

$$\kappa(\theta) = \frac{\Sigma(\theta)}{\Sigma_{cr}} \tag{7.2}$$

where Σ_{cr} is defined in Eq. 6.10. This leads the relation with the shear profiles as:

$$\gamma_t(\theta) \equiv \kappa(<\theta) - \kappa(\theta) \equiv \frac{\Delta\Sigma(\theta)}{\Sigma_{cr}} \tag{7.3}$$

Since κ can be expressed as (see sec. 2.6.3):

$$\kappa = \frac{\delta_c}{\alpha_c}. \tag{7.4}$$

where δ_c are density fluctuations and α is the slope of the magnitude at the magnitude cut of the sample.

Then the surface mass density is given by [21]:

$$\Sigma_c = \frac{\delta_c\Sigma_{cr}}{\alpha_c}, \tag{7.5}$$

where the subscript c indicates that the calculation is obtained through galaxy count fluctuations instead of magnitude fluctuations. This means that δ_m is given by:

$$\delta_c = \frac{n}{\overline{n}} - 1, \tag{7.6}$$

where $\overline{n}$ is the observed mean density over the entire sky. To estimate $\overline{n}$, we use the observed mean density as a proxy for the unlensed density n_o. While α_c is defined as [21]:

$$\alpha_c = 2.5\frac{d}{dm_*}\log_{10} n_o(m<m_*) - 1, \tag{7.7}$$

where m_* is the apparent magnitude limit of the survey.

We use the subscript c since there is another way to estimate the magnification trough the relative changes in the magnitude (flux) fluctuations due to magnification. With the convergence given by [21]:

$$\kappa = \frac{\delta_m}{\alpha_m}. \tag{7.8}$$

where now we use the subscript m:

$$\delta_m = -\frac{2.5}{\ln(10)}\left(1 - \frac{d\overline{m}}{dm_*}\right) 2\kappa \tag{7.9}$$

where $\overline{m}$ is the mean magnitude.

$$\alpha_m \equiv \frac{2.5}{\ln(10)}\left(-1 + \frac{d\overline{m}}{dm_*}\right) \tag{7.10}$$

Then the surface mass density can also be expressed using magnitude fluctuations as:

$$\Sigma_m = \frac{\delta_m \Sigma_{cr}}{2\alpha_m}, \tag{7.11}$$

In Figure 7.1 we show different values for the two defined α at various redshift using magnitude cut of $E_{VIS} < 23$.

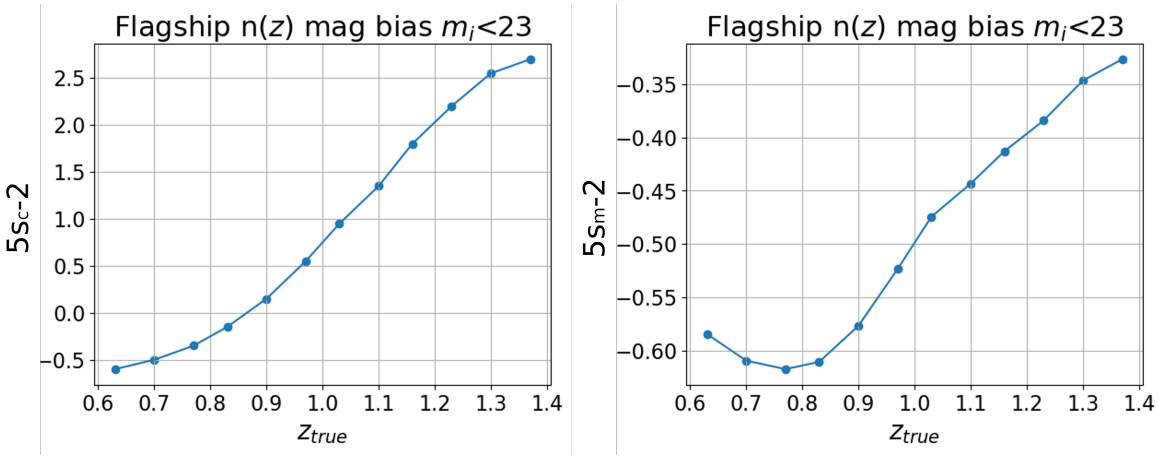

FIGURE 7.1: Values for the magnification bias factor for the magnitude fluctuations (right plot) and count fluctuations (left plot) at different z. The magnitude cut is at $E_{VIS} < 23$.

In our study, we aim to calculate the surface mass density for a group of lenses using the stacking technique (see sec. 6.2) to enhance the signal-to-noise ratio. Observationally, it is challenging to detect sufficient lens galaxies close to the source, where the magnification effect is more prominent. To account for the redshift dependence of lens galaxies, the stacked expression for $\Sigma(r)$ is given by:

$$\langle \Sigma(r) \rangle = \frac{\sum_i^{n^*} \left(n_i(r) - \overline{n}_i\right) \cdot \Sigma_{cr}}{\sum_i^{n^*} \overline{n}_i \cdot \alpha_i}, \tag{7.12}$$

where n_i^* is the number of source galaxies associated with a given cluster within the corresponding annular bin. In the case of count fluctuations we need to estimate n_o using:

$$n_o = \frac{\sum_i^{n^*} n_i(r = R_{\max})}{n_{\text{halos}} \cdot \pi \cdot (R - r)^2}. \tag{7.13}$$

To compute the density fluctuations in annular bins centered on each cluster using the stacking methodology, we employ:

$$\delta(r) = \frac{1}{n_o \cdot A_r} \sum_i^{n^*} \frac{N_i^*(r)}{1 - m_i^*(r)} - 1, \tag{7.14}$$

which corresponds to $n/\overline{n} - 1$. Here, n is the total density of source galaxies in a given bin over all clusters containing unmasked regions within that bin. N_i^* represents the number of source galaxies for a given cluster in the bin, A_r is the bin area (constant for all clusters at a given r in Mpc), and m_i^* is the mask ratio in the bin region for each cluster.

To compute n_o, the mean unlensed density, we use:

$$n_o = \frac{1}{1 - m_T} \sum_{i=1}^{n^*(r)} \frac{N_i}{A_{T_i}}, \tag{7.15}$$

where the sum is taken over the same clusters used to calculate n for the corresponding bin. N_i is the total number of source galaxies for each cluster (regardless of distance), A_{T_i} is the total physical area of the catalog at each cluster's distance, and m_T is the mask ratio for the catalog, constant across all distances.

In order to calculate the surface mass we developed a new code that combines our original code for calculating shear profiles presented in appendix B with the fast calculations of the *dsigma* code structure presented in 6.2. We modified *dsigma* to allow the magnification profiles calculations with the specifics mentioned here.

7.2.1 Galaxy mocks

We use data from two simulated catalogs: MICE v2 and Flagship v2, both accessible via Cosmohub. Clusters are selected based on their $\log_{10}$(halo mass) in $M_\odot/h$ at $z = 0.3$, using a redshift bin width of $\Delta z = 0.4$. Source galaxies are selected at $z = 1$ with $\Delta z = 0.2$ and a magnitude limit of < 23 in the E_{VIS}-band.

Both catalogs provide complete lensing information for all galaxies, enabling direct selection of convergence and magnified magnitudes based on RA and DEC. The magnified magnitude is calculated as described in Equation 3.19.

Tables 7.1 and 7.2 present the halo mass ranges used to divide the sample, along with the total number of clusters in each bin.

7.2.2 Fitting the halo profile

We aim to fit the halo profiles to NFW density profile, which is expressed as [155]:

$$\rho(r) = \frac{\delta_c \rho_c}{(r/r_s)(1 + r/r_s)^2}, \tag{7.16}$$

TABLE 7.1: Values for the different richness bins for Flagship's halos

lmhalo ($MFoF/h$)	Mean lmhalo	Nº clusters	Mean z
14.00-14.20	14.09	8733	0.353
14.20-14.40	14.29	3940	0.345
14.40-14.60	14.48	1497	0.339
14.60-14.80	14.68	500	0.326
14.80-15.00	14.88	127	0.326

TABLE 7.2: Values for the different richness bins for MICE's halos

lmhalo ($MFoF/h$)	Mean lmhalo	Nº clusters	Mean z
14.00-14.20	14.09	4753	0.363
14.20-14.40	14.28	2271	0.359
14.40-14.60	14.48	976	0.347
14.60-14.80	14.68	321	0.345

where $\rho_c = \frac{3H^2(z)}{8\pi G}$ represents the critical density of the universe at the halo's redshift z, $H(z)$ is the Hubble parameter at the same redshift, and G is Newton's gravitational constant. The scale radius $r_s = R_{200}/c$ is a characteristic radius of the cluster, with c being the dimensionless concentration parameter. The term δ_c is the characteristic overdensity of the halo, given by:

$$\delta_c = \frac{200}{3}\frac{c^3}{\ln(1+c) - c/(1+c)}. \tag{7.17}$$

The virial radius R_{200} is defined as the radius within which the average density of the halo equals $200\rho_c$ [115]. The total mass of an NFW halo within R_{200} is therefore:

$$M_{200} \equiv M(R_{200}) = \frac{800\pi}{3}\rho_c R_{200}^3 = \frac{800\pi}{3}\frac{\bar{\rho}(z)}{\Omega(z)}R_{200}^3, \tag{7.18}$$

where $\bar{\rho}(z)$ denotes the mean mass density of the universe at redshift z, and $\Omega(z)$ is the density parameter at the same redshift.

To simplify calculations [155], we introduce a dimensionless radial distance $x = R/r_s$. By integrating Eq. 7.16 along the line of sight, the radial dependence of the surface mass density for an NFW lens can be expressed as:

$$\Sigma_{\rm NFW}(x) = \begin{cases} \frac{2r_s\delta_c\rho_c}{x^2-1}\left[1 - \frac{2}{\sqrt{1-x^2}}\operatorname{arctanh}\sqrt{\frac{1-x}{1+x}}\right], & x < 1, \\ \frac{2r_s\delta_c\rho_c}{3}, & x = 1, \\ \frac{2r_s\delta_c\rho_c}{x^2-1}\left[1 - \frac{2}{\sqrt{x^2-1}}\arctan\sqrt{\frac{x-1}{1+x}}\right], & x > 1. \end{cases} \tag{11}$$

We define 24 logarithm radial bins from 0.1 Mpc to 10 Mpc. For each case we perform 5 calculations:

- δ_c : Using density fluctuations from expression 7.6.
- δ_m : Using magnified fluxes from expression 7.9.
- κ : Using directly the value of the convergence from the catalog.
- $\delta_c(nomag)$: Using density fluctuations but turning off the magnification.

- σ_T: Using the shear and calculating $\Delta\Sigma$ in order to compare the NFW parameters obtained.

In Figure 7.2, we present preliminary results for the 14.40–14.60 halos in the Flagship simulation. The κ profile exhibits excellent agreement with the NFW profile, as the values are directly extracted from the dark matter simulation (convergence maps). Similarly, the shear profile follows the NFW profile but shows a lack of signal at small scales, likely due to resolution effects on the maps, as shear is a two-component quantity. Despite these limitations, both cases recover the M_{200} value well, comparable to the FoF mass of the halos. The errorbars are given by 100 bootstraps resampling of the halos [113].

It is not expected for M_{FoF} and M_{200} to match perfectly, as they arise from different estimation methods; however, they should agree in order of magnitude. Using magnified magnitudes results in significant noise, yielding an underestimated M_{200}. Conversely, magnified counts provide a less noisy signal but result in an overestimated M_{200}. Interestingly, the unmagnified sample produces a similar amplitude to the magnified counts, leading to a comparable halo mass. This suggests a potential issue in how we calculate the density within annular bins, possibly due to inaccuracies in computing the area.

As mentioned earlier these results are preliminary, and further work is needed to refine the analysis. In particular, we plan to apply this tool to investigate potential deviations with respect to standard gravity using accurate measurements of magnification profiles e.g, around clusters of galaxies. We also plan to study the effects of systematics like blending (pairs merged due to proximity) and obscuration (galaxies not observed due to the atmosphere, extinction or data reduction) on the magnification [69].

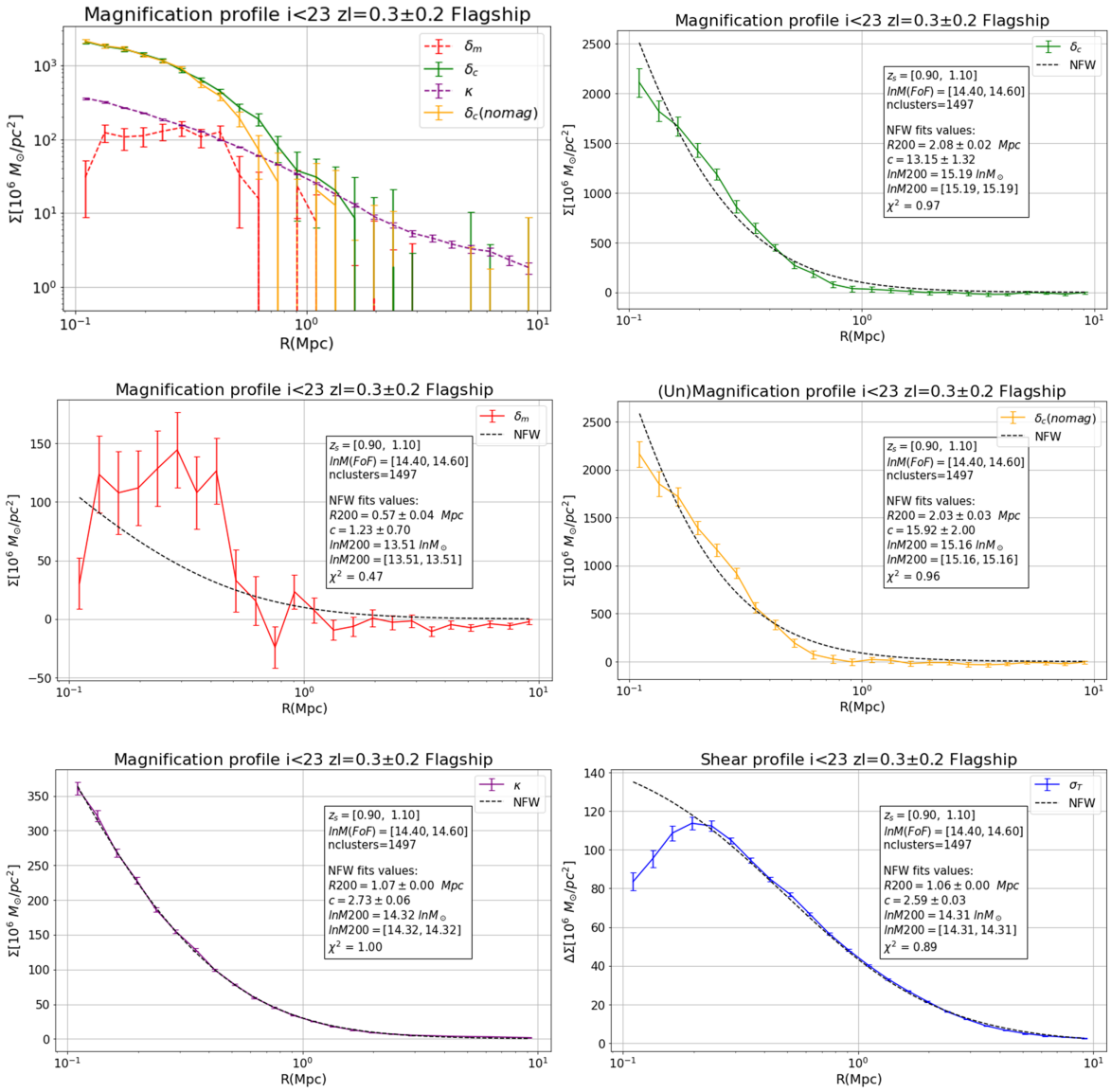

FIGURE 7.2: Halo profiles for Flagship halos at z=0.3 for each case discussed. The top left plot shows all the magnification profiles results combined. While the bottom right plot shows the results for the shear profile using the same sample. The values for the NFW fit are displayed in each respective individual plot text box. The parameter "c" corresponds to the halo concentration. The range given on M_{200} is given by the maximum and minimum value given by the errors for R_{200}.

Chapter 8

Global Conclusions

In this thesis, we investigated galaxy clustering and gravitational lensing within the framework of two gravity models: the standard General Theory of Relativity assumed in the ΛCDM model, and the Hu-Sawicki $f(R)$ model, one of the most promising alternatives to GR. Modified gravity models have emerged as valuable tools for studying accelerated cosmic expansion without relying on the cosmological constant Λ, which currently lacks a definitive physical interpretation or observational evidence. Our focus has been on developing techniques to distinguish between these gravity models and identify potential deviations from GR. Analyzing clustering in Modified Gravity models is more challenging due to the increased complexity involved in the theory predictions for these models. Such models introduce an additional degree of freedom, often referred to as a fifth force, which renders current GR emulators insufficient for accurately reproducing the data.

In Chapter 4, we present the first computation of the gravity model testing parameter E_G on GR and $f(R)$ gravity models using high-fidelity simulated galaxy catalogs. Our analysis demonstrates a method to accurately measure the scale-dependent growth rate predicted by non-standard gravity models. To capture this scale dependence, we divide the estimation of the RSD β parameter across distinct scale ranges, explicitly separating large (quasi-linear) scales from small (non-linear) scales. Using samples of mock galaxies in low-redshift bins ($z < 1$), we show that this estimator can be reliably measured, highlighting its strong discriminating power in distinguishing between competing gravity theories within this redshift range. Overall, we find that for an all-sky galaxy survey, and under the assumption of negligible observational systematics, accurate and largely unbiased estimates of E_G can be achieved for both gravity models across all redshifts. However, the error bars remain too large to decisively differentiate between the theories. Specifically, when attempting to measure the scale dependence of the E_G estimator—a potential "smoking gun" for deviations from General Relativity in redshift space—we find that limitations in state-of-the-art theoretical modeling, combined with intrinsic "prior volume effects," hinder the ability to obtain reliable and unbiased constraints. As an alternative, we propose a simple null test of gravity based on RSD clustering. We demonstrate that, provided future galaxy surveys can accurately model small-scale effects, this approach could potentially detect significant deviations from standard gravity.

In Chapter 5, we delve deeper into the biases that arise when assuming GR while analyzing a dataset generated under $f(R)$ gravity. Specifically, we examine whether the now-standard combination of photometric galaxy clustering and weak-lensing observables, known as the 3×2pt analysis, could provide a more effective method for breaking parameter degeneracies

and yielding more competitive constraints on gravity. We observe notable biases in the estimates of Ω_m and A_s, which are systematically overestimated relative to the fiducial values of the simulation. In particular, the enhanced structure formation in the $f(R)$ model leads to an apparent increase in these two cosmological parameters. Additionally, the value of S_8, that encodes the amplitude of clustering, is biased towards higher values, potentially offering an explanation for the now well-established S_8 tension within the ΛCDM model.

In Chapter 6, we presented how the tools developed in the course of this Thesis for galaxy clustering and gravitational lensing were applied to the scientific preparation of the Euclid and DESI experiments. Specifically, we provided precise estimations of the linear galaxy bias and magnification bias in galaxy mocks across different redshifts to enable accurate model predictions, thereby evaluating the capability of these missions to constrain cosmological parameters. Looking ahead, we anticipate beginning work with real observational data from Euclid in the near future (e.g, DR1).

Lastly, in Chapter 7, we outline potential future directions of the work carried out in this thesis. These efforts reflect our goal of refining our methodology with more accurate models and completing the projects we are currently pursuing. One area of particular interest is a side project focused on calculating halo profiles, which involves detailed modeling at very small scales, a sharp contrast to the larger scales predominantly examined in this thesis. Once we achieve more conclusive results from this project, we plan to extend the analysis to $f(R)$ simulations to explore how modified gravity influences halo density. However, it is likely that we will initially need to rely on halo models developed for GR until dedicated predictions for $f(R)$ become available.

All the data used in this work is derived from simulated mock catalogs. Cosmological numerical simulations are powerful and reliable tools for replicating observables, enabling the testing of theoretical models under idealized conditions. However, these simulations are vulnerable to computational or human errors during their generation. In the course of this research, we encountered two significant issues related to catalog generation, which caused delays in our progress as we initially attributed these problems to flaws in our methodology. Resolving these issues was essential to achieving reliable results. Specifically, incorrect peculiar velocities in the GR/F5 galaxy mocks affected the determination of the growth rate discussed in Chapter 4, while errors in the deflected positions in FS2 impacted the validation of magnification bias, which could have potentially influenced the halo profiles addressed in Chapter 7. Although addressing these issues delayed the primary projects, it provided an invaluable opportunity to deepen our understanding of simulation validation techniques and the generation of improved halo and galaxy mock catalogs.

Appendix A

Validating the growth rate on the GR/F5 mocks

While we were working on the E_G project from Chapter 4, we found an issue with the peculiar velocities in the GR and F5 mocks, which we will detail here. The initial fits performed with COMET-emu using the multipoles of the correlation function for these mocks exhibited a significant discrepancy in the value of the growth rate. As shown in Figure A.1, the best-fit value for the growth rate in the GR mock, indicated in the legend, is $f = 0.5$. This is considerably lower than the fiducial value of $f = 0.77$ at $z = 0.55$, as shown on the y-axis. While the fits appeared to follow the theoretical predictions reasonably well, some discrepancies were observed, particularly for the monopole, where deviations exceeded 2σ. This prompted us to investigate whether parameter degeneracies might explain the mismatch. Since the value of σ_{12} was fixed, the most plausible degeneracy affecting f would involve the linear galaxy bias. However, even considering such a degeneracy, the observed discrepancy in the growth rate was too large to be explained by this effect alone.

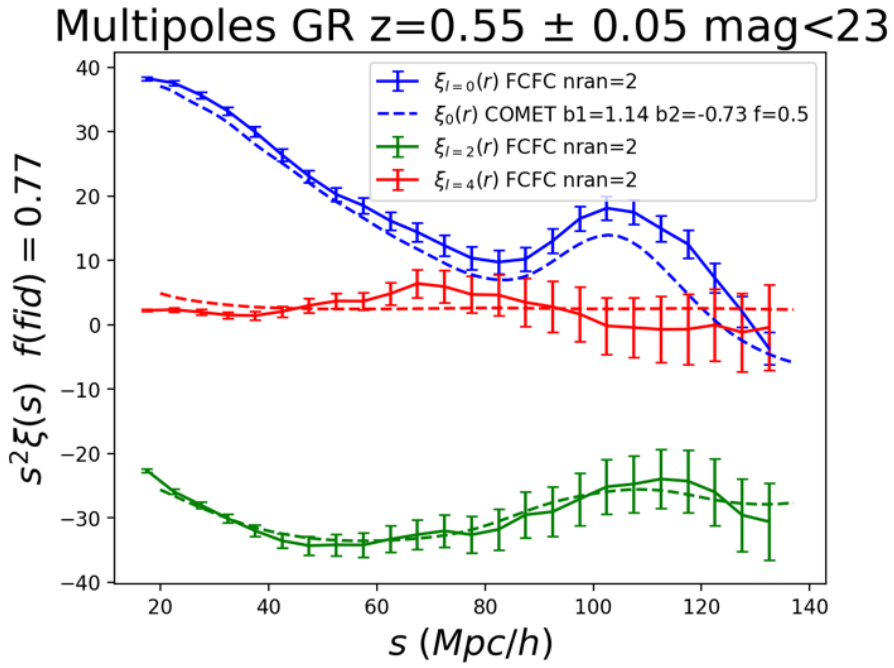

FIGURE A.1: First fits performed to the multipoles of the correlation function of the GR mock. The best-fit parameters are depicted on the legend, while the fiducial value of the growth rate is given on the y-axis label.

Following these results, we decided to fix the growth rate f to its fiducial value at the corresponding redshift and redo the fits. In Figure A.2, we observe that while the fits now avoid the large disagreement in f, they still fail to fully reproduce the expected behavior. The linear galaxy bias primarily influences the global amplitude, shifting both the monopole and quadrupole in the same direction. In contrast, the growth rate governs the relative amplitude between the monopole and quadrupole. The remaining discrepancies suggest that it is this relative scaling—controlled by f—that is not being captured accurately in the fits.

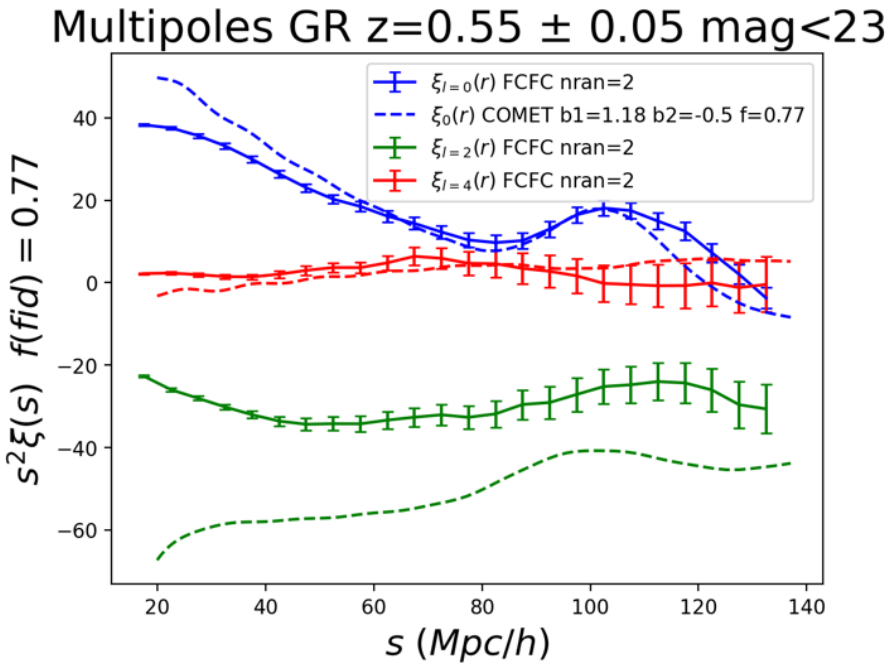

FIGURE A.2: Fits performed to the multipoles of the correlation function of the GR mock with the value of the growth rate fixed at its fiducial value. The best-fit parameters are depicted on the legend.

This discrepancy in the value of the growth rate prompted us to further investigate the mock catalogs. First, we verified our methodology by successfully re-obtaining the growth rate in the FS2 mock at a comparable redshift. Subsequently, we began exploring mock properties related to redshift-space distortions (RSD). For instance, we recalculated the observed redshifts using the peculiar velocities of each galaxy provided by CosmoHub, expressed in Cartesian components ($[v_x, v_y, v_z]$) as described in Equation 2.41. We also calculated the 2D correlation function $\xi(r_p, \pi)$ (see sec. 2.4) for both mocks and we did not see any visual artifact as shown in Figure A.3. Despite these efforts, we could not identify the source of the error, so we turned our attention to the halo catalog from which the galaxy catalog was derived [14].

We were provided with three snapshots' data of the halo catalog at $z = 1$ (step $= 175$), $z = 0.5$ (step $= 255$), and $z = 0$ (step $= 400$) in the simulation box. The data contained the position, velocities and mass of the halo groups detected by the Friends-of-Friends algorithm of P-Gadget3/MG-Gadget. In order to investigate the halo properties, we utilized a sample from CosmoHub, extracting all available information on halo positions, velocities, true redshifts, and masses at the snapshots' redshifts. To focus solely on central halos/galaxies, we filtered the dataset for entries using kind $= 0$. To adapt the halo positions from CosmoHub to the periodic box framework, we applied corrections to each coordinate, adding or subtracting multiples of the box size ($L = 768$) h/Mpc to respect periodic boundary conditions. The adjusted halo positions from the periodic box catalog were compared with those provided by

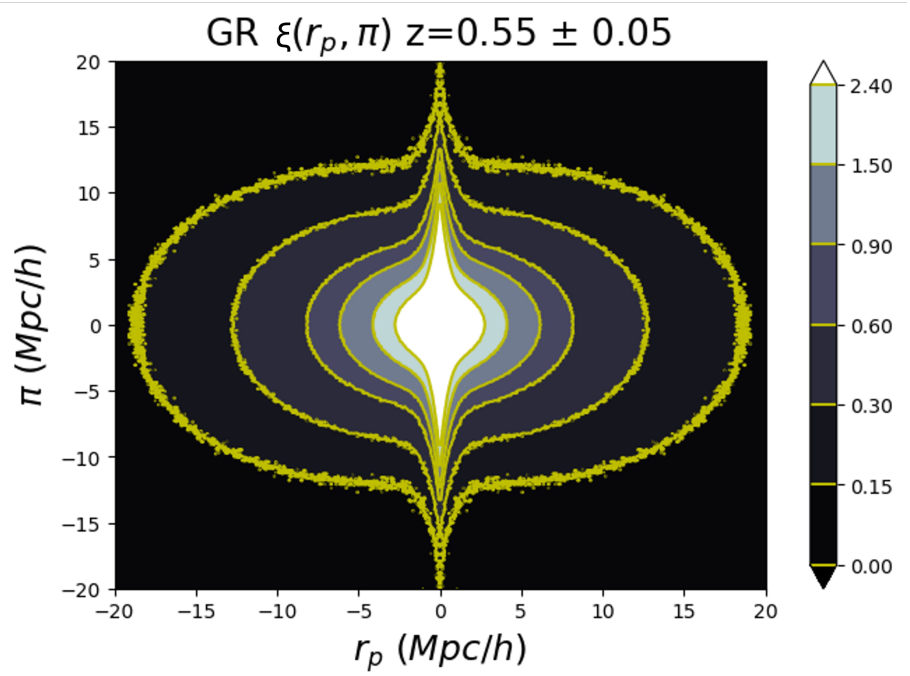

FIGURE A.3: 2D correlation function for the GR mock at z=0.55. π represents the LOS distance and r_p the projected distance over the sky.

the snapshots. Since the halos in Cosmohub and the snapshots had different ID classification we had to developed a code to match halos in each dataset by their position. Discrepancies were identified, with position differences exceeding 1% in some cases. To address this, we defined a threshold $\Delta_p = 0.2$ for the coordinate components ($p = [x, y, z]$) to identify matches. Using this criterion, the majority of halos in the CosmoHub dataset matched a corresponding halo in the periodic box catalog.

For instance, in a test involving 10,000 halos at step = 175, only 374 halos lacked a match, and no cases of multiple matches were detected. This mismatch is likely attributable to precision limitations during the transformation of periodic box data into the lightcone framework and subsequent storage in CosmoHub. Nonetheless, the high rate of successful matches and the strong similarity in properties like halo mass and velocity support the validity of the matching process. Using the matched halos, we analyzed velocity components by calculating the ratios between CosmoHub and periodic box catalog values. For each one of the steps, velocity ratios clustered around 1, indicating good agreement. However, rare outliers exhibited discrepancies up to 300%, which were excluded from the analysis. For step 400 is harder to tell due to the very small dataset since we are dealing with a very small volume at z=0.

The snapshots' dataset also had information for the subhalos instead of the halo groups used until now. Extending this analysis to subhalos revealed a systematic discrepancy: velocities from the periodic box catalog ($v_{\text{PB, subhalo}}$) were consistently larger than those from CosmoHub ($v_{\text{CH, subhalo}}$), scaling approximately as:

$$v_{\text{PB, subhalo}} \approx v_{\text{CH, subhalo}} \cdot (1 + z). \tag{A.1}$$

This trend was observed across all velocity components (v_x, v_y, v_z) and simulation steps, as illustrated in the Fig. A.4. Initially, we computed multipoles using subhalo data due to a lack of clarity regarding the distinction between halo groups and subhalos. Upon switching

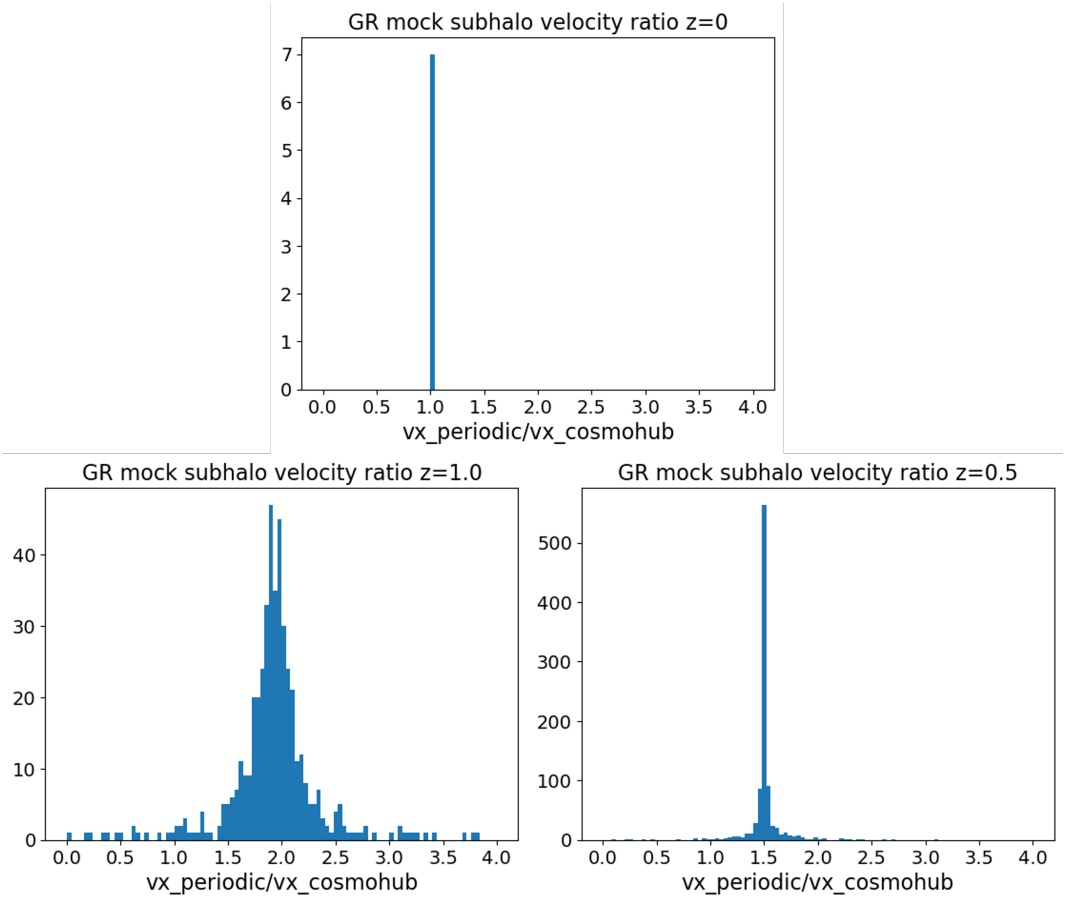

FIGURE A.4: Distribution of ratios of x-component of the velocity of halos of the snapshots over the Cosmohub velocities.

to halo groups' data for the calculations, the results aligned closely with those derived from CosmoHub. Specifically, the quadrupole moment $P_2(k)$ exhibited the known amplitude discrepancy from Figure A.1 and A.2. This confirmed that the values stored in Cosmohub had the halo group data. Analyzing the P-Gadget3's data structure, we found parallels with the data structure of the Illustris simulation[1], which specifies that group velocities (GroupVel) are box velocities. While Subhalo velocities (SubhaloVel) are peculiar velocities which confirms why there is this discrepancy with the Cosmohub values from Fig. A.4. To derive peculiar velocities for the group halos, these must be rescaled by the factor $1 + z$ (see sec. 2.3):

$$v_{\text{peculiar}} = v_{\text{box}} \cdot (1 + z). \tag{A.2}$$

This correction was missing in the original CosmoHub dataset, explaining the discrepancies in observed redshift (z_{RSD}) calculations. The center galaxies acquire the same velocities as the their respective halo so we can apply eq. A.2 directly. The peculiar velocities components for the satellite galaxies are obtained from a Gaussian centered at the respective velocity component of the center galaxy with a variance of $\sigma^2 = 0.3$. Adjusting satellite galaxy velocities required translating them to align with the corrected mean velocity of their central halo. For each velocity component $p = [x, y, z]$, the correction was:

[1] https://www.illustris-project.org/data/docs/specifications/

$$v_p^{\text{corrected}} = v_p^{\text{gal}} + v_p^{\text{halo}} \cdot (1 + z_{\text{true, halo}}) - v_p^{\text{halo}}. \tag{A.3}$$

This ensured the proper dispersion of subhalo velocities without introducing artificial scaling effects. Using this corrected velocities we can obtain the corrected observed redshift using eq. 2.41.

Recalculating the multipoles using corrected velocities led to significant improvements, particularly in the quadrupole amplitude, bringing it closer to the fiducial value. The fit quality improved, except at large scales for the quadrupole as we can see in Figure A.5. Using this correction we concluded that the problem was solved and we continued with the fitting procedure.

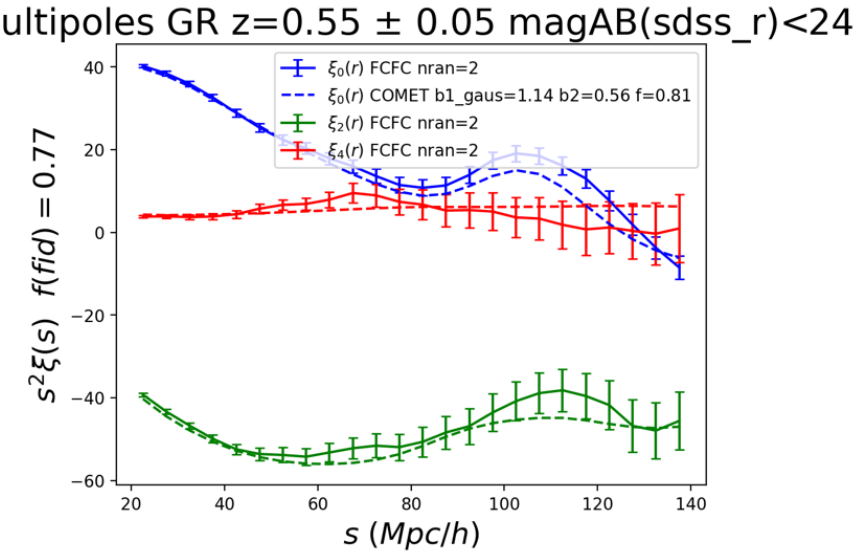

FIGURE A.5: Fits performed to the multipoles of the correlation function of the GR mock with the corrected data vectors. The best-fit parameters are depicted on the legend.

Identifying this issue took nearly a year, representing a significant setback in the development of the main project of this thesis. Nevertheless, it provided a valuable opportunity to deepen our understanding of the internal structure and processing of halo mock catalogs, as well as the implementation of redshift-space distortions (RSD) in simulations.

Appendix B

Code for calculating Halo density profiles

In this appendix we paste our original code described in sec. 6.2 to validate the DESI code *dsigma*. This code calculates the shear and shear density profile of stacked halos, see Chapter 5.

```
import pandas as pd
import numpy as np
from astropy.table import Table, join, vstack
from astropy.cosmology import LambdaCDM
from astropy.utils import NumpyRNGContext
from astropy.stats import bootstrap
from astropy import units as u

# Input cosmology
h = 0.67               # reduced hubble constant
Omega_m = 0.319        # Matter density parameter
Omeda_de = 0.681       # Dark matter density parameter

# Cosmology model
cosmology_model = LambdaCDM(H0=h * 100, Om0=Omega_m, Ode0=Omeda_de)

# Constants
SPEED_OF_LIGHT = 3e5  # [km/s]
GRAVITATIONAL_CONSTANT = 4.301e-3  # [pc Msun^-1 (km/s)^2]

# Cluster and halo parameters
halo_log_mass = 14.05

# Load cluster data and filter
cluster_data = pd.read_csv('clusters F.csv', delimiter=',', comment='#')
cluster_data = cluster_data[
    (cluster_data['ra_gal'] < 85) & (cluster_data['ra_gal'] > 5) &
    (cluster_data['dec_gal'] < 80) & (cluster_data['dec_gal'] > 0.65) &
    (cluster_data['halo_lm'] < halo_log_mass + 0.05) &
    (cluster_data['halo_lm'] > halo_log_mass - 0.05)
]
cluster_data.reset_index(drop=True, inplace=True)

# Load source data
source_data = pd.read_csv('sources shear F.csv', delimiter=',', comment='#')

def angular_separation(lon1, lat1, lon2, lat2):
```

```
    """
    Calculate the angular separation between two points on a sphere.
    """
    sin_delta_lon = np.sin(lon2 - lon1)
    cos_delta_lon = np.cos(lon2 - lon1)
    sin_lat1 = np.sin(lat1)
    sin_lat2 = np.sin(lat2)
    cos_lat1 = np.cos(lat1)
    cos_lat2 = np.cos(lat2)

    numerator1 = cos_lat2 * sin_delta_lon
    numerator2 = cos_lat1 * sin_lat2 - sin_lat1 * cos_lat2 * cos_delta_lon
    denominator = sin_lat1 * sin_lat2 + cos_lat1 * cos_lat2 * cos_delta_lon

    separation = np.arctan2(np.sqrt(numerator1**2 + numerator2**2), denominator)
    return separation

def equatorial_to_polar(ra, dec, ra_center, dec_center):
    """
    Convert equatorial coordinates to polar coordinates centered at a specified point.
    """
    ra_prime = ra - ra_center
    ra_prime[ra_prime < 0] += 2 * np.pi  # Convert to positive RA values

    quadrants = {
        "Q1": (ra_prime < np.pi) & (dec > dec_center),
        "Q2": (ra_prime < np.pi) & (dec < dec_center),
        "Q3": (ra_prime > np.pi) & (dec < dec_center),
        "Q4": (ra_prime > np.pi) & (dec > dec_center),
    }

    # Calculate separation and azimuthal angle
    separation = angular_separation(ra_prime, dec, 0, dec_center)

    # Spherical cosine law
    x = angular_separation(0, dec, 0, dec_center)
    y = angular_separation(ra_prime, dec, 0, dec)
    cos_theta = (np.cos(y) - np.cos(x) * np.cos(separation)) / (np.sin(x) * np.sin(separation))

    # Handle rounding errors
    cos_theta = np.clip(cos_theta, -1, 1)
    uncorrected_theta = np.arccos(cos_theta)

    # Assign angles to correct quadrants
    theta = np.zeros_like(uncorrected_theta)
    theta[quadrants["Q1"]] = uncorrected_theta[quadrants["Q1"]]
    theta[quadrants["Q2"]] = np.pi - uncorrected_theta[quadrants["Q2"]]
    theta[quadrants["Q3"]] = np.pi + uncorrected_theta[quadrants["Q3"]]
    theta[quadrants["Q4"]] = 2 * np.pi - uncorrected_theta[quadrants["Q4"]]

    return separation, theta

def calculate_bootstrap_errors(values_tangential, values_cross, n_iterations):
    """
    Calculate bootstrap errors for tangential and cross components.
    """
    indices = np.arange(len(values_tangential))
```

```
95      with NumpyRNGContext(1):
96          bootstrap_indices = bootstrap(indices, n_iterations)
97      bootstrap_tangential = values_tangential[bootstrap_indices]
98      bootstrap_cross = values_cross[bootstrap_indices]
99
100     weights = np.ones(len(values_tangential))
101     tangential_means = np.average(bootstrap_tangential, axis=1, weights=weights)
102     cross_means = np.average(bootstrap_cross, axis=1, weights=weights)
103
104     return np.std(tangential_means), np.std(cross_means)
105
106 # Prepare lists to store results
107 tangential_shear_list = []
108 cross_shear_list = []
109 distance_list = []
110 delta_critical_list = []
111 redshift_list = []
112 ra_list = []
113 dec_list = []
114
115 # Process each cluster
116 for idx in range(len(cluster_data)):
117     cluster_row = cluster_data.iloc[idx]
118     sources_near_cluster = source_data[
119         (source_data['ra_gal'] < cluster_row['ra_gal'] + 4) &
120         (source_data['ra_gal'] > cluster_row['ra_gal'] - 4) &
121         (source_data['dec_gal'] < cluster_row['dec_gal'] + 0.7) &
122         (source_data['dec_gal'] > cluster_row['dec_gal'] - 0.7)
123     ]
124     sources_near_cluster.reset_index(drop=True, inplace=True)
125
126     cluster_ra = cluster_row['ra_gal'] * np.pi / 180
127     cluster_dec = cluster_row['dec_gal'] * np.pi / 180
128     source_ra = sources_near_cluster['ra_gal'] * np.pi / 180
129     source_dec = sources_near_cluster['dec_gal'] * np.pi / 180
130
131     separation, theta = equatorial_to_polar(source_ra, source_dec, cluster_ra, cluster_dec)
132     theta += np.pi / 2  # Convention adjustment
133
134     # Compute distances and critical density
135     redshift = cluster_row['true_redshift_halo']
136     angular_diameter_distance = cosmology_model.angular_diameter_distance(redshift).to(u.pc)
137
138     # Calculate tangential and cross shear components
139     gamma1 = -sources_near_cluster['gamma1']
140     gamma2 = sources_near_cluster['gamma2']
141     tangential_shear = -(gamma1 * np.cos(2 * theta) + gamma2 * np.sin(2 * theta))
142     cross_shear = -gamma1 * np.sin(2 * theta) + gamma2 * np.cos(2 * theta)
143
144     tangential_shear_list.extend(tangential_shear)
145     cross_shear_list.extend(cross_shear)
```

Appendix C

Extra plots

In this appendix we add the extra plots for the E_G project from Chapter 4. This appendix was also included in the respective paper (Viglione C. et al. (2025))

C.1 Accuracy of the E_G estimator

Below we show how the different theory estimators for the E_G estimator compare to the fiducial expression given by eq.(4.27).

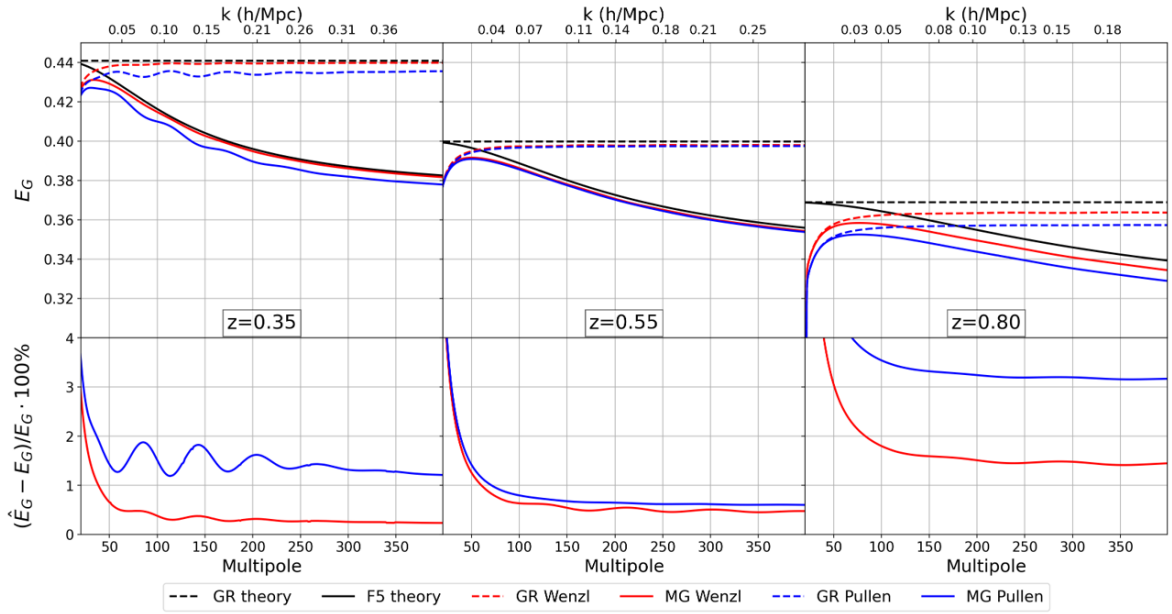

FIGURE C.1: Testing the accuracy of the estimator given by [152] (red lines) and [123] (blue lines). Each column represents one of the redshift bins (from left to right: 0.35, 0.55, 0.8). The dashed (solid) lines represent the theoretical prediction (E_G in eq.(4.27)) for GR (F5). The black lines represent the observable quantities ($\hat{E}_G^{\rm Wenzl}$ in eq.(4.49)) with theoretical C_ℓs. The plots below show the respective relative difference of $\hat{E}_G^{\rm Wenzl}$ and $\hat{E}_G^{\rm Pullen}$ with respect to the theoretical prediction using the same color legend. The F5 relative difference is not included due to overlapping since it is the same difference as for the same model in GR.

C.2 Additional plots for E_G and β PDF

In this section we show the same plots for Figure 4.7 but for the other two redshift bins used in this work: z=0.35 (Figure C.2) and z=0.8 (Figure C.3).

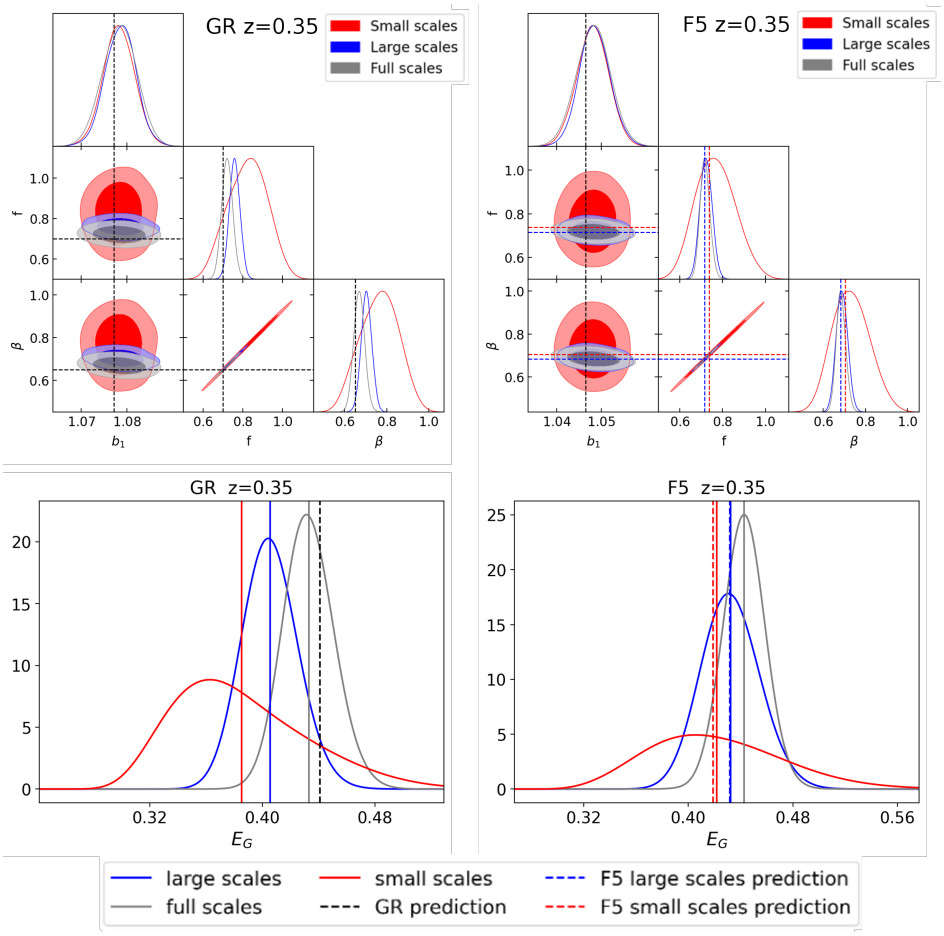

FIGURE C.2: Same as plot 4.7 but for the lowest redshift bin z=0.35. Top plots show the contours results for b_1 and f and the corresponding derived β parameter for small, large, and full scales for GR (Left) and F5 (Right). The dashed lines show the predictions for f and b_1 (estimated from the C_ℓs) for GR (black), and F5 small (red) and large (blue) scales. The bottom plots show the PDF for the EG estimator for the respective scales, the solid lines show the mean of the respective same color PDF while the dashed lines represent the predictions for the same cases discussed earlier.

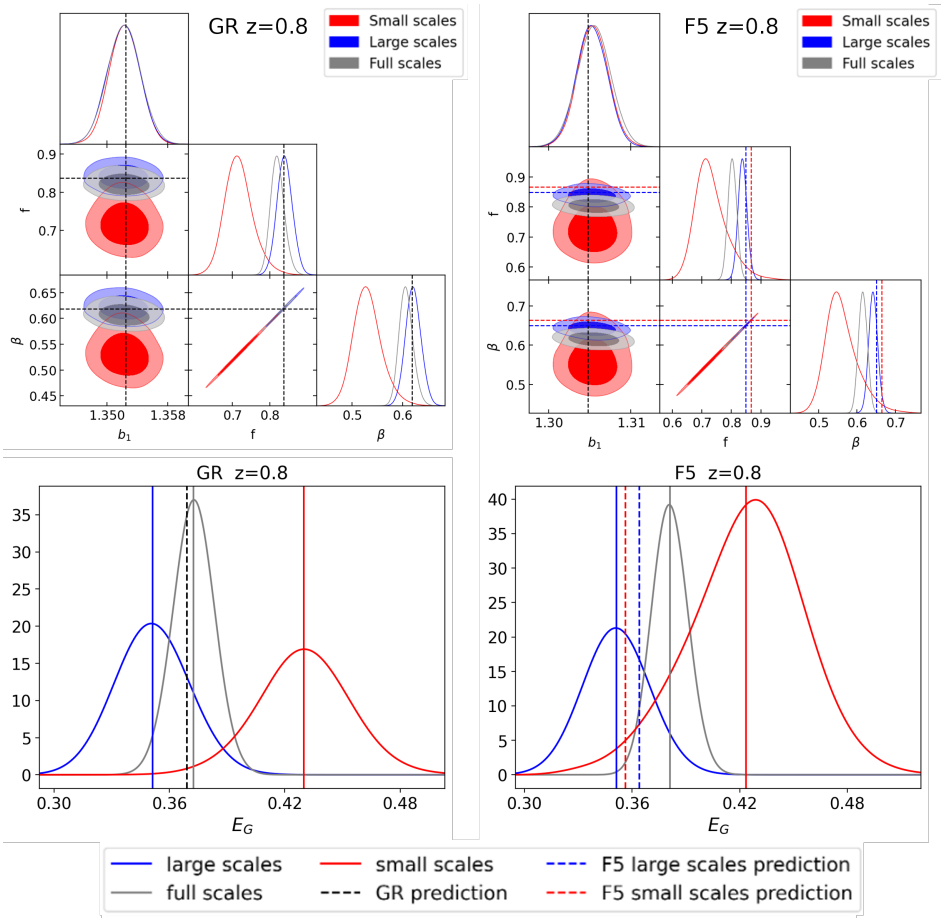

FIGURE C.3: Same as Figure C.2 but for the highest redshift bin z=0.8.

C.3 Full parameter space triangle plots for $z = 0.55$.

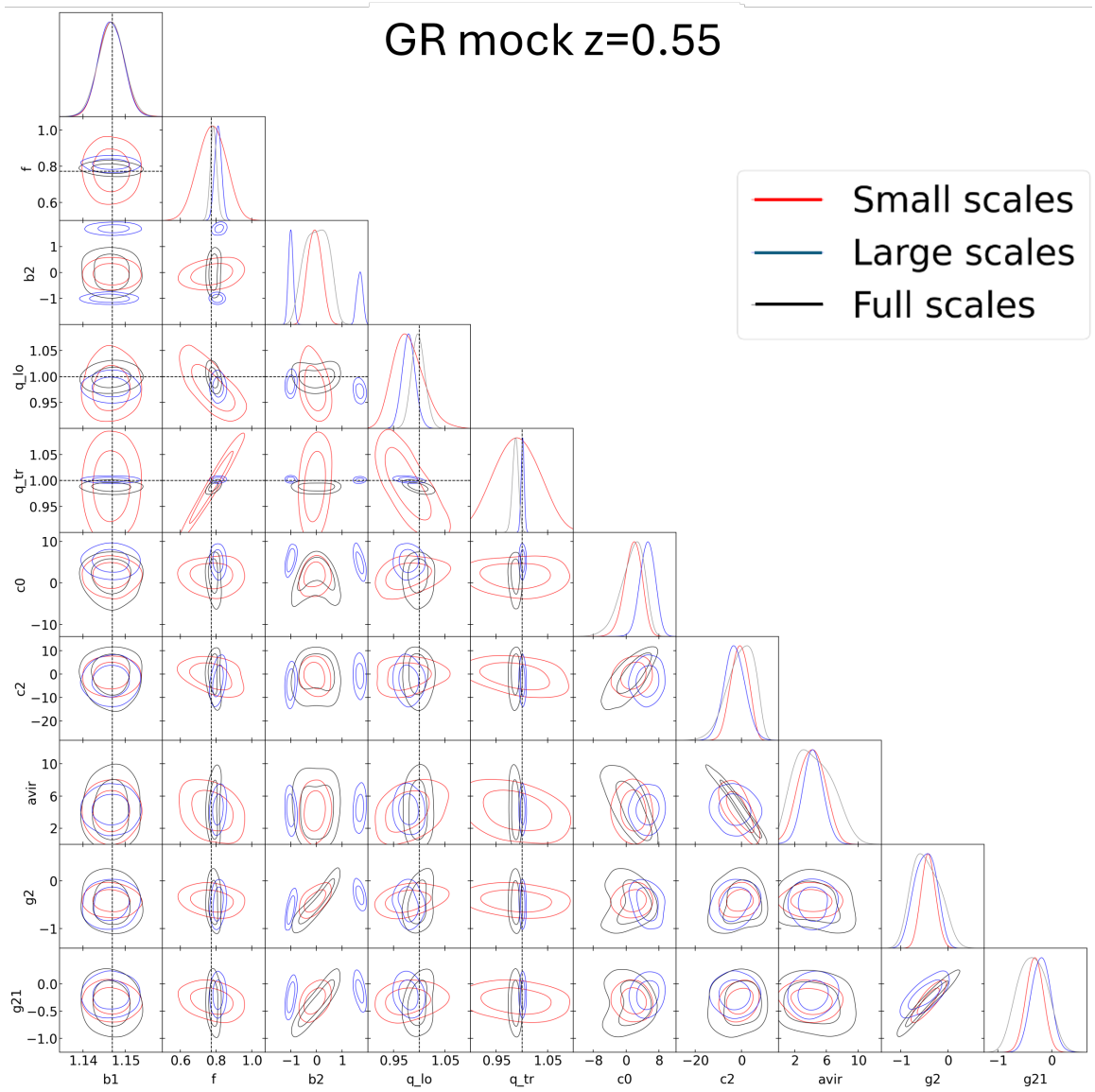

FIGURE C.4: Full triangle plot for the GR mock z=0.55 all galaxies COMET VDG fit. The contours for the small (red), large (blue) and full (black) scales are shown. While the black dashed lines represent the fiducial values of the cosmology of the simulation (b1 is from the C_ℓs fit).

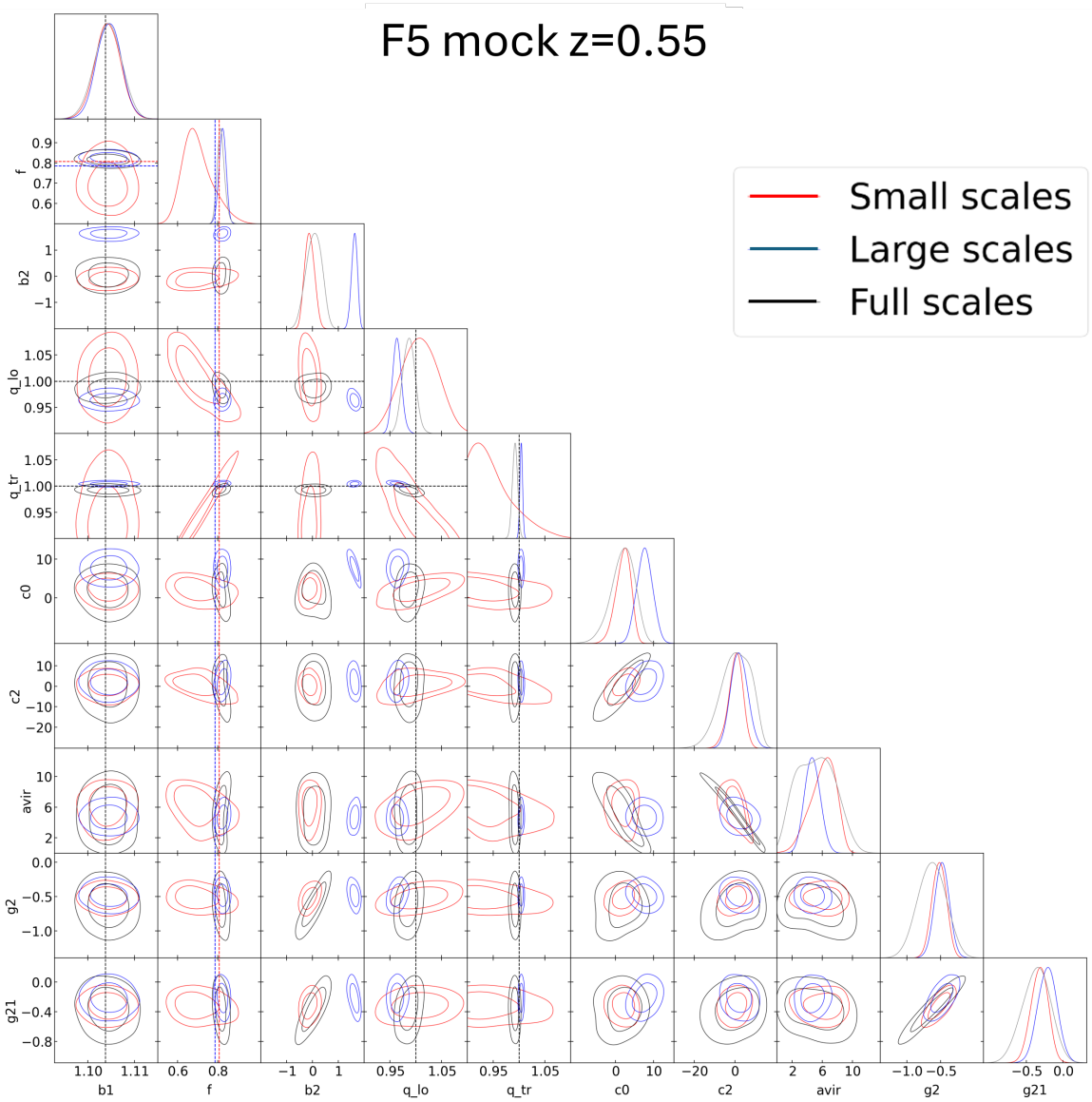

FIGURE C.5: Similar plot as Figure C.4 but for the F5 catalog using COMET VDG F5 theory fits. In this case the fiducial values for the growth rate are divided in small (red) and large (blue) scales.

C.4 An improved estimation of the linear galaxy bias

In section 4.6.1 we estimated the linear galaxy bias using *pyCCL* up to linear theory. In most cases this should be enough since we are estimating the linear bias, but due to the small redshifts used in this work this left us with a small dataset to work with at large (linear) scales since things get nonlinear fast, e.g for $\ell_{max} = 250$ at $z = 0.35$. For this reason we used the non-linear models implemented in *pyCCL* in order to extend the scales over which we can estimate the linear bias by also fitting the nonlinear bias b_2. We use the Eulerian perturbation theory and hybrid Lagrangian bias expansion correlations using the emulator baccoemu [11] to fit b_1 and b_2 over a maximum multipole of 700 independently of the redshift.

The results using the BACCO simulation model are shown in Figure C.6. We can see that for the smallest redshift bin, i.e. z=0.35, the models seems to break down as it is incapable of finding a good fit between data and theory despite that the parameters have converged, which results in a very high reduced χ_ν. The values are consistent with the ones from Table 4.2, although they are not within one sigma errors due to the small error-bars in both cases.

Just as we did in section 4.6.1 we use the values and standard deviation of b_1 obtained here as Gaussian priors for the MCMC. The value for b_2 obtained here are not used as a Gaussian prior since we cannot ensure that the b_2 from Eulerian and Bacco model corresponds to the b_2 from the VDG model. The fitted growth rate did not change much which makes sense since as stated earlier the value of b_1 is close to the one used in the standard case (Table 4.2).

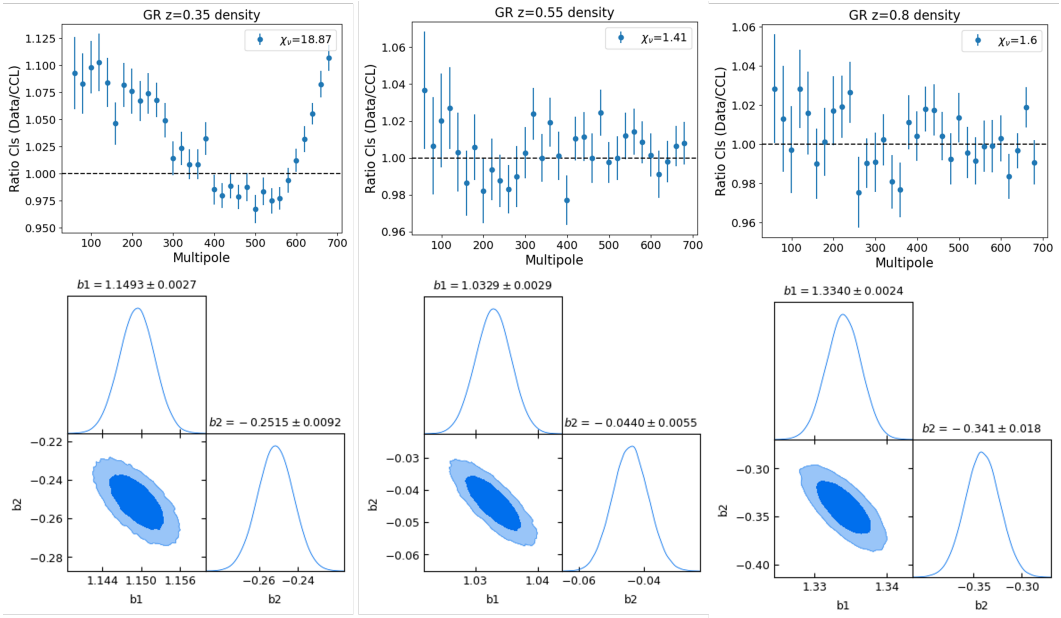

FIGURE C.6: Results for the fitting of the baccoemu nonlinear model to the angular power spectrum DV for $z = 0.35, 0.55$ and 0.8. The upper plots show the ratio of the DV C_ℓs over the best fit theorical C_ℓ obtained with *pyCCL*. The corresponding reduced chi squared is also shown. The lower plots show the tringular plots of the fits for b1 and b2.

Bibliography

[1] T. M. C. Abbott et al. "Dark Energy Survey year 1 results: Constraints on extended cosmological models from galaxy clustering and weak lensing". In: *Physical Review D* 99.12 (June 2019). ISSN: 2470-0029. DOI: 10.1103/physrevd.99.123505. URL: http://dx.doi.org/10.1103/PhysRevD.99.123505.

[2] T. M. C. Abbott et al. "Dark Energy Survey year 1 results: Cosmological constraints from galaxy clustering and weak lensing". In: *Physical Review D* 98.4 (Aug. 2018). ISSN: 2470-0029. DOI: 10.1103/physrevd.98.043526. URL: http://dx.doi.org/10.1103/PhysRevD.98.043526.

[3] T. M. C. Abbott et al. "Dark Energy Survey Year 3 results: Cosmological constraints from galaxy clustering and weak lensing". In: *Physical Review D* 105.2 (Jan. 2022). ISSN: 2470-0029. DOI: 10.1103/physrevd.105.023520. URL: http://dx.doi.org/10.1103/PhysRevD.105.023520.

[4] T.M.C. Abbott et al. "DES Y3 + KiDS-1000: Consistent cosmology combining cosmic shear surveys". In: *The Open Journal of Astrophysics* 6 (Oct. 2023). ISSN: 2565-6120. DOI: 10.21105/astro.2305.17173. URL: http://dx.doi.org/10.21105/astro.2305.17173.

[5] Muntazir M. Abidi et al. "Model-independent test for gravity using intensity mapping and galaxy clustering". In: *Physical Review D* 107.6 (Mar. 2023). ISSN: 2470-0029. DOI: 10.1103/physrevd.107.063514. URL: http://dx.doi.org/10.1103/PhysRevD.107.063514.

[6] P. A. R. Ade et al. "Planck2015 results: XIII. Cosmological parameters". In: *Astronomy andamp; Astrophysics* 594 (Sept. 2016), A13. ISSN: 1432-0746. DOI: 10.1051/0004-6361/201525830. URL: http://dx.doi.org/10.1051/0004-6361/201525830.

[7] N. Aghanim et al. "Planck2018 results: VI. Cosmological parameters". In: *Astronomy and Astrophysics* 641 (Sept. 2020), A6. ISSN: 1432-0746. DOI: 10.1051/0004-6361/201833910. URL: http://dx.doi.org/10.1051/0004-6361/201833910.

[8] Hiroaki Aihara et al. "The Hyper Suprime-Cam SSP Survey: Overview and survey design". In: *Publications of the Astronomical Society of Japan* 70.SP1 (Sept. 2017). ISSN: 2053-051X. DOI: 10.1093/pasj/psx066. URL: http://dx.doi.org/10.1093/pasj/psx066.

[9] Andreas Albrecht et al. *Report of the Dark Energy Task Force*. 2006. URL: https://arxiv.org/abs/astro-ph/0609591.

[10] Luca Amendola et al. "Cosmology and fundamental physics with the Euclid satellite". In: *Living Reviews in Relativity* 21.1 (Apr. 2018). ISSN: 1433-8351. DOI: 10.1007/s41114-017-0010-3. URL: http://dx.doi.org/10.1007/s41114-017-0010-3.

[11] Raul E Angulo et al. "The BACCO simulation project: exploiting the full power of large-scale structure for cosmology". In: *Monthly Notices of the Royal Astronomical Society* 507.4 (July 2021), pp. 5869–5881. ISSN: 0035-8711. DOI: 10.1093/mnras/stab2018. eprint: https://academic.oup.com/mnras/article-pdf/507/4/5869/40419371/stab2018.pdf. URL: https://doi.org/10.1093/mnras/stab2018.

[12] Miguel Aparicio Resco et al. "J-PAS: forecasts on dark energy and modified gravity theories". In: *Monthly Notices of the Royal Astronomical Society* 493.3 (Feb. 2020),

pp. 3616–3631. ISSN: 0035-8711. DOI: 10.1093/mnras/staa367. eprint: https://academic.oup.com/mnras/article-pdf/493/3/3616/32894632/staa367.pdf. URL: https://doi.org/10.1093/mnras/staa367.

[13] Christian Arnold, Matteo Leo, and Baojiu Li. "Realistic simulations of galaxy formation in f(R) modified gravity". In: *Nature Astronomy* 3 (8 July 2019), pp. 917–925. DOI: 10.1038/s41550-019-0823-y. URL: http://arxiv.org/abs/1907.02977http://dx.doi.org/10.1038/s41550-019-0823-y.

[14] Christian Arnold, Volker Springel, and Ewald Puchwein. "Zoomed cosmological simulations of Milky Way-sized haloes in f(R) gravity". In: *MNRAS* 462 (2016), pp. 1530–1541. DOI: 10.1093/mnras/stw1708. URL: https://academic.oup.com/mnras/article/462/2/1530/2589451.

[15] Christian Arnold et al. "forge: the f(R)-gravity cosmic emulator project – I. Introduction and matter power spectrum emulator". In: *Monthly Notices of the Royal Astronomical Society* 515.3 (Aug. 2022), pp. 4161–4175. ISSN: 0035-8711. DOI: 10.1093/mnras/stac1091. eprint: https://academic.oup.com/mnras/article-pdf/515/3/4161/45318804/stac1091.pdf. URL: https://doi.org/10.1093/mnras/stac1091.

[16] Christian Arnold et al. "The modified gravity light-cone simulation project - I. Statistics of matter and halo distributions". In: *mnras* 483.1 (Feb. 2019), pp. 790–805. DOI: 10.1093/mnras/sty3044. arXiv: 1805.09824 [astro-ph.CO].

[17] Marika Asgari et al. "KiDS-1000 cosmology: Cosmic shear constraints and comparison between two point statistics". In: *Astronomy and Astrophysics* 645 (Jan. 2021), A104. ISSN: 1432-0746. DOI: 10.1051/0004-6361/202039070. URL: http://dx.doi.org/10.1051/0004-6361/202039070.

[18] Jacobo Asorey, Martin Crocce, and Enrique Gaztañaga. "Redshift-space distortions from the cross-correlation of photometric populations". In: *Monthly Notices of the Royal Astronomical Society* 445.3 (Oct. 2014), 2825–2835. ISSN: 0035-8711. DOI: 10.1093/mnras/stu1955. URL: http://dx.doi.org/10.1093/mnras/stu1955.

[19] S Avila et al. "Dark Energy Survey Year-1 results: galaxy mock catalogues for BAO". In: *Monthly Notices of the Royal Astronomical Society* 479.1 (May 2018), pp. 94–110. ISSN: 0035-8711. DOI: 10.1093/mnras/sty1389. eprint: https://academic.oup.com/mnras/article-pdf/479/1/94/25111340/sty1389.pdf. URL: https://doi.org/10.1093/mnras/sty1389.

[20] Richard A Battye and Jonathan A Pearson. "Effective action approach to cosmological perturbations in dark energy and modified gravity". In: *Journal of Cosmology and Astroparticle Physics* 2012.07 (July 2012), 019–019. ISSN: 1475-7516. DOI: 10.1088/1475-7516/2012/07/019. URL: http://dx.doi.org/10.1088/1475-7516/2012/07/019.

[21] Anne H. Bauer et al. "Magnification of photometric LRGs by foreground LRGs and clusters in the Sloan Digital Sky Survey". In: *Monthly Notices of the Royal Astronomical Society* 440.4 (Apr. 2014), 3701–3713. ISSN: 0035-8711. DOI: 10.1093/mnras/stu530. URL: http://dx.doi.org/10.1093/mnras/stu530.

[22] Peter S Behroozi, Risa H Wechsler, and Hao-Yi Wu. "THE ROCKSTAR PHASE-SPACE TEMPORAL HALO FINDER AND THE VELOCITY OFFSETS OF CLUSTER CORES". In: *The Astrophysical Journal* 762 (2012), p. 109. DOI: 10.1088/0004-637X/762/2/109. URL: http://code.google.com/p/rockstar..

[23] Andreas A. Berlind and David H. Weinberg. "The Halo Occupation Distribution: Toward an Empirical Determination of the Relation between Galaxies and Mass". In: *The Astrophysical Journal* 575.2 (Aug. 2002), 587–616. ISSN: 1538-4357. DOI: 10.1086/341469. URL: http://dx.doi.org/10.1086/341469.

[24] F. Bernardeau et al. "Large-scale structure of the Universe and cosmological perturbation theory". In: *physrep* 367.1-3 (Sept. 2002), pp. 1–248. DOI: 10.1016/S0370-1573(02)00135-7. arXiv: astro-ph/0112551 [astro-ph].

[25] Gary M. Bernstein. "Shapes and Shears, Stars and Smears: Optimal Measurements for Weak Lensing". In: *The Astrophysical Journal* 695.1 (2009), pp. 652–665. DOI: 10.1088/0004-637X/695/1/652.

[26] Chris Blake and Karl Glazebrook. "Probing Dark Energy Using Baryonic Oscillations in the Galaxy Power Spectrum as a Cosmological Ruler". In: *The Astrophysical Journal* 594.2 (Sept. 2003), pp. 665–673. ISSN: 1538-4357. DOI: 10.1086/376983. URL: http://dx.doi.org/10.1086/376983.

[27] B Bose et al. "Fast and accurate predictions of the non-linear matter power spectrum for general models of Dark Energy and Modified Gravity". In: *Monthly Notices of the Royal Astronomical Society* 519.3 (Jan. 2023), 4780–4800. ISSN: 1365-2966. DOI: 10.1093/mnras/stac3783. URL: http://dx.doi.org/10.1093/mnras/stac3783.

[28] Benjamin Bose et al. "On the road to percent accuracy IV: ReACT – computing the non-linear power spectrum beyond LambdaCDM". In: *Monthly Notices of the Royal Astronomical Society* 498.4 (Sept. 2020), 4650–4662. ISSN: 1365-2966. DOI: 10.1093/mnras/staa2696. URL: http://dx.doi.org/10.1093/mnras/staa2696.

[29] F. R. Bouchet. *Introductory Overview of Eulerian and Lagrangian Perturbation Theories*. 1996. arXiv: astro-ph/9603013 [astro-ph]. URL: https://arxiv.org/abs/astro-ph/9603013.

[30] Anna Cabré and Enrique Gaztañaga. "Clustering of luminous red galaxies - I. Large-scale redshift-space distortions". In: *Monthly Notices of the Royal Astronomical Society* 393.4 (Mar. 2009), 1183–1208. ISSN: 1365-2966. DOI: 10.1111/j.1365-2966.2008.14281.x. URL: http://dx.doi.org/10.1111/j.1365-2966.2008.14281.x.

[31] Anna Cabré and Enrique Gaztañaga. "Clustering of luminous red galaxies - II. Small-scale redshift-space distortions". In: *Monthly Notices of the Royal Astronomical Society* 396.2 (June 2009), 1119–1131. ISSN: 1365-2966. DOI: 10.1111/j.1365-2966.2009.14782.x. URL: http://dx.doi.org/10.1111/j.1365-2966.2009.14782.x.

[32] J. Carretero et al. "An algorithm to build mock galaxy catalogues using MICE simulations". In: *Monthly Notices of the Royal Astronomical Society* 447.1 (Dec. 2014), pp. 646–670. ISSN: 0035-8711. DOI: 10.1093/mnras/stu2402. eprint: https://academic.oup.com/mnras/article-pdf/447/1/646/4911622/stu2402.pdf. URL: https://doi.org/10.1093/mnras/stu2402.

[33] J. Carretero et al. "CosmoHub and SciPIC: Massive cosmological data analysis, distribution and generation using a Big Data platform". In: *Proceedings of the European Physical Society Conference on High Energy Physics. 5-12 July*. July 2017, 488, p. 488.

[34] S. Casas et al. *Euclid: Constraints on f(R) cosmologies from the spectroscopic and photometric primary probes*. June 2023. DOI: 10.48550/arXiv.2306.11053.

[35] Santiago Casas et al. "Constraining gravity with synergies between radio and optical cosmological surveys". In: *Physics of the Dark Universe* 39 (2023), p. 101151. ISSN: 2212-6864. DOI: https://doi.org/10.1016/j.dark.2022.101151. URL: https://www.sciencedirect.com/science/article/pii/S2212686422001248.

[36] Santiago Casas et al. *Linear and non-linear Modified Gravity forecasts with future surveys*. 2017. arXiv: 1703.01271 [astro-ph.CO]. URL: https://arxiv.org/abs/1703.01271.

[37] Matteo Cataneo et al. "New constraints on $f(R)$ gravity from clusters of galaxies". In: *Physical Review D* 92.4 (2014), p. 044009. DOI: 10.1103/PhysRevD.92.044009. URL: http://arxiv.org/abs/1412.0133.

[38] Shi-Fan Chen et al. "Cosmological analysis of three-dimensional BOSS galaxy clustering and Planck CMB lensing cross correlations via Lagrangian perturbation theory".

In: *Journal of Cosmology and Astroparticle Physics* 2022.07 (July 2022), p. 041. ISSN: 1475-7516. DOI: 10.1088/1475-7516/2022/07/041. URL: http://dx.doi.org/10.1088/1475-7516/2022/07/041.

[39] Nora Elisa Chisari et al. "Core Cosmology Library: Precision Cosmological Predictions for LSST". In: *The Astrophysical Journal Supplement Series* 242.1 (May 2019), p. 2. ISSN: 1538-4365. DOI: 10.3847/1538-4365/ab1658. URL: http://dx.doi.org/10.3847/1538-4365/ab1658.

[40] Chia-Hsun Chuang and Yun Wang. "Using Multipoles of the Correlation Function to Measure H(z), D_A(z), and \beta(z) from Sloan Digital Sky Survey Luminous Red Galaxies". In: (May 2012). DOI: 10.1093/mnras/stt357.

[41] Timothy Clifton et al. "Modified gravity and cosmology". In: *Physics Reports* 513.1–3 (Mar. 2012), pp. 1–189. ISSN: 0370-1573. DOI: 10.1016/j.physrep.2012.01.001. URL: http://dx.doi.org/10.1016/j.physrep.2012.01.001.

[42] Dark Energy Survey Collaboration: et al. "The Dark Energy Survey: more than dark energy – an overview". In: *Monthly Notices of the Royal Astronomical Society* 460.2 (Mar. 2016), pp. 1270–1299. ISSN: 0035-8711. DOI: 10.1093/mnras/stw641. eprint: https://academic.oup.com/mnras/article-pdf/460/2/1270/8117541/stw641.pdf. URL: https://doi.org/10.1093/mnras/stw641.

[43] DESI Collaboration et al. "Overview of the Instrumentation for the Dark Energy Spectroscopic Instrument". In: *The Astronomical Journal* 164.5 (Oct. 2022), p. 207. ISSN: 1538-3881. DOI: 10.3847/1538-3881/ac882b. URL: http://dx.doi.org/10.3847/1538-3881/ac882b.

[44] Euclid Collaboration et al. *Euclid. I. Overview of the Euclid mission*. 2024. URL: https://arxiv.org/abs/2405.13491.

[45] Euclid Collaboration et al. *Euclid preparation. Simulations and nonlinearities beyond ΛCDM. 4. Constraints on $f(R)$ models from the photometric primary probes*. 2024. arXiv: 2409.03524 [astro-ph.CO]. URL: https://arxiv.org/abs/2409.03524.

[46] Euclid Collaboration et al. *Euclid Preparation. TBD. Impact of magnification on spectroscopic galaxy clustering*. 2023. arXiv: 2311.03168 [astro-ph.CO]. URL: https://arxiv.org/abs/2311.03168.

[47] Euclid Collaboration et al. *Euclid. V. The Flagship galaxy mock catalogue: a comprehensive simulation for the Euclid mission*. 2024. arXiv: 2405.13495 [astro-ph.CO]. URL: https://arxiv.org/abs/2405.13495.

[48] M. Crocce et al. "Clustering of photometric luminous red galaxies - I. Growth of structure and baryon acoustic feature: RSD and BAO with photometric LRGs from SDSS". In: *Monthly Notices of the Royal Astronomical Society* 417.4 (Sept. 2011), 2577–2591. ISSN: 0035-8711. DOI: 10.1111/j.1365-2966.2011.19425.x. URL: http://dx.doi.org/10.1111/j.1365-2966.2011.19425.x.

[49] M Crocce et al. "The MICE Grand Challenge lightcone simulation – II. Halo and galaxy catalogues". In: *Monthly Notices of the Royal Astronomical Society* 453.2 (Aug. 2015), pp. 1513–1530. ISSN: 1365-2966. DOI: 10.1093/mnras/stv1708. URL: http://dx.doi.org/10.1093/mnras/stv1708.

[50] Guido D'Amico, Leonardo Senatore, and Pierre Zhang. "Limits on wCDM from the EFTofLSS with the PyBird code". In: *J. Cosmol. Astropart. Phys.* 2021.01 (Mar. 2020), p. 006. DOI: 10.1088/1475-7516/2021/01/006.

[51] W. Dehnen and J. I. Read. "N-body simulations of gravitational dynamics". In: *The European Physical Journal Plus* 126.5 (May 2011). ISSN: 2190-5444. DOI: 10.1140/epjp/i2011-11055-3. URL: http://dx.doi.org/10.1140/epjp/i2011-11055-3.

[52] Joseph DeRose et al. *The Buzzard Flock: Dark Energy Survey Synthetic Sky Catalogs*. 2019. arXiv: 1901.02401 [astro-ph.CO]. URL: https://arxiv.org/abs/1901.02401.

[53] Vincent Desjacques, Donghui Jeong, and Fabian Schmidt. "The galaxy power spectrum and bispectrum in redshift space". In: *Journal of Cosmology and Astroparticle Physics* 2018.12 (Dec. 2018), pp. 035–035. ISSN: 1475-7516. DOI: 10.1088/1475-7516/2018/12/035.

[54] Harry Desmond and Pedro G. Ferreira. "Galaxy morphology rules out astrophysically relevant Hu-Sawicki $f(R)$ gravity". In: *Phys. Rev. D* 102.10 (Nov. 2020), p. 104060. DOI: 10.1103/PhysRevD.102.104060.

[55] Arjun Dey et al. "Overview of the DESI Legacy Imaging Surveys". In: *The Astronomical Journal* 157.29pp (2019), p. 168. DOI: 10.3847/1538-3881/ab089d. URL: https://doi.org/10.3847/1538-3881/ab089d.

[56] Eleonora Di Valentino et al. "In the realm of the Hubble tension—a review of solutions *". In: *Classical and Quantum Gravity* 38.15 (July 2021), p. 153001. ISSN: 1361-6382. DOI: 10.1088/1361-6382/ac086d. URL: http://dx.doi.org/10.1088/1361-6382/ac086d.

[57] S. Dodelson. *Gravitational Lensing*. Batavia, IL, 2017.

[58] S. Dodelson. *Modern Cosmology*. 2nd. San Diego, CA: Academic Press, 2021.

[59] Alexander Eggemeier, Roman Scoccimarro, and Robert E. Smith. "Bias Loop Corrections to the Galaxy Bispectrum". In: (Dec. 2018). DOI: 10.1103/PhysRevD.99.123514.

[60] Alexander Eggemeier et al. "COMET: Clustering Observables Modelled by Emulated Perturbation Theory". In: *Monthly Notices of the Royal Astronomical Society* 519 (2023), pp. 2962–2980. DOI: 10.1093/mnras/stac3667. URL: https://doi.org/10.1093/mnras/stac3667.

[61] Xiao Fang et al. "Beyond Limber: Efficient computation of angular power spectra for galaxy clustering and weak lensing". In: (Nov. 2019). DOI: 10.1088/1475-7516/2020/05/010.

[62] F. Feroz, M. P. Hobson, and M. Bridges. "MultiNest: an efficient and robust Bayesian inference tool for cosmology and particle physics". In: *Monthly Notices of the Royal Astronomical Society* 398.4 (Oct. 2009), 1601–1614. ISSN: 1365-2966. DOI: 10.1111/j.1365-2966.2009.14548.x. URL: http://dx.doi.org/10.1111/j.1365-2966.2009.14548.x.

[63] I. Ferrero et al. "Dark Energy Survey Year 3 Results: Galaxy mock catalogs for BAO analysis". In: *Astronomy andamp; Astrophysics* 656 (Dec. 2021), A106. ISSN: 1432-0746. DOI: 10.1051/0004-6361/202141744. URL: http://dx.doi.org/10.1051/0004-6361/202141744.

[64] Daniel Foreman-Mackey et al. "emcee: The MCMC Hammer". In: *Publications of the Astronomical Society of the Pacific* 125.925 (Mar. 2013), pp. 306–312. ISSN: 1538-3873. DOI: 10.1086/670067. URL: http://dx.doi.org/10.1086/670067.

[65] P Fosalba et al. "The MICE Grand Challenge light-cone simulation – III. Galaxy lensing mocks from all-sky lensing maps". In: *Monthly Notices of the Royal Astronomical Society* 447.2 (Dec. 2014), pp. 1319–1332. ISSN: 0035-8711. DOI: 10.1093/mnras/stu2464. URL: http://dx.doi.org/10.1093/mnras/stu2464.

[66] P Fosalba et al. "The MICE grand challenge lightcone simulation – I. Dark matter clustering". In: *Monthly Notices of the Royal Astronomical Society* 448.4 (Mar. 2015), pp. 2987–3000. ISSN: 0035-8711. DOI: 10.1093/mnras/stv138. URL: http://dx.doi.org/10.1093/mnras/stv138.

[67] Pablo Fosalba et al. "The onion universe: all sky lightcone simulations in spherical shells". In: *Mon. Not. R. Astron. Soc* 391 (2008), pp. 435–446. DOI: 10.1111/j.1365-2966.2008.13910.x. URL: https://academic.oup.com/mnras/article/391/1/435/1126601.

[68] Joshua A. Frieman, Michael S. Turner, and Dragan Huterer. "Dark Energy and the Accelerating Universe". In: *Annual Review of Astronomy and Astrophysics* 46.1 (Sept.

2008), 385–432. ISSN: 1545-4282. DOI: 10.1146/annurev.astro.46.060407.145243. URL: http://dx.doi.org/10.1146/annurev.astro.46.060407.145243.

[69] E Gaztanaga et al. "Blending and obscuration in weak-lensing magnification". In: *Monthly Notices of the Royal Astronomical Society* 503.4 (Feb. 2021), 4964–4975. ISSN: 1365-2966. DOI: 10.1093/mnras/stab539. URL: http://dx.doi.org/10.1093/mnras/stab539.

[70] Enrique Gaztañaga et al. "Cross-correlation of spectroscopic and photometric galaxy surveys: cosmology from lensing and redshift distortions: Cosmology from lensing and redshift distortions". In: *Monthly Notices of the Royal Astronomical Society* 422.4 (May 2012), 2904–2930. ISSN: 0035-8711. DOI: 10.1111/j.1365-2966.2012.20613.x. URL: http://dx.doi.org/10.1111/j.1365-2966.2012.20613.x.

[71] Basundhara Ghosh and Ruth Durrer. "The observable Eg statistics". In: *Journal of Cosmology and Astroparticle Physics* 2019.06 (June 2019), 010–010. ISSN: 1475-7516. DOI: 10.1088/1475-7516/2019/06/010. URL: http://dx.doi.org/10.1088/1475-7516/2019/06/010.

[72] Jérôme Gleyzes, David Langlois, and Filippo Vernizzi. "A unifying description of dark energy". In: *International Journal of Modern Physics D* 23.13 (Nov. 2014), p. 1443010. ISSN: 1793-6594. DOI: 10.1142/s021827181443010x. URL: http://dx.doi.org/10.1142/S021827181443010X.

[73] Elizabeth J Gonzalez et al. "Accurate dark-matter halo elongation from weak-lensing stacking analysis". In: *Monthly Notices of the Royal Astronomical Society* 517.4 (Oct. 2022), 4827–4844. ISSN: 1365-2966. DOI: 10.1093/mnras/stac3038. URL: http://dx.doi.org/10.1093/mnras/stac3038.

[74] Elizabeth J. Gonzalez et al. *New catalogue of dark-matter halo properties identified in MICE-GC – I. Analysis of density profile distributions*. 2022. arXiv: 2205.06827 [astro-ph.CO]. URL: https://arxiv.org/abs/2205.06827.

[75] Elizabeth Johana Gonzalez et al. *Cluster halo shapes in CDM and SIDM models: Unveiling the DM particle nature using a weak lensing approach*. 2024. arXiv: 2308.13461 [astro-ph.CO]. URL: https://arxiv.org/abs/2308.13461.

[76] K. M. Gorski et al. "HEALPix: A Framework for High-Resolution Discretization and Fast Analysis of Data Distributed on the Sphere". In: *The Astrophysical Journal* 622.2 (Apr. 2005), 759–771. ISSN: 1538-4357. DOI: 10.1086/427976. URL: http://dx.doi.org/10.1086/427976.

[77] Nastassia Grimm, Camille Bonvin, and Isaac Tutusaus. "Testing General Relativity through the Eg Statistic Using the Weyl Potential and Galaxy Velocities". In: *Physical Review Letters* 133.21 (Nov. 2024). ISSN: 1079-7114. DOI: 10.1103/physrevlett.133.211004. URL: http://dx.doi.org/10.1103/PhysRevLett.133.211004.

[78] A. H. Guth. "The Inflationary Universe: A Possible Solution to the Horizon and Flatness Problems". In: *Physical Review D* 23 (1981), pp. 347–356. DOI: 10.1103/PhysRevD.23.347.

[79] W. J. Handley, M. P. Hobson, and A. N. Lasenby. "PolyChord: nested sampling for cosmology". In: *Monthly Notices of the Royal Astronomical Society: Letters* 450.1 (Apr. 2015), L61–L65. ISSN: 1745-3925. DOI: 10.1093/mnrasl/slv047. URL: http://dx.doi.org/10.1093/mnrasl/slv047.

[80] Catherine Heymans et al. "KiDS-1000 Cosmology: Multi-probe weak gravitational lensing and spectroscopic galaxy clustering constraints". In: *Astronomy and Astrophysics* 646 (Feb. 2021), A140. ISSN: 1432-0746. DOI: 10.1051/0004-6361/202039063. URL: http://dx.doi.org/10.1051/0004-6361/202039063.

[81] K. Hoffmann et al. "Measuring the growth of matter fluctuations with third-order galaxy correlations". In: *Monthly Notices of the Royal Astronomical Society* 447.2 (Dec.

2014), 1724–1745. ISSN: 0035-8711. DOI: 10.1093/mnras/stu2492. URL: http://dx.doi.org/10.1093/mnras/stu2492.

[82] Alireza Hojjati, Levon Pogosian, and Gong-Bo Zhao. "Testing gravity with CAMB and CosmoMC". In: *Journal of Cosmology and Astroparticle Physics* 2011.08 (Aug. 2011), 005–005. ISSN: 1475-7516. DOI: 10.1088/1475-7516/2011/08/005. URL: http://dx.doi.org/10.1088/1475-7516/2011/08/005.

[83] Alireza Hojjati et al. "Searching for scalar gravitational interactions in current and future cosmological data". In: *Physical Review D* 93.4 (Feb. 2016). ISSN: 2470-0029. DOI: 10.1103/physrevd.93.043531. URL: http://dx.doi.org/10.1103/PhysRevD.93.043531.

[84] Bin Hu et al. "Testing Hu–Sawickif(R) gravity with the effective field theory approach". In: *Monthly Notices of the Royal Astronomical Society* 459.4 (Apr. 2016), 3880–3889. ISSN: 1365-2966. DOI: 10.1093/mnras/stw775. URL: http://dx.doi.org/10.1093/mnras/stw775.

[85] Wayne Hu. "Weak lensing of the CMB: A harmonic approach". In: *Physical Review D* 62.4 (July 2000). ISSN: 1089-4918. DOI: 10.1103/physrevd.62.043007. URL: http://dx.doi.org/10.1103/PhysRevD.62.043007.

[86] Wayne Hu and Bhuvnesh Jain. "Joint Galaxy-Lensing Observables and the Dark Energy". In: *Physical Review D* 70.4 (2004), p. 043009. DOI: 10.1103/PhysRevD.70.043009.

[87] Wayne Hu and Ignacy Sawicki. "Models of f(R) cosmic acceleration that evade solar system tests". In: *Physical Review D* 76.6 (Sept. 2007). ISSN: 1550-2368. DOI: 10.1103/physrevd.76.064004. URL: http://dx.doi.org/10.1103/PhysRevD.76.064004.

[88] Mustapha Ishak et al. *Modified Gravity and Dark Energy models Beyond $w(z)$CDM Testable by LSST*. 2019. arXiv: 1905.09687 [astro-ph.CO]. URL: https://arxiv.org/abs/1905.09687.

[89] Mikhail M. Ivanov, Marko Simonović, and Matias Zaldarriaga. "Cosmological parameters from the BOSS galaxy power spectrum". In: *Journal of Cosmology and Astroparticle Physics* 2020.05 (May 2020), 042–042. ISSN: 1475-7516. DOI: 10.1088/1475-7516/2020/05/042. URL: http://dx.doi.org/10.1088/1475-7516/2020/05/042.

[90] Željko Ivezić et al. "LSST: From Science Drivers to Reference Design and Anticipated Data Products". In: *The Astrophysical Journal* 873.44pp (2019), p. 111. DOI: 10.3847/1538-4357/ab042c. URL: https://doi.org/10.3847/1538-4357/ab042c.

[91] Bhuvnesh Jain, Vinu Vikram, and Jeremy Sakstein. "Astrophysical Tests of Modified Gravity: Constraints from Distance Indicators in the Nearby Universe". In: *The Astrophysical Journal* 779.1 (Nov. 2013), p. 39. ISSN: 1538-4357. DOI: 10.1088/0004-637X/779/1/39. URL: http://dx.doi.org/10.1088/0004-637X/779/1/39.

[92] Benjamin Joachimi and Sarah Bridle. "Simultaneous Constraints on Cosmology and Intrinsic Alignments in Cosmic Shear". In: *Astronomy and Astrophysics* 523 (2010), A1. DOI: 10.1051/0004-6361/201015621.

[93] Jelte T. A. de Jong et al. "The Kilo-Degree Survey". In: *Experimental Astronomy* 35.1–2 (Aug. 2012), 25–44. ISSN: 1572-9508. DOI: 10.1007/s10686-012-9306-1. URL: http://dx.doi.org/10.1007/s10686-012-9306-1.

[94] Austin Joyce, Lucas Lombriser, and Fabian Schmidt. "Dark Energy Versus Modified Gravity". In: *Annual Review of Nuclear and Particle Science* 66.1 (Oct. 2016), pp. 95–122. ISSN: 1545-4134. DOI: 10.1146/annurev-nucl-102115-044553. URL: http://dx.doi.org/10.1146/annurev-nucl-102115-044553.

[95] N. Kaiser. "On the spatial correlations of Abell clusters." In: *apjl* 284 (Sept. 1984), pp. L9–L12. DOI: 10.1086/184341.

[96] W. C. Keel. *The Road to Galaxy Formation*. 2nd. Springer Praxis Books. Berlin: Springer, 2007.

[97] Justin Khoury and Amanda Weltman. "Chameleon Cosmology". In: *Physical Review D* 69 (Sept. 2003), p. 044026. DOI: 10.1103/PhysRevD.69.044026. arXiv: astro-ph/0309411 [astro-ph].

[98] Anatoly Klypin et al. *Halo Abundance Matching: accuracy and conditions for numerical convergence*. 2013. arXiv: 1310.3740 [astro-ph.CO]. URL: https://arxiv.org/abs/1310.3740.

[99] E. W. Kolb and M. S. Turner. *The Early Universe*. Vol. 69. Frontiers in Physics. Redwood City, CA: Addison-Wesley, 1990.

[100] Raphaël Kou, Calum Murray, and James G. Bartlett. "Constraining f(R) gravity with cross-correlation of galaxies and cosmic microwave background lensing". In: *Astronomy and Astrophysics* 686 (June 2024), A193. ISSN: 1432-0746. DOI: 10.1051/0004-6361/202348639. URL: http://dx.doi.org/10.1051/0004-6361/202348639.

[101] Kazuya Koyama. "Cosmological tests of modified gravity". In: *Reports on Progress in Physics* 79.4 (Mar. 2016), p. 46902. ISSN: 1361-6633. DOI: 10.1088/0034-4885/79/4/046902. URL: http://dx.doi.org/10.1088/0034-4885/79/4/046902.

[102] K Kuijken et al. "The fourth data release of the Kilo-Degree Survey: ugri imaging and nine-band optical-IR photometry over 1000 square degrees". In: *Astronomy and Astrophysics* 625 (2019). DOI: 10.1051/0004-6361/201834918. URL: https://doi.org/10.1051/0004-6361/201834918.

[103] Stephen D. Landy and Alexander S. Szalay. "Bias and Variance of Angular Correlation Functions". In: *The Astrophysical Journal* 412 (July 1993), p. 64. ISSN: 0004-637X. DOI: 10.1086/172900.

[104] R. Laureijs et al. "Euclid Definition Study Report". In: (2011). arXiv: 1110.3193 [astro-ph.CO]. URL: https://arxiv.org/abs/1110.3193.

[105] Titouan Lazeyras et al. "Precision measurement of the local bias of dark matter halos". In: (Nov. 2015). DOI: 10.1088/1475-7516/2016/02/018.

[106] P. Lemos et al. "Assessing tension metrics with dark energy survey and Planck data". In: *mnras* 505.4 (Aug. 2021), pp. 6179–6194. DOI: 10.1093/mnras/stab1670. arXiv: 2012.09554 [astro-ph.CO].

[107] F. Lepori et al. "Euclid preparation: XIX. Impact of magnification on photometric galaxy clustering". In: *Astronomy and Astrophysics* 662 (June 2022), A93. ISSN: 1432-0746. DOI: 10.1051/0004-6361/202142419. URL: http://dx.doi.org/10.1051/0004-6361/202142419.

[108] F. Lepori et al. *Euclid: Relativistic effects in the dipole of the 2-point correlation function*. 2024. arXiv: 2410.06268 [astro-ph.CO]. URL: https://arxiv.org/abs/2410.06268.

[109] Bruce Margony. "The Sloan Digital Sky Survey". In: *Philosophical Transactions of the Royal Society of London. Series A: Mathematical, Physical and Engineering Sciences* 357.1750 (Jan. 1999). Ed. by G. P. Efstathiou et al., 93–103. ISSN: 1471-2962. DOI: 10.1098/rsta.1999.0316. URL: http://dx.doi.org/10.1098/rsta.1999.0316.

[110] Jérôme Martin. "Everything you always wanted to know about the cosmological constant problem (but were afraid to ask)". In: *Comptes Rendus. Physique* 13.6–7 (July 2012), 566–665. ISSN: 1878-1535. DOI: 10.1016/j.crhy.2012.04.008. URL: http://dx.doi.org/10.1016/j.crhy.2012.04.008.

[111] Renate Mauland, Hans A. Winther, and Cheng Zong Ruan. "Sesame: A power spectrum emulator pipeline for beyond-δCDM models". In: *Astronomy and Astrophysics* 685 (2024). ISSN: 14320746. DOI: 10.1051/0004-6361/202347892.

[112] Nareg Mirzatuny and Elena Pierpaoli. "An Accurate Fitting Function For Scale dependent Growth Rate in Hu-Sawicki f(R) Gravity". In: *Journal of Cosmology and Astroparticle Physics* 2019.09 (June 2019), p. 066. DOI: 10.1088/1475-7516/2019/09/066. arXiv: 1906.07683 [astro-ph.CO]. URL: http://arxiv.org/abs/1906.07683.

[113] Faizan G Mohammad and Will J Percival. "Creating jackknife and bootstrap estimates of the covariance matrix for the two-point correlation function". In: *Monthly Notices of the Royal Astronomical Society* 514.1 (May 2022), 1289–1301. ISSN: 1365-2966. DOI: 10.1093/mnras/stac1458. URL: http://dx.doi.org/10.1093/mnras/stac1458.

[114] Aneesh P Naik et al. "Constraints on chameleon f(R)-gravity from galaxy rotation curves of the SPARC sample". In: *Monthly Notices of the Royal Astronomical Society* 489.1 (Aug. 2019), pp. 771–787. ISSN: 0035-8711. DOI: 10.1093/mnras/stz2131. eprint: https://academic.oup.com/mnras/article-pdf/489/1/771/29218630/stz2131.pdf. URL: https://doi.org/10.1093/mnras/stz2131.

[115] Julio F. Navarro, Carlos S. Frenk, and Simon D. M. White. "The Structure of Cold Dark Matter Halos". In: *The Astrophysical Journal* 462 (May 1996), p. 563. ISSN: 1538-4357. DOI: 10.1086/177173. URL: http://dx.doi.org/10.1086/177173.

[116] Andrina Nicola, Alexandre Refregier, and Adam Amara. "Integrated Bayesian Hierarchical Modeling for Large-Scale Structure Analysis: Weak Lensing and Galaxy Clustering". In: *Physical Review D* 94.8 (2016), p. 083517. DOI: 10.1103/PhysRevD.94.083517.

[117] Hiroaki Oyaizu. "Nonlinear evolution of $f(R)$ cosmologies. I. Methodology". In: *Phys. Rev. D* 78 (12 2008), p. 123523. DOI: 10.1103/PhysRevD.78.123523. URL: https://link.aps.org/doi/10.1103/PhysRevD.78.123523.

[118] P. J. E. Peebles. *The Large-Scale Structure of the Universe*. Princeton, NJ: Princeton University Press, 1980.

[119] P J E Peebles and Bharat Ratra. "The cosmological constant and dark energy". In: *Reviews of Modern Physics* 75.2 (Apr. 2003), pp. 559–606. ISSN: 1539-0756. DOI: 10.1103/revmodphys.75.559. URL: http://dx.doi.org/10.1103/RevModPhys.75.559.

[120] Marcos Pellejero Ibañez et al. "The bacco simulation project: bacco hybrid Lagrangian bias expansion model in redshift space". In: *Monthly Notices of the Royal Astronomical Society* 520.3 (Feb. 2023), 3725–3741. ISSN: 1365-2966. DOI: 10.1093/mnras/stad368. URL: http://dx.doi.org/10.1093/mnras/stad368.

[121] A. Pocino et al. "Euclid preparation: XII. Optimizing the photometric sample of the Euclid survey for galaxy clustering and galaxy-galaxy lensing analyses". In: *Astronomy and Astrophysics* 655 (Nov. 2021), A44. ISSN: 1432-0746. DOI: 10.1051/0004-6361/202141061. URL: http://dx.doi.org/10.1051/0004-6361/202141061.

[122] Anthony R. Pullen, Shadab Alam, and Shirley Ho. "Probing gravity at large scales through CMB lensing". In: *Monthly Notices of the Royal Astronomical Society* 449.4 (Dec. 2014), pp. 4326–4335. DOI: 10.1093/mnras/stv554. URL: http://arxiv.org/abs/1412.4454http://dx.doi.org/10.1093/mnras/stv554.

[123] Anthony R. Pullen et al. "Constraining Gravity at the Largest Scales through CMB Lensing and Galaxy Velocities". In: *Monthly Notices of the Royal Astronomical Society* 460.4 (Aug. 2016), pp. 4098–4108. ISSN: 0035-8711. DOI: 10.1093/mnras/stw1249. URL: https://academic.oup.com/mnras/article-lookup/doi/10.1093/mnras/stw1249.

[124] Nesar Ramachandra et al. "Matter power spectrum emulator for $f(R)$ modified gravity cosmologies". In: *Phys. Rev. D* 103 (Oct. 2020), p. 123525. DOI: 10.1103/PhysRevD.103.123525.

[125] Robert Reischke et al. *KiDS-Legacy: Covariance validation and the unified OneCovariance framework for projected large-scale structure observables*. 2024. arXiv: 2410.06962 [astro-ph.CO]. URL: https://arxiv.org/abs/2410.06962.

[126] Jinsu Rhee, Pascal Elahi, and Sukyoung K Yi. "Performance Enhancement of Tree-based Friends-of-friends Galaxy Finder for High-resolution Simulations of Galaxy Formation". In: *The Astrophysical Journal* 927.1 (Mar. 2022), p. 129. ISSN: 1538-4357. DOI: 10.3847/1538-4357/ac4239. URL: http://dx.doi.org/10.3847/1538-4357/ac4239.

[127] Z. Sakr and M. Martinelli. "Cosmological constraints on sub-horizon scales modified gravity theories with MGCLASS II". In: *Journal of Cosmology and Astroparticle Physics* 2022.05 (May 2022), p. 030. ISSN: 1475-7516. DOI: 10.1088/1475-7516/2022/05/030. URL: http://dx.doi.org/10.1088/1475-7516/2022/05/030.

[128] Ariel G. Sanchez. "Arguments against using Mpc/h units in observational cosmology". In: *Physical Review D* 102.12 (Feb. 2020), p. 123511. DOI: 10.1103/PhysRevD.102.123511. arXiv: 2002.07829 [astro-ph.CO]. URL: http://arxiv.org/abs/2002.07829.

[129] Javier Sánchez, Kazuya Koyama, and Gong-Bo Zhao. "Evolution of the Cosmic Growth Rate in the Quasi-Static Regime". In: *Physical Review Letters* (June 2022). DOI: 10.1103/PhysRevLett.128.241302.

[130] Ignacy Sawicki and Emilio Bellini. "Limits of quasi-static approximation in modified-gravity cosmologies". In: *Phys. Rev. D* 92.8 (Mar. 2015), p. 084061. DOI: 10.1103/PhysRevD.92.084061.

[131] Roman Scoccimarro, H. M. P. Couchman, and Joshua A. Frieman. "The Bispectrum as a Signature of Gravitational Instability in Redshift Space". In: *The Astrophysical Journal* 517.2 (June 1999), 531–540. ISSN: 1538-4357. DOI: 10.1086/307220. URL: http://dx.doi.org/10.1086/307220.

[132] Shun Saito. *Galaxy Clustering in Redshift Space*. June 2016. URL: https://wwwmpa.mpa-garching.mpg.de/~komatsu/lecturenotes/Shun_Saito_on_RSD.pdf.

[133] John Skilling. "Nested sampling for general Bayesian computation". In: *Bayesian Analysis* 1.4 (2006), 833 – 859. DOI: 10.1214/06-BA127. URL: https://doi.org/10.1214/06-BA127.

[134] R. E. Smith et al. "Stable clustering, the halo model and nonlinear cosmological power spectra". In: (July 2002). DOI: 10.1046/j.1365-8711.2003.06503.x.

[135] Volker Springel et al. "Populating a cluster of galaxies – I. Results at z = 0". In: *Monthly Notices of the Royal Astronomical Society* 328.3 (Dec. 2001), pp. 726–750. ISSN: 0035-8711. DOI: 10.1046/j.1365-8711.2001.04912.x. eprint: https://academic.oup.com/mnras/article-pdf/328/3/726/4068642/328-3-726.pdf. URL: https://doi.org/10.1046/j.1365-8711.2001.04912.x.

[136] Sankarshana Srinivasan, Daniel B Thomas, and Peter L. Taylor. *Cosmological gravity on all scales IV: 3x2pt Fisher forecasts for pixelised phenomenological modified gravity*. 2024. arXiv: 2409.06569 [astro-ph.CO]. URL: https://arxiv.org/abs/2409.06569.

[137] Ramon de Sá, Micol Benetti, and Leila Lobato Graef. *An empirical investigation into cosmological tensions*. 2022. arXiv: 2209.11476 [astro-ph.CO]. URL: https://arxiv.org/abs/2209.11476.

[138] Iñigo Sáez-Casares, Yann Rasera, and Baojiu Li. "The e-MANTIS emulator: fast predictions of the non-linear matter power spectrum in f(R)CDM cosmology". In: *Monthly Notices of the Royal Astronomical Society* 527.3 (Nov. 2023), 7242–7262. ISSN: 1365-2966. DOI: 10.1093/mnras/stad3343. URL: http://dx.doi.org/10.1093/mnras/stad3343.

[139] Ariel G. Sánchez et al. "The clustering of galaxies in the completed SDSS-III Baryon Oscillation Spectroscopic Survey: Cosmological implications of the configuration-space clustering wedges". In: *Monthly Notices of the Royal Astronomical Society* 464.2 (Sept. 2016), 1640–1658. ISSN: 1365-2966. DOI: 10.1093/mnras/stw2443. URL: http://dx.doi.org/10.1093/mnras/stw2443.

[140] Ryuichi Takahashi et al. "Revising the Halofit Model for the Nonlinear Matter Power Spectrum". In: *The Astrophysical Journal* 761.2 (Aug. 2012), p. 152. DOI: 10.1088/0004-637X/761/2/152.

[141] P. Tallada et al. "CosmoHub: Interactive exploration and distribution of astronomical data on Hadoop". In: *Astronomy and Computing* 32 (2020), p. 100391. ISSN: 2213-1337. DOI: https://doi.org/10.1016/j.ascom.2020.100391. URL: http://www.sciencedirect.com/science/article/pii/S2213133720300457.

[142] E. Tempel et al. "Friends-of-friends galaxy group finder with membership refinement: Application to the local Universe". In: *Astronomy and Astrophysics* 588 (Mar. 2016), A14. ISSN: 1432-0746. DOI: 10.1051/0004-6361/201527755. URL: http://dx.doi.org/10.1051/0004-6361/201527755.

[143] Daniel B. Thomas. "Cosmological gravity on all scales: Simple equations, required conditions, and a framework for modified gravity". In: *Physical Review D* 101.12 (June 2020). ISSN: 2470-0029. DOI: 10.1103/physrevd.101.123517. URL: http://dx.doi.org/10.1103/PhysRevD.101.123517.

[144] Shinji Tsujikawa et al. "Dispersion of growth of matter perturbations in $f(R)$ gravity". In: *Phys. Rev. D* 80 (8 2009), p. 084044. DOI: 10.1103/PhysRevD.80.084044. URL: https://link.aps.org/doi/10.1103/PhysRevD.80.084044.

[145] Isaac Tutusaus, Camille Bonvin, and Nastassia Grimm. "Measurement of the Weyl potential evolution from the first three years of dark energy survey data". In: *Nature Communications* 15.1, 9295 (Nov. 2024), p. 9295. DOI: 10.1038/s41467-024-53363-6. arXiv: 2312.06434 [astro-ph.CO].

[146] Keiichi Umetsu et al. "CLASH: WEAK-LENSING SHEAR AND MAGNIFICATION ANALYSIS OF 20 GALAXY CLUSTERS". In: *The Astrophysical Journal* 795.2 (Oct. 2014), p. 163. ISSN: 1538-4357. DOI: 10.1088/0004-637x/795/2/163. URL: http://dx.doi.org/10.1088/0004-637X/795/2/163.

[147] Mark Vogelsberger et al. *Cosmological Simulations of Galaxy Formation*. 2019. arXiv: 1909.07976 [astro-ph.GA]. URL: https://arxiv.org/abs/1909.07976.

[148] L. Van Waerbeke and Y. Mellier. *Gravitational Lensing by Large Scale Structures: A Review*. 2003. arXiv: astro-ph/0305089 [astro-ph]. URL: https://arxiv.org/abs/astro-ph/0305089.

[149] R. M. Wald. *General Relativity*. Chicago, IL: University of Chicago Press, 1984.

[150] Zhuangfei Wang et al. "New MGCAMB tests of gravity with CosmoMC and Cobaya". In: *Journal of Cosmology and Astroparticle Physics* 2023.8 (2023), p. 038. DOI: 10.1088/1475-7516/2023/08/038. URL: http://arxiv.org/abs/2305.05667.

[151] David H Weinberg et al. "Observational probes of cosmic acceleration". In: *Physics Reports* 530.2 (Sept. 2013), pp. 87–255. ISSN: 0370-1573. DOI: 10.1016/j.physrep.2013.05.001. URL: http://dx.doi.org/10.1016/j.physrep.2013.05.001.

[152] Lukas Wenzl et al. "Constraining gravity with a new precision Eg estimator using Planck and SDSS BOSS data". In: *Physical Review D* 109.8 (Apr. 2024). ISSN: 2470-0029. DOI: 10.1103/physrevd.109.083540. URL: http://dx.doi.org/10.1103/PhysRevD.109.083540.

[153] Clifford M. Will. *Theory and Experiment in Gravitational Physics*. 2nd. Cambridge, UK: Cambridge University Press, 1993.

[154] Hans A. Winther et al. "Emulators for the nonlinear matter power spectrum beyond ΛCDM". In: *Phys. Rev. D* 100 (12 2019), p. 123540. DOI: 10.1103/PhysRevD.100.123540. URL: https://link.aps.org/doi/10.1103/PhysRevD.100.123540.

[155] Candace Oaxaca Wright and Tereasa G. Brainerd. *Gravitational Lensing by NFW Halos*. 1999. arXiv: astro-ph/9908213 [astro-ph]. URL: https://arxiv.org/abs/astro-ph/9908213.

[156] Shengqi Yang and Anthony R. Pullen. "Calibrating Magnification Bias for the E_G Statistic to Test General Relativity". In: *Monthly Notices of the Royal Astronomical Society* 481.2 (July 2018), pp. 1441–1454. DOI: 10.1093/mnras/sty2353. arXiv: 1807.05639 [astro-ph.CO]. URL: http://arxiv.org/abs/1807.05639.

[157] Donald G York et al. *THE SLOAN DIGITAL SKY SURVEY : TECHNICAL SUMMARY*. Tech. rep. 2000, pp. 1579–1587. URL: www.astro.princeton.edu/PBOOK/welcome.htm..

[158] Matteo Zennaro et al. "Priors on Lagrangian bias parameters from galaxy formation modelling". In: (Oct. 2021). DOI: 10.1093/mnras/stac1673.

[159] Hu Zhan and J Anthony Tyson. "Cosmology with the Large Synoptic Survey Telescope: an overview". In: *Reports on Progress in Physics* 81.6 (Apr. 2018), p. 066901. ISSN: 1361-6633. DOI: 10.1088/1361-6633/aab1bd. URL: http://dx.doi.org/10.1088/1361-6633/aab1bd.

[160] Pengjie Zhang et al. "A discriminating probe of gravity at cosmological scales". In: *Physical Review Letters* 99.14 (Apr. 2007), p. 141302. DOI: 10.1103/PhysRevLett.99.141302. arXiv: 0704.1932 [astro-ph]. URL: http://arxiv.org/abs/0704.1932.

[161] Cheng Zhao. "Fast correlation function calculator: A high-performance pair-counting toolkit". In: *Astronomy and Astrophysics* 672 (Apr. 2023), A83. ISSN: 1432-0746. DOI: 10.1051/0004-6361/202346015. URL: http://dx.doi.org/10.1051/0004-6361/202346015.

[162] Gong-Bo Zhao. "Modeling the nonlinear clustering in modified gravity models. I. A fitting formula for the matter power spectrum of f(R) gravity". In: *Astrophysical Journal Supplement Series* 211.2 (2014), p. 23. DOI: 10.1088/0067-0049/211/2/23.

[163] Gong-Bo Zhao et al. "Searching for modified growth patterns with tomographic surveys". In: *Physical Review D* 79 (8 Sept. 2008), p. 083513. DOI: 10.1103/PhysRevD.79.083513. URL: http://arxiv.org/abs/0809.3791http://dx.doi.org/10.1103/PhysRevD.79.083513.

[164] Alex Zucca et al. "MGCAMB with massive neutrinos and dynamical dark energy". In: *Journal of Cosmology and Astroparticle Physics* 2019.5 (2019), p. 001. DOI: 10.1088/1475-7516/2019/05/001. URL: http://arxiv.org/abs/1901.05956.

[165] J. Zuntz et al. "CosmoSIS: Modular cosmological parameter estimation". In: *Astronomy and Computing* 12 (Sept. 2015), 45–59. ISSN: 2213-1337. DOI: 10.1016/j.ascom.2015.05.005. URL: http://dx.doi.org/10.1016/j.ascom.2015.05.005.